Numerical Study of Interfacial Flow with Surface Tension in Two and Three Dimensions

Thesis by
Hui (Helen) Si

In Partial Fulfillment of the Requirements
for the Degree of
Doctor of Philosophy

California Institute of Technology
Pasadena, California

2000
(Submitted August 12, 1999)

Acknowledgements

Primary acknowledgement must be given to my advisor, Professor Thomas Y. Hou. I owe a great debt for his guidance, encouragement and patience. I also express appreciation to Dr. Hector D. Ceniceros for valuable discussions and suggestions. I would like to thank Professor Issac Klapper, Professor Saleh Tanveer, Professor Stephen Cowley, Professor John Hinch, Professor Monika Nitsche and Professor Pingwen Zhang for their helpful conversations and comments. I thank the many professors and instructors at Caltech who led me through my journey in Applied Mathematics.

Finally, I extend thanks on a personal level. I thank my parents for all they have done for me. I am sure my father, a great scientist and an extraordinary person, would be very proud if he could see this day. I thank the friends I made at Caltech for making my life more enjoyable.

Final and special thanks to my husband, Michael Louie, for all his help and support.

Abstract

In the first part of this thesis, we present new formulations for computing the motion of curvature driven 3-D filament and surface. The new numerical methods have no high order time step stability constraints that are usually associated with curvature regularization. This result generalizes the previous work in [23] for 2-D fluid interfaces with surface tension. Applications to 2-D vortex sheets, the Kirchhoff rod model, nearly anti–parallel vortex filaments, motion by mean curvature in 3-D and simplified water wave model are presented to demonstrate the robustness of the methods. In the second part of this thesis, we investigate numerically the effects of surface tension on the evolution of 2-D Hele-Shaw flows and 3-D axisymmetric flows through porous media with suction. Hele-Shaw flows with suction are known to form cusp singularities in finite time with zero-surface-tension. Our study focuses on identifying how these cusped flows are regularized by the presence of small surface tension, and what the limiting form of the regularization is as surface tension tends to zero. We find that, for nonzero surface tension, the motion continues beyond the zero-surface-tension cusp time, and generically breaks down only when the interface touches the sink. When the viscosity of the surrounding fluid is small or negligible, the interface develops a finger that bulges and later evolves into a wedge as it approaches the sink. Our computations reveal an asymptotic shape of the wedge as surface tension tends to zero. Moreover, for a fixed time past the zero-surface-tension cusp time, the vanishing surface tension solution is singular at the finger neck. The zero-surface-tension cusp splits into two corner singularities in the limiting solution. Larger viscosity in the exterior fluid prevents the formation of the neck and leads to the development of thinner fingers. For 3-D axisymmetric flow, similar behavior is observed. The surface develops a narrow finger which evolves into a cone as it approaches the sink. The finger diameter is smaller than the finger width for Hele-Shaw flow and the surface moves faster. The azimuthal component of the mean curvature enhances the definition of the finger neck while smoothing the interface there.

Contents

List of Figures

List of Tables

Chapter 1

Introduction and Background

Many physical problems involve the time evolution of free interfaces. For example, the evolution of a phase boundary in solidification, the breakup of drops in sprays, multi-fluid interfaces, thin film growth [46, 47], the motion of cells in the blood, and crystal growth and solidification [27, 55]. The complexity of such problems means exact analytical solutions are very difficult to obtain, and accurate numerical computation becomes very important in studying these problems.

The boundary integral method is one well accepted approach to study the interfacial flows numerically. It defines the motion of the interface in terms of integrals along the interface and thereby reduces the dimension of the problem. Boundary integral methods are also advantageous in that they avoid the difficulty of computing derivatives of the quantities which are often discontinuous across the fluid interface. Methods of boundary integral type have been used to compute nonlinear surface waves [3, 49, 52], vortex sheet motion [5, 37, 56], Rayleigh-Taylor instability [2, 49, 62], and interfaces in Hele-Shaw cells [15, 23, 10]. However, numerical simulations using boundary integral methods are still very sensitive to numerical instabilities because of the underlying physical singularity. Hence, straightforward discretizations tend to lead to numerical instabilities.

In many applications, surface tension (curvature) plays an important role on the dynamics of interfaces. We will enhance our understanding of fluid phenomena such as pattern formation in Hele-Shaw cells, the motion of capillary waves on free surfaces and the propagation of sound waves in a porous medium flow if we understand the effect of surface tension better. On the other hand, surface tension introduces terms with high order spatial derivatives both nonlinearly and nonlocally into the governing equations, and this makes the calculations with surface tension even more susceptible to numerical instabilities. If an explicit method is used, these terms induce strong stability constraints on the time step. For two fluid interfaces in Euler flow, the stability constraint is of the

form $\Delta t \leq C \cdot (\Delta s)^{3/2}$, while for Hele-Shaw flow is $\Delta t \leq C \cdot (\Delta s)^3$, where Δt is the size of the time step and Δs is the minimum grid spacing in arclength. In practice, these stability constraints are time dependent and become more severe as points cluster along the interface. A straightforward implicit discretization leads to a nonlinear and nonlocal system which is extremely difficult to invert in general. The presence of such time stability constraint is known as *stiffness*.

In this thesis, we study numerically interfacial flows with surface tension in two and three dimensions using boundary integral method. It is divided into two parts. In the first part, we propose numerical methods to remove the stiffness of surface tension in computing two-dimensional interface and three-dimensional filaments and surfaces. The second part is focused on a careful numerical study of two-dimensional Hele-Shaw flow with suction and three-dimensional axisymmetric flow with suction through porous media.

1.1 Removing Stiffness of Surface Tension in Two and Three Dimensions

In [23], Hou, Lowengrub and Shelley introduced an efficient method to remove high order stiffness in computing the motion of fluid interfaces with surface tension in two-dimensional, irrotational and incompressible fluids. Their scheme is based on a reformulation of the equations of motion in terms of variables more naturally related to the curvature and on the identification of the small-scale terms that contribute to the stiffness. The natural variables are the tangent angle to the interface θ and the arclength metric $s_\alpha = |z_\alpha|$. In these variables, the surface tension term has a very simple form because curvature $\kappa = \theta_\alpha / s_\alpha$. Furthermore, they introduced a particular tangential force T so that s_α is uniform in α. Thus, s_α evolves as the length of the interface L. This is the so-called θ-L method. Using the small scale decomposition technique, their methods identify the leading order terms and then treat them implicitly in time discretizations.

They performed well-resolved calculations for large times on the motion of a vortex sheet, Hele-Shaw and Boussinesq flows. These interfacial problems that were previously not amenable are now solvable using this method. However, this θ-L method cannot be

generalized directly to three-dimensional filaments or surfaces since the tangent angle is not well defined in three dimensions. In the first part of the thesis, we propose to use curvature κ as the new dynamical variable when computing two and three-dimensional free interfaces with curvature regularization. This is motivated by the θ-L method.

We first derive our κ-L method for computing the motion of two-dimensional interfaces. We apply our method to vortex sheets problem with surface tension which had been well studied in [23]. Our numerical study on this same problem indicates that our new formulation shares the same stability property as the θ-L formulation.

Next we extend our idea of using curvature as the new dynamical variable to three-dimensional filaments. A natural choice to describe a three-dimensional filament is to use curvature and torsion variables as given in the Frènet equations. However, we found that these variables are not suitable for computational purpose; see also [32]. The reason is that the torsion variable may be singular whenever curvature vanishes. This is purely an artificial parameterization singularity. To overcome this difficulty, we propose to use generalized curvatures and the rate of rotation as the dynamical variables, $\kappa_1, \kappa_2, \omega$. These variables can be related to the natural curvature κ and torsion τ variables but also have a physical interpretation in terms of the curvature and twist of a thin non-isotropic rod. As in two dimensions, the total arclength of the filament, $L(t)$, is also used as a dynamical variable. Together we obtain a new set of evolution equations for the filament. We show that by using this reformulation, we can easily remove the stiffness associated with curvature regularization.

To demonstrate the robustness of the method, we apply our method to a number of interesting applications. Our numerical experiments demonstrate convincingly that our methods work well for three-dimensional filament calculations, such as the motion by curvature, the Kirchhoff rod model and anti-parallel vortex filaments. The Kirchhoff rod model has received increasing interest in recent years because it can be used as a model to study the dynamics of proteins and super-coiled DNA [54]. Our numerical calculations reveal some interesting equilibrium states for the Kirchhoff rod model. With our new formulation, we can now afford to perform well resolved and long time computations for problems in computational geometry and computational biology. The dynamics of vortex filaments has been studied analytically and numerically over the past thirty years (see [36]

for references). It has important applications involving secondary three-dimensional instability in mixing layers and boundary layers in high Reynolds number flows. Here we apply our method to study the interaction of anti–parallel vortex filament pair using a simplified model proposed by Klein, Majda and Damodaran [36]. Our results compare well with those obtained in [36]. Our approach can also be applied to the case when the nonlocal term becomes important.

Generalization of our numerical methods to three-dimensional free surfaces is also reported in this thesis. Here we only consider periodic and non-closed surfaces. We begin by constructing two orthogonal directions and defining a curvature in each of those directions. We also define a corresponding arclength variable in each of the directions which we call $u = |\mathbf{X}_{\beta_1}|$ and $v = |\mathbf{X}_{\beta_2}|$. As with the two-dimensional interface case, we can add tangential forces to the system without altering the shape of the surface. In order to simplify the problem, we let $\lambda = |\mathbf{X}_{\beta_1}|/|\mathbf{X}_{\beta_2}|$ be a constant in space but can be time dependent. This determines our choice of the tangential forces. Our method then for three-dimensional surfaces is to use the mean curvature (sum of the principal curvatures in the two orthogonal directions), the corresponding arclength variable in one direction, u, and the ratio of the two arclength variables, λ, as the dynamical variables.

We first test our method on the problem of motion by mean curvature. We show that our methods do indeed remove the stiffness associated with the surface tension. We also apply our method to a simplified water wave model. The numerical simulations of surface waves are very expensive because of the high computational cost of approximating the defining integrals which give the surface velocity and velocity potential. This requires $O(N^4)$ calculations where N is the number of points used in each dimension. In this model equation, we replace the velocity integral by its leading order contribution at high modes and thus, allow us to reduce the operation count to $O(N^2 \log N)$ operations per time step. In [21], Haroldsen and Meiron studied the three-dimensional water waves with zero-surface-tension numerically. We use the same initial condition which is a Gaussian wave. Our numerical simulations on our model equation with surface tension $\tau = 0.0001$ compare well with those reported in [21]. Also, we see almost no difference between this very small surface tension case and the zero-surface-tension case. Hence the simplified model equation captures the same characteristics as the full water wave equations. We do

not observe the stiffness of surface tension using our numerical method. Our robust and efficient method also allows us to consider a wide range of surface tension coefficients. We also experimented with an initial condition of two identical and two different amplitude Gaussian waves Our results are both believable and interesting.

Finally we tested our methods on three-dimensional gravity waves. Two-dimensional deep gravity breaking waves had been studied experimentally and numerically in recent years [43, 11, 12]. But little has been done in the three-dimensional case. We start with a simple sine wave of amplitude ϵ and study its evolution with zero-surface-tension in time. No initial horizontal velocity is applied. By only changing the amplitude ϵ of the initial wave we find very interesting behaviors of the surface evolution. For certain ϵ, a focusing mechanism develops and induces jets which shoot upwards. It suggests cusps will occur but higher resolution is needed to definitively show this. An alternative scenario is obtained by considering smaller ϵ. In this case, the jets reach maximum heights and subsequently fall down. Then the wave rises up at the opposite corners and forms jets at those locations. For an even smaller ϵ, our numerical simulations show that a smooth oscillatory surface motion exists for all times. We have also experimented on gravity waves with small surface tension. By using our reformulation, we do not see the stiffness associated with surface tension.

1.2 Numerical Study of Two-Dimensional Hele-Shaw Flow with Suction and Three-Dimensional Axisymmetric Flow with Suction through Porous Media

Suction driven flows through porous media are of considerable interest to the oil industry. In a recovery process, oil surrounded by water is extracted through a well (sink) via a suction mechanism. Often this type of flow is modeled by the two-dimensional motion of a viscous fluid through a narrow gap between two parallel plates in a device known as a Hele-Shaw Cell. The connection between Hele-Shaw flows and saturated flows through porous media is Darcy's law which is assumed to govern the motion of both types of flows. Darcy's law states that the velocity field is proportional to the gradient of the pressure. The particular case of a Hele-Shaw flow in which a blob of viscous

fluid, surrounded by inviscid or less viscous fluid, is drawn radially into a point sink has attracted considerable attention. The more viscous fluid can be associated with oil, surrounded by water (inviscid fluid), that is recovered through a well (sink). Laboratory experiments [48] show that the surrounding fluid encroaches upon the oil forming long "fingers" which may reach the sink before all the oil is recovered. In the oil analogy, this fingering process could reduce the amount of recoverable oil. In the second part of this thesis, we investigate the two-dimensional Hele-Shaw flow with suction and the axisymmetric flows with suction through porous media using the θ-L method [23].

It is well know that sink flow in a Hele-Shaw cell with zero surface tension can develop finite-time singularities before the fluid interface reaches the sink. These singularities are generally in the form of 3/2-power cusps [25, 51]. From the analytical point of view, very little is known about the Hele-Shaw solutions in the presence of surface tension. There are only short-time existence results [20]. Tian [61] shows that singularity formation is inevitable if the center of the viscous blob is not at the sink. However, the type of singularity is unknown. The singularity could be caused by the interface reaching the sink or by other means.

It is natural to use the knowledge of the zero-surface-tension solutions to study the asymptotic effects of surface tension as a perturbation parameter. However, a perturbation analysis is difficult due to the ill-posedness of the underlying zero-surface-tension problem [17, 26] and to the singular nature of the perturbation. Instead, Howison, Lacey, and Ockendon [25] propose an asymptotic model in which small surface tension would cause the interface in the neighborhood of the cusp to propagate rapidly as a narrow jet, analogous to a thin crack. However, this so-called 'crack' model relies on the notion of a self-similar steady-state solution whose existence is unknown. Thus, the effects of very small surface tension past the cusp time remain unclear.

Here, we investigate numerically how surface tension regularizes the cusped flows and what the limiting form of this regularization is as surface tension tends to zero. We consider the two-phase Hele-Shaw flow, known as the Muskat problem [40], and study also the effects that the viscosity of the surrounding fluid has on the Hele-Shaw sink flow. We employ the θ-L method by Hou, Lowengrub, and Shelley [23]. With high resolution, our computations proceed up to very close to the moment when the interface touches

the sink and the solution breaks down in the classical sense.

Kelly and Hinch [29] study numerically the effects of surface tension on the Hele-Shaw flow with suction when the surrounding fluid is inviscid. Their computations show that surface tension indeed regularizes the cusped flow and that a smooth narrow finger develops past t_c. However, as we show in this thesis, Kelly and Hinch computations lack the high accuracy necessary to capture the interface behavior for sufficiently small surface tension. In addition, for a given surface tension, high resolution is needed to compute the fast interface motion as the finger gets very close to the sink. In fact, recent computations by Nie and Tian [42] provide strong evidence that the flow develops a curvature singularity (in the form of a corner) when the interface reaches the sink. However, Nie and Tian do not address the limiting behavior of the interface as surface tension tends to zero.

Numerical computations of unstable Hele-Shaw flows are known to be difficult due to the ill-posedness of the zero-surface-tension problem [16, 39]. For sufficiently small surface tension, even perturbations at the round-off error level can lead to a rapid growth of the solution high frequency components [6, 15]. In addition, surface tension introduces high order derivative terms that couple with the interface dynamics in a nonlinear and nonlocal manner. These terms lead to a severe time-step stability constraint or stiffness for explicit time-integration schemes. Here, we apply this method to a spectrally accurate discretization in space combined with a fourth-order in time implicit/explicit multi-step scheme.

Our computations focus on the evolution of an initially circular blob of viscous fluid surrounded by less viscous fluid. The blob is drawn into a point sink located inside it but not at its initial center. We find that, for nonzero surface tension, the flow continues beyond the zero-surface-tension cusp time, and breaks down only when the interface touches the sink. When the viscosity of the surrounding fluid is small or negligible, the interface develops a finger that later evolves into a wedge as it approaches the sink. As in the cases reported by Nie and Tian [42], our computations strongly suggest that the Hele-Shaw solutions, for this type of geometry, generically break down by developing a corner at the tip of the wedge when the interface reaches the sink.

Our numerical results show several new interesting phenomena as surface tension

is decreased. An asymptotic shape of the fingers is observed at the late stage of the interface motion and a wedge angle at the tip of the finger is selected in the limit as surface tension tends to zero. Moreover, for sufficiently small values of surface tension a well-defined neck develops at the top of the finger near t_c. The developing finger bulges but, being drawn strongly by the sink, quickly evolves into the wedge. The bulging of the finger contradicts the 'crack' model of Howison *et al.* It is conceivable that the neck and the bulging of the finger are due to the influence of the zero-surface-tension singularity. In fact, our computations suggest that the vanishing surface tension solution is singular at the finger neck, for any fixed time past t_c but not greater than the asymptotic time at which the interface reaches the sink. The continuation solution selected by the limit apparently splits the zero-surface-tension cusp into two corner singularities at the finger neck.

Even in the absence of surface tension, very little is known about the corresponding Muskat problem, i.e., when the viscosity of the surrounding fluid is taken into consideration. We find here that the viscosity of the exterior fluid alone does not prevent the formation of cusps. It only delays them. In the absence of surface tension, we observe generic 3/2-power cusps just as in the case of inviscid exterior fluid. However, as the viscosity ratio is decreased, we find that the zero-surface-tension cusps develop closer to the sink. In the presence of surface tension, the interface behavior for small viscosity ratios differs significantly from that corresponding the case of inviscid exterior fluid. We observe that large viscosity in the exterior fluid prevents the formation of the neck and leads to the development of thinner fingers. The fingers also tend to an asymptotic shape in the limit as surface tension tends to zero. Moreover, the asymptotic angle at the finger tip decreases as the viscosity ratio is reduced, apparently towards the zero angle (cusp) of the zero-viscosity-ratio solution.

Since surface tension acts on the fluid interface by introducing a jump in the pressure proportional to the mean curvature, it is natural to ask what the behavior of the interface would be in a three-dimensional Darcy flow for similar initial conditions. Can topological singularities occur in three dimensions for this particular type of flow? How does the presence of an additional component of the mean curvature affect the fingering process? Next, we investigate numerically these questions. We consider the three-dimensional

axisymmetric flow consisting of a blob of viscous fluid driven through a point sink located inside the blob. The surrounding fluid is assumed inviscid.

We know that boundary integral methods reduce the dimension of the problem by involving only variables on the fluid interface. However, this reduction is done at the expense of introducing singular boundary integrals which are understood in the sense of principal-value integrals. In two-dimensional motion, the boundary integrals can be desingularized and spectrally accurate approximations may be obtained for closed or periodic interfaces in the horizontal direction [57, 56]. In three-dimensional motion, the boundary integrals are much more difficult to treat. In the case of axisymmetric flow, the integrands contain a complex combination of pole and logarithmic singularities. Even if the leading order singularities are extracted, some derivative of the integrands will be singular and as a result standard quadrature rules will have a non-smooth discretization error. Moreover, as noted by Baker *et al.* [4], the integrands change rapidly at the two poles where the surface intersects the axis of symmetry. This makes the accurate evaluation of the principal-value integrals even more difficult to achieve. It is important to note that a non-smooth error, i.e., with many high frequency components whose amplitude are well above machine precision, can quickly lead to numerical instability and cause the computations to break down.

For the axisymmetric flow, de Bernadinis and Moore [7] proposed a quadrature rule with a correction to the vortex ring method to obtain an $O(h^3 \log h)$ approximation. In the vortex ring method the trapezoidal rule is used omitting the self-induced (diagonal) contribution of each vortex ring. However, de Bernadinis and Moore approximation (dBM) yields a non-smooth error which degenerates to $O(h)$ near the symmetry poles. Nitsche [44] has designed an improvement to the dBM quadrature by constructing approximate integrands near the poles. By integrating the difference between the original and approximate integrands, Nitsche obtained a uniform $O(h^3)$ quadrature. Higher order quadratures are also possible by improving the order of the approximate integrands [45]. Nie and Baker [41] have also proposed accurate quadratures for the evaluation of the boundary integrals in axisymmetric flow. Their approximations are based on adaptive local quadratures near the poles. Here, we use Nitsche's quadrature extended to yield a uniform $O(h^5)$ discretization error.

Surface tension introduces additional difficulties to the computation of the dynamically evolving fluid interface. It modifies the pressure on the interface by a term which is proportional to the local mean curvature. As a result, a nonlinear term with high order derivatives is introduced to the interface governing equations through the mean curvature. This surface tension term induces a severe time-step stability constraint for explicit time marching methods. Here, we use a highly accurate and efficient method, θ-L method, developed by Hou *et al.* [23] to remove the stiffness of the time step constraint.

Our numerical results show that the axisymmetric flow with suction in the presence of small surface tension behaves very similar to the corresponding Hele-Shaw flow. We consider an initially spherical blob of viscous fluid surrounded by inviscid fluid. The blob is drawn into an eccentric point sink inside it. Just as in the Hele-Shaw flows, a narrow finger develops. The finger tip evolves into a cone as the interface collapses by reaching the sink. For sufficiently small surface tension, the finger bulges and a well-defined neck forms at the top of the finger. The additional azimuthal component of the mean curvature enhances the definition of the finger neck while smoothing the interface there at the same time. However, this component of the curvature is not large enough to induce the neck to pinch off. The second case we consider is the evolution of a slightly perturbed spherical interface whose associated Hele-Shaw problem was studied numerically by Nie and Tian [42]. As in the Hele-Shaw flow, two long fingers grow close to the axis of symmetry and also appear to develop cones at their tips as they reach the sink. For both initial data, we observe that the axisymmetric flow develops narrower fingers than those found in the Hele-Shaw counterpart. This may be due to the stronger sink force in the three-dimensional flow.

The rest of the thesis is organized as follows. In Chapter 2 we present the numerical methods to remove the stiffness of surface tension in computing two-dimensional interface and three-dimensional filaments. In Chapter 3 we present numerical methods in computing three-dimensional surfaces. The numerical study of two-dimensional flow in Hele-Shaw cell with surface tension is given in Chapter 4, and Chapter 5 is the study of axisymmetric flow with suction through porous media with surface tension.

Chapter 2
Removing the Stiffness of Surface Tension in Computing Two-Dimensional Interfaces and Three-Dimensional Filaments

In this chapter, we present new formulations for computing two-dimensional interfaces and three-dimensional filaments with curvature regularization. In Section 2.1, we derive the κ-L formulation for two-dimensional interfaces, with an application to vortex sheets with surface tension. Section 2.2 is devoted to three-dimensional filaments using the κ_1-κ_2-ω-L formulation. As an example of illustration, we consider the motion of a three-dimensional curve by its local curvature. We then apply this idea to a couple of more interesting applications, the Kirchhoff rod model and the anti–parallel vortex filaments in Sections 2.3 and 2.4. We discuss some practical implementation issues in Section 2.5. Finally, in Section 2.6, we present some numerical results which include vortex sheets with surface tension, motion of a three-dimensional curve by curvature, the Kirchhoff rod model and the anti–parallel vortex filaments.

2.1 The κ-L Formulation for Two-Dimensional Interfaces

In this section, we derive the κ-L method for two-dimensional interfaces. We first motivate the formulation for the simple model problem of motion by curvature. Then we derive the formulation for fluid interfaces, and indicate how the κ-L formulation can be used to remove the stiffness of surface tension for fluid interface problems.

2.1.1 Motion by Curvature

We motivate the κ-L approach by considering the motion by curvature in two dimensions. Let a curve Γ be given by

$$\mathbf{X}(\alpha, t) = (x(\alpha, t), y(\alpha, t)), \qquad \alpha \in [0, 2\pi], \tag{2.1}$$

where α parameterizes the curve. Then $\mathbf{X}$ evolves by

$$\mathbf{X}_t = U\ \hat{\mathbf{n}}, \qquad U = \kappa, \tag{2.2}$$

where $\hat{\mathbf{n}} = (-y_s, x_s)$ is the right-handed normal and the signed curvature κ is given by

$$\kappa = x_s y_{ss} - x_{ss} y_s = \frac{x_\alpha y_{\alpha\alpha} - x_{\alpha\alpha} y_\alpha}{(x_\alpha^2 + y_\alpha^2)^{3/2}}.$$

Here s is arclength, and the s and α derivatives can be exchanged through the relation $\partial/\partial s = (1/s_\alpha)(\partial/\partial\alpha)$, where $s_\alpha = \sqrt{x_\alpha^2 + y_\alpha^2}$. We assume $\mathbf{X}$ is 2π-periodic in α. A "frozen coefficient" linear analysis about an arbitrary smooth solution for Eq. (2.2) gives a time-step stability constraint in the form of $\Delta t \leq C\bar{h}(t)^2$ for an explicit time-integration method, where $\bar{h}(t)$ is the minimum grid spacing at time t. An implicit integration method, like the backward Euler or Crank-Nicholson scheme, would give a more stable discretization. But since curvature is a nonlinear function of the interface position, this would give rise to a nonlinear system for the implicit solution at the next time-step.

The κ-L approach, on the other hand, makes the application of an implicit method much easier. It consists of two steps:

(A) Formulate the evolution using the κ and s_α as the new dynamical variables.

(B) Introduce a change of frame in the parameterization of Γ so that s_α is independent of α and depends only on time. Thus, the equation for s_α becomes an ODE for L, the length of the curve Γ. This reformulation of interface motion is motivated by the θ-L frame in [30] (also see [23]).

We notice that the shape of the curve is determined solely by its normal velocity U.

A tangential motion only results in a change in frame for the parameterization of the curve. Therefore, we can add a tangential force to the dynamics without changing the shape of the curve, i.e.,

$$\mathbf{X}_t = U\ \hat{\mathbf{n}} + T\ \hat{\mathbf{s}},$$

where $\hat{\mathbf{s}} = (x_s, y_s)$ is the unit tangent vector, T is the added tangential velocity which will be determined later. To derive the evolution equations for κ and s_α, we make use of the Frènet equations, $\partial_s \hat{\mathbf{s}} = \kappa \hat{\mathbf{n}}$ and $\partial_s \hat{\mathbf{n}} = -\kappa \hat{\mathbf{s}}$. The evolution equations for s_α and κ are given by

$$s_{\alpha t} = T_\alpha - U\kappa s_\alpha \tag{2.3}$$

$$\kappa_t = \frac{1}{s_\alpha}\left(\frac{U_\alpha}{s_\alpha}\right)_\alpha + \frac{T\kappa_\alpha}{s_\alpha} + U\kappa^2. \tag{2.4}$$

Given s_α and κ, the position $(x(\alpha,t), y(\alpha,t))$ can be reconstructed (see Section 2.4). For motion by curvature, we have $U = \kappa$. The evolution in terms of κ and s_α is

$$s_{\alpha t} = T_\alpha - \kappa^2 s_\alpha \tag{2.5}$$

$$\kappa_t = \frac{1}{s_\alpha}\left(\frac{\kappa_\alpha}{s_\alpha}\right)_\alpha + \frac{T\kappa_\alpha}{s_\alpha} + \kappa^3. \tag{2.6}$$

For an explicit integration method, the stability constraint from the diffusion term is of the form

$$\Delta t < C \cdot (\bar{s}_\alpha h)^2, \tag{2.7}$$

where $\bar{s}_\alpha = \min_\alpha s_\alpha$, and h is the initial grid spacing in α. Therefore, the stability constraint is determined by the minimum grid spacing (i.e., $h s_\alpha \approx \Delta s$), which is time dependent, and for motion by curvature, it is always decreasing.

In the reformulated system consisting of Eqs. (2.5) and (2.6), an implicit discretization becomes much easier since the highest order terms are linear. The discretization can be simplified further if s_α does not depend on α. This can be easily accomplished

by choosing a special tangential velocity T to force s_α to be equal to its mean:

$$s_\alpha = \frac{1}{2\pi}\int_0^{2\pi} s_{\alpha'}(\alpha', t)d\alpha' = \frac{1}{2\pi}L(t), \tag{2.8}$$

where L is the length of the curve Γ. It follows from Eq. (2.5) that T satisfies

$$T_\alpha - \kappa^2 s_\alpha = \frac{1}{2\pi}\int_0^{2\pi}(T_{\alpha'} - \kappa^2 s_{\alpha'})d\alpha',$$

which implies

$$T(\alpha, t) = T(0,t) + \frac{L}{2\pi}\int_0^\alpha \kappa^2 d\alpha' - \frac{\alpha L}{(2\pi)^2}\int_0^{2\pi}\kappa^2 d\alpha'. \tag{2.9}$$

Here $T(0,t)$ is simply an arbitrary change of frame which can be taken to be 0. Now since s_α only depends on time t, but not on α, the PDE for s_α is reduced to an ODE for L, and L and κ evolve by

$$L_t = -\frac{L}{2\pi}\int_0^{2\pi}\kappa^2 d\alpha' \tag{2.10}$$

$$\kappa_t = \left(\frac{2\pi}{L}\right)^2 \kappa_{\alpha\alpha} + \frac{2\pi}{L}T\kappa_\alpha + \kappa^3. \tag{2.11}$$

Notice that the highest order term in Eq. (2.10) has no spatially varying prefactor, an implicit method can be easily applied to the PDE for κ. It is sufficient to treat the leading order terms implicitly, and discretize the lower order terms explicitly. Also, the equation for L is free of stiffness; we can use an explicit method such as the Adams-Bashforth method. Then at every time step, L can be updated explicitly, and the implicit solution κ at the new time-step can be obtained explicitly by using the Fast Fourier Transform.

2.1.2 The Formulation for Two-Dimensional Fluid Interfaces

In the next two subsections, we will show how to generalize the idea presented in the previous subsection to fluid interface problems. The fluid interface problem is more difficult than motion by curvature because it involves nonlocal singular integral operators. To derive an efficient implicit discretization, we also use the so-called "small scale decomposition" technique which separates the leading order contribution of a singular integral

operator from the lower order contributions. Since stiffness enters only at small scales, it is enough to treat the leading order operators implicitly. For fluid interfaces, these leading order intergal operators are the Hilbert transform and its variants. They can be diagonalized using the Fast Fourier transform. Thus we obtain an efficient implicit discretization at the same cost as an explicit method.

We consider the motion of an interface Γ given by $\mathbf{X} = (x(\alpha), y(\alpha))$, separating two inviscid, incompressible and irrotational fluids. The density is assumed to be constant on each side of Γ. The velocity on either side of Γ is evolved according to the incompressible Euler equation

$$\mathbf{u}_{jt} + (\mathbf{u}_j \cdot \nabla)\mathbf{u}_j = -\frac{1}{\rho}\nabla(p_j + \rho_j g y), \qquad \nabla \cdot \mathbf{u}_j = 0. \tag{2.12}$$

Here $j = 1$ is for the fluid below Γ and $j = 2$ for the fluid above, p_j is the pressure, ρ_j is the density, and gy is the gravitational potential. The boundary conditions are:

$$(i) \quad [\mathbf{u}]_\Gamma \cdot \hat{\mathbf{n}} = 0, \qquad \text{the kinematic boundary condition,} \tag{2.13}$$

$$(ii) \quad [p]_\Gamma = \tau\kappa, \qquad \text{the dynamic boundary condition,} \tag{2.14}$$

$$(iii) \quad \mathbf{u}_j(x, y) \to (\pm V_\infty, 0) \text{ as y} \to \pm\infty, \text{ the far field boundary condition} \tag{2.15}$$

where $[\cdot]$ denotes the jump taken from above to below the interface. The velocity has a tangential discontinuity at Γ. The velocity away from Γ has the integral representation (see, e.g., [3]),

$$(u(x, y), v(x, y)) = \frac{1}{2\pi}\int \gamma(\alpha')\frac{(-(y - y(\alpha')), x - x(\alpha'))}{(x - x(\alpha'))^2 + (y - y(\alpha'))^2}d\alpha', \tag{2.16}$$

where γ is called the (unnormalized) vortex sheet strength. The true vortex sheet strength (i.e., the tangential velocity jump) is given by

$$\tilde{\gamma} = \frac{\gamma(\alpha)}{s_\alpha} = [\mathbf{u}]_\Gamma \cdot \hat{\mathbf{s}}. \tag{2.17}$$

While there is a discontinuity in the tangential component of the velocity at Γ, the

normal component, $U(\alpha)$, is continuous and given by (2.16) as

$$U(\alpha) = \mathbf{W} \cdot \hat{\mathbf{n}} \tag{2.18}$$

where

$$\mathbf{W}(\alpha) = \frac{1}{2\pi}\text{P.V.} \int \gamma(\alpha') \frac{(-(y(\alpha) - y(\alpha')), x(\alpha) - x(\alpha'))}{(x(\alpha) - x(\alpha'))^2 + (y(\alpha) - y(\alpha'))^2} d\alpha'. \tag{2.19}$$

The P.V. in front of the integral denotes the principal value integral. This integral is called the Birkhoff-Rott integral. Using the representation (2.16) for the velocity, Euler's equation at the interface and the Laplace-Young condition, the equations of motion for the interface are

$$\mathbf{X}_t = U\ \hat{\mathbf{n}} + T\ \hat{\mathbf{s}} \tag{2.20}$$

$$\begin{aligned} \gamma_t &- \partial_\alpha((T - \mathbf{W} \cdot \hat{\mathbf{s}})\gamma/s_\alpha) \\ &= -2A_\rho(s_\alpha \mathbf{W}_t \cdot \hat{\mathbf{s}} + \frac{1}{8}\partial_\alpha(\gamma/s_\alpha)^2 + g y_\alpha \\ &\quad - (T - \mathbf{W} \cdot \hat{\mathbf{s}})\mathbf{W}_\alpha \cdot \hat{\mathbf{s}}/s_\alpha) + S\kappa_\alpha. \end{aligned} \tag{2.21}$$

Here $A_\rho = (\rho_1 - \rho_2)/(\rho_1 + \rho_2)$ is the Atwood ratio and S is a rescaled surface tension parameter (see [3]). In the special case of $A_\rho = 0$, i.e., $\rho_1 = \rho_2$, the evolution equation is greatly simplified. It is reduced to a vortex sheet equation (see [53]).

2.1.3 The Equations of Motion Reposed

In the previous subsection, boundary integral formulation is given for the motion of a vortex sheet in two-dimensional, inviscid fluid. Numerical stiffness arises through the presence of high order terms (i.e., high spatial derivatives) in the evolution. In this subsection, we reformulate the equations of motion using the Small Scale Decomposition for inertial flows. The Small Scale Decomposition (SSD), which identifies and separates the dominant terms at small spatial scales, was first presented in [23]. The key idea is to identify the leading order contribution of certain singular operators at small spatial scales. Recall that the normal velocity U is given by Eqs. (2.18) and (2.19). Let the complex position of the interface be given by $z(\alpha, t) = x(\alpha, t) + iy(\alpha, t)$, then U can be

expressed as

$$U(\alpha,t) = -\frac{1}{s_\alpha} Im\left\{ \frac{z_\alpha}{2\pi i} P.V. \int_{-\infty}^{+\infty} \frac{\gamma(\alpha',t)}{z(\alpha,t)-z(\alpha',t)} d\alpha' \right\}. \tag{2.22}$$

Note that the kernel in the Birkhoff-Rott integral can be decomposed into two terms:

$$\begin{aligned} \frac{1}{z(\alpha,t)-z(\alpha',t)} &= \frac{1}{z_\alpha(\alpha-\alpha')} \\ &\quad + \left[\frac{1}{z(\alpha,t)-z(\alpha',t)} - \frac{1}{z_\alpha(\alpha-\alpha')} \right]. \end{aligned} \tag{2.23}$$

The most significant contribution comes from the first term on the right-hand side, since the bracketed term is analytic and corresponds to a smoothing operator. Therefore, we obtain the leading order behavior of U at small scales as:

$$U(\alpha,t) \sim \frac{1}{2s_\alpha} \mathcal{H}[\gamma](\alpha,t), \tag{2.24}$$

where $\mathcal{H}$ is the Hilbert transform defined as

$$(\mathcal{H}f)(\alpha) = \frac{1}{\pi} \int_{-\infty}^{+\infty} \frac{f(\alpha')}{\alpha-\alpha'} d\alpha'. \tag{2.25}$$

Its Fourier transform is given by

$$\widehat{(\mathcal{H}f)}(k) = -i(sgn(k))\hat{f}(k). \tag{2.26}$$

The notation $f \sim g$ means that the difference between f and g is smoother than f and g. In terms of the new dynamic variables, κ, s_α and γ, the equations of motion for the inertial vortex sheets are given by Eqs. (2.3), (2.4) and (2.21). Observe that the dominant term in Eq. (2.21) for γ_t is $S\kappa_\alpha$ at small scales. Now, substituting Eq. (2.24) into Eq. (2.4) gives

$$\kappa_t = \frac{1}{s_\alpha} \left(\frac{1}{s_\alpha} \left(\frac{1}{2s_\alpha} \mathcal{H}[\gamma] \right)_\alpha \right)_\alpha + P \tag{2.27}$$

$$\gamma_t = S\kappa_\alpha + Q, \tag{2.28}$$

where P and Q represent lower order terms at small spatial scales. This is the small-scale *decomposition*. If s_α is given, the dominant small scale term is linear in κ and γ, but nonlocal by the virtue of the Hilbert transform. An implicit discretization can be obtained by discretizing the leading order terms implicitly, but treating the lower order terms explicitly. However, if s_α is independent of α, the implicit solution can be obtained easily by the Fast Fourier Transform, just as in the case of motion by curvature. By choosing a particular tangential velocity, s_α can indeed be independent of α.

2.1.4 The κ-L Formulation

As we mentioned before, the tangential velocity T may be introduced into the dynamics without changing the shape of the interface. We can choose the particular expression for T so that s_α does not depend on α in its evolution. As in the case of motion by curvature, s_α is set to be equal to its mean, which is

$$s_\alpha = \frac{1}{2\pi}\int_0^{2\pi} s_{\alpha'}(\alpha', t)d\alpha' = \frac{1}{2\pi}L(t), \tag{2.29}$$

where L is the length of the interface. It follows from Eq. (2.3) that T satisfies the following equation:

$$\begin{aligned} T_\alpha - U\kappa s_\alpha &= \frac{1}{2\pi}\int_0^{2\pi}(T_{\alpha'} - U\kappa s_{\alpha'})d\alpha' \\ \Rightarrow T(\alpha, t) &= T(0,t) + \frac{L}{2\pi}\int_0^{\alpha} U\kappa d\alpha' - \frac{\alpha L}{(2\pi)^2}\int_0^{2\pi} U\kappa d\alpha'. \end{aligned} \tag{2.30}$$

The spatial constant $T(0,t)$ just gives an overall temporal shift in frame. For simplicity, it is taken to be 0. Thus, the expression for T is determined entirely by L, κ and U. Assume that Eq. (2.29) is satisfied initially, then the choice for T in Eq. (2.30) ensures that the constraint (2.29) is satisfied for all time. Now, the evolution of the interface is reformulated in terms of L and κ by

$$L_t = -\frac{L}{2\pi}\int_0^{2\pi}\kappa U d\alpha' \tag{2.31}$$

$$\kappa_t = \left(\frac{2\pi}{L}\right)^2 U_{\alpha\alpha} + \frac{2\pi}{L}T\kappa_\alpha + \kappa^2 U. \tag{2.32}$$

Given U, Eqs. (2.30), (2.31) and (2.32) give a complete formulation of the evolution problem.

The small scale decomposition for the inertial vortex sheets in the κ-L formulation is now given as:

$$\kappa_t = \left(\frac{2\pi}{L}\right)^3 \mathcal{H}[\gamma_{\alpha\alpha}] + P \tag{2.33}$$

$$\gamma_t = S\kappa_\alpha + Q, \tag{2.34}$$

where P and Q denote the lower order terms, which do not contribute to the stiffness, and will be treated explicitly. In Fourier Space, these equations are

$$\hat{\kappa}_t(k) = -i\frac{k^2}{2}\left(\frac{2\pi}{L}\right)^2 |k|\hat{\gamma}(k) + \hat{P}(k) \tag{2.35}$$

$$\hat{\gamma}_t(k) = -iSk\hat{\kappa}(k) + \hat{Q}(k), \tag{2.36}$$

where $\hat{P}$ and $\hat{Q}$ are the Fourier transforms of P and Q in Eqs. (2.33) and (2.34), and i is the imaginary unit. Now the implicit integration scheme can be easily applied together with an explicit discretization of Eq. (2.31). Since the lower order terms, P and Q, are treated explicitly, the implicit solution for κ and γ can be inverted explicitly. This gives an efficient implicit discretization of the fluid interface problem at the same cost as an explicit method. The numerical method in our computation will be discussed in Section 2.4.1.

2.2 The κ_1-κ_2-ω-L Formulation for Three-Dimensional Filaments

In this section, we generalize the κ-L method to three-dimensional filaments. The formulation is more subtle for three-dimensional filaments since there are two normal vectors (e.g., the normal and the bi-normal vectors). It turns out that the choice of orthonormal basis has a significant impact on the computational method. In particular, the conventional Frènet frame for three-dimensional filaments is not suitable for computational purpose. It can give rise to an artificial parameterization singularity when curvature vanishes. To overcome this difficulty, we use a more general orthonormal basis which

corresponds to the κ_1-κ_2-ω-L formulation for three-dimensional filaments.

Let us consider a space curve $\mathbf{X}(s,t) : [0,L] \to R^3$ where s is arc-length and L is the total length of the curve. Alternatively we may parameterize $\mathbf{X}$ by a material coordinate α, i.e., $\mathbf{X}(\alpha,t) : [0,2\pi] \to R^3$. The unit tangent vector along the curve $\mathbf{X}$ is given by $\mathbf{T}(s,t) = (d/ds)\mathbf{X}(s,t)$. A local description of the curve is provided by an appropriate set of coordinate axes. One such set is the Frènet triad consisting of the unit vectors $\mathbf{T}, \mathbf{N}$ and $\mathbf{B}$, the tangent, normal and binormal vectors respectively. This orthonormal triad satisfies the well known Frènet equations

$$\begin{aligned} \mathbf{T}' &= \kappa\mathbf{N} \\ \mathbf{N}' &= -\kappa\mathbf{T} + \tau\mathbf{B} \\ \mathbf{B}' &= -\tau\mathbf{N}, \end{aligned}$$

where a prime denotes $\partial/\partial s$. $\kappa = |d\mathbf{T}/ds|$ is the curvature and $\tau = (\mathbf{N} \times \mathbf{N}_s) \cdot \mathbf{T}$ is the torsion. Now we can write the evolution equation for the curve in the Frènet frame:

$$\mathbf{X}_t(\alpha,t) = \bar{U}\mathbf{N} + \bar{V}\mathbf{B} + \bar{W}\mathbf{T}, \tag{2.37}$$

where $\bar{U}, \bar{V}, \bar{W}$ are the normal, bi-normal and tangential velocity components respectively, each of which can depend on both α and t. In the two-dimensional case, we use s_α and κ as the new dynamical variables. Naturally, we would like to use s_α, κ, and τ as the new dynamical variables for three-dimensional filaments. Using the Frènet equations, we derive the evolution of the curve Γ in terms of s_α, κ, and τ as:

$$s_{\alpha t} = \bar{W}_\alpha - \bar{U}\kappa s_\alpha \tag{2.38}$$

$$\kappa_t = \frac{1}{s_\alpha}\left(\frac{\bar{U}_\alpha}{s_\alpha}\right)_\alpha - \frac{2\tau\bar{V}_\alpha + \tau_\alpha\bar{V} - \bar{W}\kappa_\alpha}{s_\alpha} - \bar{U}(\kappa^2 - \tau^2) \tag{2.39}$$

$$\begin{aligned} \tau_t = \frac{1}{s_\alpha}\left(\frac{\left(\frac{\bar{V}_\alpha}{s_\alpha}\right)_\alpha}{\kappa s_\alpha}\right)_\alpha + \frac{1}{s_\alpha}\left(\frac{2\bar{U}_\alpha\tau + \bar{U}\tau_\alpha - \bar{V}\tau^2 s_\alpha}{\kappa s_\alpha}\right)_\alpha \\ + \frac{\kappa\bar{V}_\alpha + \bar{W}\tau_\alpha}{s_\alpha} + 2\kappa\bar{U}\tau. \end{aligned} \tag{2.40}$$

Consider the natural generalization of motion of a closed curve by local curvature,

namely, $\bar{U} = \kappa, \bar{V} = 0$ in Eq. (2.37). $\bar{W}$ can be added to the motion of equations without altering the shape of the curve. Thus Eqs. (2.38), (2.39) and (2.40) become:

$$s_{\alpha t} = \bar{W}_\alpha - \kappa^2 s_\alpha \tag{2.41}$$

$$\kappa_t = \frac{1}{s_\alpha}\left(\frac{\kappa_\alpha}{s_\alpha}\right)_\alpha + \frac{\bar{W}\kappa_\alpha}{s_\alpha} - \kappa(\kappa^2 - \tau^2) \tag{2.42}$$

$$\tau_t = \frac{1}{s_\alpha}\left(\frac{\tau_\alpha}{s_\alpha}\right)_\alpha + 2\left(\frac{\kappa_\alpha \tau}{\kappa s_\alpha}\right)_\alpha + \frac{\bar{W}\tau_\alpha}{s_\alpha} + 2\kappa^2\tau. \tag{2.43}$$

Now, if s_α is given, the highest order terms in the equations for κ and τ are linear in κ and τ respectively. Thus, an implicit integration method can be applied. Similar to the two-dimensional case, we can choose a special expression for $\bar{W}$ to enforce s_α to be independent of α. Then the highest order terms in Eqs. (2.42) and (2.43) do not have spatially varying prefactors. So the implicit discretization of κ and τ can be updated explicitly. The stability constraint has the form

$$\max_\alpha \left(\frac{2|\kappa_\alpha|}{\kappa s_\alpha}, \frac{|\bar{W}|}{s_\alpha}\right)\Delta t < h. \tag{2.44}$$

Note that the stability constraint depends on curvature. If κ becomes very small, we will get very strong stability constraint in the numerical computation. In fact, in the Frènet triad, $\mathbf{N}$, $\mathbf{B}$ and τ are only defined when the curvature does not vanish. In general $\mathbf{N}$ varies discontinuously through points where $\kappa = 0$ even for smooth curves. This would lead to the blowup of τ since τ depends on $\mathbf{N}_s$. This discontinuity in $\mathbf{N}$ through points where κ vanishes is artificial and is due to a poor choice of coordinate frame. For this reason, the Frénet frame is not a good choice for computational purpose.

Instead, we propose to use a more general orthogonal basis $\mathbf{T}, \mathbf{N}_1, \mathbf{N}_2 = \mathbf{T} \times \mathbf{N}_1$ in our numerical calculation of three-dimensional filaments. The Frènet system is replaced by

$$\begin{aligned} \mathbf{T}' &= \kappa_1 \mathbf{N}_1 - \kappa_2 \mathbf{N}_2 \\ \mathbf{N}_1{}' &= -\kappa_1 \mathbf{T} + \omega \mathbf{N}_2 \\ \mathbf{N}_2{}' &= \kappa_2 \mathbf{T} - \omega \mathbf{N}_1, \end{aligned} \tag{2.45}$$

where $\kappa_1 = \kappa\mathbf{N}\cdot\mathbf{N}_1$ and $\kappa_2 = -\kappa\mathbf{N}\cdot\mathbf{N}_2$.

There are natural relationships between $\kappa_1, \kappa_2, \omega$ and κ, τ:

$$\kappa = \sqrt{\kappa_1^2 + \kappa_2^2} \tag{2.46}$$

$$\tau = \omega + \frac{\kappa_2\kappa_{1s} - \kappa_1\kappa_{2s}}{\kappa}. \tag{2.47}$$

If we make the special choice of $\omega = \tau$, then the new orthonormal basis is reduced to the Frènet triad. In this case, we have $\kappa_1 = \kappa, \kappa_2 = 0$.

The unit tangent vector $\mathbf{T}(s) = (d/ds)\mathbf{X}(s)$ is determined once the curve $\mathbf{X}(s)$ is known. Then we choose vectors $\mathbf{N}_1(0), \mathbf{N}_2(0)$ such that $(\mathbf{T}(0), \mathbf{N}_1(0), \mathbf{N}_2(0))$ are a set of orthonormal vectors. By choosing a smooth function for the rate of rotation, ω, and using the relations $\kappa_1 = \kappa\mathbf{N}\cdot\mathbf{N}_1, \kappa_2 = -\kappa\mathbf{N}\cdot\mathbf{N}_2$, we integrate the last two equations in (2.45) along the arclength, s, to determine $\mathbf{N}_1(s)$ and $\mathbf{N}_2(s)$. Notice that the first equation in (2.45) is automatically satisfied since we have used it to construct κ_1 and κ_2. Thus we obtain a smooth orthonormal basis set $(\mathbf{T}(s), \mathbf{N}_1(s), \mathbf{N}_2(s))$. Clearly, this orthonormal basis is smooth as long as the curvature is smooth, even though the curvature may vanish at some points.

Now we rewrite the evolution equation for the curve in our newly chosen orthonormal basis $(\mathbf{T}, \mathbf{N}_1, \mathbf{N}_2)$:

$$\mathbf{X}_t(\alpha, t) = U\mathbf{N}_1 + V\mathbf{N}_2 + W\mathbf{T}.$$

Since we have relationships between $\mathbf{N}, \mathbf{B}$ and $\mathbf{N}_1, \mathbf{N}_2$, namely

$$\begin{aligned} \kappa\mathbf{N} &= \kappa_1\mathbf{N}_1 - \kappa_2\mathbf{N}_2 \\ \kappa\mathbf{B} &= \kappa_2\mathbf{N}_1 + \kappa_1\mathbf{N}_2, \end{aligned} \tag{2.48}$$

it is straightforward to determine the relationships between U, V, W and $\bar{U}, \bar{V}, \bar{W}$.

The fact that $\mathbf{X}$ has continuous second order derivatives in space and time implies that the cross derivatives of α and t commute. To carry out the computations associated with this relationship it is convenient to write the time derivatives of the basis $\mathbf{T}, \mathbf{N}_1, \mathbf{N}_2$

as

$$\mathbf{T}_t = \Lambda_F \times \mathbf{T}, \quad \mathbf{N}_{1t} = \Lambda_F \times \mathbf{N}_1, \quad \mathbf{N}_{2t} = \Lambda_F \times \mathbf{N}_2, \tag{2.49}$$

where $\Lambda_F(\alpha, t) = \lambda_1 \mathbf{N}_1 + \lambda_2 \mathbf{N}_2 + \lambda_3 \mathbf{T}$ is the rotation vector whose components $\lambda_1, \lambda_2, \lambda_3$ are related to U, V, W and hence $\kappa_1, \kappa_2, \omega$:

$$\begin{aligned} \lambda_1 &= -\frac{V_\alpha}{s_\alpha} - U\omega + W\kappa_2 \\ \lambda_2 &= \frac{U_\alpha}{s_\alpha} - V\omega + W\kappa_1, \end{aligned} \tag{2.50}$$

and λ_3 will be determined later. It can be shown (also see [28]) that the equations of motion for $s_\alpha, \kappa_1, \kappa_2, \omega$ in terms of U, V, W take the form:

$$s_{\alpha t} = W_\alpha + (V\kappa_2 - U\kappa_1)s_\alpha \tag{2.51}$$

$$\begin{aligned} \kappa_{1t} &= \frac{1}{s_\alpha}\left(\frac{U_\alpha}{s_\alpha}\right)_\alpha - \frac{2\omega V_\alpha + \omega_\alpha V - W\kappa_{1\alpha}}{s_\alpha} - U\omega^2 \\ &\quad + \kappa_1(U\kappa_1 - V\kappa_2) + \omega\kappa_2 W - \lambda_3\kappa_2 \end{aligned} \tag{2.52}$$

$$\begin{aligned} \kappa_{2t} &= -\frac{1}{s_\alpha}\left(\frac{V_\alpha}{s_\alpha}\right)_\alpha - \frac{2\omega U_\alpha + \omega_\alpha U - W\kappa_{2\alpha}}{s_\alpha} + V\omega^2 \\ &\quad + \kappa_2(U\kappa_1 - V\kappa_2) - \omega\kappa_1 W - \lambda_3\kappa_1 \end{aligned} \tag{2.53}$$

$$\omega_t = \frac{\kappa_1 V_\alpha + \kappa_2 U_\alpha - \omega W_\alpha}{s_\alpha} + 2\omega(U\kappa_1 - V\kappa_2) + \frac{\lambda_{3\alpha}}{s_\alpha}. \tag{2.54}$$

As a final remark, note that we now have four functions s,κ_1, κ_2 and ω to describe a curve in R^3. ω measures the twist rate of the $\mathbf{N}_1$-$\mathbf{N}_2$ plane around $\mathbf{T}$, and may (e.g., the Kirchhoff rod model) or may not (e.g. motion by curvature) have physical significance.

As in the two-dimensional case, we can choose a tangential velocity W to force s_α to be everywhere equal to its mean,

$$s_\alpha = \frac{1}{2\pi}\int_0^{2\pi} s_{\alpha'}(\alpha', t)d\alpha' = \frac{1}{2\pi}L(t), \tag{2.55}$$

where L is the length of the curve Γ. Specifically

$$\begin{aligned} W_\alpha - (U\kappa_1 - V\kappa_2)s_\alpha &= \frac{1}{2\pi}\int_0^{2\pi}(W_{\alpha'} - (U\kappa_1 - V\kappa_2))s_{\alpha'}d\alpha' \\ \Rightarrow W(\alpha,t) &= \frac{L}{2\pi}\int_0^{\alpha}(U\kappa_1 - V\kappa_2)d\alpha - \frac{\alpha L}{(2\pi)^2}\int_0^{2\pi}(U\kappa_1 - V\kappa_2)d\alpha'. \end{aligned} \tag{2.56}$$

Now since s_α depends only on t and not α, the PDE for s_α reduces to an ODE for L. Equations for L and $\kappa_1, \kappa_2, \omega$ then reduce to

$$L_t = -\frac{L}{2\pi}\int_0^{2\pi}(U\kappa_1 - V\kappa_2)d\alpha' \tag{2.57}$$

$$\begin{aligned} \kappa_{1t} &= \left(\frac{2\pi}{L}\right)^2 U_{\alpha\alpha} - \frac{2\pi}{L}(2\omega V_\alpha + \omega_\alpha V - W\kappa_{1\alpha}) - U\omega^3 \\ &\quad + \kappa_1(U\kappa_1 - V\kappa_2) + \omega\kappa_2 W - \lambda_3\kappa_2 \end{aligned} \tag{2.58}$$

$$\begin{aligned} \kappa_{2t} &= -\left(\frac{2\pi}{L}\right)^2 V_{\alpha\alpha} - \frac{2\pi}{L}(2\omega U\alpha + \omega_\alpha U - W\kappa_{2\alpha}) + V\omega^2 \\ &\quad + \kappa_2(U\kappa_1 - V\kappa_2) - \omega\kappa_1 W - \lambda_3\kappa_1 \end{aligned} \tag{2.59}$$

$$\omega_t = \frac{2\pi}{L}(\kappa_1 V_\alpha + \kappa_2 U_\alpha - \omega W_\alpha) + 2\omega(U\kappa_1 - V\kappa_2) + \frac{2\pi}{L}\lambda_{3\alpha}. \tag{2.60}$$

We now show that for motion by curvature this reformulation leads to efficient implicit discretization. To obtain the velocity in this new basis, we project the original equation $\mathbf{X}_t = \kappa\mathbf{N}$ into the new orthonormal basis. Using the relationships between $\mathbf{N}$ and $\mathbf{N}_1, \mathbf{N}_2$, we have $U = \kappa_1$ and $V = -\kappa_2$. Simply substitute U, V into Eqs. (2.57) – (2.60) and take λ_3 to be 0 (see subsection 2.5.3), we derive the formulation in terms of $\kappa_1, \kappa_2, \omega$ and L as

$$L_t = -\frac{L}{2\pi}\int_0^{2\pi}(\kappa_1^2 + \kappa_2^2)d\alpha' \tag{2.61}$$

$$\begin{aligned} \kappa_{1t} &= \left(\frac{2\pi}{L}\right)^2 \kappa_{1\alpha\alpha} + \frac{2\pi}{L}(2\omega\kappa_{2\alpha} + \omega_\alpha\kappa_2 + W\kappa_{1\alpha}) \\ &\quad + \kappa_1(\kappa_1^2 + \kappa_2^2 - \omega^2) + \omega\kappa_2 W \end{aligned} \tag{2.62}$$

$$\begin{aligned} \kappa_{2t} &= \left(\frac{2\pi}{L}\right)^2 \kappa_{2\alpha\alpha} - \frac{2\pi}{L}(2\omega\kappa_{1\alpha} - \omega_\alpha\kappa_1 + W\kappa_{2\alpha}) \\ &\quad + \kappa_2(\kappa_1^2 + \kappa_2^2 - \omega_2) - \omega\kappa_1 W \end{aligned} \tag{2.63}$$

$$\omega_t = \frac{2\pi}{L}(\kappa_2\kappa_{1\alpha} - \kappa_1\kappa_{2\alpha}). \tag{2.64}$$

As in the two-dimensional case, L and ω can be updated using an explicit integration method. The highest order terms in Eqs. (2.58) and (2.59) do not have spatially varying prefactors. We can invert the implicit discretization for the diffusion terms in the κ_1 and κ_2 equations efficiently.

2.3 Application to the Kirchhoff Rod Model

We now apply our method to the physically interesting problem of the Kirchhoff rod. The study of elastic rods is the subject of continued scientific and mathematical interest. Applications of the dynamics of rods and filaments include the dynamics of proteins and super-coiled DNA [54], writhing instability in fibers and cables [65], three-dimensional scroll waves [64], magnetic flux tubes and the formation of sunspots [38], etc. Under some simplifying assumptions, the motion of an elastic rod filament can be well described by a one-dimensional system of equations. One such set of equations, the Kirchhoff rod equations [31], can be constructed as follows [19]. The rod is represented by its center line $\mathbf{X}(s,t) : [0,L] \to R^3$ and twist (defined below) $\omega(s,t) : [0,L] \to R$. Here s is arclength and L is the length of the rod. For simplicity we assume that the cross section of the filament is always circular with constant radius in space. Define a reference ribbon by a pair of curves $(\mathbf{X}, \mathbf{X} + \epsilon\mathbf{N}_1)$ where $\mathbf{N}_1(s,t) : [0,L] \to R^3$ is a unit vector field such that $\mathbf{N}_1 \cdot \mathbf{T} = 0$ ($\mathbf{T}$ is the unit tangent vector along the curve $\mathbf{X}$) and ϵ is the width of the ribbon. The twist ω (with respect to the reference ribbon $(\mathbf{X}, \mathbf{X} + \epsilon\mathbf{N}_1)$) is defined to be the rotation rate of $\mathbf{N}_1$ around $\mathbf{T}$ moving along $\mathbf{X}$; i.e., $\omega(s,t) = (\mathbf{N}_1(s,t) \times (d/ds)\mathbf{N}_1(s,t)) \cdot \mathbf{T}$. The Frènet triad is a particular choice of ribbon which corresponds to choosing $\mathbf{N}_1 = \mathbf{N}$. Recall that $\mathbf{N}$ has the same direction as $(d/ds)\mathbf{T}(s,t)$. More typically $\mathbf{N}_1$ might point in the direction of one of the principle axes of the cross section of the rod. The equations of motion can be written as

$$\frac{d^2}{dt^2}\mathbf{X} = \frac{d}{ds}\mathbf{F} - \eta_1 \frac{d}{dt}\mathbf{X} + \mathbf{g} \tag{2.65}$$

$$\frac{d}{ds}\mathbf{M} = \mathbf{F} \times \mathbf{T} + \ddot{\theta}|_{\mathbf{x}}\mathbf{T} + \mathbf{W}_1 + \eta_2(\dot{\theta}|_{\mathbf{x}} + \mathbf{W}_2) + \mathbf{H} \tag{2.66}$$

$$\mathbf{M} = \Gamma^{-1}\kappa\mathbf{B} + \omega\mathbf{T}, \tag{2.67}$$

where $\mathbf{g}$ contains the other external forces such as gravity, contact force, etc., Γ and η_i measure respectively the relative energetic importance of twist and flexure and the relative time scales of viscosity and inertia. The rod shearing terms $\mathbf{W}_1$ and $\mathbf{W}_2$ are set to be 0 and Γ to be 1.

We rewrite the velocity of $\mathbf{X}$ in terms of the ribbon basis as

$$\mathbf{X}_t(\alpha, t) = U\mathbf{N}_1 + V\mathbf{N}_2 + W\mathbf{T},$$

where $\mathbf{N}_2 = \mathbf{T} \times \mathbf{N}_1$. To compute the main force $\mathbf{F}$, we decompose it into the local orthonormal ribbon basis:

$$\mathbf{F} = F_1\mathbf{N}_1 + F_2\mathbf{N}_2 + F_T\mathbf{T}.$$

The normal and bi-normal components of $\mathbf{F}$ can be determined immediately from Eqs. (2.66) and (2.67), that is $F_1 = -\kappa_{1s}$ and $F_2 = \kappa_{2s}$. The determination of the tangential force $F_T = F \cdot \mathbf{T}$ is more subtle. We will derive it later. Using Eqs. (2.45), (2.49), (2.65), (2.66) and (2.67), we obtain the evolution equations for $\kappa_1, \kappa_2, \omega$, and s_α as follows:

$$s_{\alpha t} = W_\alpha - (U\kappa_1 - V\kappa_2)s_\alpha \tag{2.68}$$

$$\kappa_{1t} = \frac{1}{s_\alpha}\left(\frac{U_\alpha}{s_\alpha}\right)_\alpha - \frac{2\omega V_\alpha + \omega_\alpha V - W\kappa_{1\alpha}}{s_\alpha} - U\omega^2 + \kappa_1(U\kappa_1 - V\kappa_2) + \omega\kappa_2 W - \lambda_2\kappa_2 \tag{2.69}$$

$$U_t = -\frac{1}{s_\alpha}\left(\frac{\kappa_{1\alpha}}{s_\alpha}\right)_\alpha - \frac{\omega\kappa_{2\alpha}}{s_\alpha} + F_T\kappa_1 - W\lambda_2 + V\lambda_3 - \eta_1 U + g_1 \tag{2.70}$$

$$\kappa_{2t} = -\frac{1}{s_\alpha}\left(\frac{V_\alpha}{s_\alpha}\right)_\alpha - \frac{2\omega U_\alpha + \omega_\alpha U - W\kappa_{2\alpha}}{s_\alpha} + V\omega^2 + \kappa_2(U\kappa_1 - V\kappa_2) - \omega\kappa_1 W - \lambda_2\kappa_1 \tag{2.71}$$

$$V_t = \frac{1}{s_\alpha}\left(\frac{\kappa_{2\alpha}}{s_\alpha}\right)_\alpha - \frac{\omega\kappa_{1\alpha}}{s_\alpha} - F_T\kappa_2 + W\lambda_1 - U\lambda_3 - \eta_1 V + g_2 \tag{2.72}$$

$$\omega_t = \frac{\lambda_{3\alpha}}{s_\alpha} + \frac{\kappa_1 V\alpha + \kappa_2 U\alpha}{s_\alpha} + 2\omega(U\kappa_1 - V\kappa_2) - \omega\frac{W_\alpha}{s_\alpha} \tag{2.73}$$

$$\lambda_{3t} = \frac{\omega_\alpha}{s_\alpha} - \eta_2\frac{\lambda_3}{s_\alpha}, \tag{2.74}$$

where $g_1 = \mathbf{g} \cdot \mathbf{N}_1$ and $g_2 = \mathbf{g} \cdot \mathbf{N}_2$.

Eq. (2.74) is derived from Eqs. (2.66) and (2.67). To see this, we observe that

Eqs. (2.66) and (2.67) give

$$\omega_\alpha = \ddot{\theta}|_{\mathbf{X}} s_\alpha + \eta_2 \dot{\theta}|_{\mathbf{X}}, \tag{2.75}$$

where $\dot{\theta}|_{\mathbf{X}}$ refers to $\dot{\theta}$ at a fixed filament position $\mathbf{X}$ (see [33]) (Here the dot denotes $\partial/\partial t$). If we hold $\mathbf{X}$ steady and allow twisting, we have $\mathbf{N}_{1t} = \lambda_3(\alpha, t)\mathbf{T} \times \mathbf{N}_1$. Over an element of the filament from $\mathbf{X}(\alpha)$ to $\mathbf{X}(\alpha + \Delta\alpha)$

$$\frac{d}{dt}\Delta\theta = \lambda_3(\alpha + \Delta\alpha, t) - \lambda_3(\alpha, t),$$

where $\theta = \int^{s(\alpha)} \omega ds = \int^{\alpha} s_\alpha \omega d\alpha$ is the angle of rotation of the reference ribbon at $\mathbf{X}(\alpha, \mathbf{t})$. Thus when $\mathbf{X}$ is fixed, $\dot{\theta}|_{\mathbf{X}} = \lambda_3$, and $\ddot{\theta}|_{\mathbf{X}} = \dot{\lambda}_3$. Substituting these relations into Eq. (2.75) gives Eq. (2.74).

Now we are going to determine the tension $F_T = F \cdot \mathbf{T}$. From $\frac{\partial \mathbf{X}}{\partial \alpha} = s_\alpha \mathbf{T}$, we get

$$\begin{aligned} \frac{\partial \mathbf{X}}{\partial \alpha} \cdot \frac{\partial \dot{\mathbf{X}}}{\partial \alpha} &= s_\alpha \mathbf{T} \cdot (s_{\alpha t}\mathbf{T} + s_\alpha \mathbf{T}_t) \\ &= s_\alpha s_{\alpha t} = r s_\alpha^2, \end{aligned} \tag{2.76}$$

provided that the rod has prescribed extension rate $r(\alpha, t)$, i.e., $s_{\alpha t} = r(\alpha, t) s_\alpha$, which is true by our choice of W from Eq. (2.56). Differentiating this equation with respect to time t, we get

$$\begin{aligned} \frac{\partial \mathbf{X}}{\partial \alpha} \cdot \frac{\partial \ddot{\mathbf{X}}}{\partial \alpha} &= -\frac{\partial \dot{\mathbf{X}}}{\partial \alpha} \cdot \frac{\partial \dot{\mathbf{X}}}{\partial \alpha} + \dot{r} s_\alpha^2 + 2 r s_\alpha s_{\alpha t} \\ &= s_\alpha^2 (r^2 + \dot{r} - |\mathbf{T}_t|^2). \end{aligned} \tag{2.77}$$

From Eq. (2.49), we get $|\mathbf{T}_t| = \sqrt{\lambda_1^2 + \lambda_2^2}$. It can be shown that λ_1 and λ_2 are related to U, V, W by

$$\begin{aligned} \lambda_1 &= -\frac{V_\alpha}{s_\alpha} - U\omega + W\kappa_2 \\ \lambda_2 &= \frac{U_\alpha}{s_\alpha} - V\omega + W\kappa_1. \end{aligned} \tag{2.78}$$

Furthermore, we have

$$\begin{aligned}\frac{\partial \mathbf{X}}{\partial \alpha}\cdot\frac{\partial \ddot{\mathbf{X}}}{\partial \alpha} &= s_\alpha \mathbf{T}\cdot\frac{\partial}{\partial \alpha}\ddot{\mathbf{X}} \\ &= s_\alpha \mathbf{T}\cdot\frac{\partial}{\partial \alpha}\left(\frac{d\mathbf{F}}{ds}-\eta\frac{d\mathbf{X}}{dt}+\mathbf{g}\right) \\ &= s_\alpha^2 \mathbf{T}\cdot(\mathbf{F}_{ss}+\mathbf{g}_s). \end{aligned} \tag{2.79}$$

Thus F_T satisfies

$$\begin{aligned}\frac{d^2}{ds^2}F_T-(\kappa_1^2+\kappa_2^2)F_T &= 2F_{1s}\kappa_1-2F_{2s}\kappa_2+F_1\kappa_{1s}-F_2\kappa_{2s}-\omega(F_1\kappa_2+F_2\kappa_1) \\ &\quad +\tau^2+\dot{\tau}-(\lambda_1^2+\lambda_2^2)+\kappa_1 g_1-\kappa_2 g_2-\mathbf{g}_{ts}, \end{aligned} \tag{2.80}$$

with $F_1=-\kappa_{1s}$, $F_2=\kappa_{2s}$ and $g_t=\mathbf{g}\cdot\mathbf{T}$. The right-hand side of the equation for F_T depends only on known qualities and hence the tension is determined with the appropriate periodic boundary conditions for closed filaments.

We now summarize the small scale decomposition in the κ_1,κ_2 and ω formulae as follows:

$$\begin{aligned}\kappa_{1t} &\sim \left(\frac{2\pi}{L}\right)^2 U_{\alpha\alpha}+P_1 \\ U_t &\sim -\left(\frac{2\pi}{L}\right)^2 \kappa_{1\alpha\alpha}+Q_1 \\ \kappa_{2t} &\sim -\left(\frac{2\pi}{L}\right)^2 V_{\alpha\alpha}+P_2 \\ V_t &\sim \left(\frac{2\pi}{L}\right)^2 \kappa_{2\alpha\alpha}+Q_2, \end{aligned}$$

with $\omega_t\sim\frac{2\pi}{L}\lambda_{3\alpha}+P_3$ and $\lambda_{3t}\sim\frac{2\pi}{L}\omega_\alpha+Q_3$, where P_i and $Q_i, i=1,2,3$ are the lower order terms. The highest order terms in the equations for $\kappa_1,\kappa_2,U,V,\omega$ and λ_3 now appear linearly. After updating L explicitly, it is a straightforward exercise to apply an implicit integration method to these equations.

2.4 Application to Nearly Parallel Vortex Filaments

Another interesting problem we consider is a nearly parallel pair of vortex filaments. Vortex filaments with large strength and narrow cross section are prominent fluid mechanical structures in mixed layers, boundary layers and trailing wakes. It is interesting to study the interaction of nearly parallel and anti–parallel vortex filaments in high Reynolds number flows. An ensemble of vortex filaments interacts via the three-dimensional Biot-Savart integrals for the induced velocities on the filament centerlines [34]. The induced motion of each filament consists of self- and foreign- induced velocity contributions. It has been shown by Callegari and Ting [9], Klein and Majda [35] and, using a totally different analytical approach, by Klein(1994) and Klein and Knio [34] that the geometrical evolution of the filaments in the regime considered obeys the propagation law

$$\frac{\partial \mathbf{X}_i}{\partial t} = (\ln(\frac{1}{\delta}) + C_i)\frac{\Gamma_i}{4\pi}(\kappa \mathbf{B})_i + Q_i^f + Q_i^{outer}. \tag{2.81}$$

The first term points in the direction of the local binormal vector $\mathbf{B}_i$, and via the expression $\ln(\frac{1}{\delta}) + C_i$, describes the influence of the vortex core structure on the filament motion. Here $\delta \ll 1$ relates to the small effective core sizes and C_i is a quadratically nonlinear functional of the detailed core vorticity distribution of the ith filament(see [9], [35] and [34]). Q_i^f is the filament motion due to non-local self stretching [35] and the foreign-induced velocity Q_i^{outer} has been analyzed in [36]. Klein, Majda and Damodaran derived simplified equations for a pair of interacting vortex filaments in [36]:

$$\frac{\partial \mathbf{X}_i}{\partial t} = \Gamma_i(\kappa \mathbf{B})_i + 2t_0 \times \Gamma_j \frac{\mathbf{X}_i - \mathbf{X}_j}{|\mathbf{X}_i - \mathbf{X}_j|^2}, \tag{2.82}$$

where $t_0 = (0, 0, 1)$ and $i, j = 1, 2$. These simplified equations retain the important physical effects of linearized local self-induction and nonlinear potential vortex interaction among filaments but neglect other non-local effects of self-stretching and mutual induction. Now we apply our method to the nearly parallel vortex filament pair using the equations above. Notice that $\kappa \mathbf{B} = \kappa_2 \mathbf{N}_1 + \kappa_1 \mathbf{N}_2$. Using Eqs. (2.57) – (2.60), it is easy to derive the formulation in terms of $\kappa_{1i}, \kappa_{2i}, \omega_i$ and L_i and the small scale decomposition

in the κ_{1i}, κ_{2i} formulae is as follows:

$$\begin{aligned}
\kappa_{1it} &\sim \Gamma_i \left(\frac{2\pi}{L_i}\right)^2 \kappa_{2i\alpha\alpha} + P_i \\
\kappa_{2it} &\sim -\Gamma_i \left(\frac{2\pi}{L_i}\right)^2 \kappa_{1i\alpha\alpha} + Q_i,
\end{aligned}$$

where P_i and Q_i are the lower order terms, $i = 1, 2$. As before, the implicit solutions are easily obtained using the Fast Fourier Transform.

2.5 Some Implementation Issues

This section is devoted to addressing a few practical implementation issues. This includes the question of what implicit discretization scheme we will use, the reconstruction of the interface from the curvature variable, and the choice of orthogonal basis in the Kirchhoff rod model.

2.5.1 Time-Stepping Considerations

The time integration scheme we used in this thesis is a fourth order multi-step implicit/explicit scheme studied in [1] by Ascher, Ruuth and Wetton. This is one of the better high order implicit/explicit schemes to use in the sense that it has a large stability region. Consider a time-dependent PDE in which the spatial derivatives have been discretized by either central differences or by pseudo-spectral methods. This gives rise to a large system of ODEs in time which typically has the form

$$\frac{du}{dt} = f(u) + \nu g(u), \tag{2.83}$$

where g is a linear operator containing high order derivatives and $f(u)$ is a nonlinear function which we do not want to integrate implicitly in time. To avoid using excessively small time steps, we would like to treat the $\nu g(u)$ implicitly while treating the nonlinear term $f(u)$ explicitly. Typically $f(u)$ involves only first order derivatives from the convective terms, so the stiffness induced from the nonlinear term is not as severe as that from the linear operator $g(u)$.

The fourth order implicit/explicit scheme considered by Ascher, Ruuth and Wetton is given as follows:

$$\frac{1}{\Delta t}(\frac{25}{12}u^{n+1} - 4u^n + 3u^{n-1} - \frac{4}{3}u^{n-2} + \frac{1}{4}u^{n-3}) =$$
$$4f(u^n) - 6f(u^{n-1}) + 4f(u^{n-2}) - f(u^{n-3}) + \nu g(u^{n+1}). \tag{2.84}$$

We simply apply this fourth order implicit/explicit scheme to our problems. For example, we use this scheme in the inertial vortex sheet problem:

$$\kappa_t = \frac{1}{2s_\alpha}\left(\frac{1}{s_\alpha}\left(\frac{1}{2s_\alpha}\mathcal{H}[\gamma]\right)_\alpha\right)_\alpha + P \tag{2.85}$$
$$\gamma_t = S\kappa_\alpha + Q, \tag{2.86}$$

where P and Q represent the lower order terms. We obtain the following time discrete system:

$$\frac{1}{\Delta t}(\frac{25}{12}\kappa^{n+1} - 4\kappa^n + 3\kappa^{n-1} - \frac{4}{3}\kappa^{n-2} + \frac{1}{4}\kappa^{n-3}) =$$
$$\frac{1}{2s_\alpha}\left(\frac{1}{s_\alpha}\left(\frac{1}{2s_\alpha}\mathcal{H}[\gamma^{n+1}]\right)_\alpha\right)_\alpha + 4P^n - 6P^{n-1} + 4P^{n-2} - P^{n-3}$$

and

$$\frac{1}{\Delta t}(\frac{25}{12}\gamma^{n+1} - 4\gamma^n + 3\gamma^{n-1} - \frac{4}{3}\gamma^{n-2} + \frac{1}{4}\gamma^{n-3}) =$$
$$S\kappa_\alpha^{n+1} + 4Q^n - 6Q^{n-1} + 4Q^{n-2} - Q^{n-3}.$$

Then with our special choice of the tangential velocity T, s_α is independent of α, and we can solve for κ^{n+1} and γ^{n+1} explicitly using the Fast Fourier Transform.

2.5.2 Reconstruction of the Interface from Curvature

The construction of the initial equal arclength parameterization is the same as in [23]. The idea is to solve the nonlinear equation for the equal arclength grid points using

Newton's method and Fourier interpolation. The equation that must be solved is

$$\int_0^{\beta_j} s_{\alpha'} d\alpha' = \frac{jh}{2\pi} \int_0^{2\pi} s_{\alpha'} d\alpha' = jh\frac{L}{2\pi},$$

for β_j as $j = 0, .., N$ with $h = 2\pi/N$. Here α is a given parameterization. β_j gives the location of points in the α parameterization that are equally spaced in arclength. L is obtained by trapezoidal integration of $s_{\alpha'}$ over its period.

Moreover, it is important to discuss the reconstruction of the two-dimensional interface (x, y) from (L, κ), and the three-dimensional filament (x, y, z) from $(L, \kappa_1, \kappa_2, \omega)$.

One natural way to reconstruct (x, y) from curvature is to integrate the Frènet equations along the interface. This will generate the tangent vector $\mathbf{T}$. We can then integrate the tangent vector along the interface to obtain the interface position. This involves two numerical integrations for each time step, and we need to keep track of two initial conditions at the beginning point of the interface. An alternative is to use the evolution equation for the interface. Recall that Γ evolves according to $\mathbf{X}_t = U\hat{\mathbf{n}} + T\hat{\mathbf{s}}$. We can reconstruct (x, y) through integration of these original equations. In the inertial vortex sheets problem, we know that

$$U(\alpha, t) \sim \frac{1}{2s_\alpha}\mathcal{H}[\gamma](\alpha, t),$$

so we get

$$\mathbf{X}_t = \frac{1}{2s_\alpha}\mathcal{H}[\gamma]\hat{\mathbf{n}} + P, \tag{2.87}$$

where P includes the lower order terms. In the computation, we treat $\frac{1}{2s_\alpha}\mathcal{H}[\gamma]$ implicitly and all the other terms explicitly. However, due to the numerical error, the points on the curve are no longer equally distributed (i.e., s_α is not exactly $L/(2\pi)$ everywhere). This makes Eq. (2.87) incompatible with Eqs. (2.27) and (2.28). This difficulty is overcome by redistributing (x, y). For example, we can make use of the formula

$$\mathbf{X}_\alpha = \frac{L}{2\pi}\mathbf{T}, \tag{2.88}$$

where $\mathbf{T} = \mathbf{X}_\alpha/|\mathbf{X}_\alpha|$.

We denote the solution of Eq. (2.87) by $\bar{\mathbf{X}}$. Then integrate the equation

$$\mathbf{X}_\alpha = \frac{L}{2\pi|\bar{\mathbf{X}}_\alpha|}\bar{\mathbf{X}}_\alpha \tag{2.89}$$

with respect to α to get $\mathbf{X}$ for the new time step. Of course, in the absence of numerical errors, the coefficient in front of $\bar{\mathbf{X}}_\alpha$ should be 1. We have considered other ways of redistribution, but we have found that this approach gave the best performance numerically. This method of reconstruction using the original evolution equation for $\mathbf{X}$ also applies to three-dimensional surfaces.

In the case of three-dimensional filaments, a space curve Γ evolves according to $\mathbf{X}_t = \bar{U}\mathbf{N} + \bar{V}\mathbf{B} + \bar{W}\mathbf{T}$, where $\mathbf{X} = (x(\alpha,t), y(\alpha,t), z(\alpha,t))$. If we simply reconstruct (x,y,z) by integrating these three equations, we will get a stability constraint of the form $\Delta t \leq Ch^2$, since $\mathbf{N}$ involves a second derivative of $\mathbf{X}$. So, we try to reconstruct $\mathbf{X}$ using the first approach we mentioned earlier. First, we integrate Eq. (2.45) to get the tangential vector $\mathbf{T}$, then integrate Eq. (2.88) to get $\mathbf{X}$. By doing this, we can still have a stability constraint of the form $\Delta t \leq Ch$.

2.5.3 Contact Force in the Kirchhoff Rod Model

In practice, a contact force $\mathbf{g}$ is added to Eq. (2.65) to avoid self crossing of the filament. The contact force becomes important when the rod deforms in such a manner that points separated by large differences in arc-length become close to one another in space. The contact force can be modeled by the following integral formula (see [18])

$$\mathbf{g}(s) = -\int M(s,\sigma)\frac{U'(|r(s)-r(\sigma)|)}{|r(s)-r(\sigma)|}[r(s)-r(\sigma)]d\sigma, \tag{2.90}$$

where U is a self-potential generating a central force between pairs of points along the rod, and M is a mollifier leading to total energy and corresponding, for example, to a nonzero radius of the rod. In our example, we take the potential U to be proportional to $|r(s)-r(\sigma)|^{-9}$.

Another point we should stress is that in the case of motion by curvature, we simply take λ_3 to be 0 which makes the formulation much easier. But this cannot be done in the case of the Kirchhoff rod model. The reason is that in the case of motion by curvature,

we are only concerned with the shape of the curve Γ which is solely determined by the tangential vector. Therefore, we can choose a particular $\mathbf{N}_1$ and $\mathbf{N}_2$ by taking λ_3 to be 0. In the Kirchhoff rod model, we do not just study a space curve. Instead, we study a rod with some thickness. Thus the twist ω is important in the evolution of the rod and in fact depends on λ_3.

2.6 Numerical Results

In this section, the results of numerical simulations are presented for several two and three-dimensional problems. All of these simulations use the appropriate small scale decomposition, together with the associated numerical methods discussed in the previous sections. In Section 2.6.1, we consider motion by curvature in two dimensions for both periodic curves and closed curves. In Section 2.6.2, we consider motion by $\kappa - < \kappa >$ in two dimensions. Section 2.6.3 presents the motion of inertial vortex sheets and the comparison of the κ-L frame with the θ-L frame presented by Hou, Lowengrub and Shelley in [23]. In Section 2.6.4, we compute the motion by curvature in three dimensions and compare the stability constraints using our κ_1-κ_2-ω-L method and a straightforward explicit method in (x, y, z) coordinates. Motions for the Kirchhoff Rod Model and the anti–parallel vortex filaments are presented in Section 2.6.5 and 2.6.6 respectively.

2.6.1 Motion By Curvature in Two Dimensions

In the next two subsections, we perform several numerical tests on motion by curvature in two dimensions to demonstrate the effectiveness of our method. These tests all demonstrate that our reformulated implicit method has only a linear stability constraint, i.e., Δt is of the same order of the spatial mesh size. This linear stability constraint is expected since we treat the convection terms explicitly. From our stability analysis for the convection equation, we can see a dependence of the CFL condition on the maximum curvature. This is also verified numerically.

We consider a plane curve Γ evolving according to

$$\mathbf{X}_t = \kappa\, \hat{\mathbf{n}}. \tag{2.91}$$

In our numerical calculations, we use the length of the curve and the curvature as our dynamic variables. They evolve by Eqs. (2.10) and (2.11). The reconstruction of the position of the curve is done by directly integrating the evolution equation (2.91).

In our first example, we choose the initial curve as $\mathbf{X} = (\alpha + .2\cos(4\pi\alpha), .5\sin(2\pi\alpha)), 0 \leq \alpha \leq 1$. We graph the position of the curve at various times. In Fig. 2.1 (a)-(d), we show the continued evolution of the curve from $t = 0.0$ to $t = 0.08$. There are $N = 128$ mesh points in the unit interval with time step $\Delta t = 0.00025$.

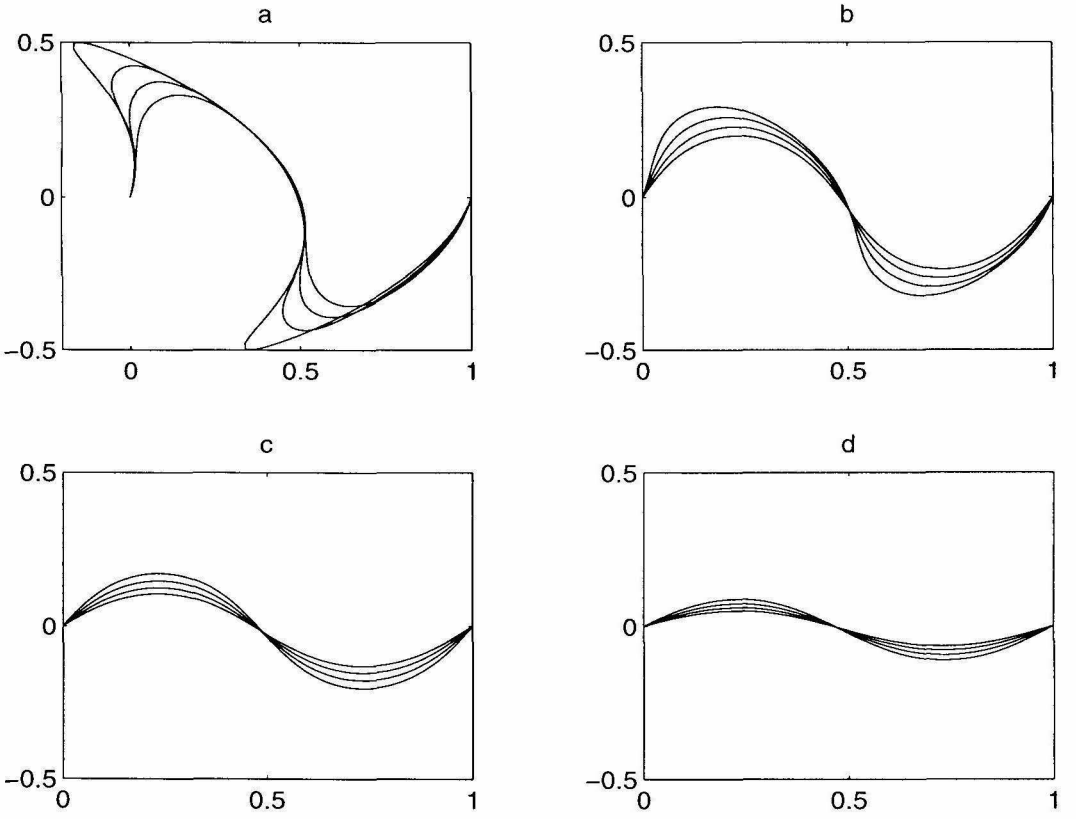

Figure 2.1: Motion by curvature; initial sin curve; $N = 128, \Delta t = 0.00025$; curve portrayed every 0.005: (a) 0 to 0.02, (b) 0.02 to 0.04, (c) 0.04 to 0.06, (d) 0.06 to 0.08.

In fact, Δt can be increased as time progresses. We list the maximum time steps that can be used at various times in Fig. 2.2. The time step Δt is chosen to be so small initially is due to the stability constraint. From Eqs. (2.10) and (2.11), we derive the stability constraint of the form

$$\max_{\alpha} |\bar{T}| \Delta t < C \cdot Lh. \tag{2.92}$$

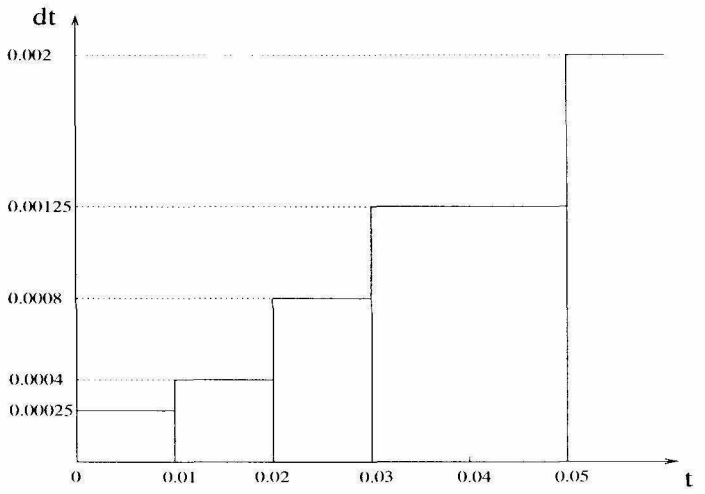

Figure 2.2: Maximum time steps at various times.

Here $\bar{T} = \int_0^\alpha (\kappa^2) d\alpha' - \alpha \int_0^1 (\kappa^2) d\alpha'$. Thus Δt is related to the magnitude of curvature through $\bar{T}$. We print out the curvature of this curve in Fig. 2.3. The maximum curvature of this curve is around 130. Since initially the curvature is large along some part of the

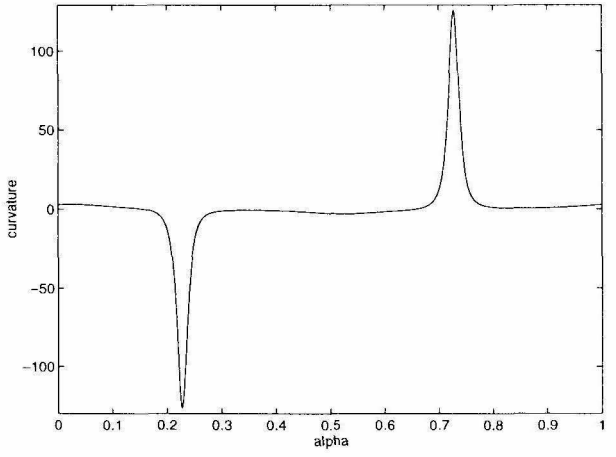

Figure 2.3: Curvature of the initial sin curve.

curve, the time step has to be small to satisfy the stability constraint. We see that this periodic curve moves faster where it has bigger curvature and it relaxes to a straight line with increasing time. When we increase the number of points in the calculation, we do see the time step decreases linearly.

We next consider the initial curve $\mathbf{X} = (\alpha + .1\sin(2\pi\alpha), .5\cos(2\pi\alpha)), 0 \leq \alpha \leq 1$, evolving according to Eq. (2.91). The maximum curvature of this initial curve is around

143. We graph the position of the curve at various times. In Fig. 2.4 (a)-(d), we show the continued evolution of the curve from $t = 0.0$ to $t = 0.08$. $N = 128$ mesh points were used and the time step $\Delta t = 0.00005$. This periodic curve relaxes quickly to a straight

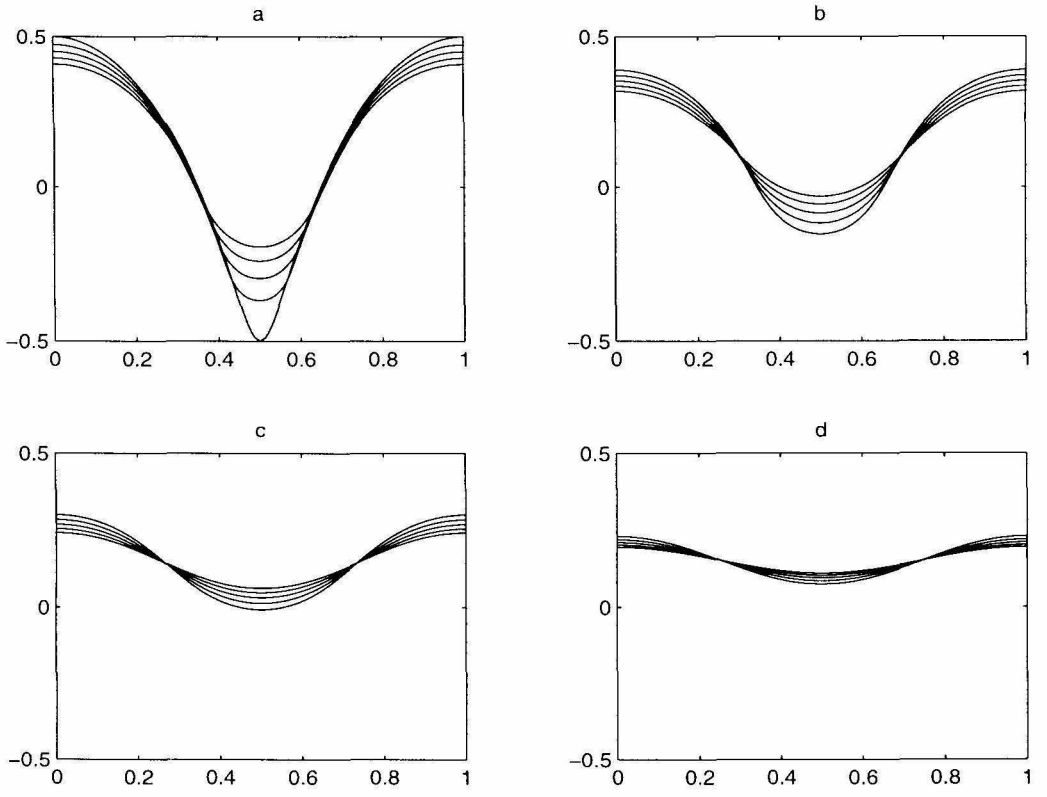

Figure 2.4: Motion by curvature: $N = 128, \Delta t = 0.00005$; curve portrayed every 0.004: (a) 0 to 0.02, (b) 0.02 to 0.04, (c) 0.04 to 0.06, (d) 0.06 to 0.08.

line as time increases. In Fig. 2.5, we list the maximum time steps that can be used at various times.

We also consider the evolution of an initial closed curve

$$\mathbf{X} = (1 + 0.4\sin(10\pi\alpha))(\cos(2\pi\alpha), \sin(2\pi\alpha)), \quad 0 \leq \alpha \leq 1,$$

according to Eq. (2.91). With $N = 256$ mesh points, and time step $\Delta t = 0.001$, we show in Fig. 2.6 (a)-(d) the continued evolution of the curve from $t = 0.0$ to $t = 0.2$. The plots show that this star-shaped curve quickly relaxes to a circle.

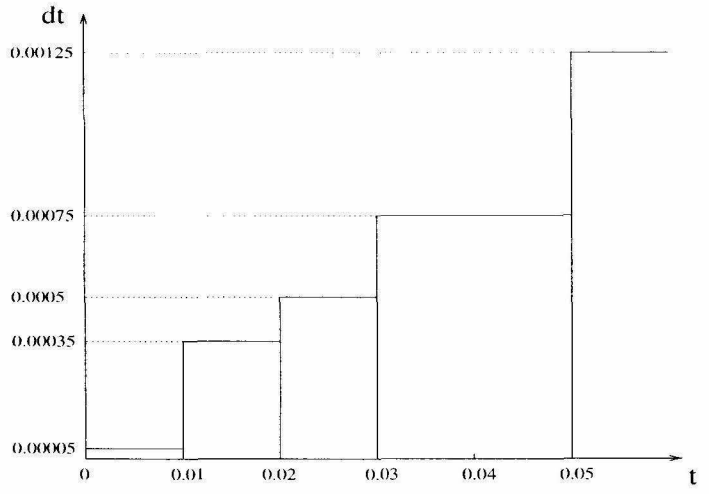

Figure 2.5: Maximum time steps at various times.

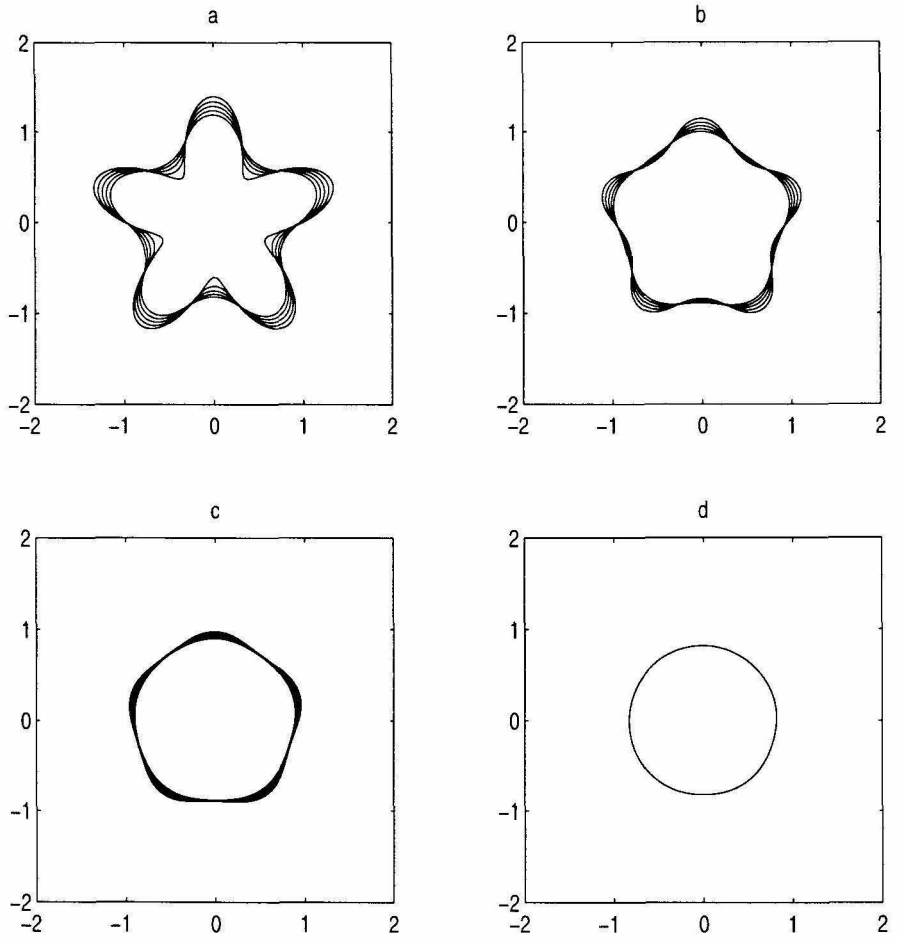

Figure 2.6: Motion by curvature; star-shaped curve: $N = 256, \Delta t = 0.001$; curve portrayed every 0.01: (a) 0 to 0.05, (b) 0.05 to 0.1, (c) 0.1 to 0.15, (d) 0.2.

2.6.2 *Motion by* $\kappa - < \kappa >$ *in Two Dimensions*

We consider the initial curve $\mathbf{X} = (-2\sin(2\pi\alpha), \cos(2\pi\alpha))$ evolving according to

$$\mathbf{X}_t = (\kappa - < \kappa >)\, \hat{\mathbf{n}}, \tag{2.93}$$

here $< \kappa >$ is the mean of κ, i.e., $\int_0^1 \kappa d\alpha$. With $N = 256$ mesh points and $\Delta t = 0.005$, we show the continued evolution from $t = 0.0$ to $t = 2.0$ in Fig. 2.7. We see that a circle is the equilibrium state for this ellipse under the motion by $\kappa - < \kappa >$.

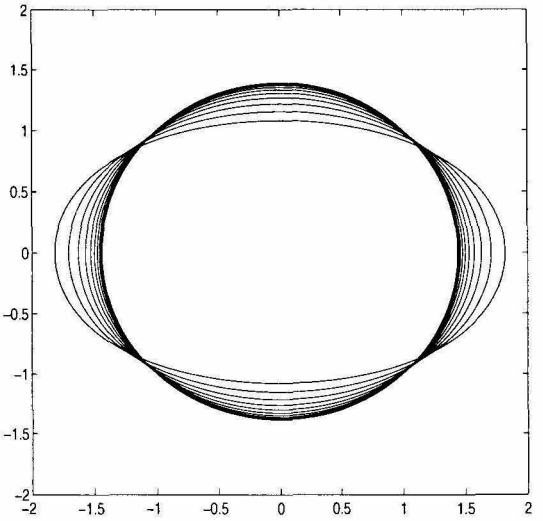

Figure 2.7: Motion by $\kappa - < \kappa >$; elliptic-shaped curve: $N = 256, \Delta t = 0.005, t = 0.0, 2.0(0.2)$.

We also compute the same initial curve evolving according to Eq. (2.91). $N = 256$ mesh points and $\Delta t = 0.0025$ are used and the evolution from $t = 0.0$ to $t = 1.0$ are shown in Fig. 2.8. Here we see that the ellipse shrinks to a point under Eq. (2.91).

To test the dependence of Δt on the magnitude of curvature and the spatial mesh size h, we perform a series of resolution studies for three examples. These examples give the same shapes of curves, but with increasing curvature by a constant factor, 2. In the first example, the initial curve is given by $\mathbf{X}_1 = (-4\sin(2\pi\alpha), 2\cos(2\pi\alpha))$. It evolves according to Eq. (2.91) and Eq. (2.93). Table 2.1 gives the largest possible time steps that give stable discretizations are shown. Using Eq. (2.91), we only calculate until $t = 4.0$ at which time the curve essentially becomes a point.

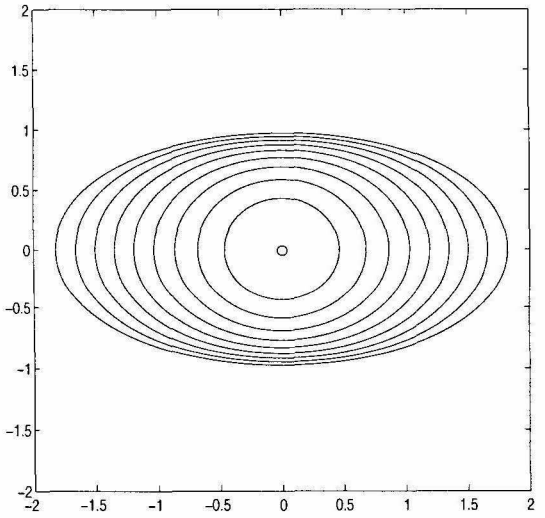

Figure 2.8: Motion by curvature; elliptic-shaped curve: $N = 256, \Delta t = 0.0025, t = 0.0, 1.0(0.1)$.

No. of points	$U = \kappa$	$U = \kappa - <\kappa>$
128	0.02	0.025
256	0.01	0.0125
512	0.005	0.00625

Table 2.1: Largest possible time steps that give stable discretizations for motion by curvature problem. The initial curve is $\mathbf{X}_1 = (-4\sin(2\pi\alpha), 2\cos(2\pi\alpha))$.

No. of points	$U = \kappa$	$U = \kappa - <\kappa>$
128	0.005	0.0075
256	0.0025	0.005
512	0.00125	0.0025

Table 2.2: Largest possible time steps that give stable discretizations for motion by curvature problem. The initial curve is $\mathbf{X}_2 = (-2\sin(2\pi\alpha), \cos(2\pi\alpha))$.

No. of points	$U = \kappa$	$U = \kappa - <\kappa>$
128	0.002	0.002
256	0.001	0.001
512	0.0005	0.0005

Table 2.3: Largest possible time steps that give stable discretizations for motion by curvature problem. The initial curve is $\mathbf{X}_3 = (-\sin(2\pi\alpha), 0.5\cos(2\pi\alpha))$.

In the second example, we scale the initial curve of the first example by a factor of 2, i.e., $\mathbf{X}_2 = (-2\sin(2\pi\alpha), \cos(2\pi\alpha))$. We evolve it by the same equations, Eq. (2.91) and Eq. (2.93). The largest possible time steps that give stable discretizations are given in Table 2.2. Using Eq. (2.91), we only calculate until $t = 1.0$ before it is essentially a point.

In the third example, we scale the initial curve of the first example by a factor of 4, i.e., $\mathbf{X}_3 = (-\sin(2\pi\alpha), 0.5\cos(2\pi\alpha))$, and evolve it by the same equations. Again we list in Table (2.3) the largest possible time steps that give stable discretizations. Using Eq. (2.91), it will essentially be a point after $t = 0.25$.

Basically the curvature of $\mathbf{X}_3$ is two times the curvature of $\mathbf{X}_2$ and four times the curvature of $\mathbf{X}_1$. From Eqs. (2.31) and (2.32), the stability constraint is of the form

$$\max_{\alpha} |\bar{T}| \Delta t < CLh, \tag{2.94}$$

under the motion by κ or $\kappa - < \kappa >$. Here $\bar{T} = \int_0^\alpha (U\kappa) d\alpha' - \alpha \int_0^1 (U\kappa) d\alpha'$. Since $\bar{T}$ is proportional to κ^2, the time step constraint for $\mathbf{X}_3$ is approximately four times smaller than that for $\mathbf{X}_2$. Similarly the time step constraint of $\mathbf{X}_2$ is approximately four times smaller than that for $\mathbf{X}_1$. This is exactly what we observed from the numerical calculations.

The above calculations all demonstrate that our numerical method is free of severe time step constraint. The time step is proportional to the space grid size in all these calculations. In fact, the particle grid spacing is decreasing in almost all the cases since the curve shrinks to a point. Without using our implicit discretization, the method would have become unstable very early on.

2.6.3 Inertial Vortex Sheets

Next, we apply our reformulated implicit scheme to the inertial vortex sheet problem with surface tension. This problem has been well studied by Hou, Lowengrub and Shelley in [23] using the θ-L formulation. Significant improvement on stability constraint was observed over conventional explicit discretizations, e.g., the fourth order Runge-Kutta method. It is natural for us to compare the performance of the θ-L method and our κ-L

method. Our numerical experiments indicate that these two reformulated schemes give the same stability constraint. This is also explained analytically in this subsection. This is an important and encouraging comparison, because our reformulation can be applied to three-dimensional problems.

In order to compare our methods with the θ-L frame presentedy in [23], we examine the long-time evolution of inertial vortex sheets with surface tension. We use the same initial condition as in [23]:

$$\begin{aligned} x(\alpha,0) &= \alpha + 0.01\sin 2\pi\alpha, \qquad y(\alpha,0) = -0.01\sin 2\pi\alpha, \\ \gamma(\alpha,0) &= 1.0\,, \end{aligned} \tag{2.95}$$

and choose $S = 0.005$ as in their calculation. In Fig. 2.9, a time sequence of interface positions is given, starting from the initial condition. Also we plot the vortex sheet strength γ and the curvature κ at various times in Figs. 2.10 and Fig. 2.11 respectively. Our calculation uses $N = 1024$ and $\Delta t = 1.25 \times 10^{-4}$. We also compare directly our numerical solutions with those obtained by the θ-L frame presented in Hou *et al* [23]. We found that the θ-L frame and the κ-L frame give us essentially the same numerical result. Also we have checked the stability constraint using these two formulations. We find that using the same number of points, the largest possible time steps that give stable discretizations are of the same order for the two methods. This can also be explained analytically. Using the θ-L frame (assume that $\alpha \in [0, 2\pi]$), the equations of motion are given by

$$L_t = -\int_0^{2\pi} \theta_{\alpha'} U d\alpha' \tag{2.96}$$

$$\theta_t = \left(\frac{2\pi}{L}\right)(U_\alpha + \theta_\alpha T) \tag{2.97}$$

$$\gamma_t = \frac{2\pi}{L} S\theta_{\alpha\alpha} + \partial_\alpha((T - \mathbf{W}\cdot\hat{\mathbf{s}})\gamma/s_\alpha), \tag{2.98}$$

where T is given by

$$T(\alpha,t) = \int_0^\alpha \theta_{\alpha'} U d\alpha' - \frac{\alpha}{2\pi}\int_0^{2\pi} \theta_{\alpha'} U d\alpha'. \tag{2.99}$$

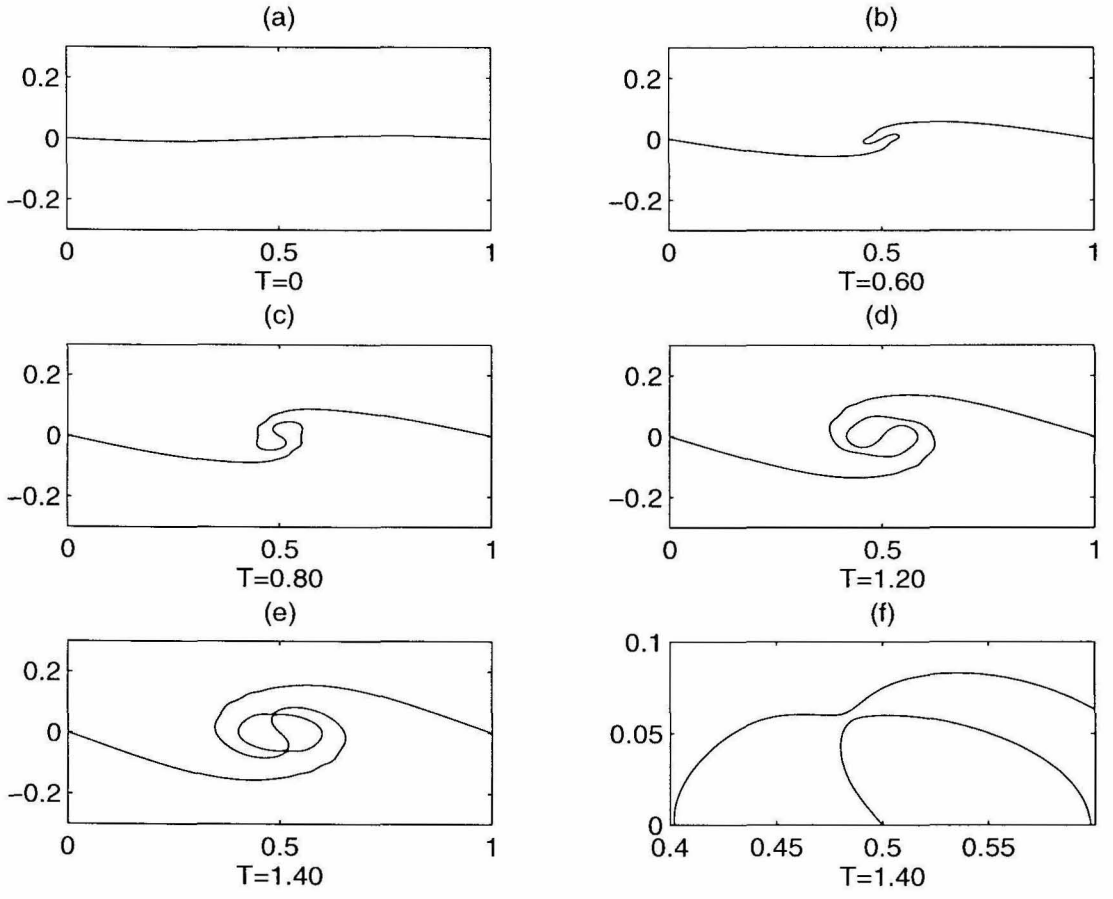

Figure 2.9: Inertial vortex sheets; sequence of interface positions: $S = 0.005, N = 1024, \Delta t = 1.25 \times 10^{-4}$: (a) $t = 0$, (b) $t = 0.60$, (c) $t = 0.80$, (d) $t = 1.20$, (e) $t = 1.40$, (f) close-up of top pinching region, $t = 1.40$.

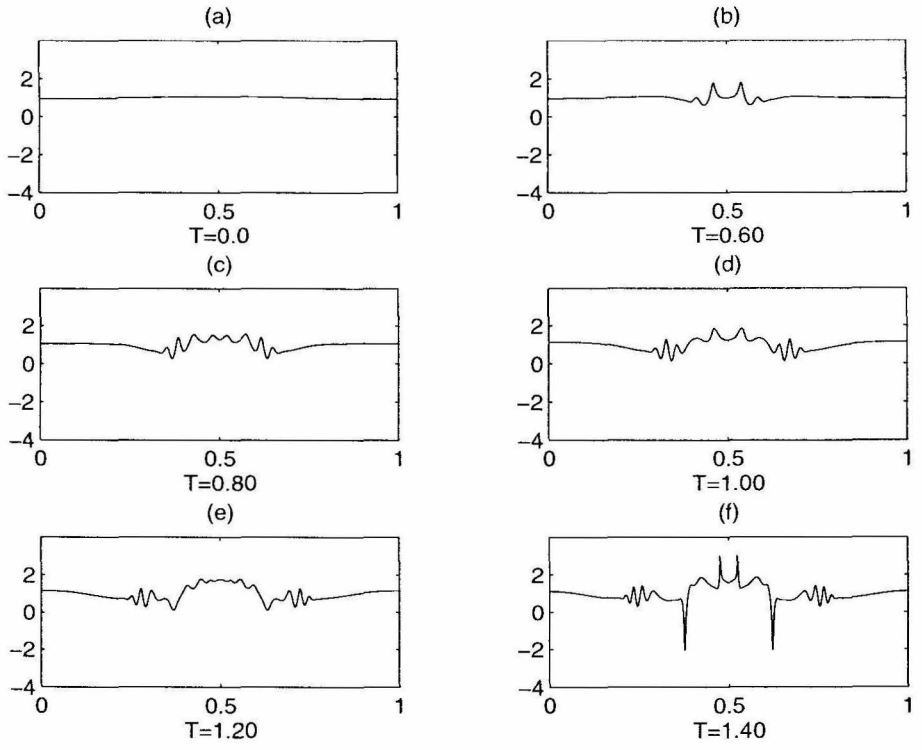

Figure 2.10: Inertial vortex sheets; sequence of γ: $S = 0.005, N = 1024, \Delta t = 1.25 \times 10^{-4}$: (a) $t = 0$,(b) $t = 0.60$, (c) $t = 0.80$, (d) $t = 1.00$, (e) $t = 1.20$, (f) $t = 1.40$.

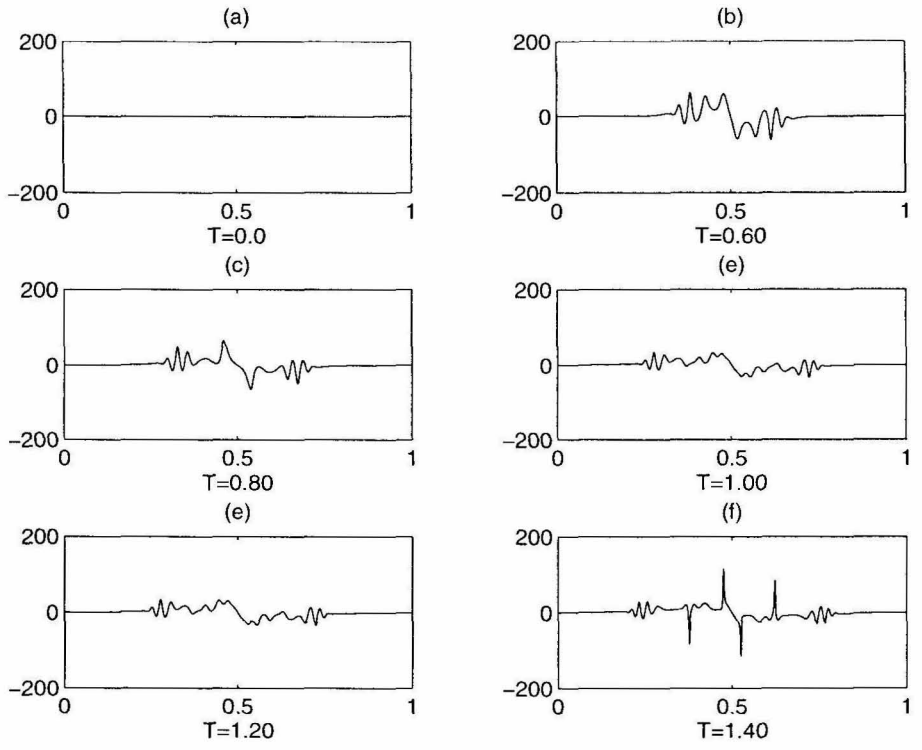

Figure 2.11: Inertial vortex sheets; sequence of κ: $S = 0.005, N = 1024, \Delta t = 1.25 \times 10^{-4}$: (a) $t = 0$, (b) $t = 0.60$, (c) $t = 0.80$, (d) $t = 1.00$, (e) $t = 1.20$, (f) $t = 1.40$.

By using an implicit discretization like the one we discussed before, we will get a stability constraint of the form

$$\max_{\alpha} |T| \Delta t < C \cdot \frac{L}{2\pi} h. \tag{2.100}$$

Using the κ-L frame, the equations of motion are given by Eqs. (2.31), (2.32) and (2.21), so the stability constraint is of the form

$$\max_{\alpha} |T_1| \Delta t < C \cdot \frac{L}{2\pi} h, \tag{2.101}$$

where T_1 is given by

$$T_1(\alpha, t) = \frac{L}{2\pi} \int_0^{\alpha} \kappa U d\alpha' - \frac{\alpha L}{(2\pi)^2} \int_0^{2\pi} \kappa U d\alpha'. \tag{2.102}$$

Using the relationships between θ and κ, $\kappa = \theta_\alpha / s_\alpha$, for here $s_\alpha = L/(2\pi)$, it is easy to see to that $T = T_1$. This shows that the κ-L frame and θ-L frame have the same order stability constraints.

The reason that we use this κ-L frame is that we could use the similar idea to the computation of three-dimensional curves and surfaces. The comparison of the results by using the κ-L frame and θ-L frame shows that our κ-L frame shares the same stability property as the θ-L frame, and yet has the advantage of being applicable to three-dimensional filaments and surfaces.

2.6.4 Motion by Curvature for Three-Dimensional Filaments

We now turn our attention to three-dimensional filaments. First we test our method for the simple motion by curvature in three dimensions. We basically confirm the similar performance we observed for the corresponding two-dimensional problem. We perform a careful comparison with an explicit fourth order Runge-Kutta discretization. For $N = 512$, the maximum allowable time step for our method is 3200 times larger than that for the Runge-Kutta method. We also test the reformulation using the Frènet frame. We found that the computation breaks down at a relative early time due to the formation of a vanishing curvature point. This corresponds to a blow-up in the torsion

No. of points	Explicit Method	κ_1-κ_2-ω-L Method
128	0.000125	0.0750
256	0.00003125	0.0375
512	0.00000625	0.0200

Table 2.4: Comparison of the maximum time step for explicit method and κ_1-κ_2- ω-L method.

variable. This is an artificial parameterization singularity. The filament is very smooth at this time. Using the generalized curvature κ_1 and κ_2, we can compute well beyond this time without any difficulty.

Consider the three-dimensional curve

$$\mathbf{X} = (\sin(2\alpha), \cos(\alpha), \sin(\alpha) + 2\cos(2\alpha)), \qquad \alpha \in (0, 2\pi),$$

evolving according to motion by curvature, $\mathbf{X}_t = \kappa\mathbf{N}$. Using our κ_1-κ_2-ω-L formulation, with $N = 256$ mesh points, and time step $\Delta t = 0.0005$, we show in Fig. 2.12 the continued evolution of the curve from $t = 0.0$ to $t = 1.4$. We observe that this space curve relaxes to a circle and eventually shrinks to a point.

We compare our method with a straightforward explicit discretization of $\mathbf{X}_t = \kappa\mathbf{N}$ in (x, y, z) coordinates. This involves using a spectral method for the spatial derivatives and fourth order Runge-Kutta method in time. We list below the maximum time step that can be taken to get a stable solution using these two methods. Due to the particle clustering, we can only compute up to $t = 1.0$ using the explicit method. Clearly we can see the huge advantage of using our implicit discretization.

The motion of a three-dimensional filament by curvature is somewhat different from that of the two-dimensional counterpart. In the two-dimensional case, it is possible to interpret the geometrical significance of positive or negative curvature. However, for three-dimensional curves, the curvature is defined by

$$\kappa = \sqrt{\ddot{\mathbf{X}} \cdot \ddot{\mathbf{X}}} = |\ddot{\mathbf{X}}|. \tag{2.103}$$

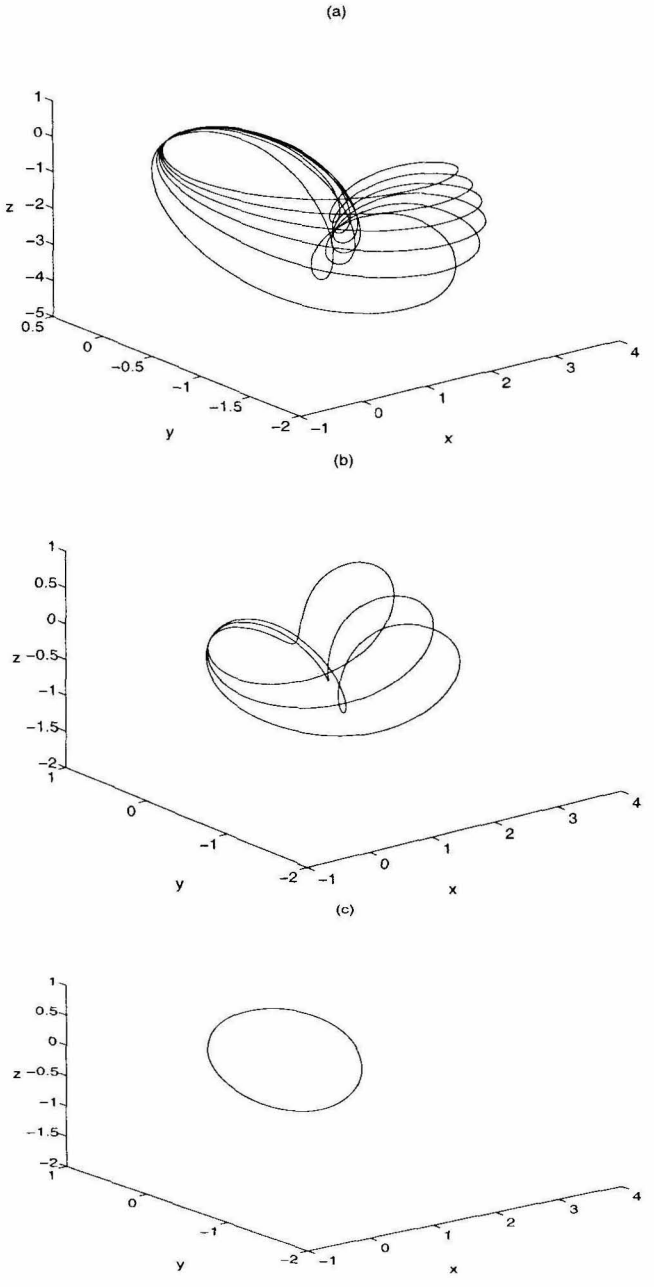

Figure 2.12: $N = 256, \Delta t = 0.0005$: (a) $t = 0.0, 0.6(0.1)$, (b) $t = 0.7, 1.0(0.1)$, (c) $t = 1.4$.

The positive square root is taken in Eq. (2.103) and thus the curvature is always non-negative, $\kappa \geq 0$. When it passes through points where $\kappa = 0$, the normal vector $\mathbf{N}$ varies discontinuously. Moreover, at points where $\kappa = 0$, the torsion is not well defined. Recall that the definition of torsion is

$$\tau = \kappa^{-2}(\dot{\mathbf{X}} \cdot \ddot{\mathbf{X}} \times \dddot{\mathbf{X}}). \tag{2.104}$$

It is obvious that the torsion is only defined when the curvature does not vanish.

We have tried the same example using κ-τ-L formulation (2.41), (2.42) and (2.43). We began to have numerical difficulties around $t = 1.015$ when the curvature became close to zero at some point on the curve. In fact, we were only able to compute up to $t = 1.015$ using 256 points, no matter how small a time step we took. This is due to the stability constraints we derived from Eq. (2.44). On the other hand, we had no difficulty computing past $t = 1.015$ when using the κ_1-κ_2-ω-L formulation. In Fig. 2.13, we compare the plots of curvature at $t = 1.015$ using the κ-τ-L formulation and κ_1-κ_2-ω-L formulation by taking the time step to be $\Delta t = 0.00125$ and $\Delta t = 0.01$ respectively. Here we have used the relationship $\kappa = \sqrt{\kappa_1^2 + \kappa_2^2}$.

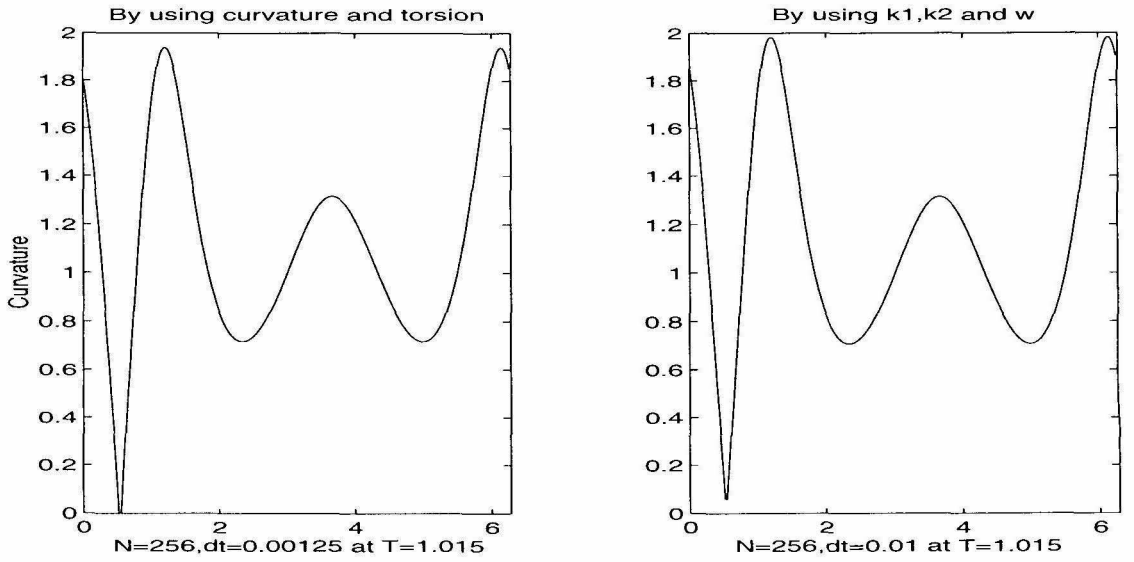

Figure 2.13: Comparison of curvature at $t = 1.015$ using κ-τ-L and κ_1-κ_2-ω-L formulation.

We note the similarity in the two plots of the curvature. We also note the jump in

the derivative of the curvature as the curvature approaches zero. This means that κ_α is not continuous and the Eqs. (2.42) and (2.43) break down.

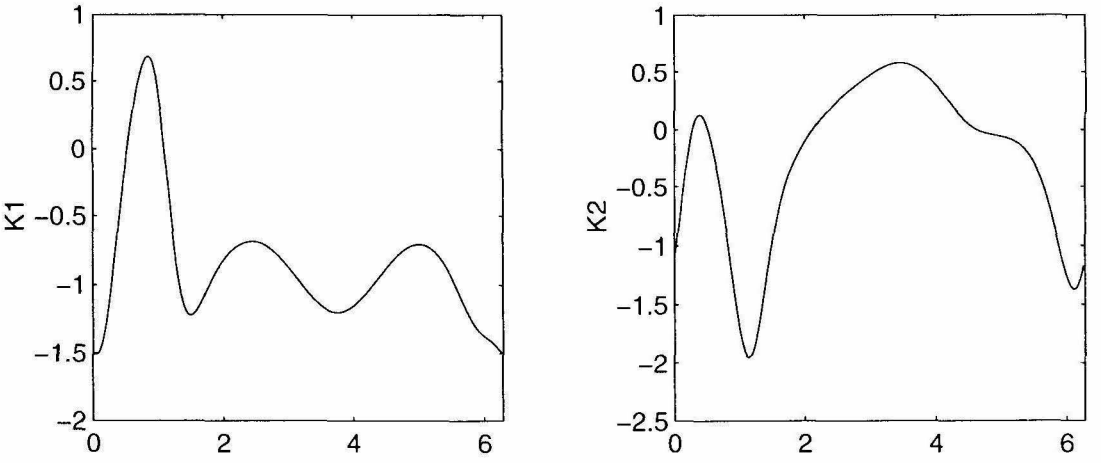

Figure 2.14: κ_1 and κ_2 at $t = 1.02$ with $N = 256$ and $\Delta t = 0.01$.

We also plot the variables κ_1 and κ_2 at $t = 1.02$ in Fig. 2.14. Note that these variables remain smooth along the entire curve. Thus we see the advantage and indeed, necessity of using the κ_1-κ_2-ω-L formulation instead of the $\kappa - \tau - L$ formulation.

2.6.5 Motion of the Kirchhoff Rod Model

Next we test our numerical methods on the motion of the elastic rods. Two interesting equilibrium states are reached using two different initial perturbation of a circular initial filament. As before, no stiffness is observed using our reformulated implicit schemes. A sequence of snapshots of the dynamics approaching to equilibrium for two examples (radius $r = 1$) are shown in Fig. 2.15 and Fig. 2.16. In both examples, we choose as initial conditions a circular conformation with total twist $\mathbf{T}\omega = 5$. Here $\mathbf{T}\omega(\mathbf{X}) = \frac{1}{2\pi}\oint \omega(\mathbf{X}(s))ds$. In the first example, we choose the initial twist to be distributed uniformly with a small localized perturbation. In particular, we choose

$\omega(s,0) = (5+\omega_1)/(5+\frac{1}{2\pi}\oint \omega_1 ds)$, where

$$\omega_1 = \begin{cases} 0 & |x-\pi| \le \frac{\pi}{2}, \\ \frac{1}{4\cosh^2(\frac{x-\pi}{2x-\pi})} & \frac{\pi}{2} < x \le \pi, \\ \frac{1}{4\cosh^2(\frac{\pi-x}{3\pi-2x})} & \pi < x < \frac{3\pi}{2}. \end{cases} \tag{2.105}$$

In the second example, we use the same parameters and a similar initial condition as the first one, except that the initial twist includes an order one non-localized perturbation from uniformity. More precisely, we choose $\omega(s,0) = 2\pi L^{-1}\mathbf{T}\omega*(1+0.8*\sin(2\pi s/L))$. In both of these examples, we use 256 grid points in our calculations, and a time step $\Delta t = 0.00125$. For the first example, the solutions are plotted at $t = 0, 1.6, 2.1, 2.6, 4, 12$ respectively. For the second example, the solutions are plotted at $t = 0, 1.2, 2.4, 2.8, 4, 6, 12$ respectively.

In these two examples, the rods start twisting around $t = 1.6$ and $t = 1.2$ respectively. Because of the contact force, the rods cannot self-cross, thus it would keep twisting until it approaches to the equilibrium configurations. We have also investigated using different values for the parameters η_1, η_2 in Eqs. (2.65) and (2.66). We find that there is little change in the equilibrium states in both examples, but the rate at which the rods evolve to these states is affected.

We should mention the construction of the initial condition for these two examples. In our methods, it is necessary to specify initial values of κ_1, κ_2 and ω. The twist of the circle ω is already given, so we need to determine κ_1 and κ_2 from the curvature κ and the torsion τ. Since $\kappa_1^2 + \kappa_2^2 = \kappa^2$, we parameterize κ_1, κ_2 by κ and ϕ as follows:

$$\begin{aligned} \kappa_1 &= \kappa\cos\phi \\ \kappa_2 &= \kappa\sin\phi. \end{aligned} \tag{2.106}$$

Note that the torsion τ is zero everywhere for an unit circle. Substituting the above equations into Eq. (2.47), we get

$$\phi_s = \omega.$$

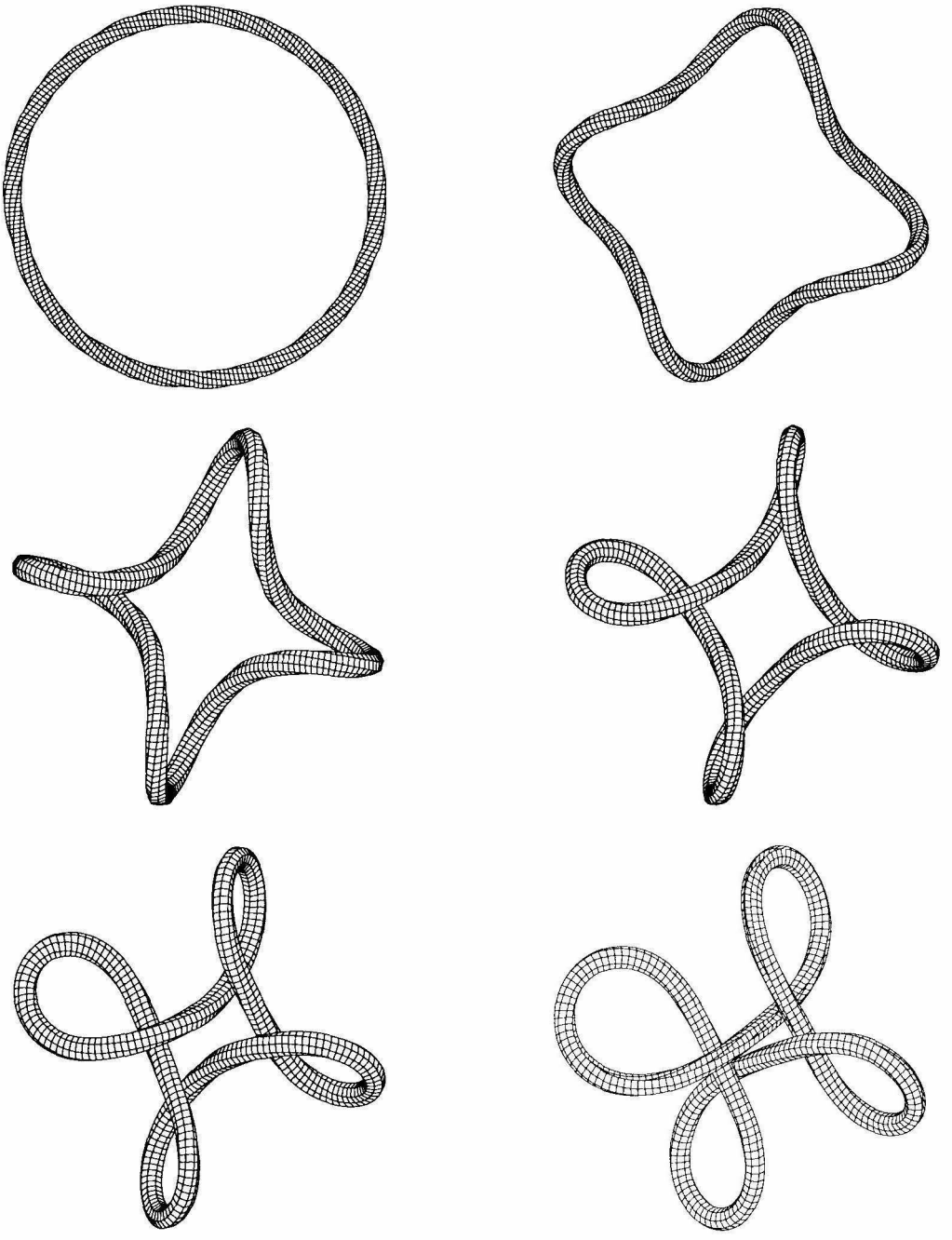

Figure 2.15: Approach to equilibrium "clover" configuration. $t = 0, 1.6, 2.1, 2.6, 4, 12$.

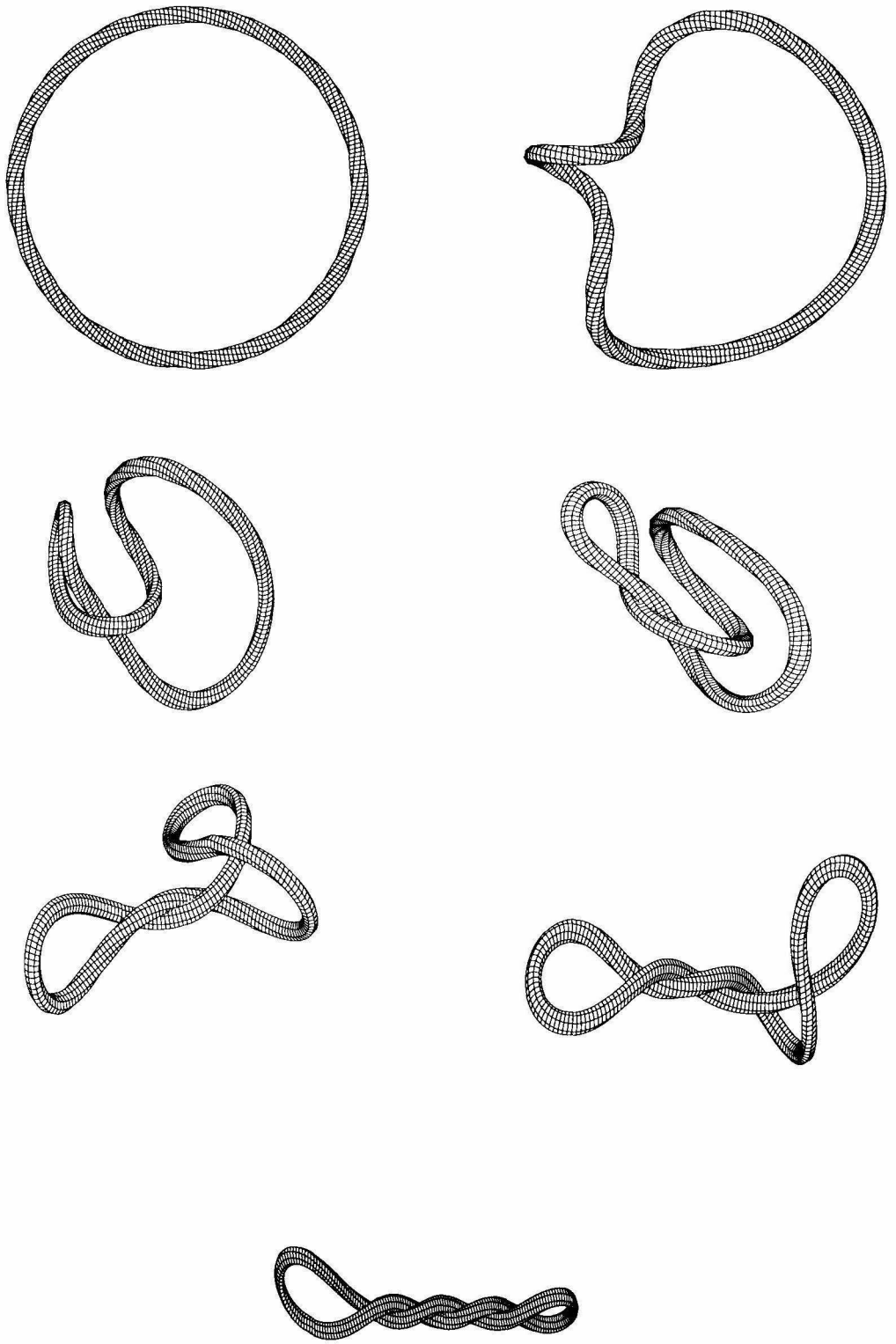

Figure 2.16: Approach to equilibrium "plectonemic" configuration. $t = 0, 1.2, 2.4, 2.8, 4, 6, 12$.

Thus we are able to calculate ϕ. The curvature of the unit circle is 1. Thus κ_1 and κ_2 are completely determined by Eq. (2.106).

Finally, it is necessary to include some sort of contact force $\mathbf{g}(s)$ to prevent the elastic rod from self-crossing. In a similar way to [32] we have set

$$\mathbf{g}(s) = -\int M(r(s), r(\sigma)) \frac{r(s) - r(\sigma)}{(|r(s) - r(\sigma)|)^{10}} d\sigma. \tag{2.107}$$

The purpose of the mollifier M is three-fold. First, some distinction must be made between nearest neighbor points along the curve and other points that are far away in arclength but close in space. Clearly, for those points which are nearest neighbors along the curve, no contact force is necessary and therefore M is set to be zero. However, if two points which are separated by a large distance in arc-length become close to another in space, M must be non-zero to activate the contact force. Therefore, M helps prevent self-crossing while ensuring that points along the curve are not forced apart.

Secondly, the magnitude of the contact force needs to be controlled to prevent overly large forces from destabilizing our solution. The contact force has the form of a stiff inverse power law ($\propto r^{-10}$) so some care must be taken in choosing a constant of proportionality. This is the other role that M plays when the contact force is in effect. We assume the radius of the rod is approximately 3 times the grid spacing, i.e., hs_α, thus M needs to be chosen so that the distance between any two points which are not close in arc-length cannot be smaller than $6hs_\alpha$. We do not have an explicit expression for M here. In our first example, we simply take M to be 0.005 if the distance is less than $12hs_\alpha$ and 0.1 if the distance is less than $8hs_\alpha$. In our calculation $s_\alpha = L/2\pi$ is very close to 1. In our second example, we take M to be 0.004 if the distance is less than $14hs_\alpha$ and 0.04 if the distance is less than $8hs_\alpha$.

Third, by setting $M = 0$ when $r(s)$ and $r(\sigma)$ are distant, we reduce the computational cost in evaluating (2.107) from $O(n^2)$ to $O(n)$. This step is absolutely necessary in order to prevent the evaluation of $g(s)$ from dominating the entire computation.

By way of comparison, reference [32] used a similar model to calculate the evolution of an elastic rod. The method there was to directly discretize Eqs. (2.65) – (2.67) using second-order centered differences. Here we have the considerable advantage that no high order time step stability constraints are imposed. This advantage is crucial if accurate,

long-time computations (such as DNA modeling) are to be attempted.

It is interesting that both of these examples start from unit circles with the same total twist. The only difference is the distribution of the initial twist. But they approach to two totally different equilibrium states. The clover-like structures are also observed in Langevin dynamics simulations [50] and the plectonemic conformation is similar to DNA studies.

2.6.6 Motion of Anti–parallel Pair of Vortex Filaments

Finally, we are going to test our method on the motion of the anti–parallel vortex filaments. We consider large amplitude antisymmetric helical initial perturbations of the anti–parallel pair ([14] & [36]):

$$\mathbf{X}_1 = (-0.5 + 0.3\cos\alpha, 0.3\sin\alpha, \alpha) \tag{2.108}$$

$$\mathbf{X}_2 = (\ 0.5 + 0.3\cos\alpha, 0.3\sin\alpha, \alpha), \qquad \alpha \in (0, 2\pi). \tag{2.109}$$

The circulation strengths Γ_1, Γ_2 in Eq. (2.82) are taken to be 1 and -1 respectively. We apply the fourth order implicit-explicit scheme in our numerical experiments and find that the time step is indeed linearly dependent on the spatial mesh size as we expected. However, the fourth order scheme for this particular problem requires a small time step for stability constraint. Instead, we use the second order implicit-explicit scheme in our computation. The second order implicit-explicit scheme simply uses the leap frog scheme for the lower order term and the implicit Crank-Nicholson scheme for the leading order term:

$$\frac{1}{2\Delta t}(u^{n+1} - u^{n-1}) = f(u^n) + \frac{\nu}{2}[g(u^{n+1}) + g(u^{n-1})]. \tag{2.110}$$

Snapshots of the evolving filaments at times $t = 0$, 0.73 and 0.79 are given in Figs. 2.18 –2.20 where 1024 mesh points and time step $\Delta t = 0.00125$ are used. The initial separation distance between the two filaments is constant, and as time evolves, the minimum separation distance decreases until the pair collapses around $t = 0.79$. In Fig. 2.17, we also show the curvature κ and the twist ω of the second filament $\mathbf{X}_2$ at time $t = 0.79$. Using our method, we are also able to include the other non-local effects that are neglected

in the simplified equations (2.82).

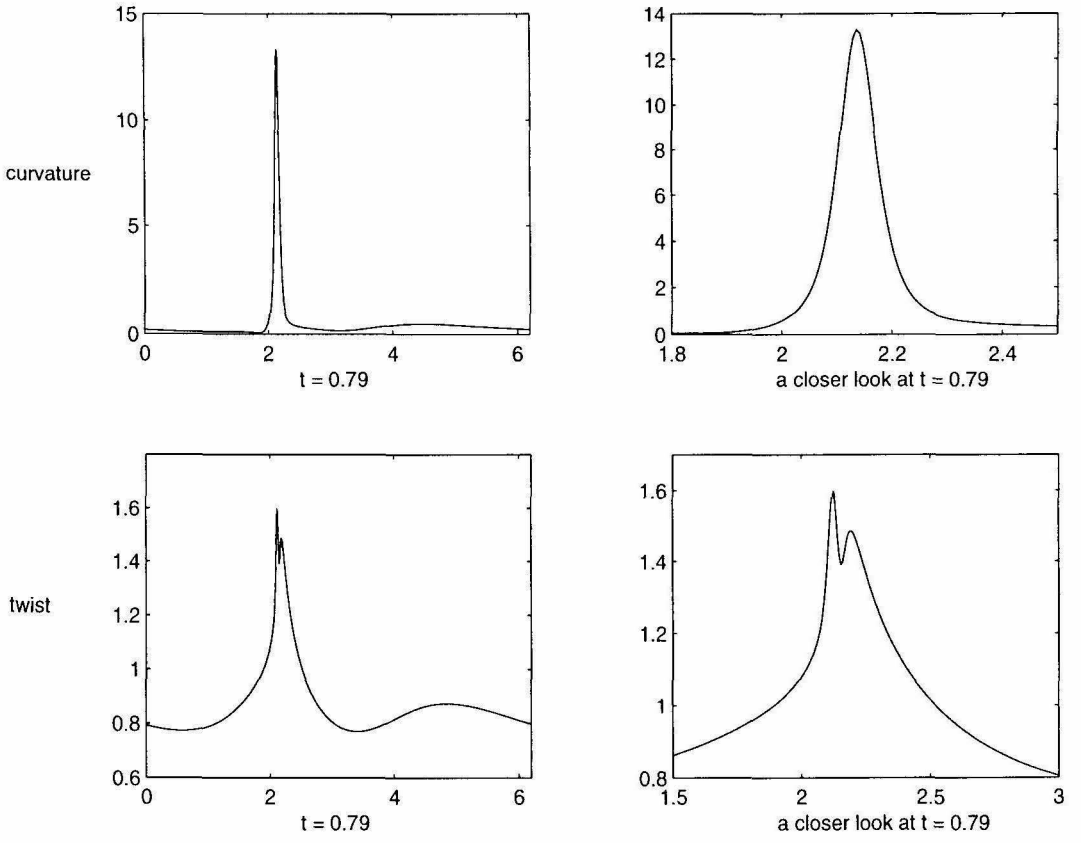

Figure 2.17: Curvature and twist of the second filament at $t = 0.79$.

2.7 Appendix: Evolution Equations for κ_1, κ_2 and ω for Three-Dimensional Filaments

We assume the space curve $\mathbf{X}$ evolves by

$$\mathbf{X}_t(\alpha, t) = U\mathbf{N}_1 + V\mathbf{N}_2 + W\mathbf{T}$$

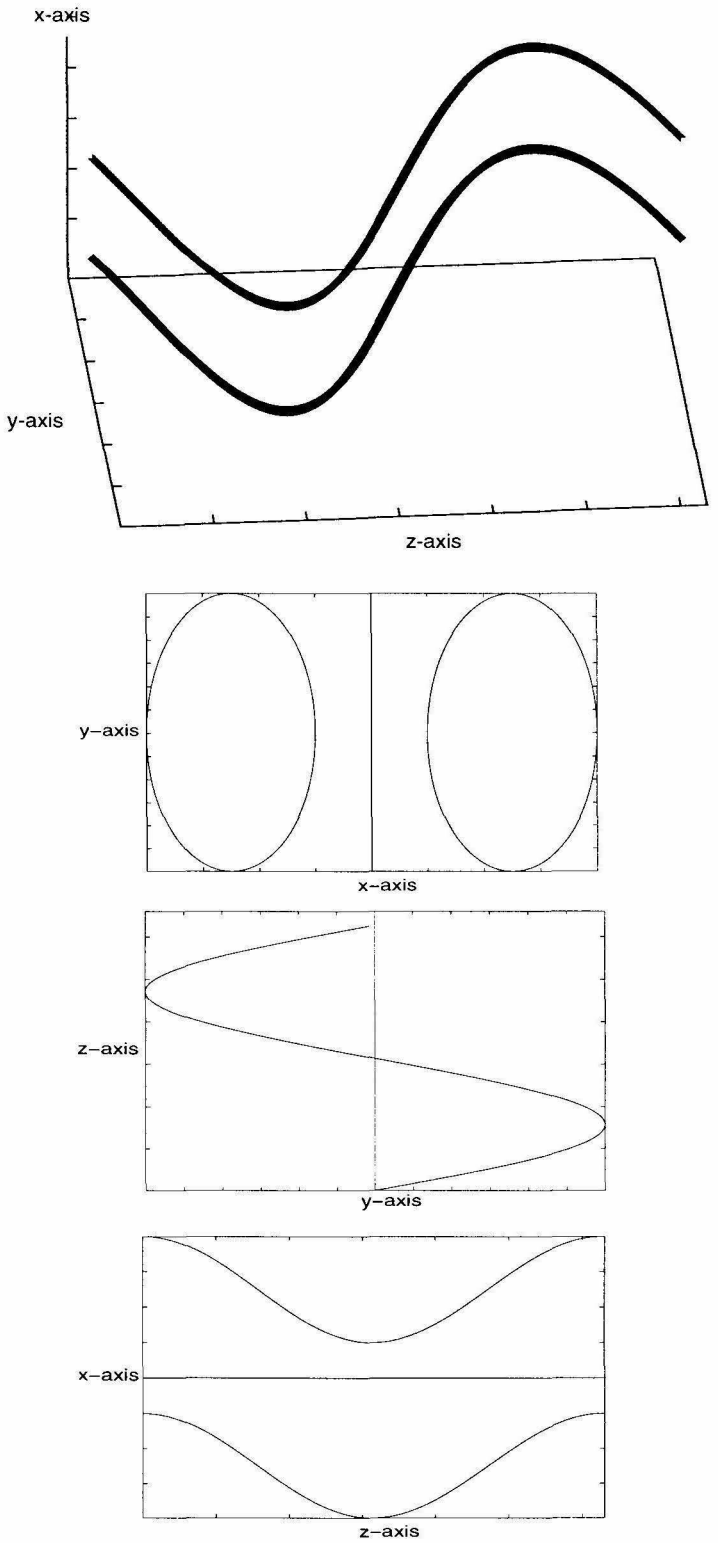

Figure 2.18: Snapshot of filaments for antisymmetric perturbation at time $t = 0$.

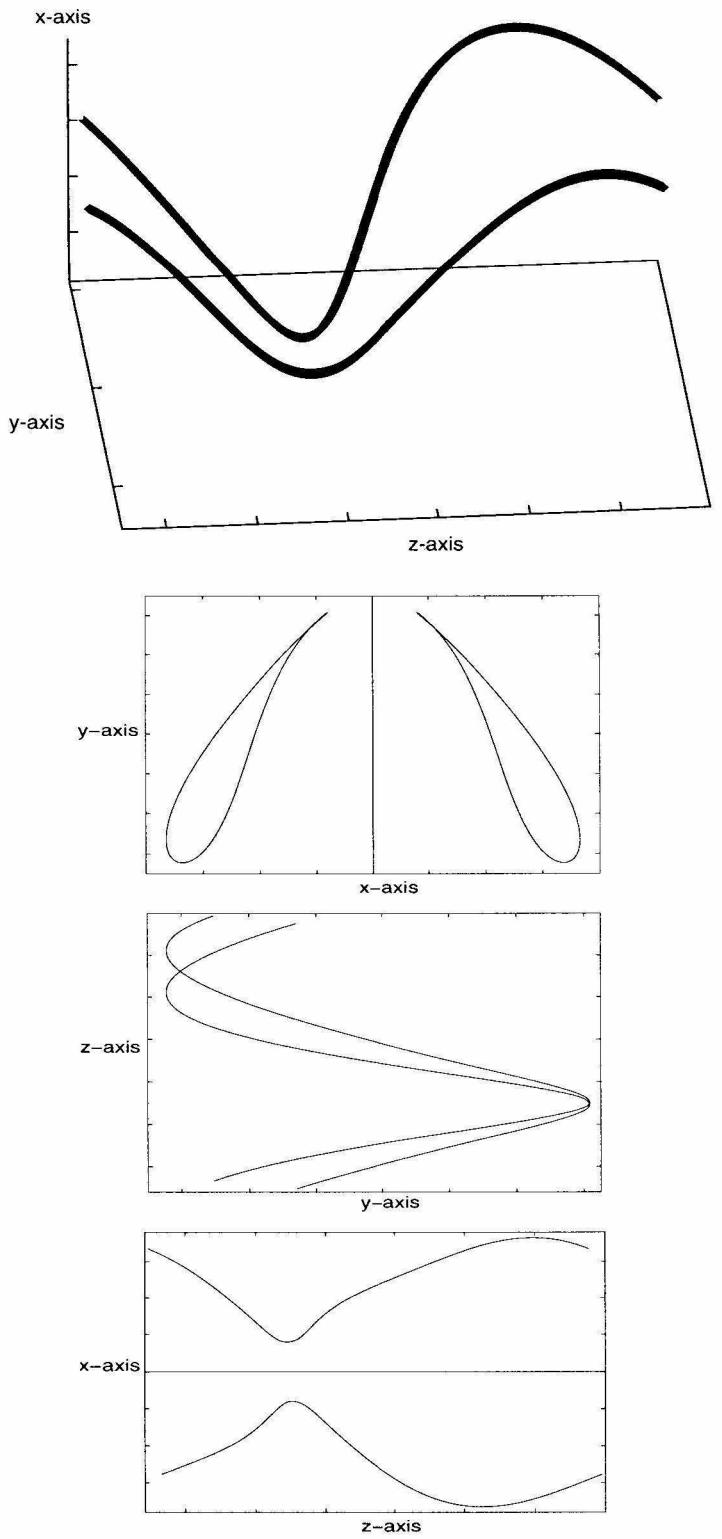

Figure 2.19: Snapshot of filaments for antisymmetric perturbation at time $t = 0.73$.

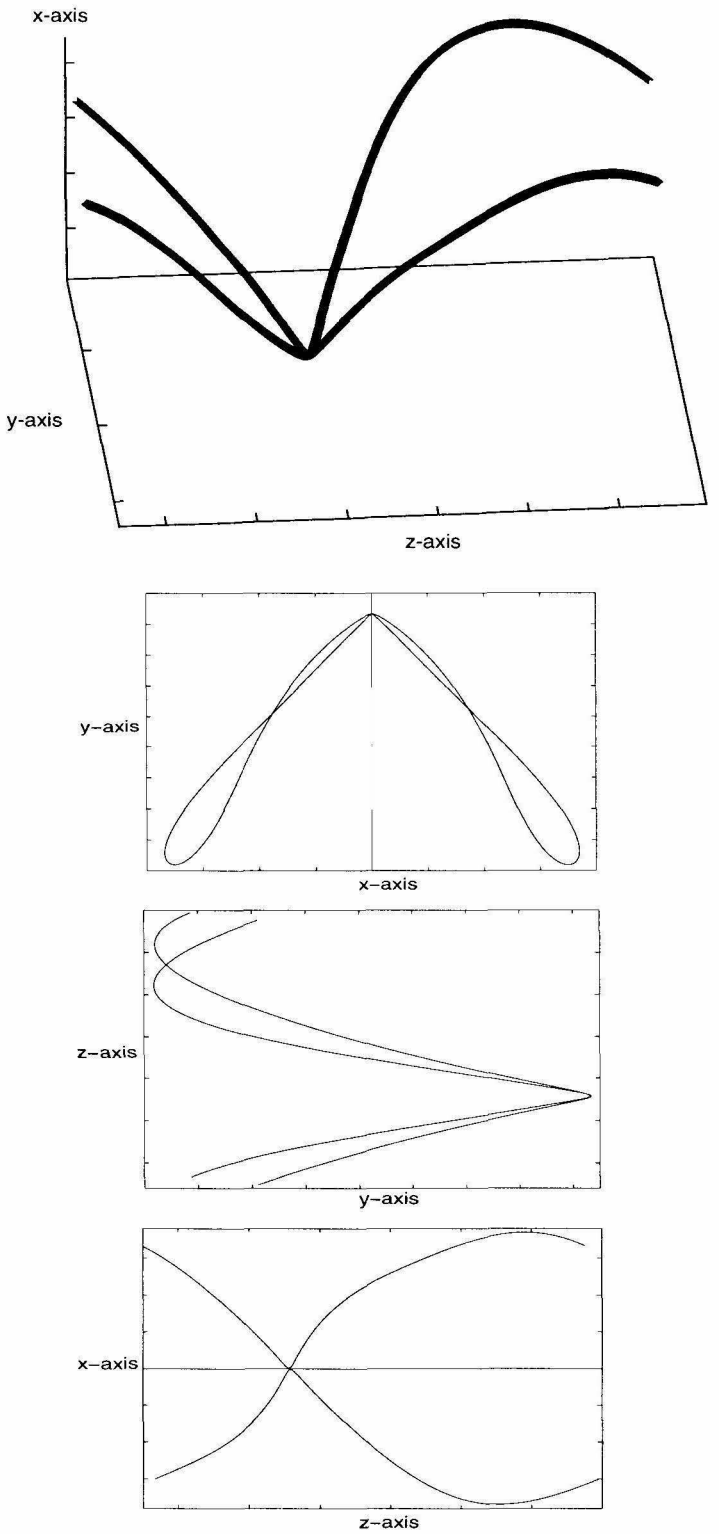

Figure 2.20: Snapshot of filaments for antisymmetric perturbation at time $t = 0.79$.

where U, V, W are the velocity components with respect to the orthonormal basis $\mathbf{N}_1, \mathbf{N}_2, \mathbf{T}$ which satisfies

$$\begin{aligned} \frac{d}{ds}\mathbf{T} &= \Omega_F \times \mathbf{T} \\ \frac{d}{ds}\mathbf{N}_1 &= \Omega_F \times \mathbf{N}_1 \\ \frac{d}{ds}\mathbf{N}_2 &= \Omega_F \times \mathbf{N}_2, \end{aligned} \tag{2.111}$$

where $\Omega_F(\alpha, t) = \kappa_2 \mathbf{N}_1 + \kappa_1 \mathbf{N}_2 + \omega \mathbf{T}$.

Also we write the time dependence of the basis $\mathbf{T}, \mathbf{N}_1, \mathbf{N}_2$ as

$$\begin{aligned} \frac{d}{dt}\mathbf{T} &= \Lambda_F \times \mathbf{T} \\ \frac{d}{dt}\mathbf{N}_1 &= \Lambda_F \times \mathbf{N}_1 \\ \frac{d}{dt}\mathbf{N}_2 &= \Lambda_F \times \mathbf{N}_2, \end{aligned} \tag{2.112}$$

where $\Lambda_F(\alpha, t) = \lambda_1 \mathbf{N}_1 + \lambda_2 \mathbf{N}_2 + \lambda_3 \mathbf{T}$ is the rotation vector whose components $\lambda_1, \lambda_2, \lambda_3$ are related to $U, V, W-$ and hence $\kappa_1, \kappa_2, \omega$. From $\frac{d}{ds}\mathbf{X} = \mathbf{T}$, we get

$$\frac{d}{d\alpha}\mathbf{X} = s_\alpha \mathbf{T}.$$

Self consistency requires equality of the α and t cross derivatives, namely

$$\frac{d^2}{d\alpha dt}\mathbf{X} = \frac{d^2}{dt d\alpha}\mathbf{X}. \tag{2.113}$$

Straightforward computations show that

$$s_{\alpha t} = W_\alpha + (V\kappa_2 - U\kappa_1)s_\alpha \tag{2.114}$$

$$\lambda_1 = -\frac{V_\alpha}{s_\alpha} - U\omega + W\kappa_2 \tag{2.115}$$

$$\lambda_2 = \frac{U_\alpha}{s_\alpha} - V\omega + W\kappa_1. \tag{2.116}$$

Further calculation leads to the equations of motion for $\kappa_1 s_\alpha, \kappa_2 s_\alpha$ and ωs_α:

$$\begin{aligned}
(\kappa_1 s_\alpha)_t &= \omega\lambda_1 s_\alpha - \lambda_3\kappa_2 s_\alpha + \lambda_{2\alpha} \\
(\kappa_2 s_\alpha)_t &= -\omega\lambda_2 s_\alpha - \lambda_3\kappa_1 s_\alpha + \lambda_{1\alpha} \\
(\omega s_\alpha)_t &= \lambda_2\kappa_2 - \lambda_1\kappa_1)s_\alpha + \lambda_{3\alpha}.
\end{aligned}$$

Using Eqs. (2.114) – (2.116), we obtain the equations of motion for κ_1, κ_2 and ω as follows:

$$\begin{aligned}
\kappa_{1t} &= \frac{1}{s_\alpha}\left(\frac{U_\alpha}{s_\alpha}\right)_\alpha - \frac{2\omega V_\alpha + \omega_\alpha V - W\kappa_{1\alpha}}{s_\alpha} - U\omega^2 \\
&\quad + \kappa_1(U\kappa_1 - V\kappa_2) + \omega\kappa_2 W - \lambda_2\kappa_2 \qquad (2.117) \\
\kappa_{2t} &= -\frac{1}{s_\alpha}\left(\frac{V_\alpha}{s_\alpha}\right)_\alpha - \frac{2\omega U_\alpha + \omega_\alpha U - W\kappa_{2\alpha}}{s_\alpha} + V\omega^2 \\
&\quad + \kappa_2(U\kappa_1 - V\kappa_2) - \omega\kappa_1 W - \lambda_2\kappa_1 \qquad (2.118) \\
\omega_t &= \frac{\kappa_1 V_\alpha + \kappa_2 U_\alpha - \omega W_\alpha}{s_\alpha} + 2\omega(U\kappa_1 - V\kappa_2) + \frac{\lambda_{3\alpha}}{s_\alpha}. \qquad (2.119)
\end{aligned}$$

So the equations of motion for $s_\alpha, \kappa_1, \kappa_2, \omega$ in terms of U, V, W take the forms of Eqs. (2.114), (2.117), (2.118) and (2.119).

Chapter 3
Removing the Stiffness of Surface Tension in Computing Three-Dimensional Surfaces

In this chapter, we present new formulations for computing three-dimensional surfaces with curvature regularization. In Section 3.1, we derive the κ- λ - u formulation for three-dimensional surfaces. As an example of illustration, we consider the motion of a three-dimensional surfaces by its local mean curvature. We then apply this idea to a simplified water wave model in Sections 3.2. Some practical implementation issues are presented in Section 3.3. Finally, in Section 3.4, we show some numerical results which include motion of a three-dimensional surface by mean curvature, simplified three-dimensional water wave model on Gaussian waves and gravity waves.

3.1 The κ - λ - u Formulation for Three-Dimensional Surfaces

In this section, we derive the κ -λ - u method for computing the motion of three-dimensional interfaces. We first motivate the formulation for the problem of motion by mean curvature. Then we derive the formulation for fluid interfaces, and indicate how the κ - λ - u formulation can be used to remove the stiffness of surface tension for fluid interface problems.

3.1.1 Motion by Mean Curvature

We motivate the κ - λ - u approach by considering the motion by mean curvature in three space dimensions. We parameterize the surface using parameters α_1 and α_2

so that $\mathbf{X}(\alpha_1, \alpha_2, t) = (x(\alpha_1, \alpha_2, t), y(\alpha_1, \alpha_2, t), z(\alpha_1, \alpha_2, t))$, where t is time. In order to simplify our computation, it is important to use an orthogonal parameterization of the free surface; we call it $\beta = (\beta_1, \beta_2)$, instead of the original Lagrangian variable, $\alpha = (\alpha_1, \alpha_2)$. i.e.,

$$\mathbf{X}_{\beta_1} \cdot \mathbf{X}_{\beta_2} = 0.$$

We now want to show how to construct an orthogonal parameterization. First we introduce some notation (also see [59].) If ρ is a point on a surface $\mathbf{X}$, then for each tangent vector v to $\mathbf{X}$ at ρ, let

$$S_\rho(v) = -\nabla_v \mathbf{U} = -\frac{d}{dt}\mathbf{U}(\rho + tv)|_{t=0},$$

where $\mathbf{U}$ is the unit normal vector field on a neighborhood of ρ in $\mathbf{X}$. S_ρ is called the shape operator of $\mathbf{X}$ at ρ (derived from $\mathbf{U}$). It is the rate of change of $\mathbf{U}$ at ρ in direction v. It can be shown that all curves on $\mathbf{X}$ with a given direction v at point ρ have the same normal component of acceleration at ρ, namely $S_\rho(v) \cdot v$. This is the component of acceleration which the bending of $\mathbf{X}$ forces the curves to have.

Let v be a unit tangent vector, then the number $\kappa(v) = S_\rho(v) \cdot v$ is called the normal curvature of $\mathbf{X}$ in the v–direction. The maximum and minimum values of the normal curvature $\kappa(v)$ of $\mathbf{X}$ at ρ are called the principal curvatures of $\mathbf{X}$ at ρ. They are denoted by κ_1 and κ_2 respectively. The corresponding directions are called principal directions with the unit vectors in these directions being the principal vectors. It can be proved that if $\kappa_1 \neq \kappa_2$, there exists one pair of orthogonal directions $\hat{e}_1$ and $\hat{e}_2$ for which the values of κ take on maximum and minimum values κ_1 and κ_2. Furthermore,

$$S(\hat{e}_1) = \kappa_1 \hat{e}_1, \qquad S(\hat{e}_2) = \kappa_2 \hat{e}_2. \tag{3.1}$$

There are two cases that have $\kappa_1 = \kappa_2$: the planar point case and the special elliptic case in which it becomes a circle point. In these exceptional cases, all directions are regarded as principal directions and obviously the normal curvatures are then the same for all directions. This means we can easily choose one pair of orthogonal directions.

Thus, the orthogonal frame is constructed such that the two normal tangent vectors $\hat{\mathbf{T}}_1$ and $\hat{\mathbf{T}}_2$ are the two principal vectors of the surface $\mathbf{X}$. They are defined by

$$\hat{\mathbf{T}}_1 = \frac{\mathbf{X}_{\beta_1}}{u}$$
$$\hat{\mathbf{T}}_2 = \frac{\mathbf{X}_{\beta_2}}{v},$$

where $u = |\mathbf{X}_{\beta_1}|, v = |\mathbf{X}_{\beta_2}|$. Then normal vector $\hat{\mathbf{N}}$ is defined by

$$\hat{\mathbf{N}} = \hat{\mathbf{T}}_1 \times \hat{\mathbf{T}}_2.$$

The construction of the orthogonal parameterization numerically will be discussed in Section 3.3. For motion by mean curvature, the surface $\mathbf{X}$ evolves by

$$\mathbf{X}_t = \frac{\kappa}{2}\,\hat{\mathbf{N}}, \tag{3.2}$$

where the mean curvature

$$\begin{aligned} \kappa = \kappa_1 + \kappa_2 &= S(\hat{\mathbf{T}}_1)\cdot\hat{\mathbf{T}}_1 + S(\hat{\mathbf{T}}_2)\cdot\hat{\mathbf{T}}_2 \\ &= -\nabla_{\hat{\mathbf{T}}_1}\hat{\mathbf{N}}\cdot\hat{\mathbf{T}}_1 - \nabla_{\hat{\mathbf{T}}_2}\hat{\mathbf{N}}\cdot\hat{\mathbf{T}}_2 \\ &= -\left(\frac{\hat{\mathbf{N}}_{\beta_1}\cdot\hat{\mathbf{T}}_1}{u} + \frac{\hat{\mathbf{N}}_{\beta_2}\cdot\hat{\mathbf{T}}_2}{v}\right), \end{aligned} \tag{3.3}$$

is the sum of the two principal curvatures κ_1 and κ_2. We assume $\mathbf{X}$ is 2π-periodic in β_1 and β_2 and has continuous derivatives in space. This implies that the cross derivatives of β_1 and β_2 commute. From $\mathbf{X}_{\beta_1\beta_2} = \mathbf{X}_{\beta_2\beta_1}$, we get

$$u\,(\hat{\mathbf{N}}_{\beta_2}\cdot\hat{\mathbf{T}}_1) = v\,(\hat{\mathbf{N}}_{\beta_1}\cdot\hat{\mathbf{T}}_2) \tag{3.4}$$

$$\hat{\mathbf{T}}_{1_{\beta_1}}\cdot\hat{\mathbf{T}}_2 = -\frac{u_{\beta_2}}{v} \tag{3.5}$$

$$\hat{\mathbf{T}}_{1_{\beta_2}}\cdot\hat{\mathbf{T}}_2 = \frac{v_{\beta_1}}{u}\,. \tag{3.6}$$

As in two-dimensional problems, adding tangential motions does not alter the shape of the surface, but the parameterization frame of the surface. Thus, we introduce two tangential velocities into the dynamics and rewrite the evolution equation for the surface

as

$$\mathbf{X}_t = f_1\hat{\mathbf{T}}_1 + f_2\hat{\mathbf{T}}_2 + f_3\hat{\mathbf{N}}; \tag{3.7}$$

of course $f_3 = \kappa/2$ here. f_1 and f_2 are the added forces along the two tangential directions which will be determined later. Now we want to derive the evolution equations in terms of u, v and κ. The equations for u and v are derived by differentiating $u = \mathbf{X}_{\beta_1} \cdot \mathbf{T}_1$ and $v = \mathbf{X}_{\beta_2} \cdot \mathbf{T}_2$ with respect to time t:

$$u_t = f_{1\beta_1} + f_2\frac{u_{\beta_2}}{v} + f_3\ \hat{\mathbf{N}}_{\beta_1} \cdot \hat{\mathbf{T}}_1, \tag{3.8}$$

$$v_t = f_{2\beta_2} + f_1\frac{v_{\beta_1}}{u} + f_3\ \hat{\mathbf{N}}_{\beta_2} \cdot \hat{\mathbf{T}}_2. \tag{3.9}$$

Differentiating Eq. (3.3) with respect to t and making use of Eqs. (3.4) – (3.6), we get the evolution equation for κ:

$$\begin{aligned}
\kappa_t = \ & \frac{f_{3_{\beta_1\beta_1}}}{u^2} + \frac{f_{3_{\beta_2\beta_2}}}{v^2} - \frac{1}{u^2}[f_1\ (\hat{\mathbf{N}}_{\beta_1} \cdot \hat{\mathbf{T}}_1)_{\beta_1} + f_2\ (\hat{\mathbf{N}}_{\beta_1} \cdot \hat{\mathbf{T}}_2)_{\beta_1} + f_3\ \hat{\mathbf{N}}_{\beta_1} \cdot \hat{\mathbf{N}}_{\beta_1} + \\
& (2f_{2_{\beta_1}} - f_1\frac{u_{\beta_2}}{v})\ \hat{\mathbf{N}}_{\beta_1} \cdot \hat{\mathbf{T}}_2 + (2f_{1_{\beta_1}} + f_2\frac{u_{\beta_2}}{u})\ \hat{\mathbf{N}}_{\beta_1} \cdot \hat{\mathbf{T}}_1)] - \frac{1}{v^2}[\\
& f_1\ (\hat{\mathbf{N}}_{\beta_2} \cdot \hat{\mathbf{T}}_1)_{\beta_2} + f_2\ (\hat{\mathbf{N}}_{\beta_2} \cdot \hat{\mathbf{T}}_2)_{\beta_2} + (2f_{2_{\beta_2}} + f_1\frac{v_{\beta_2}}{u})\ \hat{\mathbf{N}}_{\beta_2} \cdot \hat{\mathbf{T}}_2 + (2f_{1_{\beta_2}} \\
& -f_2\frac{v_{\beta_1}}{u})\hat{\mathbf{N}}_{\beta_2} \cdot \hat{\mathbf{T}}_1 + f_3\hat{\mathbf{N}}_{\beta_2} \cdot \hat{\mathbf{N}}_{\beta_2}] + 2\frac{u_t}{u^2}\ \hat{\mathbf{N}}_{\beta_1} \cdot \hat{\mathbf{T}}_1 + 2\frac{v_t}{v^2}\ \hat{\mathbf{N}}_{\beta_2} \cdot \hat{\mathbf{T}}_2 \\
& +(\frac{v_{\beta_1}}{u^2v} - \frac{u_{\beta_1}}{u^3})[f_{3_{\beta_1}} - f_1\ \hat{\mathbf{N}}_{\beta_1} \cdot \hat{\mathbf{T}}_1 - f_2\ \hat{\mathbf{N}}_{\beta_1} \cdot \hat{\mathbf{T}}_2] \\
& +(\frac{u_{\beta_2}}{uv^2} - \frac{v_{\beta_2}}{v^3})[f_{3_{\beta_2}} - f_1\ \hat{\mathbf{N}}_{\beta_2} \cdot \hat{\mathbf{T}}_1 - f_2\ \hat{\mathbf{N}}_{\beta_2} \cdot \hat{\mathbf{T}}_2].
\end{aligned} \tag{3.10}$$

Note that the high order terms in the above equation come from the first two terms in the right-hand side. It can be simplified if we have $v = \lambda(t)u$, where λ is only time dependent. We propose that this can be assured by choosing the specific tangential motions (f_1, f_2). This will be discussed in Section 3.3.

Combining Eqs. (3.8) and (3.9), one can easily derive the motion equation for λ:

$$\lambda_t = \frac{f_1\lambda u_{\beta_1} - f_2 u_{\beta_2}}{u^2} + \frac{f_{2\beta 2} - \lambda f_{1\beta 1}}{u} + \frac{f_3[\hat{\mathbf{N}}_{\beta_2} \cdot \hat{\mathbf{T}}_2 - \lambda\hat{\mathbf{N}}_{\beta_2} \cdot \hat{\mathbf{T}}_1]}{u}. \tag{3.11}$$

Now v_t can be omitted. Instead, u_t and v_t are combined as one equation

$$u_t = \frac{1}{2}\left(f_{1\beta_1} + \frac{f_{2\beta_2}}{\lambda} + \frac{f_2\, u_{\beta_2}}{\lambda u} + \frac{f_1\, u_{\beta_1}}{u} + f_3\left(\hat{\mathbf{N}}_{\beta_1}\cdot\hat{\mathbf{T}}_1 + \frac{\hat{\mathbf{N}}_{\beta_2}\cdot\hat{\mathbf{T}}_2}{\lambda}\right)\right). \tag{3.12}$$

When $f_3 = \kappa/2$, the evolution equations in terms of κ, λ and u become

$$\begin{aligned}
\kappa_t &= \frac{\kappa_{\beta_1\beta_1}}{2u^2} + \frac{\kappa_{\beta_2\beta_2}}{2\lambda^2u^2} - \frac{1}{u^2}(f_1\,[(\hat{\mathbf{N}}_{\beta_1}\cdot\hat{\mathbf{T}}_1)_{\beta_1} + \frac{1}{\lambda^2}(\hat{\mathbf{N}}_{\beta_2}\cdot\hat{\mathbf{T}}_1)_{\beta_2}] + f_2\,[(\hat{\mathbf{N}}_{\beta_1}\cdot\hat{\mathbf{T}}_2)_{\beta_2} \\
&\quad + \frac{1}{\lambda^2}(\hat{\mathbf{N}}_{\beta_2}\cdot\hat{\mathbf{T}}_2)_{\beta_2}]) - \frac{1}{u^2}((2f_{2\beta_1} - \frac{f_1u_{\beta_2}}{\lambda u})\hat{\mathbf{N}}_{\beta_1}\cdot\hat{\mathbf{T}}_2 + \frac{f_2u_{\beta_2}}{\lambda u}\hat{\mathbf{N}}_{\beta_1}\cdot\hat{\mathbf{T}}_1 + (2\frac{f_{1\beta_2}}{\lambda^2} - \frac{f_2u_{\beta_1}}{\lambda u}) \\
&\quad \hat{\mathbf{N}}_{\beta_2}\cdot\hat{\mathbf{T}}_1 + \frac{f_1u_{\beta_1}}{\lambda u}\,\hat{\mathbf{N}}_{\beta_2}\cdot\hat{\mathbf{T}}_2) + \frac{2f_2u_{\beta_2}}{\lambda u^3}\,\hat{\mathbf{N}}_{\beta_1}\cdot\hat{\mathbf{T}}_1 + \frac{2f_1u_{\beta_1}}{\lambda u^3}\,\hat{\mathbf{N}}_{\beta_2}\cdot\hat{\mathbf{T}}_2 + \frac{\kappa}{2u^2}((\hat{\mathbf{N}}_{\beta_1}\cdot\hat{\mathbf{T}}_1)^2 \\
&\quad -(\hat{\mathbf{N}}_{\beta_1}\cdot\hat{\mathbf{T}}_2)^2 + \frac{1}{\lambda^2}(\hat{\mathbf{N}}_{\beta_2}\cdot\hat{\mathbf{T}}_2)^2 - \frac{1}{\lambda^2}(\hat{\mathbf{N}}_{\beta_2}\cdot\hat{\mathbf{T}}_1)^2)
\end{aligned} \tag{3.13}$$

$$\begin{aligned}
\lambda_t &= \frac{1}{(2\pi)^2}\int_0^{2\pi}\int_0^{2\pi}(\frac{f_2\beta_2 - \lambda f_{1\beta_1}}{u} + \frac{f_1\lambda u_{\beta_1} - f_2u_{\beta_2}}{u^2} \\
&\qquad + f_3\,\frac{\hat{\mathbf{N}}_{\beta_2}\cdot\hat{\mathbf{T}}_2 - \lambda\,\hat{\mathbf{N}}_{\beta_1}\cdot\hat{\mathbf{T}}_1}{u})\,d\beta_1 d\beta_2,
\end{aligned} \tag{3.14}$$

$$u_t = \frac{1}{2}\left(f_{1\beta_1} + \frac{f_{2\beta_2}}{\lambda} + \frac{f_2u_{\beta_2}}{\lambda u} + \frac{f_1u_{\beta_1}}{u} - \frac{u\kappa^2}{2}\right). \tag{3.15}$$

In the above equations, we see that the equations for λ and u are free of stiffness, we can use an explicit method to solve λ and u at every time step. The high order terms in Eq. (3.13) are the first two terms. Since we know the new updated λ and u at every time step, we can treat $\frac{\kappa_{\beta_1\beta_1}}{2u^2} + \frac{\kappa_{\beta_2\beta_2}}{2\lambda^2u^2}$ implicitly and the rest of the terms in Eq. (3.13) explicitly. For two-dimensional interfaces, we set the arclength variable s_α to be constant in space. For three-dimensional surfaces, we cannot set u to be independent of β. It is impossible to have both u and λ to be constant and keep the frame orthogonal at the same time. Thus, κ cannot be solved explicitly using the Fast Fourier transform (FFT). However, we can still use an iterative method to solve for κ using FFT which will be discussed later in Section 3.3.

3.2 The Equations of Motion of Three-Dimensional Water Wave Problems

We now describe the motion of a three-dimensional surface separating two inviscid, incompressible, irrotational fluids using the boundary integral formulation. We label the

region above the surface as region 1 and the one below as region 2. Since the flow in each region is irrotational, we introduce the velocity potentials ϕ_1 and ϕ_2 given by $\mathbf{u}_1 = \nabla\phi_1$ and $\mathbf{u}_2 = \nabla\phi_2$ with $\mathbf{u}_1/\mathbf{u}_2$ being the velocity above/below the surface. The surface can be considered as a distribution of dipoles of strength density; following, the potential in the fluid domain off the surface is defined as

$$\phi(\mathbf{X}) = \int \mu(\mathbf{X}')(\mathbf{X}_{\beta_1} \times \mathbf{X}_{\beta_2})(\mathbf{X}') \cdot \nabla_{\mathbf{X}'} G(\mathbf{X}, \mathbf{X}') dS' \tag{3.16}$$

where

$$G(\mathbf{X}, \mathbf{X}') = -\frac{1}{4\pi|\mathbf{X} - \mathbf{X}'|}, \quad \nabla_{\mathbf{X}'} G = -\frac{\mathbf{X} - \mathbf{X}'}{4\pi|\mathbf{X} - \mathbf{X}'|^3}, \tag{3.17}$$

and the dipole strength $\mu = \phi_- - \phi_+$ is to be determined by ϕ. Using the limit for the double layer potential, we obtain a Fredholm integral equation of the second kind for μ on the surface

$$\mu = 2\phi(\mathbf{X}(\beta)) - \int \mu(\mathbf{X}')(\mathbf{X}_{\beta_1} \times \mathbf{X}_{\beta_2})(\mathbf{X}') \cdot \nabla_{\mathbf{X}'} G(\mathbf{X}, \mathbf{X}') dS'. \tag{3.18}$$

This equation can be solved by iteration on μ. By differentiating (3.16) with respect to $\mathbf{X}$ and then integrating by parts, we obtain the velocity on the surface to be

$$w(x, y, z) = \nabla\phi(\mathbf{X}(\beta)) = w_0(\beta) + w_{loc}(\beta), \tag{3.19}$$

$$w_0(x, y, z) = \int K(\mathbf{X}') \times \nabla_{\mathbf{X}'} G(\mathbf{X}, \mathbf{X}') dS', \tag{3.20}$$

$$w_{loc}(x, y, z) = \frac{1}{2} K(\mathbf{X}) \times (\mathbf{X}_{\beta_1} \times \mathbf{X}_{\beta_2}) / |\mathbf{X}_{\beta_1} \times \mathbf{X}_{\beta_2}|^2, \tag{3.21}$$

here

$$K(\mathbf{X}') = \frac{\partial\mu}{\partial\beta_1}\mathbf{X}_{\beta_2} - \frac{\partial\mu}{\partial\beta_2}\mathbf{X}_{\beta_1}.$$

The evolution equation for the surface is then given by

$$\frac{\partial\mathbf{X}}{\partial t} = w(x, y, z). \tag{3.22}$$

The continuity of normal stresses gives the Bernoulli's equation which described the evolution equation for $\phi(\beta, t)$.

$$\left.\frac{\partial \phi}{\partial t}\right|_{\mathbf{X}} + \frac{1}{2}|w|^2 + gz = \tau\kappa. \tag{3.23}$$

Here g is the gravity constant, τ is the surface tension and κ is the mean curvature. The $\tau\kappa$ term comes from the pressure difference at the surface. The Eqs. (3.22), and (3.23) together with the relations (3.18) and (3.19), completely specify the motion of the system.

3.2.1 A Simplified Water Wave Model

Numerical simulations for three-dimensional water wave problem demand a great computational effort. The main work is spent in evaluating the surface velocity and velocity potential which requires $O(N^4)$ calculations where N is the number of particles used to discretize the surface in each dimension. In addition, as with the two-dimensional problems, the three-dimensional water wave problem is susceptible to severe numerical instabilities.

Motivated by the small scale decomposition, we can derive a simplified model equation to approximate the velocity integral. More precisely, we replace the boundary integral for the surface velocity by its leading contribution at high modes. First, we write the surface evolution equation in the form of Eq. (3.7). Also, noticing $w_{loc} \cdot \hat{\mathbf{N}} = 0$, we have the normal velocity

$$f_3(\beta) = \left(\int \left(\frac{\partial \mu}{\partial \beta_1} \mathbf{X}_{\beta_2} - \frac{\partial \mu}{\partial \beta_2} \mathbf{X}_{\beta_1} \right) \times \left(-\frac{\mathbf{X}(\beta) - \mathbf{X}(\beta')}{4\pi \left| \mathbf{X}(\beta) - \mathbf{X}(\beta') \right|^3} \right) d\beta' \right) \cdot \hat{\mathbf{N}}(\beta). \tag{3.24}$$

In order to get the leading contribution at high modes for f_3, we expand $\mathbf{X}(\beta)$ at $\beta = \beta'$ and it leads to

$$f_3 \sim \int \left(\frac{\left(\mu_1(\beta') \hat{\mathbf{N}}(\beta')(\beta_1 - \beta_1') + \mu_2(\beta') \hat{\mathbf{N}}(\beta')(\beta_2 - \beta_2') \right) |\mathbf{X}_{\beta_1}(\beta')||\mathbf{X}_{\beta_2}(\beta')|}{4\pi \left(|\mathbf{X}_{\beta_1}|^2 (\beta_1 - \beta_1')^2 + |\mathbf{X}_{\beta_2}|^2 (\beta_2 - \beta_2')^2 \right)^{3/2}} \right) \cdot \hat{\mathbf{N}}(\beta) d\beta' \tag{3.25}$$

Here to simplify notations, we write $\mu_1 = \frac{\partial \mu}{\partial \beta_1}$ and $\mu_2 = \frac{\partial \mu}{\partial \beta_2}$.

Next we expand $\hat{\mathbf{N}}(\beta)$ at $\beta = \beta'$ and make use of the orthogonality of the frame

$(\hat{\mathbf{T}}_1, \hat{\mathbf{T}}_2, \hat{\mathbf{N}})$, we get

$$f_3 \sim \frac{|\mathbf{X}_{\beta_1}||\mathbf{X}_{\beta_2}|}{4\pi} \int \frac{\mu_1(\beta')(\beta_1 - \beta_1') + \mu_2(\beta')(\beta_2 - \beta_2')}{\left(|\mathbf{X}_{\beta_1}|^2(\beta_1 - \beta_1')^2 + |\mathbf{X}_{\beta_2}|^2(\beta_2 - \beta_2')^2\right)^{3/2}} \, d\beta'. \tag{3.26}$$

Now we introduce the Rietz transforms $\mathcal{H}_1$, $\mathcal{H}_2$ and Λ, defined by

$$(\mathcal{H}_l f)(\alpha) = \frac{1}{2\pi} \int \frac{(\alpha_l - \alpha_l')f(\alpha_l')}{(|\mathbf{X}_{\alpha_1}|^2(\alpha_1 - \alpha_1')^2 + |\mathbf{X}_{\alpha_2}|^2(\alpha_2 - \alpha_2')^2)^{3/2}} \, d\alpha', \quad l = 1, 2, \tag{3.27}$$

and

$$(\Lambda f)(\alpha) = \frac{1}{2\pi} \int \frac{f(\alpha) - f(\alpha')}{(|\mathbf{X}_{\alpha_1}|^2(\alpha_1 - \alpha_1')^2 + |\mathbf{X}_{\alpha_2}|^2(\alpha_2 - \alpha_2')^2)^{3/2}} \, d\alpha'. \tag{3.28}$$

Using integration by parts, one can show that the Λ operator is related to $\mathcal{H}_l$, $l = 1, 2$ by

$$\Lambda f = (\mathcal{H}_1 D_1 + \mathcal{H}_2 D_2) f, \tag{3.29}$$

where D_l, $l = 1, 2$ is a derivative operator with respect to β_l.

Hou *et al.* [24] have proved that the Rietz transforms have the following spectral representation:

$$(\mathcal{H}_l f)(\alpha) = \int \frac{-i\xi_l \hat{f}(\xi) e^{i\xi\cdot\alpha}}{|\mathbf{X}_{\alpha_l}|^2(|\mathbf{X}_{\alpha_2}|^2\xi_1^2 + |\mathbf{X}_{\alpha_1}|^2\xi_2^2)^{1/2}} \, d\xi, \quad l = 1, 2, \tag{3.30}$$

and

$$\Lambda f = \int \frac{(|\mathbf{X}_{\alpha_2}|^2\xi_1^2 + |\mathbf{X}_{\alpha_1}|^2\xi_2^2)^{1/2}}{|\mathbf{X}_{\alpha_1}|^2|\mathbf{X}_{\alpha_2}|^2} \hat{f}(\xi) e^{i\xi\cdot\alpha} \, d\xi. \tag{3.31}$$

Making use of Eqs. (3.18) and (3.31), we obtain the leading order behavior of f_3 at small scales as

$$\begin{aligned} f_3 &\sim \frac{|\mathbf{X}_{\beta_1}||\mathbf{X}_{\beta_2}|}{2} \left(\mathcal{H}_1(D_1\mu) + \mathcal{H}_2(D_2\mu)\right) \\ &\sim |\mathbf{X}_{\beta_1}||\mathbf{X}_{\beta_2}| \, \Lambda(\phi) \\ &= \int \frac{(|\mathbf{X}_{\beta_1}|^2\xi_1^2 + |\mathbf{X}_{\beta_2}|^2\xi_2^2)^{1/2}}{|\mathbf{X}_{\beta_1}||\mathbf{X}_{\beta_2}|} \hat{\phi}(\xi) e^{i\xi\cdot\alpha} \, d\xi. \end{aligned} \tag{3.32}$$

Remember we have set $v = \lambda u$, i.e., $|\mathbf{X}_{\beta_2}| = \lambda |\mathbf{X}_{\beta_1}|$, the above relation is thus simplified to be

$$f_3 \sim \frac{1}{u} \int (\xi_1^2 + \frac{\xi_2^2}{\lambda^2})^{1/2} \hat{\phi}(\xi) e^{i\xi\cdot\alpha} \, d\xi = \frac{\bar{\Lambda}(\phi)}{u} \, . \tag{3.33}$$

Here $\bar{\Lambda}(\phi)$ is defined as $\int (\xi_1^2 + \frac{\xi_2^2}{\lambda^2})^{1/2} \hat{\phi}(\xi) e^{i\xi\cdot\alpha} \, d\xi$.

We denote the velocity of the Lagrangian particles on the surface as $\tilde{w}$. It can be different from the velocity w from Eq. (3.19) because we have freedom to select the tangential force. Thus,

$$\frac{\partial \mathbf{X}}{\partial t} = \tilde{w}(x, y, z). \tag{3.34}$$

Now, Bernoulli's equation can be evaluated in this Lagrangian frame, by noting that

$$\left.\frac{\partial \phi}{\partial t}\right|_{\alpha} = \left.\frac{\partial \phi}{\partial t}\right|_{\mathbf{X}} + Re\{\tilde{w} \cdot w\}. \tag{3.35}$$

Substituting Eq. (3.23) into the above equation, we get

$$\left.\frac{\partial \phi}{\partial t}\right|_{\alpha} = Re\{\tilde{w} \cdot w\} - \frac{1}{2}|w|^2 - gz + \tau\kappa. \tag{3.36}$$

Observing that the dominant term for ϕ_t is $\tau\kappa$ (check Eq. (3.23)) at small scales and substituting Eq. (3.33) into Eq. (3.10) give us

$$\kappa_t = \frac{1}{u^2} \left(\frac{\bar{\Lambda}(\phi)}{u} \right)_{\beta_1\beta_1} + \frac{1}{\lambda^2 u^2} \left(\frac{\bar{\Lambda}(\phi)}{u} \right)_{\beta_2\beta_2} + P \tag{3.37}$$

$$\phi_t = \tau\kappa + Q, \tag{3.38}$$

where P and Q represent lower order terms at small spatial scales which do not contribute to the stiffness. If λ and u are given, the dominant small scale terms are linear in κ and ϕ, but nonlocal by virtue of the Rietz transform. An implicit discretization can be obtained by discretizing the leading order terms implicitly, but treating the lower order terms explicitly.

3.3 Some Implementation Issues

In this section, we first discuss the construction of the initial orthogonal parameterization of the surface $\mathbf{X}(\beta_1, \beta_2) = (x(\beta_1, \beta_2), y(\beta_1, \beta_2), z(\beta_1, \beta_2))$ such that

$$\mathbf{X}_{\beta_1} \cdot \mathbf{X}_{\beta_2} = 0 \tag{3.39}$$

$$\mathbf{X}_{\beta_1} \cdot \mathbf{X}_{\beta_1} = \lambda \mathbf{X}_{\beta_2} \cdot \mathbf{X}_{\beta_2}. \tag{3.40}$$

We cannot prove the existence of such a parameterization yet. In our computation, we assume this condition holds where λ only depends on time. A tangential motion is introduced into the dynamics to enforce that without changing the shape of the surface. We then discuss how to choose the tangential motion (f_1, f_2). At last, we talk about the reconstruction of the surface from curvature and the preconditioned conjugate gradient method for solving κ.

3.3.1 Initial Orthogonal System

The surface we consider is given by

$$Z = (x, y, \eta(x, y)) \tag{3.41}$$

with x and y being the two parameters. We want to find a mapping $(x, y) \Rightarrow (\beta_1, \beta_2)$ such that

$$Z_{\beta_1} \cdot Z_{\beta_2} = C_1 Z_{\beta_2} \cdot Z_{\beta_2} \tag{3.42}$$

$$Z_{\beta_1} \cdot Z_{\beta_1} = C_2 Z_{\beta_2} \cdot Z_{\beta_2}. \tag{3.43}$$

Suppose we have

$$x = \beta_1 + S_1(\beta_1, \beta_2), \tag{3.44}$$

$$y = \beta_2 + S_2(\beta_1, \beta_2), \tag{3.45}$$

where S_1 and S_2 are periodic in β. By the chain rule, we get

$$Z_{\beta_1} = (x_{\beta_1}, y_{\beta_1}, \eta_x x_{\beta_1} + \eta_y y_{\beta_1}) = (1 + S_{1,\beta_1}, S_{2,\beta_1}, \eta_x(1 + S_{1,\beta_1}) + \eta_y S_{2,\beta_1}) \quad (3.46)$$

$$Z_{\beta_2} = (x_{\beta_2}, y_{\beta_2}, \eta_x x_{\beta_2} + \eta_y y_{\beta_2}) = (S_{1,\beta_2}, 1 + S_{2,\beta_2}, \eta_x S_{1,\beta_2} + \eta_y(1 + S_{2,\beta_2})). \quad (3.47)$$

Thus,

$$Z_{\beta_1} \cdot Z_{\beta_2} = S_{1,\beta_2} + S_{2,\beta_1} + S_{1,\beta_1} S_{1,\beta_2} + S_{2,\beta_1} S_{2,\beta_2} + (\eta_x(1 + S_{1,\beta_1}) + \eta_y S_{2,\beta_1}) \cdot (\eta_x S_{1,\beta_2} + \eta_y(1 + S_{2,\beta_2})) \quad (3.48)$$

$$Z_{\beta_1} \cdot Z_{\beta_1} = 1 + 2S_{1,\beta_1} + (S_{1,\beta_1})^2 + (S_{2,\beta_1})^2 + (\eta_x(1 + S_{1,\beta_1}) + \eta_y S_{2,\beta_1})^2 \quad (3.49)$$

$$Z_{\beta_2} \cdot Z_{\beta_2} = 1 + 2S_{2,\beta_2} + (S_{2,\beta_2})^2 + (S_{1,\beta_2})^2 + (\eta_x S_{1,\beta_2} + \eta_y(1 + S_{2,\beta_2}))^2. \quad (3.50)$$

Substituting these equations into Eqs. (3.42) and (3.43), we get the coupled equations for S_1 and S_2:

$$\frac{\partial S_1}{\partial \beta_2} + \frac{\partial S_2}{\partial \beta_1} = C_1(Z_{\beta_2} \cdot Z_{\beta_2}) - (Z_{\beta_1} \cdot Z_{\beta_2} - S_{1,\beta_2} - S_{2,\beta_1}) \equiv F_1, \quad (3.51)$$

$$\frac{\partial S_1}{\partial \beta_1} - C_2 \frac{\partial S_2}{\partial \beta_2} = (S_{1,\beta_1} - \frac{Z_{\beta_1} \cdot Z_{\beta_1}}{2}) - C_2(S_{2,\beta_2} - \frac{Z_{\beta_2} \cdot Z_{\beta_2}}{2}) \equiv F_2 \quad (3.52)$$

where

$$C_1 = \frac{< Z_{\beta_1} \cdot Z_{\beta_2} >}{< Z_{\beta_2} \cdot Z_{\beta_2} >} \quad , \qquad C_2 = \frac{< Z_{\beta_1} \cdot Z_{\beta_1} >}{< Z_{\beta 2} \cdot Z_{\beta 2} >} \quad .$$

(3.51) and (3.52) can be changed to

$$\frac{\partial^2 S_1}{\partial^2 \beta_1} + C_2 \frac{\partial^2 S_1}{\partial^2 \beta_2} = C_2 \frac{\partial F_1}{\partial \beta_2} + \frac{\partial F_2}{\partial \beta_1} \quad (3.53)$$

$$\frac{\partial^2 S_2}{\partial^2 \beta_1} + C_2 \frac{\partial^2 S_2}{\partial^2 \beta_2} = \frac{\partial F_1}{\partial \beta_1} - \frac{\partial F_2}{\partial \beta_2}. \quad (3.54)$$

We implement an iterative method to solve this system. The iteration scheme can be written as

$$\frac{\partial^2 S_1^{n+1}}{\partial^2 \beta_1} + C_2 \frac{\partial^2 S_1^{n+1}}{\partial^2 \beta_2} = C_2 \frac{\partial F_1^n}{\partial \beta_2} + \frac{\partial F_2^n}{\partial \beta_1} \tag{3.55}$$

$$\frac{\partial^2 S_2^{n+1}}{\partial^2 \beta_1} + C_2 \frac{\partial^2 S_2^{n+1}}{\partial^2 \beta_2} = \frac{\partial F_1^n}{\partial \beta_1} - \frac{\partial F_2^n}{\partial \beta_2}. \tag{3.56}$$

This quasi-Poisson equations for S_1 and S_2 are easily solved using FFT. In our computation, C_1 is taken to be 0 for simplicity. For our numerical examples, the orthogonal coordinate system can be found.

Suppose the surface cannot be described as (3.41); instead it is given in the form of $\mathbf{Z} = (x(\alpha_1), y(\alpha_2), \epsilon z(\alpha))$ which is a perturbation of a plane. Using the same idea, we can also derive an iteration method to construct the orthogonal coordinate system.

3.3.2 Tangential Velocities

In order to have the system satisfy (3.39) and (3.40) for all time, we introduce a tangential motion (f_1, f_2). First, by differentiating $v = \lambda(t)u$ with respect to t and making use of Eqs. (3.8) and (3.9), we get

$$\lambda f_{1\beta_1} - f_{2\beta_2} = \frac{1}{u}(\lambda f_1 u_{\beta_1} - f_2 u_{\beta_2}) + f_3(\hat{\mathbf{N}}_{\beta_2} \cdot \hat{\mathbf{T}}_2 - \lambda \hat{\mathbf{N}}_{\beta_1} \cdot \hat{\mathbf{T}}_1) - \lambda_t u \equiv F_1. \tag{3.57}$$

Also from $(\mathbf{X}_{\beta_1} \cdot \mathbf{X}_{\beta_2})_t = 0$, we get

$$f_{1\beta_2} + \lambda f_{2\beta_1} = \frac{1}{u}(f_1 u_{\beta_2} + \lambda f_2 u_{\beta_1}) - f_3(\hat{\mathbf{N}}_{\beta_2} \cdot \hat{\mathbf{T}}_1 + \lambda \hat{\mathbf{N}}_{\beta_1} \cdot \hat{\mathbf{T}}_2) \equiv F_2. \tag{3.58}$$

We then rewrite the system for f_1 and f_2 by differentiating Eqs. (3.57) and (3.58),

$$\Delta f_1 + (\lambda - \frac{1}{\lambda}) f_{2_{\beta_1\beta_2}} = \frac{\partial F_2}{\partial \beta_2} + \frac{1}{\lambda}\frac{\partial F_1}{\partial \beta_1}$$

$$\Delta f_2 + (-\lambda + \frac{1}{\lambda}) f_{1_{\beta_1\beta_2}} = \frac{1}{\lambda}\frac{\partial F_2}{\partial \beta_1} + \frac{\partial F_1}{\partial \beta_2}.$$

As in Section 3.3.1, we also solve these equations iteratively. The iteration scheme can be written as

$$\Delta f_1^{n+1} + (\lambda - \frac{1}{\lambda}) f_{2\beta_1\beta_2}^{n+1} = \frac{\partial F_2^n}{\partial \beta_2} + \frac{1}{\lambda}\frac{\partial F_1^n}{\partial \beta_1} \equiv G_1^n \tag{3.59}$$

$$\Delta f_2^{n+1} + (-\lambda + \frac{1}{\lambda}) f_{1\beta_1\beta_2}^{n+1} = \frac{1}{\lambda}\frac{\partial F_2^n}{\partial \beta_1} + \frac{\partial F_1^n}{\partial \beta_2} \equiv G_2^n. \tag{3.60}$$

They are easy to solve using FFT in each iteration. In the Fourier space, the above two equations become

$$\begin{bmatrix} \hat{f_1}^{n+1}(\xi_1,\xi_2) \\ \hat{f_2}^{n+1}(\xi_1,\xi_2) \end{bmatrix} = \frac{\begin{bmatrix} -(\xi_1^2+\xi_2^2) & \xi_1\xi_2(\lambda - \frac{1}{\lambda}) \\ -\xi_1\xi_2(\lambda - \frac{1}{\lambda}) & -(\xi_1^2+\xi_2^2) \end{bmatrix}}{(\xi_1^2+\xi_2^2)^2 + (\xi_1\xi_2)^2(\lambda - \frac{1}{\lambda})^2} \begin{bmatrix} \hat{G_1}^n(\xi_1,\xi_2) \\ \hat{G_2}^n(\xi_1,\xi_2) \end{bmatrix}. \tag{3.61}$$

In our numerical experiments, it only takes a few iterations to converge with an iteration error of 10^{-11}.

3.3.3 Reconstruction of the Surface from Curvature

We use the same idea to reconstruct the surface from curvature as the two-dimensional cases. We reconstruct (x, y, z) through integration of the original evolution equation (3.7). Making use to (3.33), we get

$$\mathbf{X}_t = \frac{\bar{\Lambda}(\phi)}{u}\hat{\mathbf{N}} + P, \tag{3.62}$$

where P includes the lower order terms. In our computation, we treat $\bar{\Lambda(\phi)}/u$ implicitly and all the other terms explicitly. We denote the solution of Eq. (3.62) by $\bar{\mathbf{X}}$. Due to the numerical error, $\bar{\mathbf{X}}_{\beta_1}$ is not exactly u and $\bar{\mathbf{X}}_{\beta_2}$ is not exactly λu. This makes Eq. (3.62) not compatible with Eqs. (3.11), (3.12), (3.37) and (3.38). In order to overcome this difficulty, we enforce $\mathbf{X}_{\beta_1} = u$ and $\mathbf{X}_{\beta_2} = \lambda u$ to be satisfied. This is achieved by integrating the equations

$$\mathbf{X}_{\beta_1} = \frac{u}{|\bar{\mathbf{X}}_{\beta_1}|}\bar{\mathbf{X}}_{\beta_1} \equiv F_1(\beta_1,\beta_2), \tag{3.63}$$

$$\mathbf{X}_{\beta_2} = \frac{\lambda u}{|\bar{\mathbf{X}}_{\beta_2}|}\bar{\mathbf{X}}_{\beta_2} \equiv F_2(\beta_1,\beta_2), \tag{3.64}$$

with respect to β_1 and β_2 to get $\mathbf{X}$ for the next time step. For flows which are periodic in x and y, it requires $\mathbf{X} = \mathbf{X}(\beta_1, \beta_2, t)$ to be periodic in β_1 and β_2. In particular, the coefficient of the linear terms in β_1 and β_2 should be 0. Unfortunately, integrating Eqs. (3.63) and (3.64) using the DFT perturbs the coefficients slightly due to the numerical error. This difficulty is fixed by forcing the coefficients to be exactly 0, after the reconstruction process. From Eq. (3.63), we get

$$\mathbf{X} = \int_0^{\beta_1} F_1 \, d\beta_1 - \frac{\beta_1}{2\pi} \int_0^{2\pi} F_1 \, d\beta_1 + F_3(\beta_2). \tag{3.65}$$

Differentiating (3.65) with respect to β_2 gives us

$$\mathbf{X}_{\beta_2} = \int_0^{\beta_1} (F_1)_{\beta_2} \, d\beta_1 - \frac{\beta_1}{2\pi} \int_0^{2\pi} (F_1)_{\beta_2} \, d\beta_1 + F_3'. \tag{3.66}$$

Making use of $(F_1)_{\beta_2} = (F_2)_{\beta_1}$ and (3.64), we derive one formulation for $\mathbf{X}$

$$\mathbf{X} = \mathbf{X}(0,0,t) + \int_0^{\beta_1} F_1 d\beta_1 - \frac{\beta_1}{2\pi} \int_0^{2\pi} F_1 d\beta_1 + \int_0^{\beta_2} F_2(0, \beta_2') d\beta_2 - \frac{\beta_2}{2\pi} \int_0^{2\pi} F_2(0, \beta_2') d\beta_2 \tag{3.67}$$

Similarly we get

$$\mathbf{X} = \mathbf{X}(0,0,t) + \int_0^{\beta_2} F_2 d\beta_2 - \frac{\beta_2}{2\pi} \int_0^{2\pi} F_2 d\beta_2 + \int_0^{\beta_1} F_1(\beta_1', 0) d\beta_1 - \frac{\beta_1}{2\pi} \int_0^{2\pi} F_1(\beta_1', 0) d\beta_1 \tag{3.68}$$

Thus combining the above two equations, we reconstruct $\mathbf{X}$ by using

$$\begin{aligned} \mathbf{X}(\beta_1, \beta_2, t) \;=\; & \mathbf{X}(0,0,t) + \frac{1}{2}\Big(\int_0^{\beta_1} G_1 \, d\beta_1 - \frac{\beta_1}{2\pi} \int_0^{2\pi} G_1 \, d\beta_1 + \\ & \int_0^{\beta_2} G_2 \, d\beta_2 - \frac{\beta_2}{2\pi} \int_0^{2\pi} G_2 \, d\beta_2\Big), \end{aligned} \tag{3.69}$$

where

$$G_1 = F_1(\beta_1, \beta_2) + F_1(\beta_1, 0), \tag{3.70}$$

$$G_2 = F_2(\beta_1, \beta_2) + F_2(0, \beta_2). \tag{3.71}$$

$$\tag{3.72}$$

3.3.4 Preconditioned Conjugate Gradient Method

We apply the fourth order multi-step implicit/explicit scheme studied in [1] by Ascher, Ruuth and Wetton to our problem (3.37) and (3.38). We obtain the following system:

$$\frac{1}{\Delta t}(\frac{25}{12}\kappa^{n+1} - 4\kappa^n + 3\kappa^{n-1} - \frac{4}{3}\kappa^{n-2} + \frac{1}{4}\kappa^{n-3}) = \frac{1}{u^{n+1^2}}\left(\frac{\bar{\Lambda}^{n+1}(\phi^{n+1})}{u^{n+1}}\right)_{\beta_1\beta_1} + \frac{1}{(\lambda^{n+1}u^{n+1})^2}\left(\frac{\bar{\Lambda}^{n+1}(\phi^{n+1})}{u^{n+1}}\right)_{\beta_2\beta_2} + 4P^n - 6P^{n-1} + 4P^{n-2} - P^{n-3}$$

and

$$\frac{1}{\Delta t}(\frac{25}{12}\phi^{n+1} - 4\phi^n + 3\phi^{n-1} - \frac{4}{3}\phi^{n-2} + \frac{1}{4}\phi^{n-3}) = \tau\kappa^{n+1} + 4Q^n - 6Q^{n-1} + 4Q^{n-2} - Q^{n-3}.$$

By substituting ϕ^{n+1} into the equation for κ^{n+1}, we can eliminate ϕ^{n+1} and obtain a single equation for κ^{n+1}, which takes the form:

$$(u^{n+1})^2\kappa^{n+1} - \tau(\frac{12}{25}\Delta t)^2\left((\frac{\bar{\Lambda}^{n+1}(\phi^{n+1})}{u^{n+1}})_{\beta_1\beta_1} + (\frac{\bar{\Lambda}^{n+1}(\phi^{n+1})}{(\lambda^{n+1})^2u^{n+1}})_{\beta_2\beta_2}\right) = N(\beta_1,\beta_2,t), \tag{3.73}$$

where N is a known quantity depending on the solutions at the previous time steps. The spatial derivative is discretized by a spectral method. Since u^{n+1} depends on β, the equation is no longer diagonalized by the Fourier transform. Consequently, we use an iterative method to solve for κ^{n+1}. Note that the linear operator in the left-hand side of (3.73) is symmetric, positive definite, we use the Preconditioned conjugate gradient method. The preconditioning operator M is given by:

$$M(\kappa^{n+1}) = u_{max}^2\kappa^{n+1} - \frac{\tau}{u_{min}}(\frac{12}{25}\Delta t)^2\left(\bar{\Lambda}(\kappa^{n+1}))_{\beta_1\beta_1} + \frac{1}{(\lambda^{n+1})^2}\bar{\Lambda}(\kappa^{n+1}))_{\beta_2\beta_2}\right), \tag{3.74}$$

where $u_{max} = \max_\beta u^{n+1}$ and $u_{min} = \min_\beta u^{n+1}$. Thus M is constant coefficient and is diagonalized by the Fourier transform:

$$\hat{M}(\kappa)(\xi_1, \xi_2) = \left(u_{max}^2 + \frac{\tau}{u_{min}} (\frac{12}{25}\Delta)^2 \, (\xi_1^2 + \frac{\xi_2^2}{(\lambda^{n+})^2})^{3/2} \right) \hat{\kappa}(\xi_1, \xi_2). \tag{3.75}$$

Note that M can be inverted in $N^2 \log N$ operations using FFT. Empirically, it only takes two to three iterations to converge with an iterative error of 10^{-11}. The error we consider is the maximum change of successive iterates.

3.4 Numerical Results

3.4.1 Motion By Mean Curvature for Three-Dimensional Surfaces

We begin our numerical experiments with motion by mean curvature for three-dimensional surfaces. First we consider a surface which is extended from a two-dimensional curve

$$\mathbf{X} = (\alpha_1 + 0.5\cos(2\alpha_1),\ \alpha_2,\ 2\sin(\alpha_1)), \qquad 0 \le \alpha_1, \alpha_2 \le 2\pi.$$

Using our κ-λ-u formulation, with $N = 64$ mesh points and time step $\Delta t = 0.025$, we show in Fig. 3.1 the shape of the surface at $t = 0, 0.5, 1.5$ and $t = 5.0$. We observe that the surface moves faster where it has greater curvature and relaxes to a flat surface eventually.

We compare our method with a straightforward explicit discretization of $\mathbf{X}_t = \kappa \mathbf{N}$ in (x, y, z) coordinates. This involves using a spectral method for the spatial derivatives and fourth order Runge-Kutta method in time. We list below the maximum time step that can be taken to get a stable solution using these two methods in Table 3.1.

Next we consider the initial surface given by

$$\mathbf{X} = (\alpha_1,\ \alpha_2,\ 0.5\cos(\alpha_1)\sin(2\alpha_2)), \qquad 0 \le \alpha_1, \alpha_2 \le 2\pi.$$

Using our κ-λ-u formulation, with $N = 64$ mesh points and time step $\Delta t = 0.01$, we show in Fig. 3.2 the shape of the surface at $t = 0, 0.4, 0.8$ and $t = 1.2$. The surface relaxes quickly to a flat surface. When we increase the number of points, we do see the

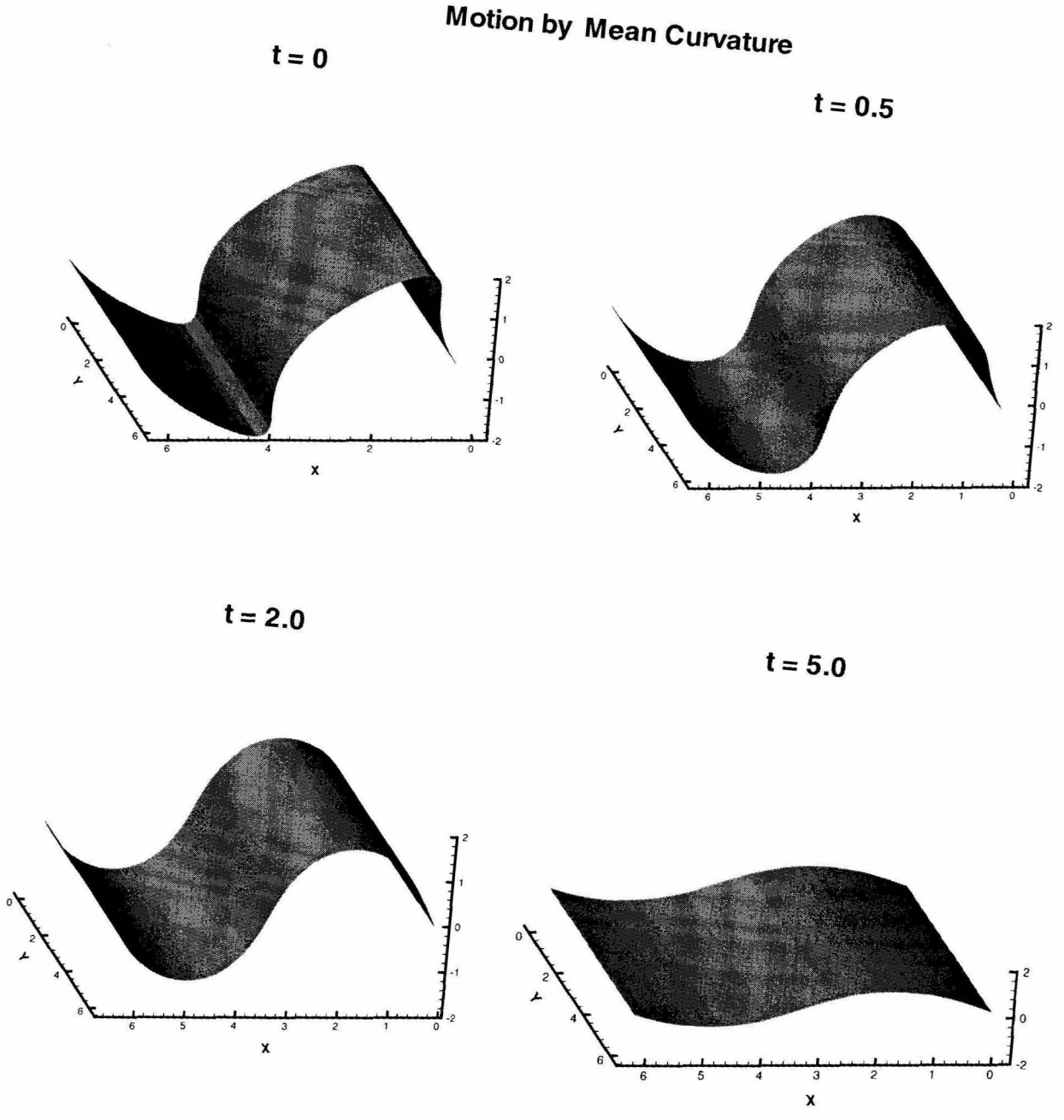

Figure 3.1: Motion by mean curvature: $N = 64, \Delta t = 0.05$; (a) $t = 0$, (b) $t = 0.5$, (c) $t = 2.0$, (d) $t = 5.0$.

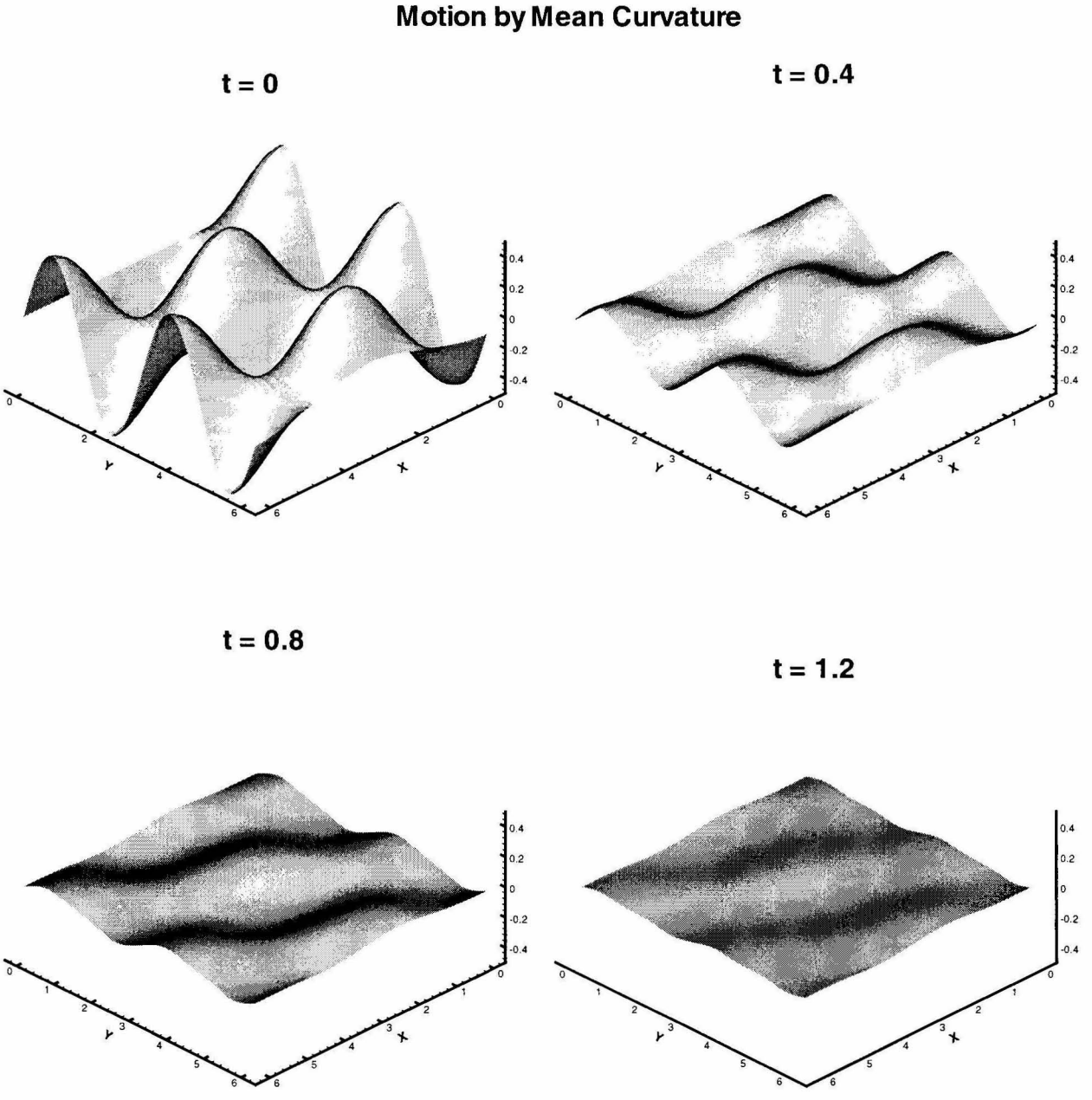

Figure 3.2: Motion by mean curvature: $N = 64, \Delta t = 0.002$; (a) $t = 0$, (b) $t = 0.4$, (c) $t = 0.8$, (d) $t = 1.2$.

No. of points	Explicit Method	κ-λ-u Method
16	0.05	0.1
32	0.0075	0.05
64	0.00125	0.025
128	0.0003125	0.01

Table 3.1: Comparison of the maximum time step for explicit method and κ-λ- u method on motion by mean curvature problem in three dimensions.

time step decreases linearly. The above computation shows that our method does not have severe time step constraint.

3.4.2 Simplified Water Wave Model Approximation

Next we test our numerical methods on the simplified water wave model developed in the previous chapters. The initial condition is given by

$$\begin{aligned} z(x,y) &= \frac{\exp(-10(x-\pi)^2+(y-\pi)^2)}{10}, \\ \phi &= 0. \end{aligned}$$

The initial wave profile is shown in Fig. 3.3. For our first experiment, we choose the surface tension to be 0.01. In Figures 3.4 – 3.8 we show the wave profile at times $t = 0.6, 0.8, 1.2, 1.8, 3.0$ respectively. There are $N = 128$ points in each dimension and the time step used is $\Delta t = 0.005$. We see that the wave drops around $t = 0.6$ but has rebounded with a lower maximum amplitude, by $t = 0.8$. It has droped down again by about $t = 1.4$. After that, it starts spreading out and two ripples have formed at $t = 3.0$.

For our next experiment, we use the same initial condition but choose a smaller surface tension, $\tau = 1 \times 10^{-4}$. Initially, the wave profiles look very similar to the surface tension $\tau = 0.01$ case. We plot the wave at $t = 0.8$ in Fig. 3.9. Comparing this with the $\tau = 0.01$ case, we see that the peak of the wave is pointier, which is expected since a larger surface tension tends to smooth the surface more. We also show the wave profile at times $t = 1.4, 1.8, 2.4$ and 3.0 in Figs. (3.4.2) – (3.13) respectively.

The wave begins propagating outward after $t = 1.8$ for both cases. One difference

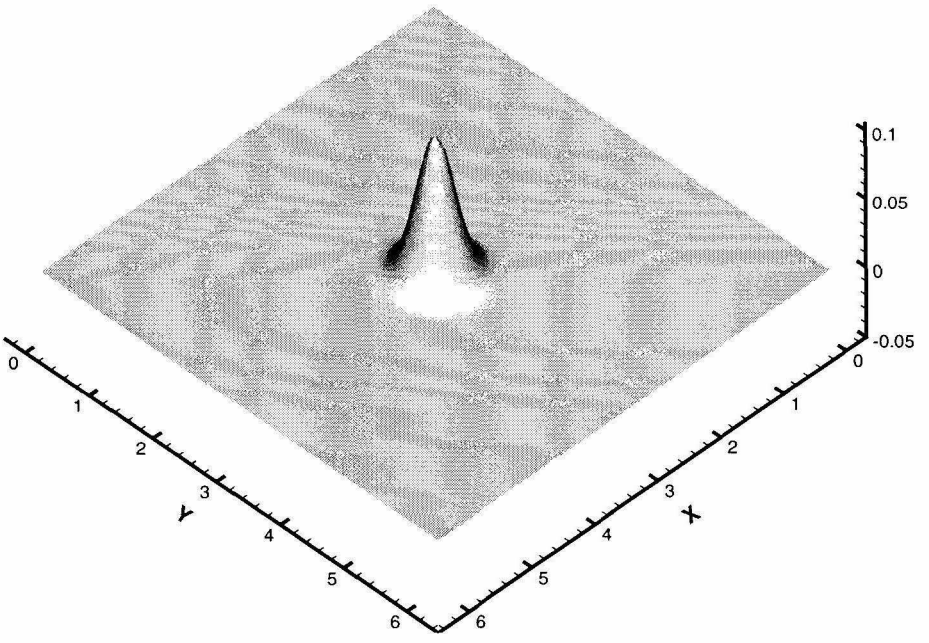

Figure 3.3: Gaussian wave initial condition.

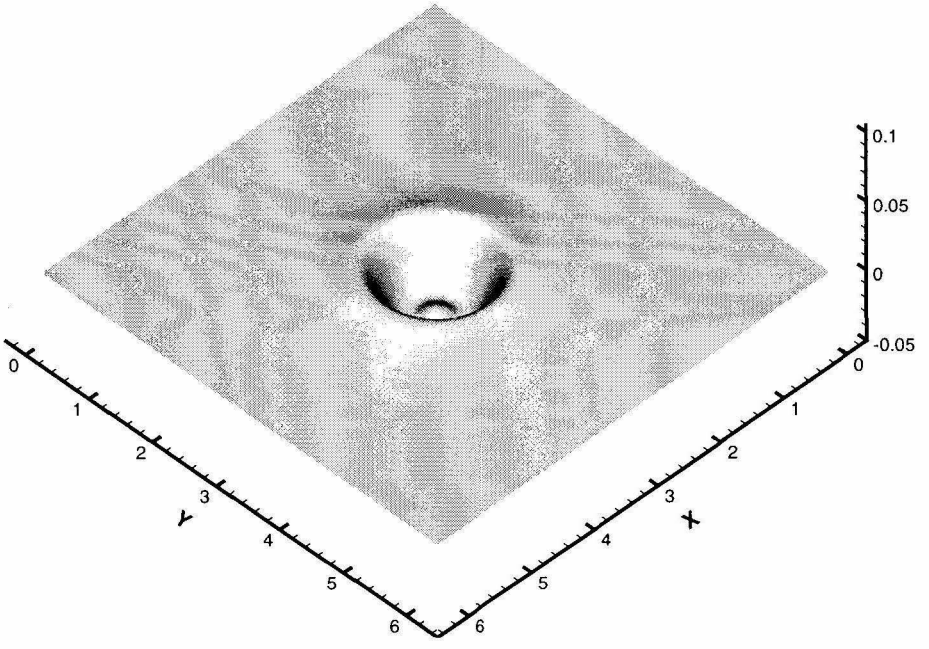

Figure 3.4: Gaussian wave at $t = 0.6$ with surface tension $\tau = 0.01$.

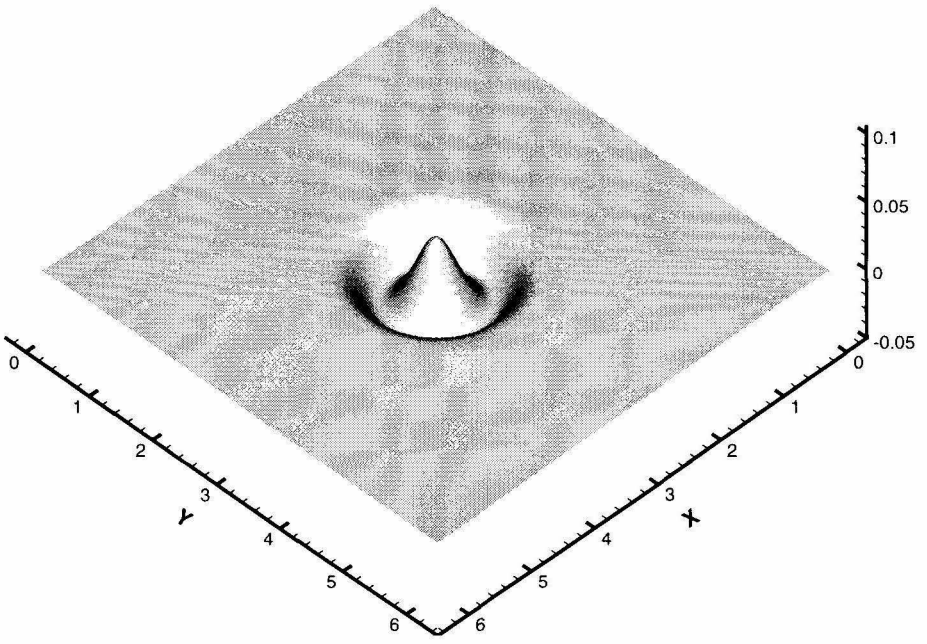

Figure 3.5: Gaussian wave at $t = 0.8$ with surface tension $\tau = 0.01$.

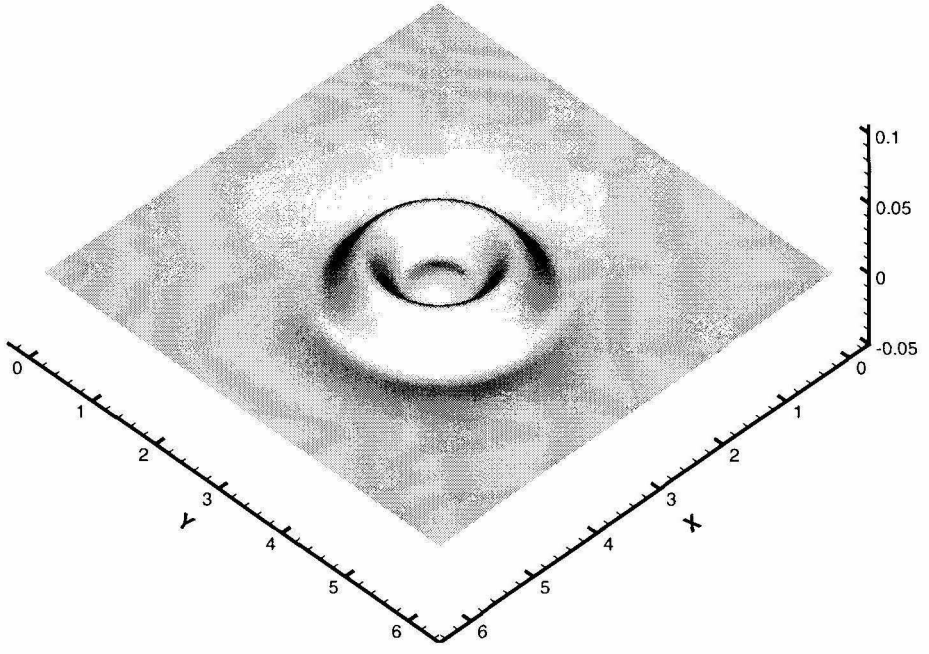

Figure 3.6: Gaussian wave at $t = 1.4$ with surface tension $\tau = 0.01$.

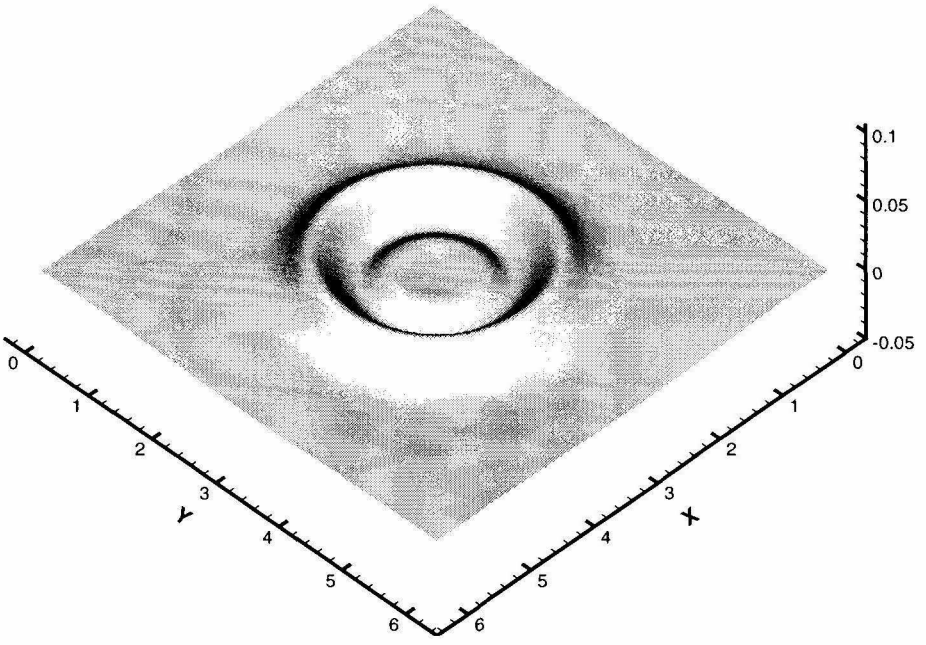

Figure 3.7: Gaussian wave at $t = 1.8$ with surface tension $\tau = 0.01$.

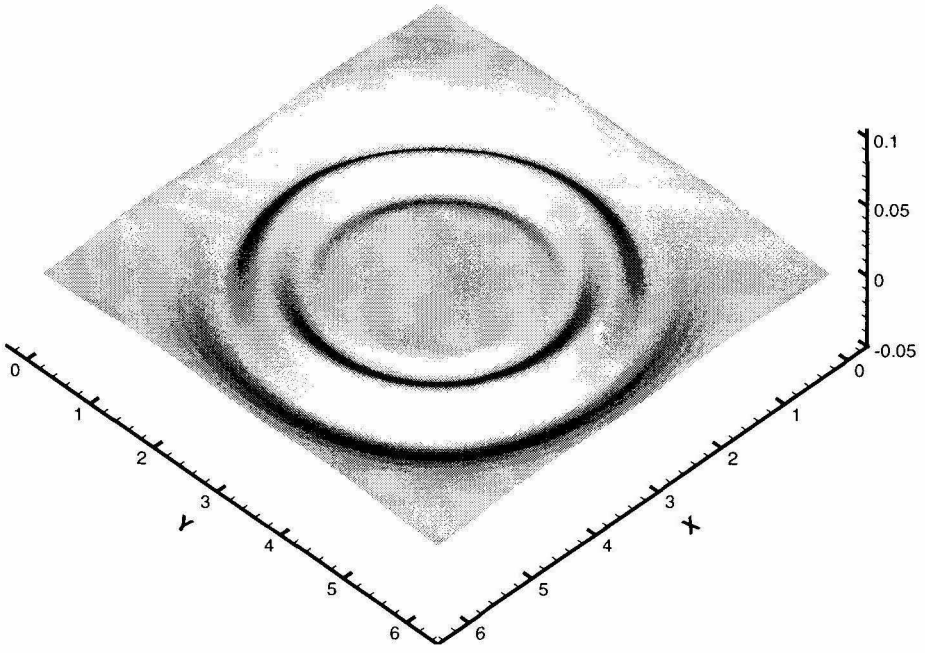

Figure 3.8: Gaussian wave at $t = 3.0$ with surface tension $\tau = 0.01$.

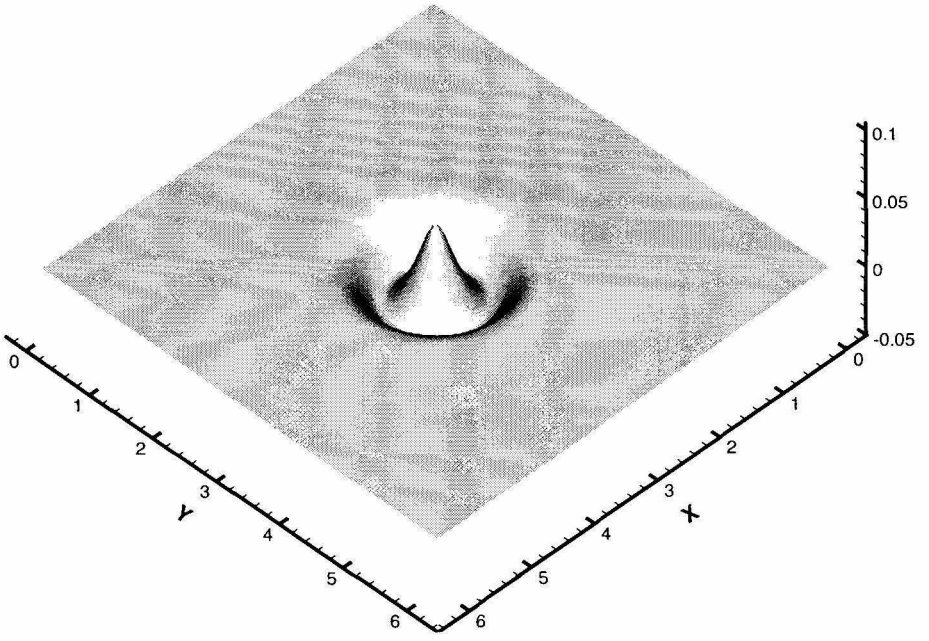

Figure 3.9: Gaussian wave at $t = 0.8$ with surface tension $\tau = 1 \times 10^{-4}$.

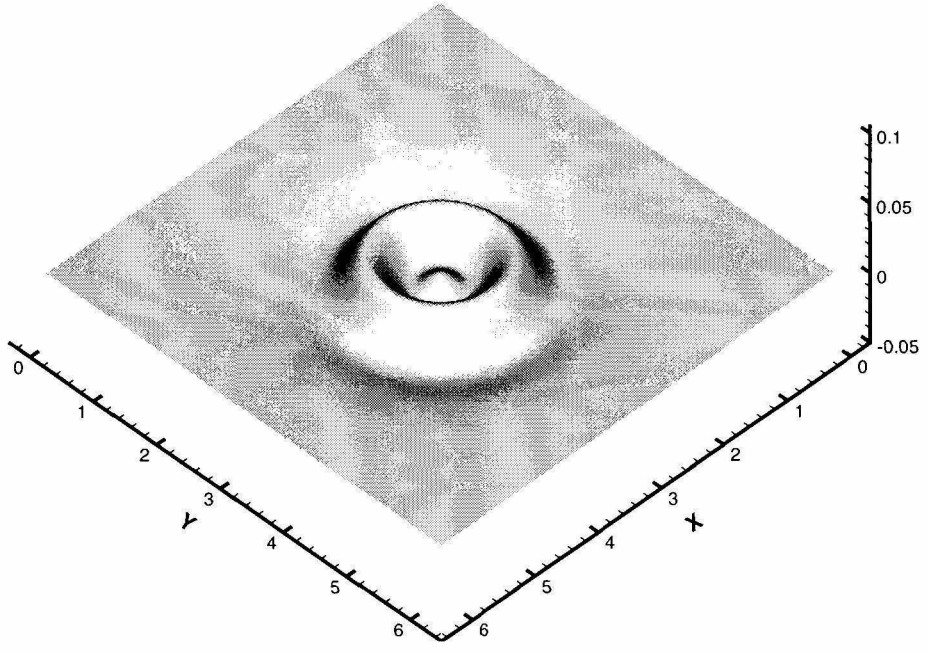

Figure 3.10: Gaussian wave at $t = 1.4$ with surface tension $\tau = 1 \times 10^{-4}$.

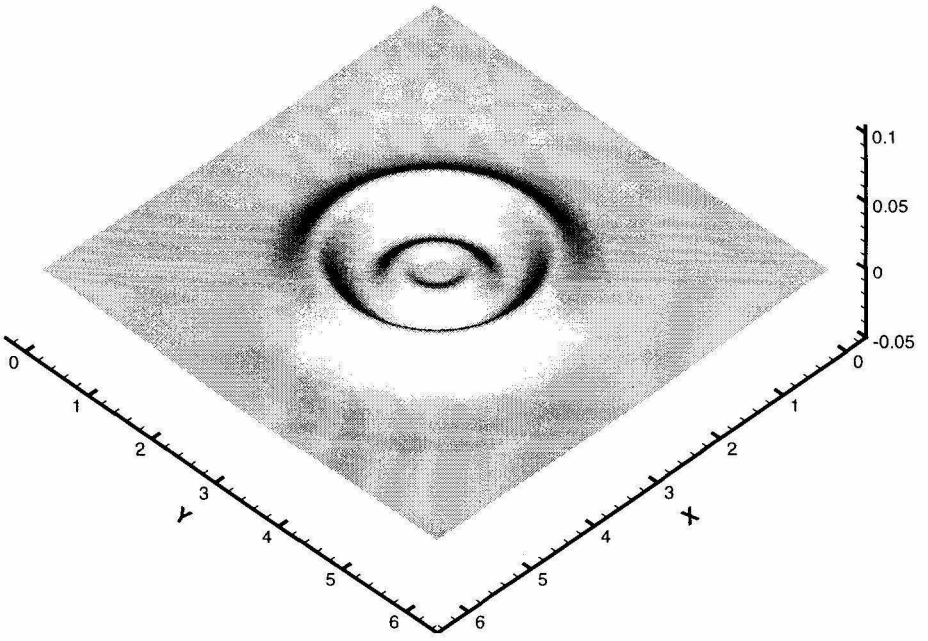

Figure 3.11: Gaussian wave at $t = 1.8$ with surface tension $\tau = 1 \times 10^{-4}$.

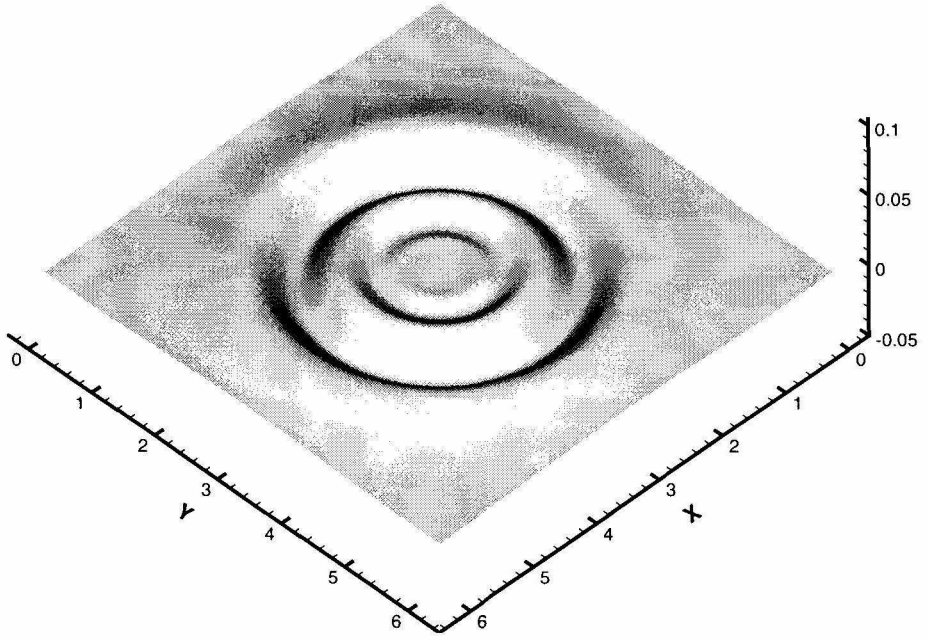

Figure 3.12: Gaussian wave at $t = 2.4$ with surface tension $\tau = 1 \times 10^{-4}$.

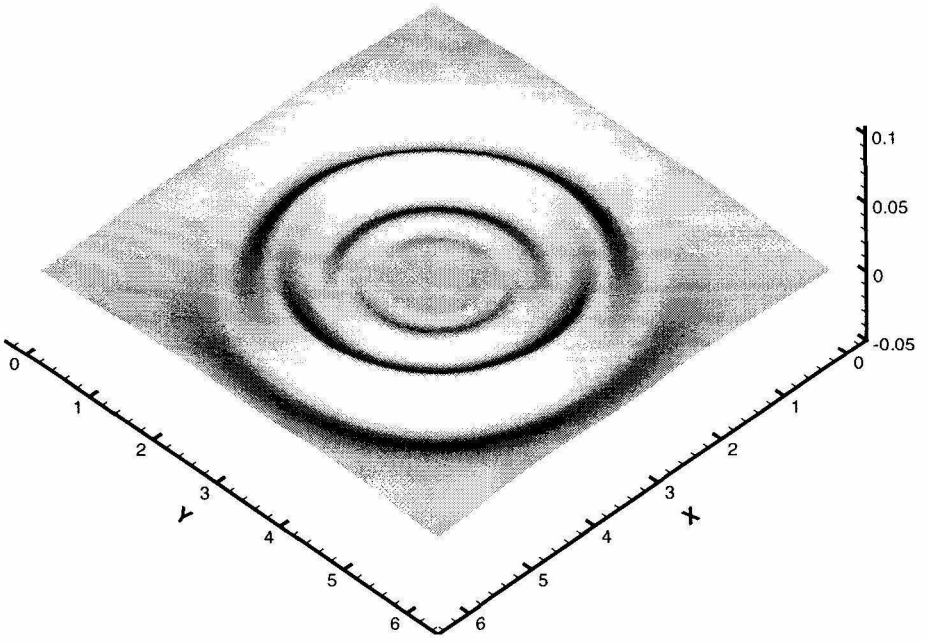

Figure 3.13: Gaussian wave at $t = 3.0$ with surface tension $\tau = 1 \times 10^{-4}$.

we notice between these two cases at $t = 3.0$ is that for surface tension $\tau = 1 \times 10^{-4}$, we observe more ripples than the $\tau = 0.01$ case. If we look at Figs. 3.4.2 and 3.11, we notice that near the origin for the $\tau = 1 \times 10^{-4}$ case, the wave has greater amplitude and this eventually generates the additional ripple that we see at later times. We also set the surface tension to be zero and observe almost no difference in the profiles of the surface wave with the $\tau = 1 \times 10^{-4}$ case. Haroldsen and Meiron in [21] presented numerical calculation of water waves using the full equations with the same initial data and zero-surface-tension. Our numerical simulations compare well with their results. Our robust and efficient numerical method also allows us to consider a wide range of surface tension coefficients. Also as before, no stiffness is observed using our methods.

In order to see how two Gaussian waves interact with each other, we consider placing two Gaussian waves next to each other. The velocity potential ϕ is still set to be zero initially. First we let the two initial Gaussian waves have the same height and width; see Fig. 3.14. We take surface tension $\tau = 1 \times 10^{-4}$. Again, we take $N = 128$ and $\Delta t = 0.005$ in our calculations. The two Gaussian waves move at the same speed. Fig. 3.15 shows that the two Gaussian waves meet at about $t = 0.8$. The wave profile at times $t = 1.6, 2.0, 2.4$ and 3.0 are also plotted in Figs. (3.16) – (3.19) respectively. At $t = 3.0$, we see that the outer ripples from each wave are joined together and the inner

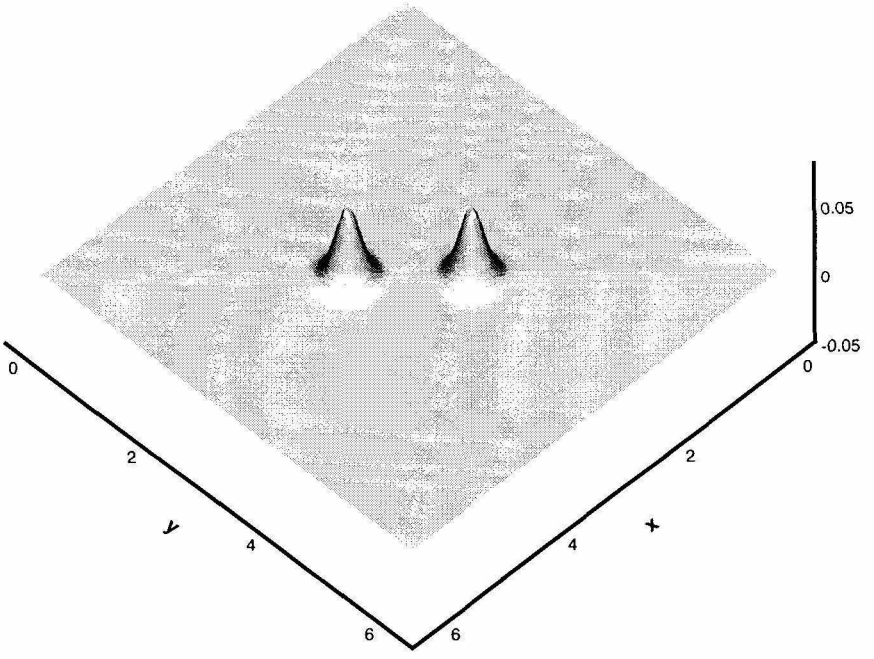

Figure 3.14: Two identical Gaussian waves at $t = 0$.

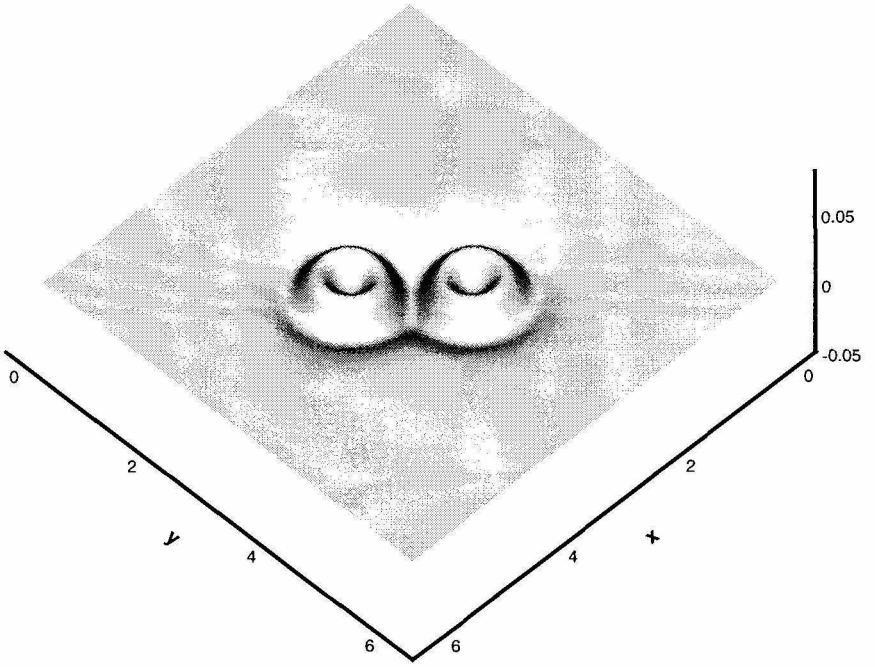

Figure 3.15: Two identical Gaussian waves at $t = 0.8$ with surface tension $\tau = 1 \times 10^{-4}$.

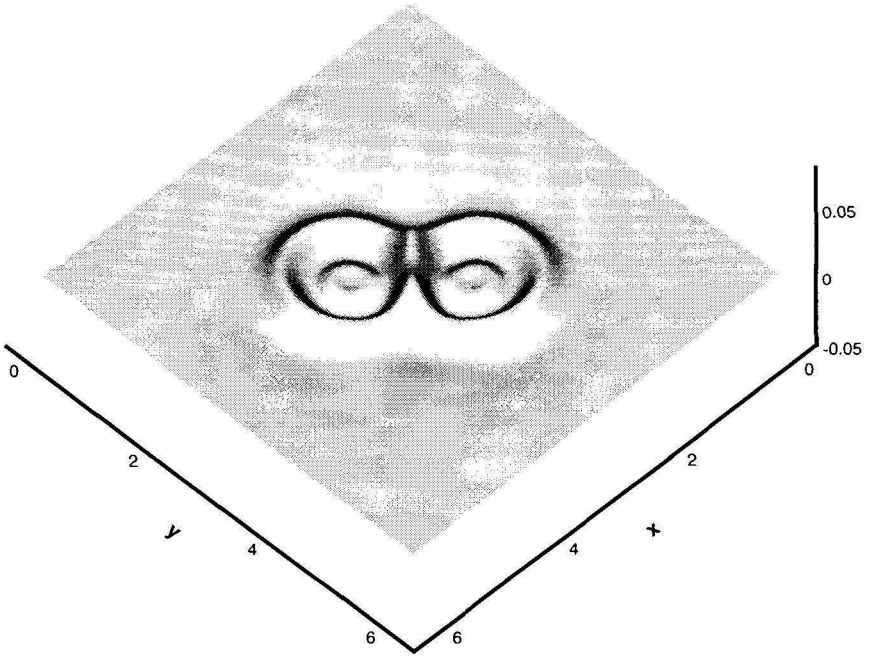

Figure 3.16: Two identical Gaussian waves at $t = 1.6$ with surface tension $\tau = 1 \times 10^{-4}$.

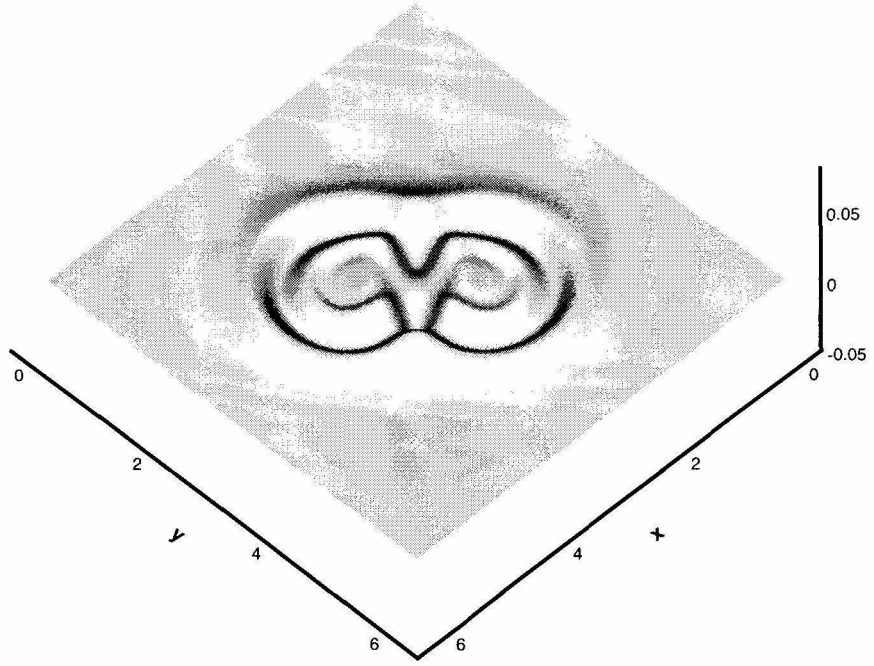

Figure 3.17: Two identical Gaussian waves at $t = 2.0$ with surface tension $\tau = 1 \times 10^{-4}$.

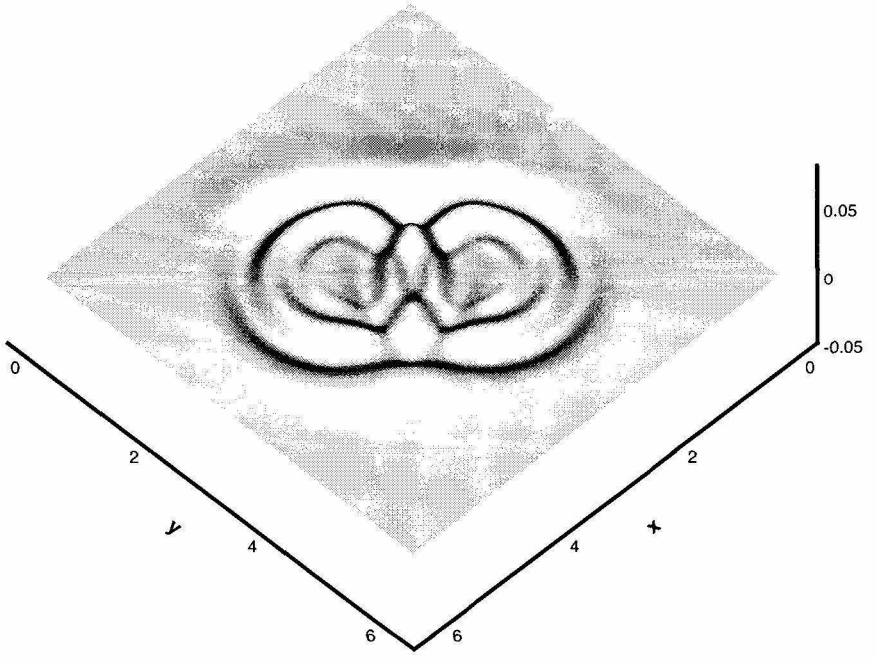

Figure 3.18: Two identical Gaussian waves at $t = 2.4$ with surface tension $\tau = 1 \times 10^{-4}$.

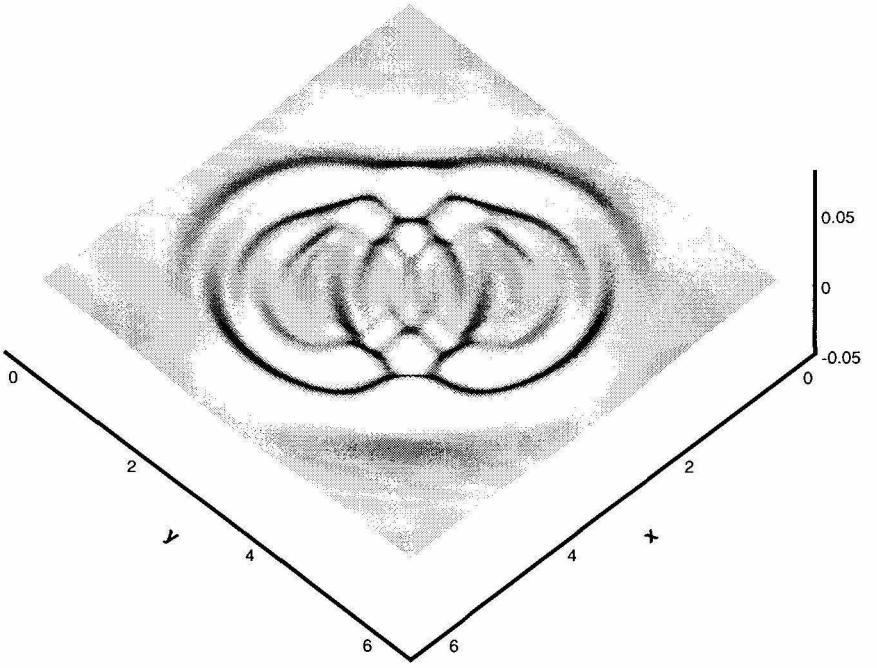

Figure 3.19: Two identical Gaussian waves at $t = 3.0$ with surface tension $\tau = 1 \times 10^{-4}$.

two cross each other. We also started with two uneven initial Gaussian waves. One of them is two times higher than the other. (See Fig. 3.20). Since their amplitudes are

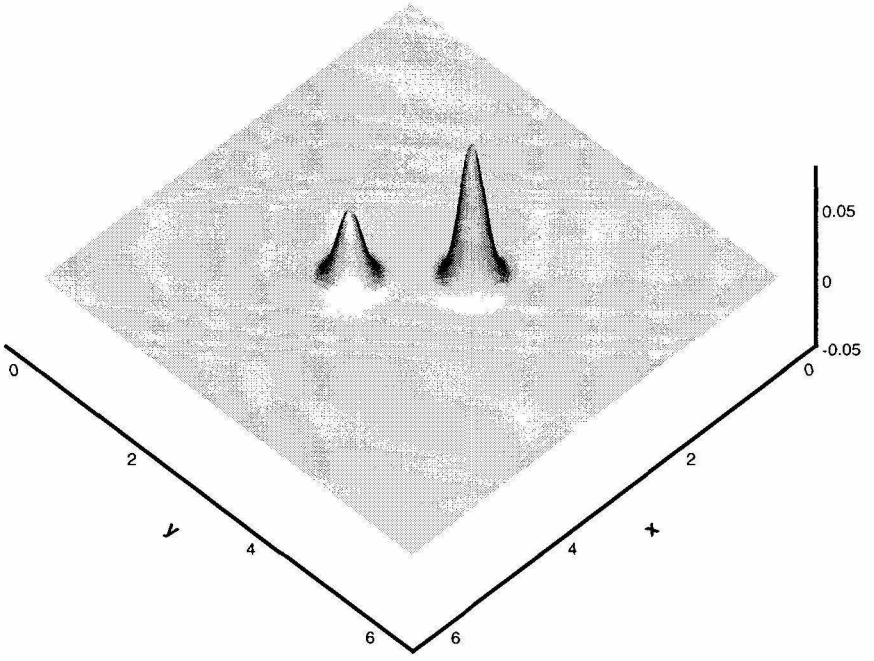

Figure 3.20: Two uneven Gaussian waves at $t = 0$.

different, they move at different speeds. The lower one moves faster but not two times faster, as can be seen in Fig. 3.21. We plot the final stage of the wave profile at $t = 3.0$ in Fig. 3.21. It is clearly shown that the larger amplitude Gaussian waves dominates the smaller one.

3.4.3 Gravity Waves

The intriguing problem of wave breaking has been a subject of great interest in recent years. The interesting formation of upward-pointing thin jets occurring in two-dimensional gravity waves impinging on a vertical wall has been observed experimentally by Nishimura and Takewaka [43] and by Chan and Melville [11]. Due to the experimental difficulties involved, the exsiting documented works are mainly under two-dimensional conditions. There has also been great effort in establishing numerical models to study in detail the breaking wave kinematics. The numerical simulations of steep waves meeting a wall reported by Cooker and Peregrine [12, 13] also show the surprising formation

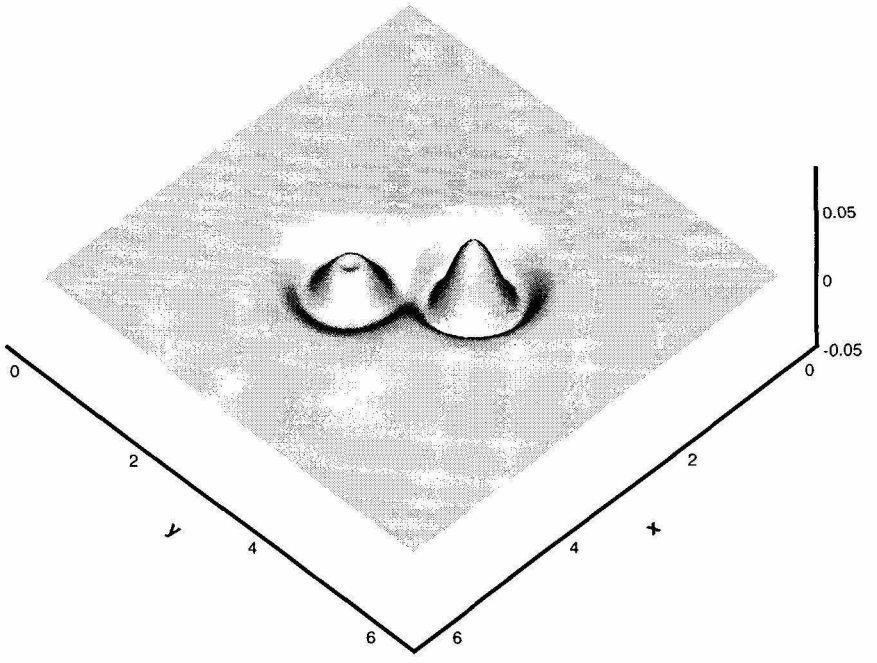

Figure 3.21: Two uneven Gaussian waves at $t = 0.8$ with surface tension $\tau = 1 \times 10^{-4}$.

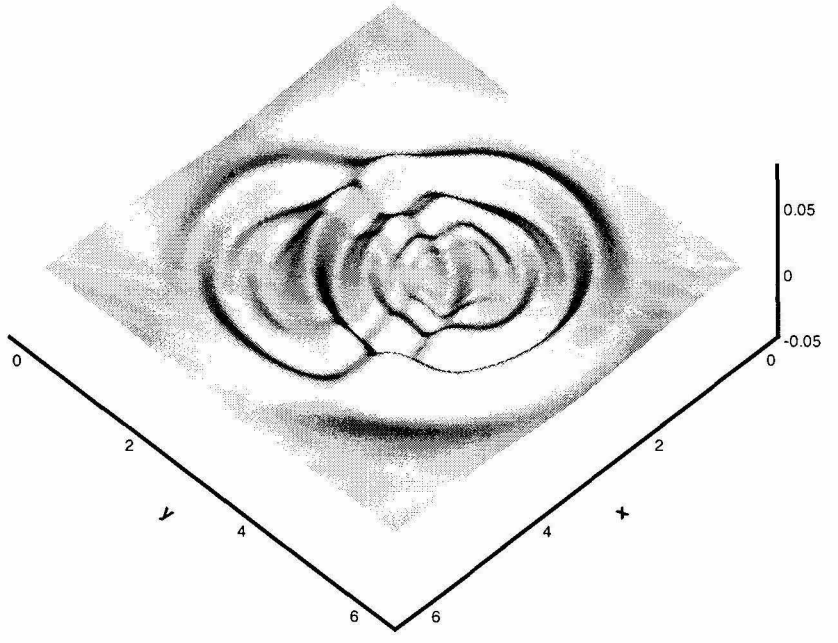

Figure 3.22: Two uneven Gaussian waves at $t = 3.0$ with surface tension $\tau = 1 \times 10^{-4}$.

of a thin jet in a very violent motion accompanied with large accelerations and pressures. However, the existing work on breaking waves has been mainly restricted to two-dimensional conditions.

In our calculations, we use the simplified water wave model to study the three-dimensional gravity waves. We observe an interesting variety of surface evolutions for simple initial data by only changing the small amplitude of the initial waves. The initial data is given by

$$\begin{aligned} x(\alpha_1, \alpha_2, 0) &= \alpha_1, \\ y(\alpha_1, \alpha_2, 0) &= \alpha_2, \\ z(\alpha_1, \alpha_2, 0) &= \epsilon \sin(\alpha_1 - 0.5) \sin(\alpha_2 - 0.5), \\ \phi(\alpha, 0) &= 0, \end{aligned}$$

where $0 \leq \alpha_1, \alpha_2 \leq 1$. All the following computations use this initial data. Our first experiment is for $\epsilon = 0.06$ with zero-surface-tension. Figure 3.23 shows the wave profile at various times. We see that oscillatory waves exists for all time.

We now consider a larger amplitude $\epsilon = 0.12$. The motion begins with the wave troughs rising up and the wave crests fall down (See Fig. 3.24). The localized humps appear in the rising-up regions at $t = 0.15$ (Fig. 3.25) and then quickly develop into thin jets shooting upwards near $t = 0.19$ (Fig. 3.26). We used $N = 256$ in each direction and $\Delta t = 1 \times 10^{-4}$. It looks like the thin jets are going to form sharp cusps. Unfortunately, due to the limited computer memory, we do not have the necessary resolution here to compute the wave motion further to determine whether the motion will become singular.

Although we do not show any results for $\epsilon = 0.09$, we will briefly describe what we found in this case. We see similarities with the $\epsilon = 0.12$ case up to $t = 0.15$ except the amplitudes are smaller. But instead of the jets continuing to increase in amplitude, when $\epsilon = 0.09$, they reach a maximum height and subsequently fall down. Then the wave rises up in the opposite corners and forms jets at these locations. At this point, these jets form structures much like we see in Figure 3.26 at around $t = 0.76$. Again our computation stops when the jets seem to form sharp cusps. This is mostly likely because the orthogonal coordinate system breaks down near the point of the cusp.

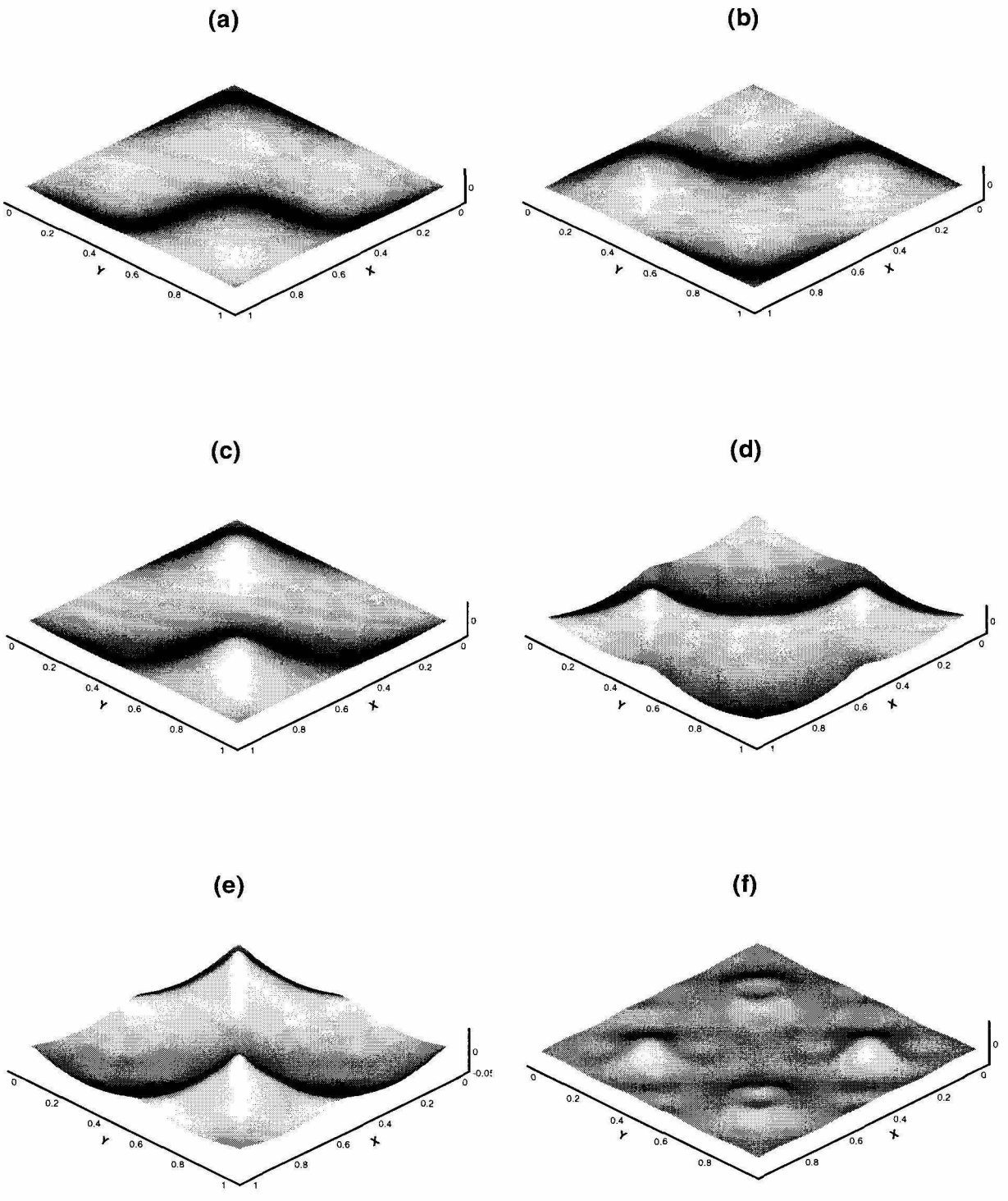

Figure 3.23: Sequence of wave profiles at various times for $\epsilon = 0.06$. $N = 128$ and $\Delta t = 0.005$. (a) $t = 0.0$, (b) $t = 0.1$, (c) $t = 0.2$, (d) $t = 0.5$, (e) $t = 0.6$, (f) $t = 0.65$.

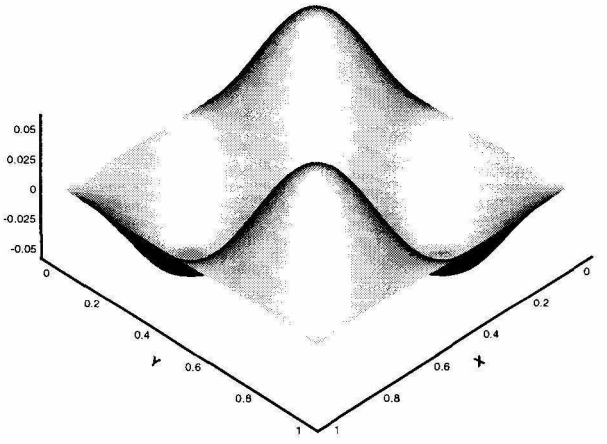

Figure 3.24: Gravity wave profile at $t = 0.1$ for $\epsilon = 0.12$. $N = 256$ and $\Delta t = 1 \times 10^{-4}$.

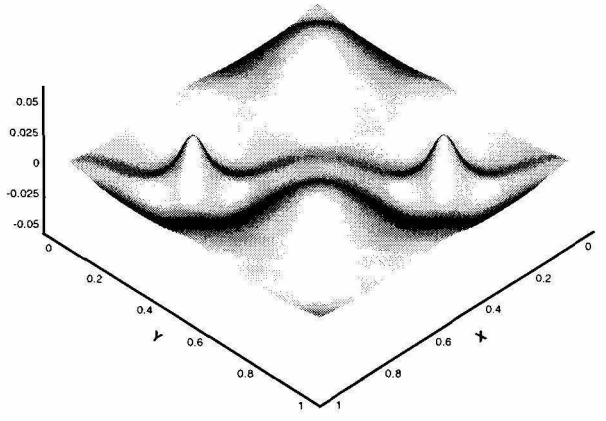

Figure 3.25: Gravity wave profile at $t = 0.15$ for $\epsilon = 0.12$. $N = 256$ and $\Delta t = 1 \times 10^{-4}$.

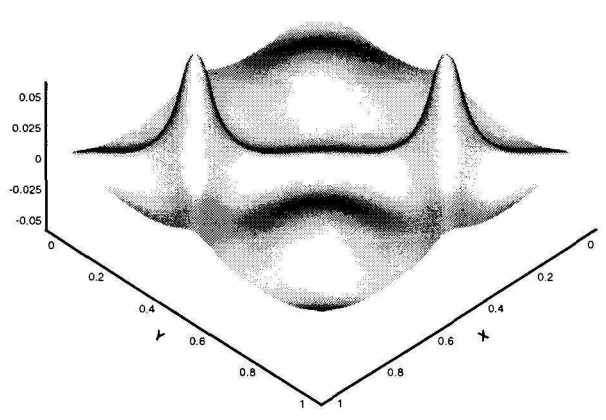

Figure 3.26: Gravity wave profile at $t = 0.19$ for $\epsilon = 0.12$. $N = 256$ and $\Delta t = 1 \times 10^{-4}$.

We also considered surface tension $\tau = 0.001$ for the initial amplitude $\epsilon = 0.12$. We tested using $N = 64$, 128, 256 points in each dimension, and the time steps that were used were $\Delta t = 0.001$, 0.0005 and 0.00025. Using our method, we do not see the stiffness associated with the surface tension.

Chapter 4
Numerical Study of Hele-Shaw Flow with Suction

It is well known that sink flow in a Hele-Shaw cell with zero-surface-tension can develop a finite-time cusp singularity. In fact, for an initial limacon of fluid containing a sink, Howison *et al* [25] constructed an analytic solution which forms a 3/2-power cusp in finite time. For non-zero surface tension, no analytic solution exists for the suction problem. It is generally believed that surface tension regularizes the cusp singularity, and allows the solution to exist after the singularity time for the zero-surface-tension solution. However, it is still not very clear how the regularized solution behaves beyond the singularity time for the non-zero surface tension case. Our study focuses on identifying how these cusped flows are regularized by the presence of small surface tension, and what the limiting form of the regularization is as surface tension tends to zero. The two-phase Hele-Shaw flow, known as the Muskat problem, is considered.

4.1 The Governing Equations

Typically in a Hele-Shaw cell, two viscous fluids are confined between two closely-spaced parallel plates. Here, we consider the case of a blob of viscous fluid being sucked by an interior sink. The blob is surrounded by a less viscous fluid which fills the rest of the Hele-Shaw cell. For simplicity, we assume that the fluids are immiscible and incompressible with constant but differing viscosities. We use the subscripts 1 and 2 to refer to the fluids in the interior and exterior of the blob. The velocity field $\mathbf{u}_j$ of each fluid is given by Darcy's law,

$$\mathbf{u}_j = -\frac{b^2}{12\mu_j}\nabla p_j, \tag{4.1}$$

where b is the cell gap, μ_j is the viscosity, and p_j is the pressure. $M = b^2/12\mu_j$ is the fluid mobility. The incompressibility condition implies that $\nabla \cdot \mathbf{u}_j = 0$ and therefore the pressure in each fluid satisfies Laplace's equation:

$$\nabla^2 p_j = 0. \tag{4.2}$$

In other words, the interior and exterior fluids are potential. Consequently, the flow can be obtained from the dynamics of the free interface (blob boundary) between the two fluids. Denote the fluid interface by Γ. The interface motion is subject to the following conditions

$$[\mathbf{u} \cdot \hat{\mathbf{n}}]|_\Gamma = 0, \tag{4.3}$$

$$[p]|_\Gamma = \tau\kappa, \tag{4.4}$$

where $[\cdot]$ denotes the jump across the interface taken as the difference of the interior minus the exterior quantity. Here, $\hat{\mathbf{n}}$ is the exterior unit normal to Γ, τ is the surface tension, and κ is the interface mean curvature. The kinematic boundary condition (4.3) states that the normal component of the velocity field is continuous across the interface. This implies that particles on the interface remain there. The relation (4.4), known as the Laplace-Young boundary condition, gives an account of how the presence of surface tension modifies the pressure across the interface.

We assume that there is a point sink at the origin, inside the fluid blob. For large distances away from the sink, the velocity field tends to the simple radial flow:

$$\mathbf{u}(\mathbf{x}) \to Q\frac{\mathbf{x}}{|\mathbf{x}|^2}, \quad \text{as} \quad |\mathbf{x}| \to \infty. \tag{4.5}$$

Here, Q is the suction rate which is assumed constant and negative.

Let the interface Γ be represented, at any instant t, by $(x(\alpha,t), y(\alpha,t))$, where α in $[0, 2\pi]$ defines a counterclockwise parameterization of Γ. Both x and y are periodic functions of α. The interface governing equations can be put in a convenient form by introducing the the complex position variable $z(\alpha,t) = x(\alpha,t) + iy(\alpha,t)$ and the complex conjugate velocity $W(\alpha,t) = u(\alpha,t) - iv(\alpha,t)$. This interface velocity can be

represented by a boundary integral plus the sink contribution as follows (for a derivation, see, e.g., [63]):

$$W = \frac{Q}{z(\alpha,t)} + \frac{1}{2\pi i}\,\text{P.V.}\int_0^{2\pi} \frac{\gamma(\alpha',t)}{z(\alpha,t)-z(\alpha',t)}d\alpha', \tag{4.6}$$

where the P.V. denotes the principal value integral. γ is the (unnormalized) vortex sheet strength which measures the tangential velocity jump across the interface by

$$\gamma = s_\alpha[\mathbf{u}]|_\Gamma \cdot \hat{\mathbf{s}}, \tag{4.7}$$

where $s_\alpha = \sqrt{x_\alpha^2 + y_\alpha^2}$, the subscript α denotes differentiation with respect to that variable, and $\hat{\mathbf{s}}$ is the unit tangential vector on Γ. $W(\alpha,t)$ gives, in complex form, the average velocity $(u,v) = \frac{1}{2}(\mathbf{u}_1 + \mathbf{u}_2)$ on the interface and satisfies the boundary condition (4.5), provided γ has zero mean. To close the system, an equation for γ can be derived by using Eq. (4.1). We have that

$$\begin{aligned}(\nabla p_1 - \nabla p_2)\cdot\hat{\mathbf{s}} &= (\frac{12\mu_2}{b^2}\mathbf{u}_2 - \frac{12\mu_1}{b^2}\mathbf{u}_1)\cdot\hat{\mathbf{s}} \\ &= -\frac{12}{b^2}(\Delta\mu\mathbf{u} + \bar{\mu}(\mathbf{u}_1 - \mathbf{u}_2))\cdot\hat{\mathbf{s}},\end{aligned} \tag{4.8}$$

where $\Delta\mu = \mu_1 - \mu_2, \bar{\mu} = \frac{1}{2}(\mu_1 + \mu_2)$. Thus,

$$\gamma = -s_\alpha\frac{\Delta\mu}{\bar{\mu}}\mathbf{u}\cdot\hat{\mathbf{s}} - s_\alpha\frac{b^2}{12\bar{\mu}}\nabla(p_1 - p_2)\cdot\hat{\mathbf{s}}. \tag{4.9}$$

Using the dynamic boundary condition (4.4) and the complex conjugate velocity, we obtain the following equation for γ

$$\gamma = 2A_\mu \text{Re}\{z_\alpha W\} + S\kappa_\alpha. \tag{4.10}$$

Here, $A_\mu = (\mu_1 - \mu_2)/(\mu_1 + \mu_2)$ is the viscosity Atwood ratio and $S = \frac{b^2}{12\bar{\mu}}\tau$ is a scaled surface tension parameter. We nondimensionalize the equations of motion by taking the initial blob radius to be 1 and by setting $Q = -1$. Taking into account that there is freedom in selecting the tangential velocity at the interface, the evolutions equations can

be written as

$$\bar{z}_t(\alpha,t) = -\frac{1}{z(\alpha,t)} + \frac{1}{2\pi i}\,\mathrm{P.V.}\int_0^{2\pi}\frac{\gamma(\alpha',t)}{z(\alpha,t)-z(\alpha',t)}d\alpha' + A(\alpha,t)\frac{\bar{z}_\alpha(\alpha,t)}{|z_\alpha(\alpha,t)|} \quad (4.11)$$

$$\gamma(\alpha,t) = 2A_\mu \mathrm{Re}\left(-\frac{z_\alpha(\alpha,t)}{z(\alpha,t)} + \frac{z_\alpha(\alpha,t)}{2\pi i}\,\mathrm{P.V.}\int_0^{2\pi}\frac{\gamma(\alpha',t)}{z(\alpha,t)-z(\alpha',t)}d\alpha'\right) + S\kappa_\alpha, \quad (4.12)$$

where the bar denotes the complex conjugate. Here, $A(\alpha,t)$ is arbitrary and only determines the parameterization (frame) of the interface but does not affect its dynamics. For example, the frequently used Lagrangian frame is obtained by taking $A = \gamma/(2|z_\alpha|)$.

4.2 The Numerical Method

A spectrally accurate spatial discretization of equations (4.11) and (4.12) can be achieved easily by computing the space derivatives with the pseudo-spectral approximation, i.e., using the Fast Fourier Transform. The principal value integral can also be computed with spectral accuracy by employing the alternate-point trapezoidal rule [57]:

$$\mathrm{P.V.}\int_0^{2\pi}\frac{\gamma(\alpha')}{z(\alpha_i)-z(\alpha')}d\alpha' \approx \sum_{\substack{j=0 \\ (j-i)\ \mathrm{odd}}}^{N-1}\frac{\gamma_j}{z_i - z_j}2h, \quad (4.13)$$

where N is the number of computational particles on the interface, $h = 2\pi/N$, and $\alpha_i = ih$ for $i = 0 \ldots N-1$. The quantities with subscripts are the corresponding discrete approximations. However, surface tension introduces a term (κ_α) with high-order derivatives that couple into the interface dynamics in a nonlinear and nonlocal manner. This leads to a high-order stability constraint (stiffness) for explicit time-integration methods and makes implicit methods difficult to implement. We use the θ-L scheme that Hou *et al.* designed in [23]. Their method uses two natural variables $\theta = \tan^{-1}(y_\alpha/x_\alpha)$ which is the tangent angle to the interface and L which is the total

length of the interface. The evolution equations are given by

$$L_t = -\int_0^{2\pi} \theta_{\alpha'} U d\alpha', \tag{4.14}$$

$$\theta_t = \frac{2\pi}{L}(U_\alpha + \theta_\alpha T), \tag{4.15}$$

where U is the normal velocity and the tangential velocity T is chosen as

$$T(\alpha, t) = \int_0^\alpha \theta_{\alpha'} U d\alpha' - \frac{\alpha}{2\pi}\int_0^{2\pi} \theta_{\alpha'} U d\alpha'. \tag{4.16}$$

The stiffness is hidden at the small spatial scales of U_α in the equation for θ. The leading order behavior of U at small scales is given by [23]

$$U(\alpha, t) \sim \frac{\pi}{L}\mathcal{H}[\gamma](\alpha, t), \tag{4.17}$$

where $\mathcal{H}$ is the Hilbert transform which is diagonalizable by the Fourier transform as $\hat{\mathcal{H}}[f] = -i\text{sign}(k)\hat{f}$. Moreover, γ is dominated by the surface tension term at small scales, that is

$$\gamma(\alpha, t) \sim S\kappa_\alpha = S\frac{2\pi}{L}\theta_{\alpha\alpha}. \tag{4.18}$$

Therefore,

$$U(\alpha, t) \sim S\frac{\pi}{L}\mathcal{H}[\theta_{\alpha\alpha}](\alpha, t). \tag{4.19}$$

The equations of motion can now be written as

$$L_t = -\int_0^{2\pi} \theta_{\alpha'} U d\alpha', \tag{4.20}$$

$$\theta_t = \frac{S}{2}\left(\frac{2\pi}{L}\right)^3 \mathcal{H}[\theta]_{\alpha\alpha\alpha} + P, \tag{4.21}$$

where P represents lower order terms at small spatial scales. L can be updated by an explicit method as Eq. (4.20) is free of stiffness. To remove the high-order stiffness it is sufficient to discretize implicitly the leading order term in Eq. (4.21) and treat the

lower order term P explicitly. This gives a linear time-step stability constraint, i.e., $\Delta t \leq Ch$, where Δt is the time-step size. Moreover, because of its constant coefficients, the implicit term can be easily inverted by using FFT. Here, we use the following fourth order explicit/implicit method studied by Ascher, Ruuth, and Wetton [1]

$$\frac{1}{\Delta t}\left(\frac{25}{12}\theta^{n+1} - 4\theta^{n} + 3\theta^{n-1} - \frac{4}{3}\theta^{n-2} + \frac{1}{4}\theta^{n-3}\right) = \frac{S}{2}\left(\frac{2\pi}{L^{n+1}}\right)^{3}\mathcal{H}[\theta^{n+1}]_{\alpha\alpha\alpha} + 4P^{n} - 6P^{n-1} + 4P^{n-2} - P^{n-3}. \tag{4.22}$$

L is updated first using a fourth order explicit Adams-Bashforth multi-step scheme to obtain L^{n+1} before computing θ^{n+1} via FFT.

Note that, at each time step, γ has to be obtained from (4.12) to compute the velocities. It has been shown [3] that the Fredholm integral equation for γ has a globally convergent Neumann series. We solve for γ by fixed point iteration, accelerated by constructing a fourth order extrapolated initial guess from previous time steps. It typically takes a few iterations to obtain a convergent solution for γ when the interface is relatively smooth. The overall method is fourth order in time and spectrally accurate in space.

4.3 Numerical Results

We consider an initially circular blob of viscous fluid surrounded by less viscous fluid. The center of the initial blob is at $(0, -0.1)$ and the sink is placed at the origin. Our numerical results focus on the regularizing effect of surface tension, past the $S = 0$ singularity time, and on the limiting behavior of the interface as surface tension tends to zero. The results are divided in two main parts. First, we present the case where the viscosity of the surrounding fluid is negligible, which corresponds to $A_\mu = 1$. In the second part, we investigate the additional effect that non-zero viscosity in the surrounding fluid has on the interface dynamics, i.e., $A_\mu < 1$.

All the computations presented here are performed in 64-bit arithmetic (standard double precision). Krasny filtering [37] is used to prevent the spurious growth of the high-frequency components of the round-off error. This nonlinear numerical filter is implemented by setting to zero all the Fourier modes of the solution whose magnitude are below a certain level. In our computations we set this filter level to be 10^{-12}. The

number N of uniformly spaced points along the interface is chosen so that all the Fourier modes of the tangent angle $\theta(\alpha, t)$ are well-resolved. Initially, we use $N = 2048$ for most of the computations. The time step Δt is selected so that, decreasing it further, would not produce any appreciable difference within plotting resolution in the curvature of the interface. We double N as soon as the magnitude of the highest frequency mode of $\theta(\alpha, t)$ is greater than the filter level. Very small values of Δt are required to compute accurately the interface motion as it approaches the sink. At the latest stage of the motion, the number of grid points typically increases to $N = 8192$ or $N = 16384$ and $\Delta t = 2 \times 10^{-7}$. A detailed resolution study is presented later in this section.

4.3.1 Development of the Interface for $A_\mu = 1$

Zero-surface-tension Cusp Formation

In the absence of surface tension, an initially circular blob whose center is not at the sink develops a 3/2-power cusp singularity in finite time.

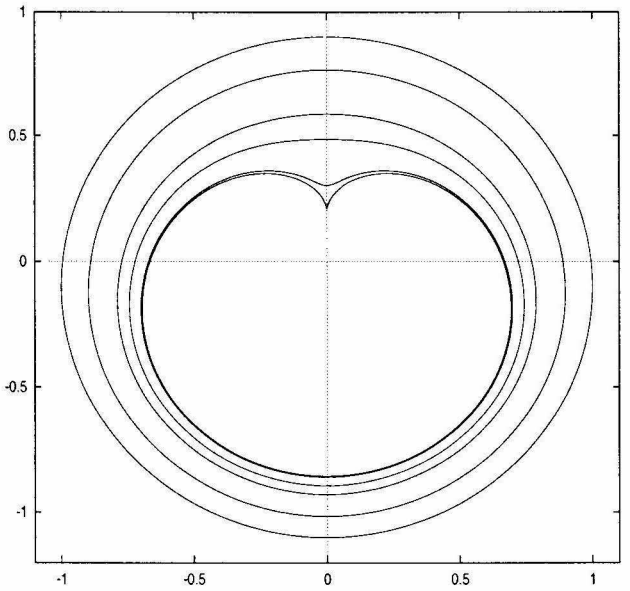

Figure 4.1: Evolution and collapse of the interface for the initially circular blob centered at $(0, -0.1)$ being sucked by a point sink at the origin. $S = 0$ and $A_\mu = 1$. The curves, from the outer perimeter inwards, correspond to the times $t = 0$, 0.1, 0.2, 0.24, 0.28, and 0.2842. The cusp is formed approximately at $t = 0.2842$. The computation was performed using $N = 2048$ and $\Delta t = 1 \times 10^{-5}$ in the Lagrangian frame.

Fig. 4.1 shows the evolution and collapse of the fluid interface for $A_\mu = 1$ and $S = 0$. The cusp occurs at approximately $t_c = 0.2842$ and is located at $(0, 0.2305)$ for this particular case where the blob is initially centered at $(0, -0.1)$. To resolve well the interface up to times very close to the formation of the cusp, we take advantage of the particle clustering characteristic of the Lagrangian frame. That is, for this special case ($S = 0$), we discretize directly equations (4.11) and (4.12) with $A = \gamma/(2|z_\alpha|)$ using the pseudo-spectral approximation for the derivatives and the alternate-point trapezoidal rule (4.13) for the singular integral. An explicit fourth order Adams-Bashforth scheme is used to integrate in time.

The Regularizing Effect of Surface Tension

The presence of surface tension regularizes the cusped flow in a very special way. Fig. 4.2 shows the fluid interface at different times for $S = 0.01$.

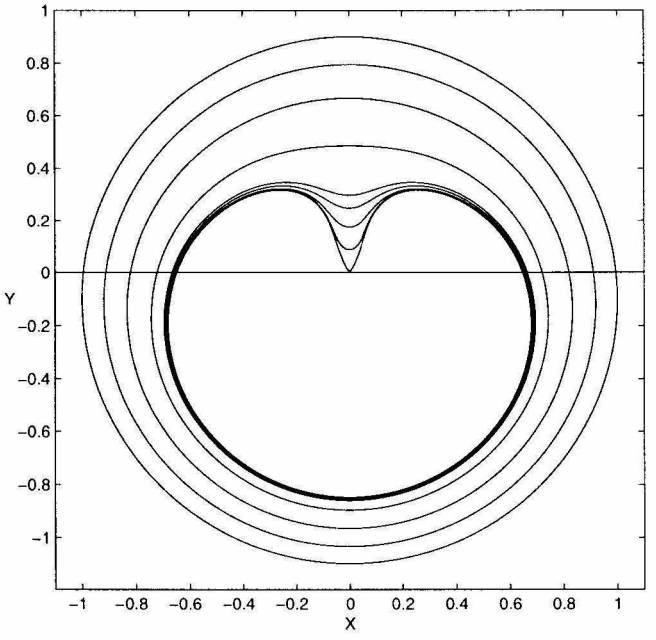

Figure 4.2: Evolution of the initially circular fluid blob for $S = 0.01$ and $A_\mu = 1$. The curves, from the outer perimeter inwards, correspond to the times $t = 0$, 0.080, 0.160, 0.240, 0.284, 0.290, 0.296, 0.300, and 0.301419. The distance of the tip of the finger to the sink, for the last computed interface ($t = 0.301419$), is 5.9848×10^{-3}. $N = 8192$ and $\Delta t = 2 \times 10^{-7}$ for the last stage of the motion.

A smooth finger with a rounded tip develops past the zero-surface-tension breakdown time $t_c = 0.2842$. As the interface gets closer to the sink, the finger evolves rapidly into a wedge. We stop the computation when the distance of the finger tip to the sink is 5.9848×10^{-3}. We use $N = 8192$ and $\Delta t = 2 \times 10^{-7}$ for the last stage of the computation. The formation of the wedge as the interface approaches the sink is consistent with the results reported by Nie and Tian [42] for the two values of surface tension they computed.

We decrease now surface tension to the value $S = 4 \times 10^{-4}$. A time sequence of the interface evolution for this small surface tension is presented in Fig. 4.3.

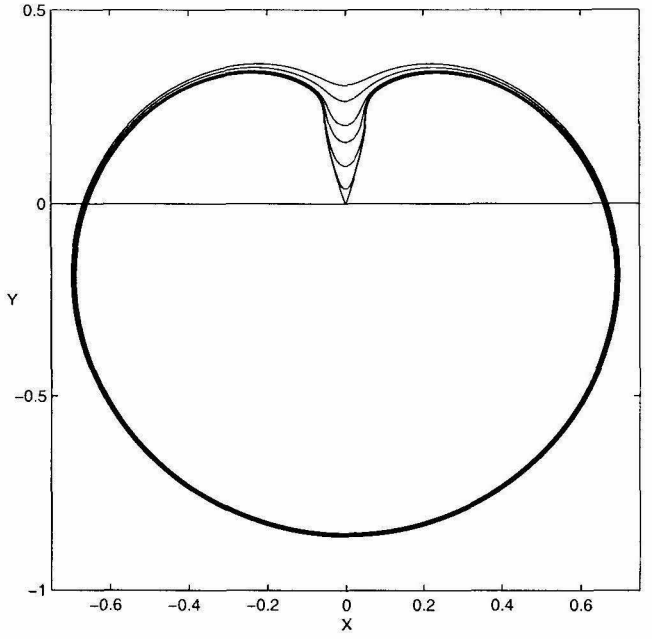

Figure 4.3: Evolution of the initially circular fluid blob for $S = 4 \times 10^{-4}$ and $A_\mu = 1$. The interface is plotted at times around $t_c = 0.2842$ and well past it. From the the outer perimeter inwards, the curves correspond to the times $t = 0.280$, 0.284, 0.288, 0.290, 0.292, 0.293, and 0.2932. $N = 16384$ and $\Delta t = 2 \times 10^{-7}$ for the last stage of the motion.

The interface passes smoothly the zero-surface-tension cusp time t_c. Soon after t_c, we observe the appearance of an almost straight finger that begins to bulge but is quickly drawn into the sink forming a wedge. Note that the top of this finger is narrower than the one corresponding to the larger surface tension $S = 0.01$ (Fig. 4.2). A look at the tangent angle $\theta(\alpha, t)$ around the finger tip for $S = 4 \times 10^{-4}$, shown in Fig. 4.4, strongly suggests the formation of a corner when the interface touches the sink.

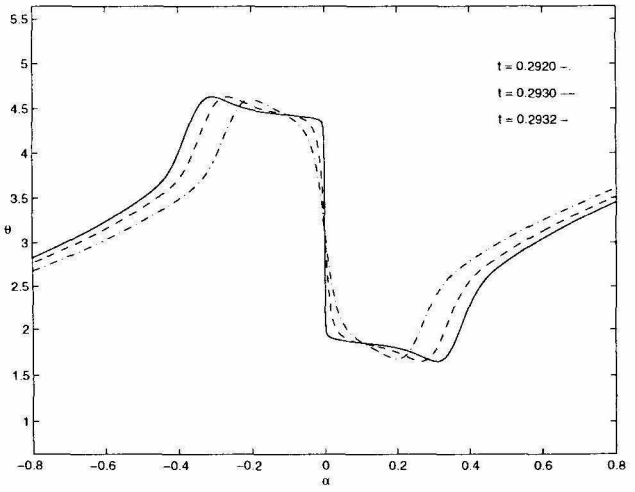

Figure 4.4: Behavior of the tangent angle $\theta(\alpha, t)$ around the finger tip ($\alpha = 0$) as the interface is about to collapse, for $S = 4 \times 10^{-4}$ and $A_\mu = 1$. The tangent angle, plotted against the parameterization variable α at the times $t = 0.2920$, 0.2930, and 0.2932, appears to develop a discontinuity. $N = 16384$ and $\Delta t = 2 \times 10^{-7}$.

The tangent angle θ appears to develop a discontinuity at the finger tip ($\alpha = 0$), precisely when the Hele-Shaw solution breaks down. The computations of Nie and Tian [42], for another type of initial data, also suggest this breakdown scenario. The formation of the wedge and the tip corner seem to be generic for this type of flow.

Smaller values of surface tension reveal new features in the interface evolution. Figure 4.5 shows the interface shape for $S = 5 \times 10^{-5}$.

The finger clearly bulges and develops a well-defined neck before it becomes a wedge. It is interesting to note that this neck appears at a height close to that of the zero-surface-tension cusp. It is conceivable that the formation of the neck and the bulging of the finger are due to the influence of the zero-surface-tension singularity. In fact, a look at the curvature shown at Fig. 4.6(a) for the time $t = 0.2860$, which is very close to $t_c = 0.2842$, shows already the appearance of two symmetric spikes corresponding to the location of the neck. The behavior of the interface curvature at subsequent times is shown in Figs. 4.6(c) and 4.6(d).

Note in particular that the curvature grows almost ten times in magnitude from $t = 0.2916$ (Fig. 4.6(c)) to $t = 0.2918$ (Fig. 4.6(d)). The sharp and large spike at $\alpha = 0$ is

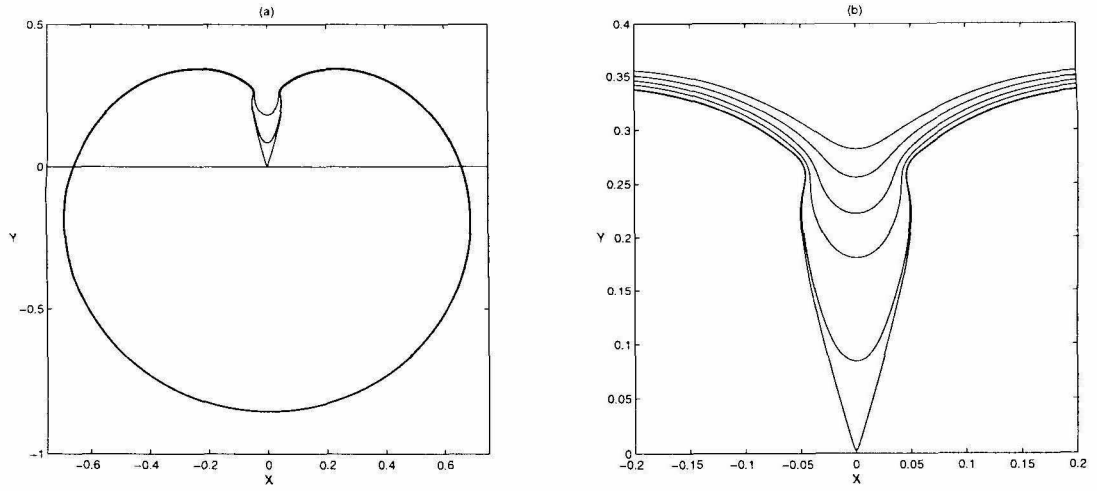

Figure 4.5: Evolution of the initially circular fluid blob past t_c, for $S = 5 \times 10^{-5}$ and $A_\mu = 1$. (a) The interface plotted at $t = 0.2880, 0.2900$, and 0.29181. (b) A close-up of the interface finger at the times $t = 0.2840, 0.2860, 0.2880, 0.2900$, and 0.29181. $N = 16384$ and $\Delta t = 2 \times 10^{-7}$ for the last stage of the motion.

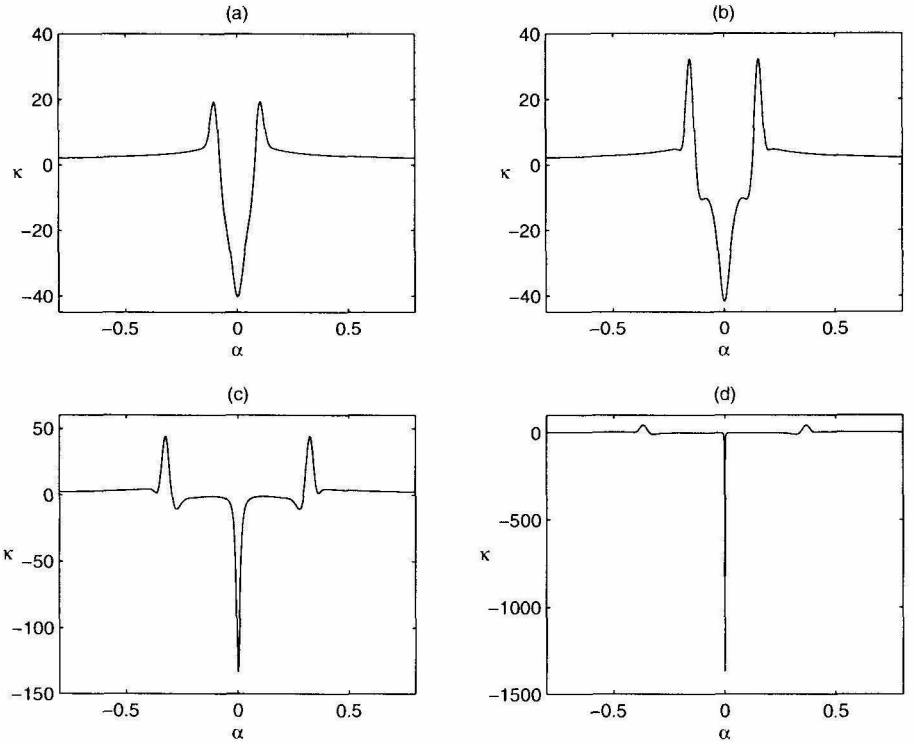

Figure 4.6: Interface curvature $\kappa(\alpha, t)$ versus α around the finger tip ($\alpha = 0$) at different times past t_c for $S = 5 \times 10^{-5}$ and $A_\mu = 1$. (a) $t = 0.2860$. (b) $t = 0.2880$. (c) $t = 0.2916$. (d) $t = 0.29181$. $N = 16384$ and $\Delta t = 2 \times 10^{-7}$ were used to resolve the largest curvature (d).

y	$\Delta(0.0008, 0.0004)$	$\Delta(0.0004, 0.0002)$	$\Delta(0.0002, 0.0001)$	$\Delta(0.0001, 0.00005)$
0.1	1.63×10^{-3}	1.17×10^{-3}	8.96×10^{-4}	6.62×10^{-4}
0.06	1.24×10^{-3}	9.14×10^{-4}	6.98×10^{-3}	5.39×10^{-4}
0.02	5.99×10^{-4}	4.57×10^{-4}	3.45×10^{-4}	2.47×10^{-4}

Table 4.1: Change in the finger widths as surface tension is decreased for $A_\mu = 1$. The first column shows the height level at which the fingers are compared. Columns 2-5 give the difference $\Delta(S, S/2)$ between the width of the finger corresponding to a surface tension S and that corresponding to $S/2$.

an indication of the corner singularity forming as the tip of the wedge touches the sink. We use $N = 16384$ and $\Delta t = 2 \times 10^{-7}$ to resolve accurately this large curvature motion.

The Interface Limiting Behavior as $S \to 0$

We investigate now the interface limiting behavior before and past t_c. We present numerical evidence to show that an asymptotic corner angle is selected in the limit as surface tension tends to zero when the finger tip is about to reach the sink. The computations presented here also suggest that the vanishing surface tension solution is singular at the finger neck.

To obtain information on the behavior of the wedge angle in the limit as surface tension tends to zero, we compare the interfaces for a set of decreasing values of surface tension. Since the velocity of the interface depends on surface tension, we compare the interfaces when their finger tips reach the same level above the sink rather than at a fixed time. As surface tension is reduced, the finger tip reaches the given level faster. Figure 4.7 provides some indication of the asymptotic trend of the fingers as surface tension is successively halved from $S = 8 \times 10^{-4}$ to $S = 5 \times 10^{-5}$. The fixed level is $y = 0.01$ so that the finger tips are very close to the sink.

As surface tension is decreased, the fingers develop a neck at about $y = 0.27$. However, away from the neck, the finger width changes very little. More precisely, as surface tension is reduced, the change in the finger width decreases. Table 4.1 gives the difference $\Delta(S, S/2)$ between the width of the finger corresponding to a surface tension S and that corresponding to $S/2$ at three different levels. It is observed that $\Delta(S, S/2)$ decreases

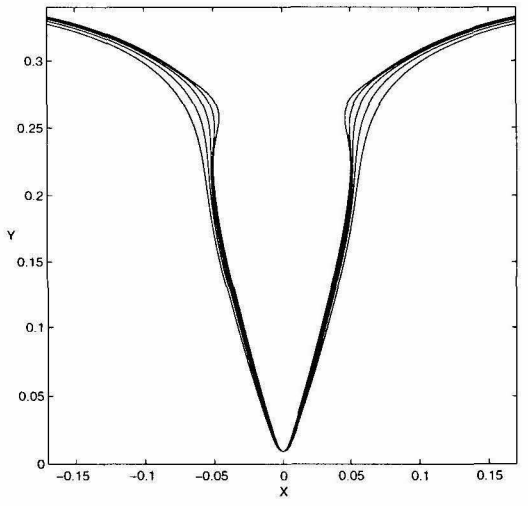

Figure 4.7: Comparison of the interface finger for a sequence of surface tensions with $A_\mu = 1$. From the outer curve inwards, the fingers correspond to the surface tension values $S = 8 \times 10^{-4}$, 4×10^{-4}, 2×10^{-4}, 1×10^{-4}, and 5×10^{-5}. Each interface is plotted when the tip of the finger reaches the fixed level $y = 0.01$ at $x = 0$. $N = 16384$ and $\Delta t = 2 \times 10^{-7}$.

as surface tension is reduced. The fingers are converging to an asymptotic shape. Table 4.2 suggests that an asymptotic angle is selected for the wedge as it touches the sink. The difference between consecutive angles (corresponding to surface tensions S and $2S$) decreases as surface tension is reduced. Note also that there is an asymptotic time at which the limiting wedge reaches the sink.

While the asymptotic trend of the wedge angle is clear, the limiting behavior of the interface in the vicinity of the neck is not obvious. More precisely, we would like to find the form of the continuation solution selected in the limit as surface tension tends to zero

S	Wedge angle	Variation
8×10^{-4}	0.67459	–
4×10^{-4}	0.65719	0.0174
2×10^{-4}	0.64399	0.0132
1×10^{-4}	0.63660	0.0074
5×10^{-5}	0.63359	0.0030

Table 4.2: The angle of the wedge (in radiants) for a decreasing set of surface tensions. The variation (third column) is the difference between consecutive angles, corresponding to surface tensions S and $2S$.

for any fixed time past t_c but before the time at which the limiting wedge reaches the sink. As expected, before t_c, the interface converges to the smooth zero-surface-tension solution as $S \to 0$. This is illustrated in Fig. 4.8 which shows a close-up picture of the interface for a set of decreasing surface tensions at a time ($t = 0.2840$) slightly before t_c. The zero-surface tension solution is also shown in Fig. 4.8.

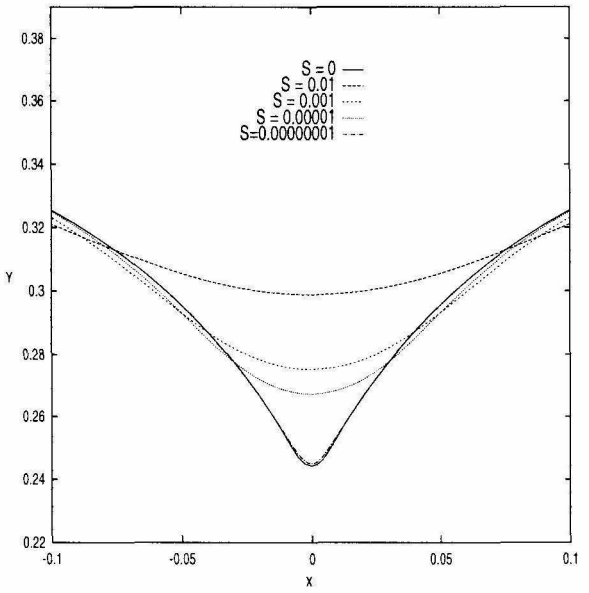

Figure 4.8: Limiting behavior of the interface before $t_c = 0.2842$ for $A_\mu = 1$. This figure shows a close-up picture of the interface around $x = 0$ for a set of surface tension values, decreasing from top to bottom, and plotted at time $t = 0.2840$. The zero-surface-tension solution is also shown. $N = 4096$ and $\Delta t = 5 \times 10^{-5}$.

We observe a very different behavior past t_c. Figure 4.9 presents close-up pictures of the interface finger developing just past t_c. The interfaces correspond to the surface tension values $S = 1 \times 10^{-5}$ and $S = 5 \times 10^{-6}$, plotted at $t = 0.2857$.

Note that the width of the small finger is approximately the same for both surface tensions. But a more pronounced neck with two corners can be observed for $S = 5 \times 10^{-6}$ in Fig. 4.9(b). Unfortunately, well-resolved computations for surface tensions smaller than this value are extremely difficult due to interface singular behavior and to growth of the round-off error noise. Nevertheless, the non-smooth transition observed for the previous values of surface tension hints a possible singularity formation in the limit.

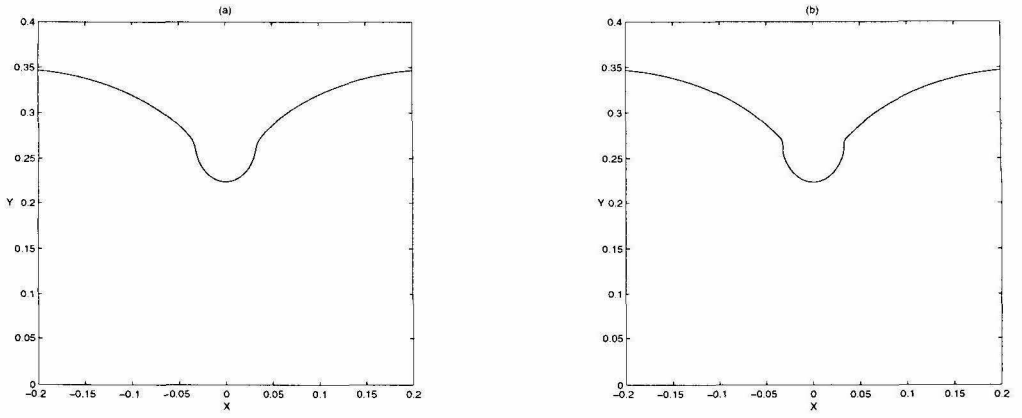

Figure 4.9: Close-up of the interface around $x = 0$ at $t = 0.2857$ (just past t_c) for $A_\mu = 1$. The interfaces correspond to (a) $S = 10^{-5}$ and (b) $S = 5 \times 10^{-6}$. $N = 8192$ and $\Delta t = 5 \times 10^{-6}$.

Indeed, a look at the tangent angle $\theta(\alpha, t)$ in Fig. 4.10 provides further indication of a singularity scenario in the limit as $S \to 0$.

The two spikes in θ correspond to the finger neck. While the tangent angle changes smoothly around the finger tip, two small kinks observed for $S = 5 \times 10^{-6}$ mark an almost discontinuous transition in θ at the finger neck. We use $N = 8192$ and $\Delta t = 5 \times 10^{-5}$ to resolve accurately both θ and the curvature for this case. Figure 4.11 shows the curvature near the finger tip at two very close times for $S = 5 \times 10^{-6}$.

There is a rapid growth of the curvature at the neck. A comparison with the curvature corresponding to $S = 5 \times 10^{-5}$ (Fig.4.6(a)) shows the singular trend of the interface limiting behavior. Although the numerical evidence is somewhat limited and further study is required for smaller values of surface tension, we conjecture that the neck will asymptote to corners in the limit as $S \to 0$.

4.3.2 $A_\mu < 1$: The Effect of the Surrounding-fluid Viscosity

Zero-surface-tension Cusp Formation

Very little is known for the Hele-Shaw flow with suction when $A_\mu < 1$, i.e., for the two-phase (Muskat) problem, even if surface tension is neglected. We first present a series of computations for several Atwood ratios in the absence of surface tension. These compu-

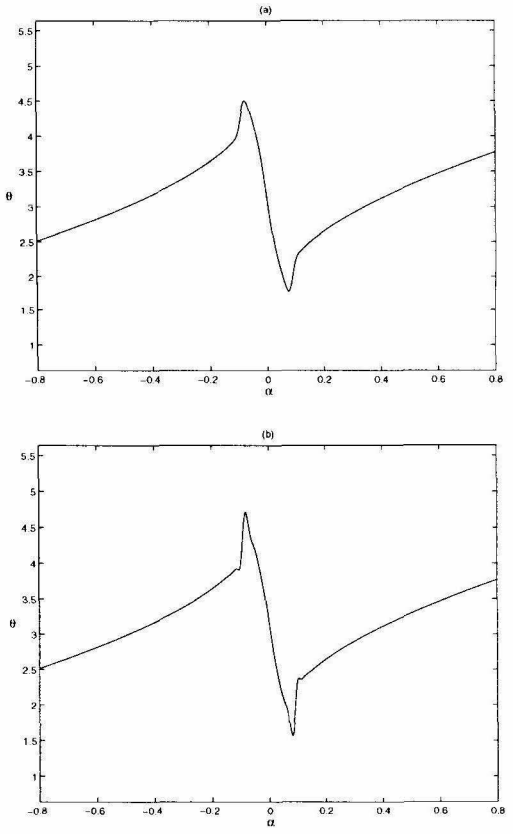

Figure 4.10: The tangent angle $\theta(\alpha, t)$ versus α around the finger tip ($\alpha = 0$) at $t = 0.2857$ for $A_\mu = 1$. The plots correspond to (a) $S = 10^{-5}$ and (b) 5×10^{-6}. $N = 8192$ and $\Delta t = 5 \times 10^{-6}$.

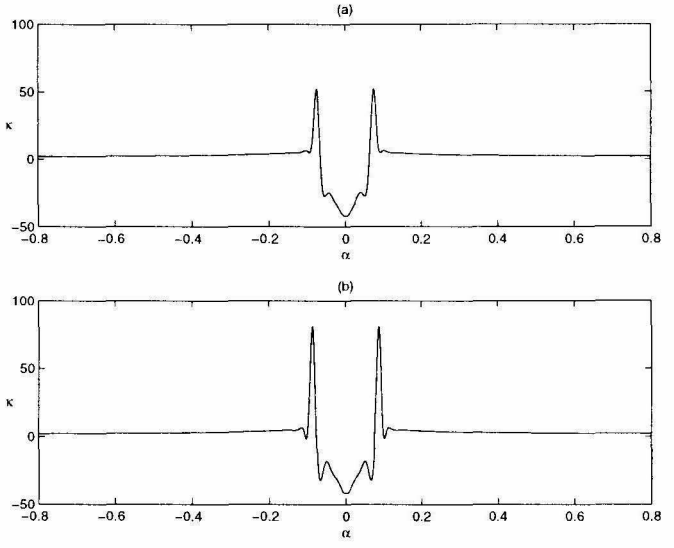

Figure 4.11: The curvature $\kappa(\alpha, t)$ versus α around the finger tip ($\alpha = 0$) for $A_\mu = 1$ and $S = 5 \times 10^{-6}$, at (a) $t = 0.2850$ and (b) $t = 0.2855$. $N = 8192$ and $\Delta t = 5 \times 10^{-6}$.

tations for $S = 0$ are performed in the Lagrangian frame as explained in Section 4.3.1. Figure 4.12 shows the breakdown of the Hele-Shaw solution for $A_\mu = 0.8$ and $A_\mu = 0.2$.

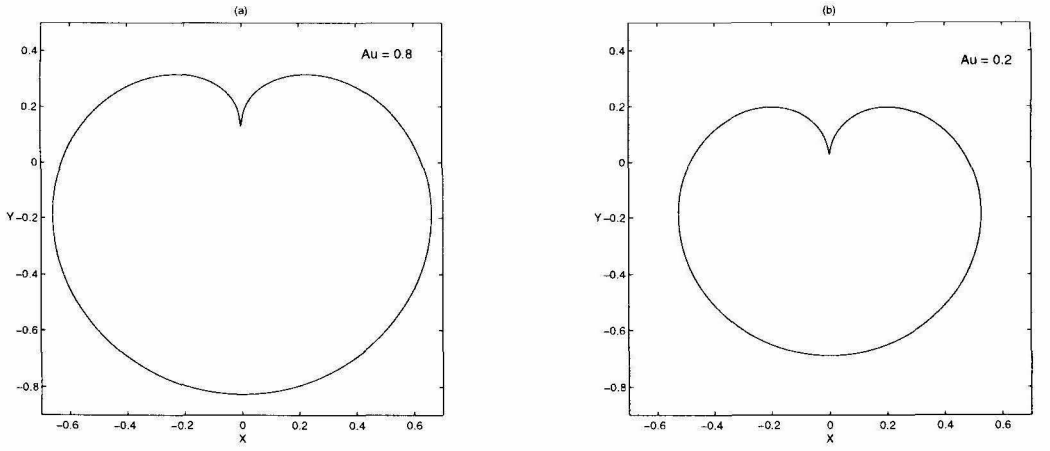

Figure 4.12: Collapse of the interface in the absence of surface tension. (a) $A_\mu = 0.8$. The cusp is formed approximately at $t_c = 0.3070$. (b) $A_\mu = 0.2$. The cusp is formed approximately at $t_c = 0.3809$. The computations were performed using $N = 2048$ and $\Delta t = 1 \times 10^{-5}$ in the Lagrangian frame.

The viscosity of the exterior fluid alone does not prevent the formation of cusps in the interface. Note that the breakdown times occur later than that for the $A_\mu = 1$ flow. As a result, more interior fluid gets sucked as A_μ decreases. Figure 4.13 presents close-up plots of the zero-surface-tension cusps for $A_\mu = 1$, 0.4, 0.2, and 0.08.

As the fitting curves demonstrate, the 3/2-power cusp singularity appears to be very generic. In all these cases the cusps are formed before the interface reaches the sink. However, as A_μ is reduced, the cusps develop closer and closer to the sink. It may be thought that for sufficiently small A_μ the cusp singularity will be formed only when the interface touches the sink. Nevertheless, at least for A_μ as small as 0.01, we find no evidence of this. The cusp still forms before the interface reaches the sink. Apparently, only for $A_\mu = 0$ the cusp occurs right at the sink.

Surface Tension and Large Viscosity Ratio

We consider now the flow for $A_\mu = 0.8$ with surface tension $S = 5 \times 10^{-5}$. Figure 4.14 shows the interface at different times as it evolves. Just as in the $A_\mu = 1$ case, a finger develops past t_c and evolves into a wedge as it is drawn into the sink.

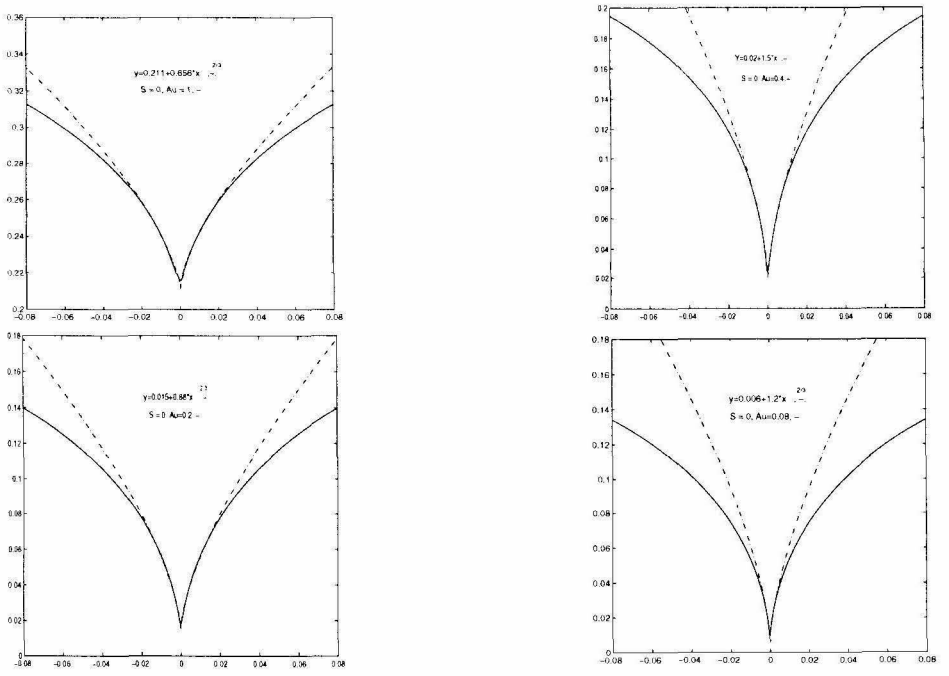

Figure 4.13: Zero-surface-tension cusps and 3/2-power fitting curves for different values of the viscosity Atwood ratio, shown at the approximate breakdown time t_c. (a) $A_\mu = 1.0$ at $t_c = 0.2842$. (b) $A_\mu = 0.4$ at $t_c = 0.3745$. (c) $A_\mu = 0.2$ at $t_c = 0.3807$. (d) $A_\mu = 0.08$ at $t_c = 0.40135$. The computations were performed using $N = 2048$ and $\Delta t = 1 \times 10^{-5}$ in the Lagrangian frame.

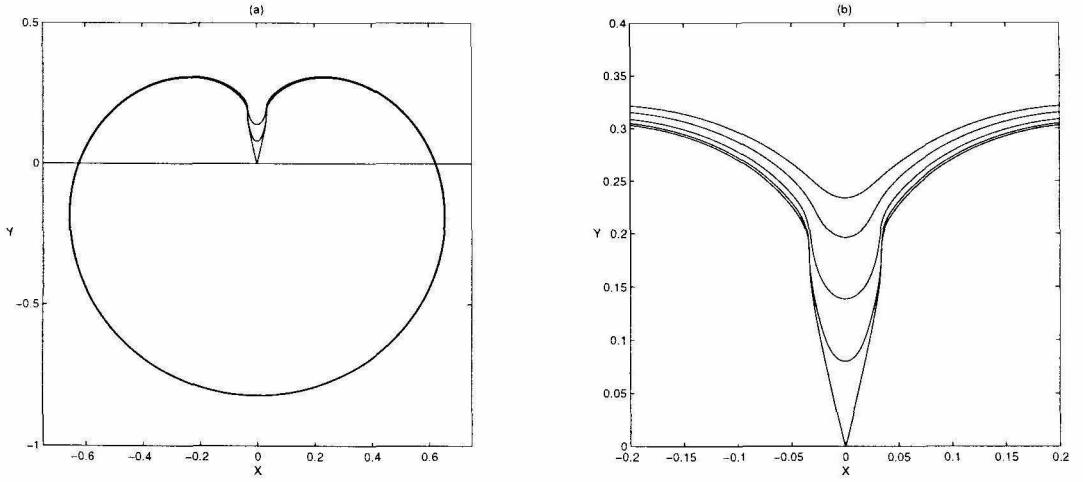

Figure 4.14: Evolution of the initially circular fluid blob past t_c, for $S = 5 \times 10^{-5}$ and $A_\mu = 0.8$. (a) The interface plotted at $t = 0.3106, 0.3126$ and 0.3136. (b) A close-up of the interface finger at the times $t = 0.304, 0.3076, 0.3106, 0.3126$, and 0.3136. $N = 16384$ and $\Delta t = 2 \times 10^{-7}$ for the last stage of the motion.

This particular value of surface tension was also considered for $A_\mu = 1$ (see Fig. 4.5). A comparison of these two cases, $A_\mu = 1$ and $A_\mu = 0.8$, shows a smoothing effect of the exterior-fluid viscosity on the interface. For $A_\mu = 0.8$, the finger has a less pronounced neck. The behavior resembles that of $A_\mu = 1$ with much larger surface tension, except that the finger is thinner for $A_\mu = 0.8$. However, the side indentations of the finger neck do develop for smaller surface tension as Fig. 4.15 demonstrates.

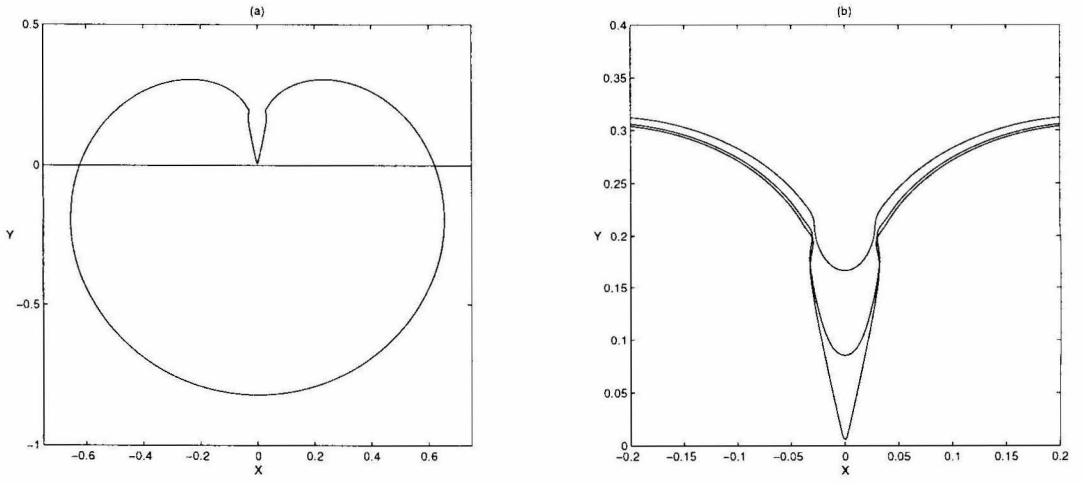

Figure 4.15: Evolution of the initially circular fluid blob past t_c, for $S = 1 \times 10^{-5}$ and $A_\mu = 0.8$. (a) The interface plotted at $t = 0.31222$. (b) A close-up of the interface finger at the times $t = 0.3080, 0.3111$, and 0.31222. $N = 32768$ and $\Delta t = 1 \times 10^{-7}$ for the last stage of the motion.

The interface motion shown in this figure corresponds to $S = 1 \times 10^{-5}$. We use $N = 32768$ and $\Delta t = 1 \times 10^{-7}$ to resolve the last stage of the flow. Note that the wedge angle is smaller than that corresponding to $A_\mu = 1$. The formation of a corner at the finger tip can be clearly appreciated in Fig. 4.16 which is a plot of θ around the finger at $t = 0.31222$.

At this time, the distance of the finger tip to the sink is 9×10^{-3}. In addition to the discontinuity at $\alpha = 0$, we observe two abrupt changes in θ corresponding to the finger neck. This is analogous to the almost discontinuous transition in θ observed for $A_\mu = 1$ and $S = 5 \times 10^{-6}$ in Fig. 4.10(b) and which we believe will lead to the formation of pair of curvature singularities at the neck in the limit as $S \to 0$.

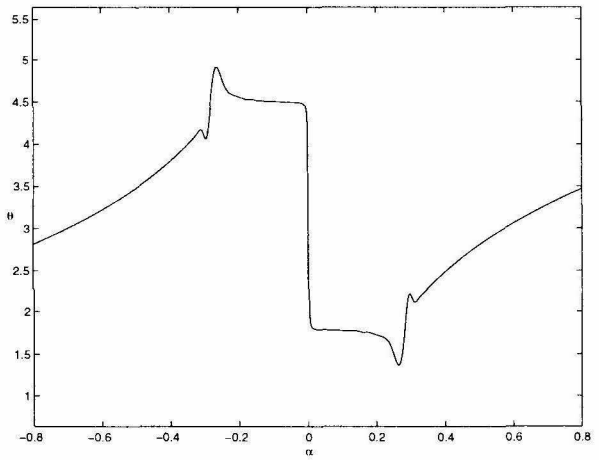

Figure 4.16: Tangent angle $\theta(\alpha, t)$ versus α around the finger tip at $t = 0.31222$ for $S = 1 \times 10^{-5}$ and $A_\mu = 0.8$. $N = 32768$ and $\Delta t = 10^{-7}$.

Surface Tension and Small Viscosity Ratio

The Hele-Shaw flow for small Atwood ratios differs significantly from the $A_\mu = 1$ flow. Figure 4.17 shows the evolution of the interface for $A_\mu = 0.2$ as it approaches the sink for several values of surface tension.

The interface develops a very thin finger whose width decreases with surface tension. Unlike the larger A_μ flows, for $A_\mu = 0.2$ the zero-surface-tension cusp occurs already very close to the sink so that small surface tension acts very briefly past t_c. In the short time interval from t_c to the time where the interface touches the sink, the sink flow is dominant and the interface profile is similar to that with zero-surface-tension. The effect of small surface tension is to round slightly the tip of the thin finger. This is illustrated clearly in Fig. 4.18(a) where a close-up picture of the finger, for $A_\mu = 0.2$ and $S = 1 \times 10^{-5}$, is shown as the interface is about to collapse at $t = 0.38124$.

We use $N = 32768$ and $\Delta t = 1 \times 10^{-7}$ to resolve the interface motion up to this time. The zero-surface-tension $A_\mu = 0.2$ cusp is also shown. Figure 4.18(b) is a plot of the tangent angle $\theta(\alpha, t)$ around the finger tip. This plot suggests once more the formation of a corner singularity at the finger tip as it touches the sink. Note also that there are no signs of neck formation for this case, as reflected in θ.

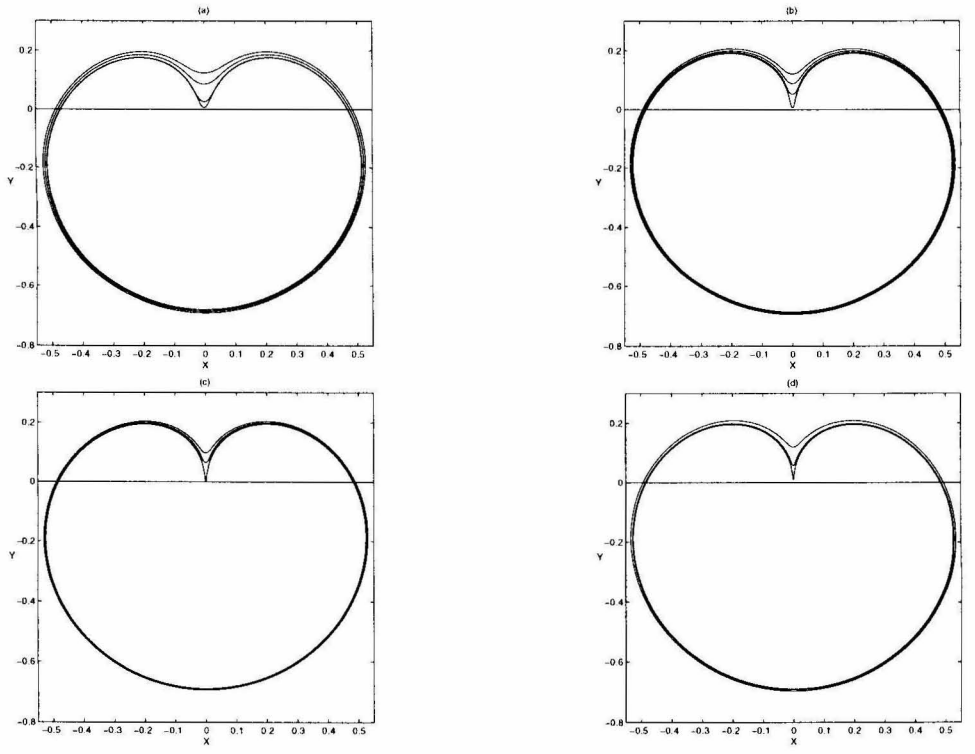

Figure 4.17: Evolution of the interface for $A_\mu = 0.2$ with different surface tensions as it approaches the sink. (a) $S = 1 \times 10^{-2}$, (b) $S = 1 \times 10^{-3}$, (c) $S = 1 \times 10^{-4}$, and (d) $S = 1 \times 10^{-5}$. $N = 8192$ and $\Delta t = 5 \times 10^{-6}$.

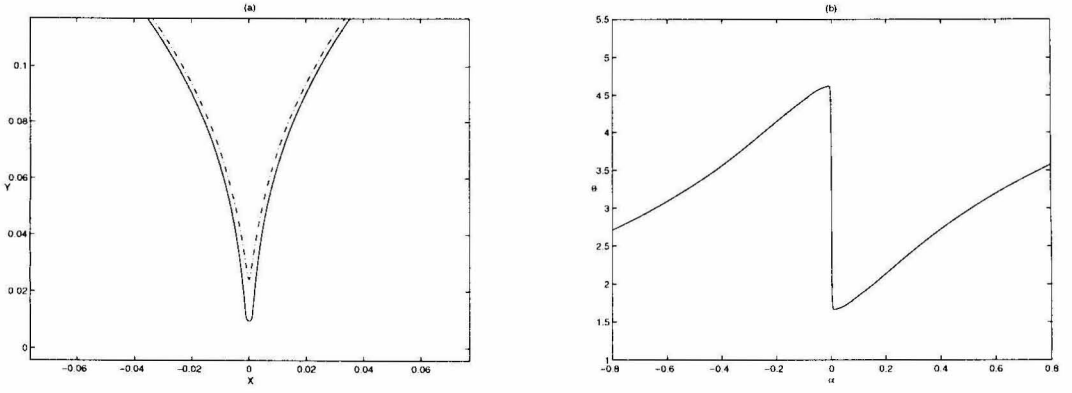

Figure 4.18: Collapse of the interface for $A_\mu = 0.2$ and $S = 1 \times 10^{-5}$. (a) Close-up of the finger tip at $t = 0.38124$. The distance of the tip to the sink is 0.00951. The dotted line curve corresponds to the zero-surface-tension cusp at $t_c = 0.3809$. (b) tangent angle $\theta(\alpha, t)$ near the interface tip ($\alpha = 0$) at $t = 0.38124$. This computation ended with $N = 32768$ and $\Delta t = 1 \times 10^{-7}$.

Finally, we study the asymptotic behavior of the thin fingers for $A_\mu = 0.2$ in the limit as surface tension tends to zero. Figure 4.19 provides a close-up of the fingers at $t = 0.3800$, just before t_c. As expected, the fingers converge to the zero-surface-tension solution.

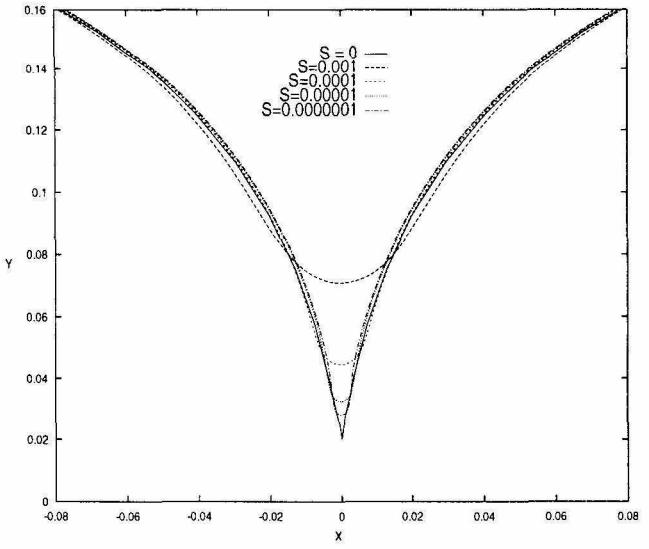

Figure 4.19: Limiting behavior of the interface before $t_c = 0.3809$ for $A_\mu = 0.2$. This figure shows a close-up picture of the interface around $x = 0$ for a set of surface tension values, decreasing from top to bottom, and plotted at time $t = 0.3810$. The zero-surface-tension solution is also shown. $N = 4096$ and $\Delta t = 1 \times 10^{-5}$.

To study the interface asymptotic behavior past t_c we compare the fingers, for a decreasing set of surface tension values, when they reach a given fixed level close to the sink. This comparison is given in Fig. 4.20 for surface tension ranging from $S = 1 \times 10^{-2}$ to $S = 1 \times 10^{-5}$. The interfaces correspond to different times past t_c.

An asymptotic shape of the fingers is apparent. Table 4.3 shows the converging trend of the finger widths as surface tension is decreased. Note that the asymptotic wedge angle for $A_\mu = 0.2$ is smaller than the angles observed for $A_\mu = 0.8$ and $A_\mu = 1$. The asymptotic angle decreases with A_μ, apparently towards the zero angle of the $A_\mu = 0$ cusp.

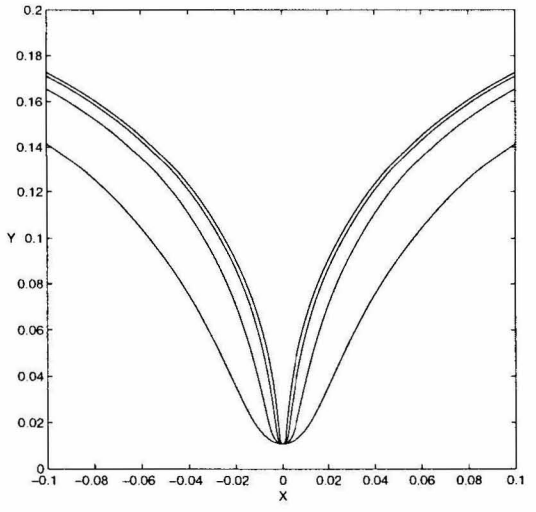

Figure 4.20: Comparison of the interface finger for a sequence of surface tensions with $A_\mu = 0.2$. From the outer curve inwards, the fingers correspond to the surface tension values $S = 1 \times 10^{-2}$, 1×10^{-3}, 1×10^{-4}, and 1×10^{-5}. Each interface is plotted when the tip of the finger reaches the fixed level $y = 0.01$ at $x = 0$. $N = 8192$ and $\Delta t = 1 \times 10^{-6}$ for $S = 1 \times 10^{-2}$ and $S = 1 \times 10^{-3}$. $N = 16384$ and $\Delta t = 2 \times 10^{-7}$ for $S = 1 \times 10^{-4}$ and $S = 1 \times 10^{-5}$.

y	$\Delta(10^{-2}, 10^{-3})$	$\Delta(10^{-3}, 10^{-4})$	$\Delta(10^{-4}, 10^{-5})$
0.04	0.01148	0.00445	0.00174
0.03	0.00914	0.00377	0.00148
0.02	0.006138	0.002874	0.001218

Table 4.3: Change in the finger widths as surface tension is decreased for $A_\mu = 0.2$. The first column shows the height level at which the fingers are compared. Columns 2-4 give the difference $\Delta(S, S/10)$ between the width of the finger corresponding to a surface tension S and that corresponding to $S/10$.

4.3.3 An Analysis of Numerical Errors

As described in the beginning of this section, our computations are performed so that all the Fourier modes of the tangent angle $\theta(\alpha, t)$ are well-resolved at all times. To achieve this we successively double the number of points N as soon as the magnitude of the highest frequency mode of $\theta(\alpha, t)$ is greater than the filter level. The time-step size Δt is selected so that decreasing it further would not produce any appreciable difference within plotting resolution in the curvature of the interface.

We now present a resolution study for the long-time computation that is most difficult to resolve. This is the case corresponding to $A_\mu = 1$ and $S = 5 \times 10^{-5}$ for the 10% offset initial data. In lack of an exact solution, we compare two different resolutions computed as follows. One computation starts with $N = 1024$ and $\Delta t = 1 \times 10^{-4}$ and ends with $N = 16384$ and $\Delta t = 2 \times 10^{-7}$. The other computation uses twice the number of points and half the time-step, i.e., it starts with $N = 2048$ and $\Delta t = 5 \times 10^{-5}$ and ends with 32768 points and $\Delta t = 10^{-7}$. The number of digits in the maximum difference between these two resolutions for θ is presented in Fig. 4.21. Up to the end, the computations agree within at least three digits of accuracy for θ. A similar resolution study for $A_\mu = 0.2$ and $S = 1 \times 10^{-5}$ gives a maximum difference of 2.8×10^{-4} at $t = 0.38124$.

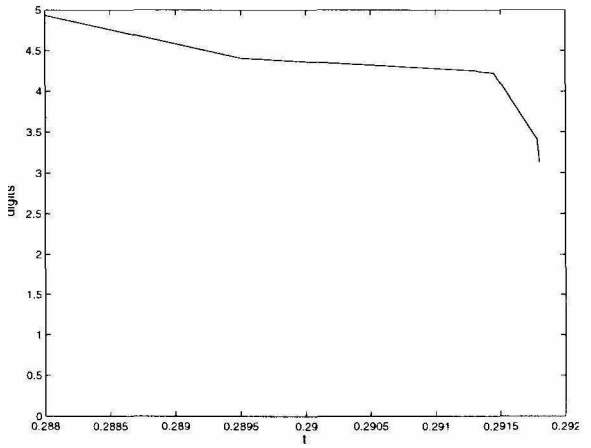

Figure 4.21: The digits of accuracy in θ versus time for $S = 5 \times 10^{-5}$ and $A_\mu = 1$ as reflected by the maximum difference between two computations with different resolutions. One computation starts with $N = 1024$ and $\Delta t = 1 \times 10^{-4}$ and ends with $N = 16384$ and $\Delta t = 2 \times 10^{-7}$. The other computation uses twice the number of points and half the time-step, i.e., it starts with $N = 2048$ and $\Delta t = 5 \times 10^{-5}$, and ends with 32768 points and $\Delta t = 1 \times 10^{-7}$.

By monitoring closely the spectrum of the solution at all times, we verify the resolution in Fourier space and check for signs of numerical instability and noise. The spectrum of the vortex sheet strength γ at various times for $A_\mu = 1$ and $S = 5 \times 10^{-5}$ flow is shown in Fig. 4.22. The spectra appear free of any sign of numerical instability and noise pollution is inappreciable.

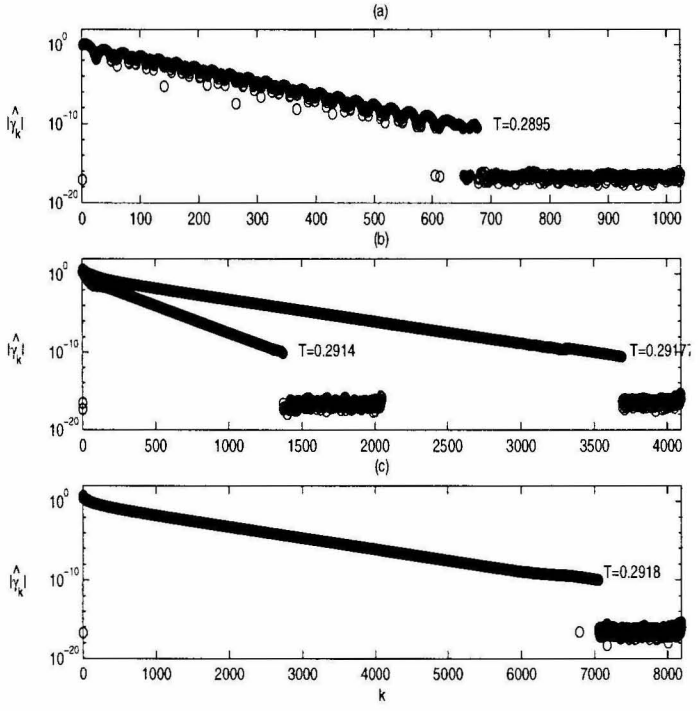

Figure 4.22: The spectrum of γ at various times for $S = 5 \times 10^{-5}$ and $A_\mu = 1$.

Another useful check for the numerics is the conservation of the first moment for $A_\mu = 1$:

$$\dot{I} = \frac{d}{dt} \int \int_{\Omega(t)} z dx dy = 0 \tag{4.23}$$

where Ω is the domain of the viscous fluid and z denotes the complex position of the fluid particles. This identity can be easily shown by noting that

$$\dot{I} = \int_{\Gamma(t)} zU ds = -M \int_{\Gamma(t)} z \nabla p \cdot \hat{\mathbf{n}} ds, \tag{4.24}$$

where again $\Gamma(t)$ is the free boundary, U is the normal velocity, and we have used

$U = -M\nabla p \cdot \hat{\mathbf{n}}$. Since p and both the real and imaginary part of z are harmonic functions, a Green's identity implies that

$$\int_{\Gamma(t)} z\nabla p \cdot \hat{\mathbf{n}} ds = \int_{\Gamma(t)} p\nabla z \cdot \hat{\mathbf{n}} ds. \tag{4.25}$$

Moreover, $p|_\Gamma = \tau\kappa$ for $A_\mu = 1$. Thus,

$$\begin{aligned} \dot{I} &= -M\int_{\Gamma(t)} z\nabla p \cdot \hat{\mathbf{n}} ds = -M\int_{\Gamma(t)} p\nabla z \cdot \hat{\mathbf{n}} ds = -M\tau\int_{\Gamma(t)} \kappa\nabla z \cdot \hat{\mathbf{n}} ds \\ &= iM\tau\int_{\Gamma(t)} \theta_s e^{i\theta} ds = iM\tau\int_0^{2\pi} e^{i\theta} d\theta = 0, \end{aligned} \tag{4.26}$$

where we have used $\kappa = \theta_s$. Throughout all the computations for $A_\mu = 1$, $|\dot{I}|$ remains of order 10^{-12} or smaller.

4.3.4 Effect of Offset Shift

We consider now the effect of a shift in the position of the center of the initially circular blob. In Fig. 4.23, we compare a 20% offset sink (the blob center is $(0, -0.2)$ initially), with a 10% offset sink (the blob center is $(0, -0.2)$ initially), with surface tension $S = 0.01$ and $A_\mu = 1.0$.

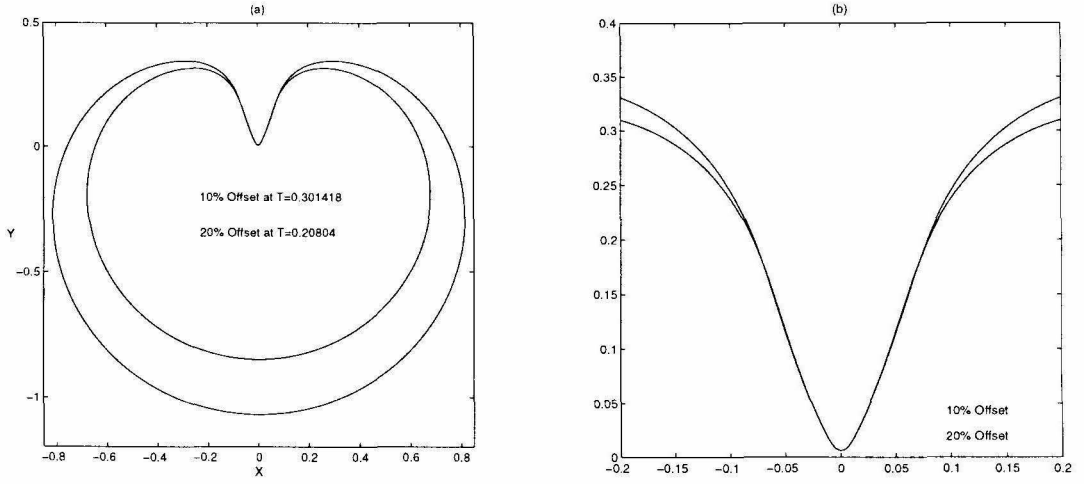

Figure 4.23: Comparison of finger widths for 10% and 20% offset sinks, with S = 0.01 and $A_\mu = 1.0$. The interface for the 10% offset initial data is plotted at t=0.301418 and that for the 20% offset case is plotted at t =0.20804. (a) The two interfaces and (b) a close-up of the fingers. $N = 8192$ and $\Delta t = 1 \times 10^{-6}$ for the last stage of the motion.

Although the viscous finger forms much earlier for the 20% offset case, the width and shape of the finger are unaffected by the offset shift. We now consider a similar comparison for $S = 5 \times 10^{-5}$ and $A_\mu = 1.0$. This is shown in Fig. 4.24.

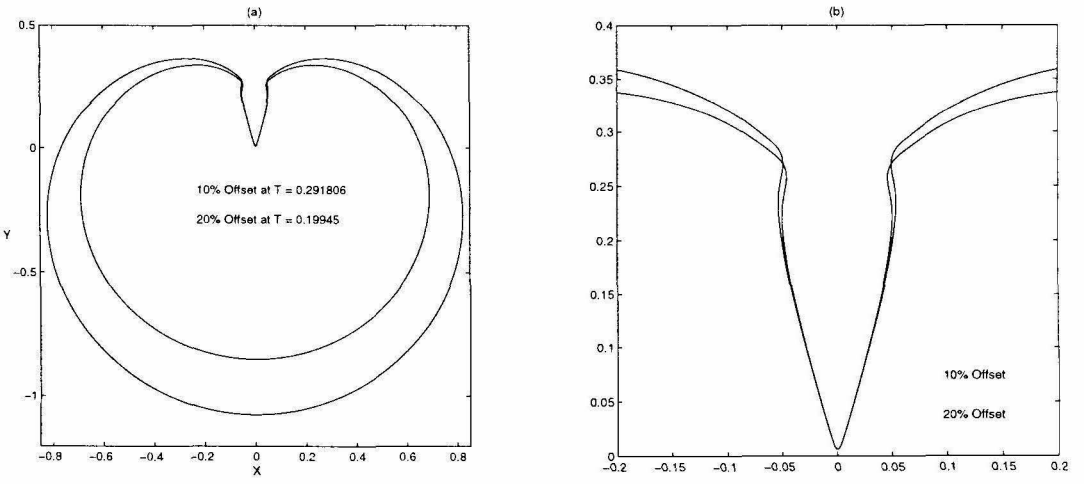

Figure 4.24: Comparison of finger widths for 10% and 20% offset sinks with $S = 5 \times 10^{-5}$. The interface for the 10% offset initial data is at t=0.291806 and that for the 20% offset case is plotted at t =0.19945. $N = 16384$ and $\Delta t = 2 \times 10^{-7}$ for the last stage of the motion.

We find that the finger tips match very well and thus, the corresponding solutions break down with the same corner angle. The overall development of the two finger is qualitatively the same. In particular, similar side indentations at the neck are formed and the fingers slightly bulge before becoming a wedge.

4.4 Further Discussion

Surface tension regularizes the cusped Hele-Shaw flows with suction. In the presence of small surface tension, and when the viscosity of the surrounding fluid is neglected, a long finger develops after the zero-surface-tension singularity time. This finger evolves rapidly into a wedge as it approaches the sink. The Hele-Shaw solutions for $A_\mu = 1$ appear to generically break down by forming a corner at the wedge tip when the interface touches the sink.

As surface tension is decreased systematically, new features of the Hele-Shaw flow are discovered. The angle at the tip of the wedge converges to a selected asymptotic

value in the limit as $S \to 0$. Moreover, for sufficiently small values of surface tension, side indentations forming a neck develop at the top of the finger. As opposed to the predicted behavior of the crack model of Howison *et al.* [25], the developing finger for $A_\mu = 1$ bulges after the zero-surface-tension cusp time t_c. The formation of the neck and the bulging of the finger are intriguing phenomena that could be linked to the influence of the zero-surface-tension singularity for very small values of surface tension.

It could also be argued that this somewhat singular behavior is caused by the impact of a curvature-induced complex singularity. This so-called daughter singularity, whose concept was introduced by Tanveer [60], is generated by a zero in the derivative of the conformal map that describes the Hele-Shaw flow. The daughter singularity is spawn by the zero through the surface tension term, in the complex plane outside the physical domain. The zero and the daughter singularity travel with different speeds towards the physical domain. Depending on the initial data, the daughter singularity may or may not impact the physical domain before the zero does. For the particular initial data that we use here, the daughter singularity would hit the physical domain well after the zero, i.e., much later than t_c. The daughter singularity impact time can be estimated by solving an ordinary differential equation [60, 58]. Since the neck formation and the bulging of the finger are observed around t_c, we rule out the effects of the daughter singularity for the particular flow we consider here.

The numerical evidence presented here also suggests that the limiting solution as $S \to 0$ is singular at the finger neck, for any fixed time past t_c but before the asymptotic time at which the wedge tip touches the sink. Unfortunately, well-resolved computations are difficult to achieve due to the rapid growth of the round-off level noise for very small surface tension and to the singular interface behavior. Although further numerical study is required to compute effectively the limit, we believe that corners will develop at the finger neck in the limit as $S \to 0$. The vanishing surface tension solution selects a continuation solution past t_c in which the zero-surface-tension cusp is split into a pair of corner singularities.

The viscosity of the exterior fluid alone does not prevent the formation of cusps. It only delays them. In the absence of surface tension, we observe generic 3/2-power cusps just as in the case of $A_\mu = 1$. However, as the viscosity ratio A_μ is decreased, we observe

that the zero-surface-tension cusps develop closer and closer to the sink. We find that even for values of A_μ as small as 0.01, the cusp singularity develops before the interface reaches the sink. In the presence of surface tension and for large viscosity ratios, the interface evolution is very similar to that of $A_\mu = 1$ but with larger surface tension. The viscosity of the exterior fluid has a smoothing effect on the flow and a thinner finger develops. The interface behavior is significantly different for small viscosity ratios. In this case, the zero-surface-tension cusp occurs already very close to the sink. Small surface tension only rounds slightly the tip of the cusp before this part of the interface rapidly accelerates to the sink. As a result, thin cusp-like fingers develop for small viscosity ratios. These fingers appear to converge also to an asymptotic shape as surface tension is reduced. It is noted that the angle of the asymptotic wedges decreases with A_μ. We believe that this angle will collapse to zero (a cusp) in the limit as $A_\mu \to 0$.

Chapter 5

Numerical Study of Axisymmetric Flow with Suction through Porous Media

Through the similarity in their governing equations, three-dimensional saturated flows through porous media are linked with Hele-Shaw flows with suction. In the following chapter, we study the axisymmetric flow consisting of a blob of viscous fluid driven through a point sink located inside the blob. The surrounding fluid is assumed inviscid. In Section 5.1, we present the equations of motion for the axisymmetric flow through porous media in a boundary integral formulation. We describe the numerical method in Section 5.2, The main idea to construct the uniform order quadratures of Nitsche is outlined here. We also explain how to adapt the technique of Hou *et al.* to obtain an efficient non-stiff time discretization for the computation of the axisymmetric flow in the presence of surface tension. Several important numerical issues such as numerical stability and filtering are also discussed in Section 5.2. As a test to the numerical method, we compute the evolution of an initially spherical vortex sheet [41, 45]. Section 5.3 is devoted to present the numerical results on the axisymmetric flow with suction along with some comparisons with the corresponding Hele-Shaw flow.

5.1 The Governing Equations

We consider an axisymmetric blob of incompressible viscous fluid surrounded by air or gas whose density is so light (compare to that of the viscous fluid) that the motion of the gas is unimportant. The velocity field $\mathbf{u}$ of the viscous fluid is given by Darcy's law:

$$\mathbf{u} = -\frac{k}{\mu}\nabla p, \tag{5.1}$$

where k is the permeability of the medium, μ is the viscosity of the fluid, and p is the pressure. The incompressibility of the fluid expressed as $\nabla \cdot \mathbf{u} = 0$ implies that the pressure satisfies Laplace's equation

$$\nabla^2 p = 0. \tag{5.2}$$

The nonlinearity of the flow comes from the boundary conditions on the fluid interface (the boundary of the fluid blob). Denoting the interface by Γ, these conditions can be written in the following form:

$$[\mathbf{u} \cdot \hat{\mathbf{n}}]|_\Gamma = 0, \tag{5.3}$$

$$[p]|_\Gamma = \tau\kappa, \tag{5.4}$$

where $[\cdot]$ denotes the jump across the interface. Here, $\hat{\mathbf{n}}$ is the exterior unit normal to Γ, τ is the surface tension coefficient, and κ is the mean curvature of the interface. The kinematic boundary condition (5.3) states that the normal component of the velocity field is continuous across the interface. This implies that particles on the interface remain there. The relation (5.4), known as the Laplace-Young boundary condition, gives an account of how the presence of surface tension modifies the pressure across the interface.

We assume that there is a point sink at the origin, inside the fluid blob. For large distances away from the sink, the velocity field tends to the simple radial flow:

$$\mathbf{u}(\mathbf{X}) \to Q\frac{\mathbf{X}}{|\mathbf{X}|^3}, \quad \text{as } |\mathbf{X}| \to \infty. \tag{5.5}$$

Since the flow is potential, it can be described by the dynamics of the free interface Γ. Furthermore, we assume that the flow is axisymmetric. Thus, the surface Γ can be represented by its cross section with the $x - y$ plane, as depicted in Fig. 5.1 for the case of a spherical surface. At any time t, we write Γ in parametric form as $(x(\alpha, t), y(\alpha, t))$, where α is a Lagrangian parameter. Both x and y are 2π periodic functions in α. Note that, because of symmetry, $(x(\alpha, t), y(\alpha, t))$ with $\alpha \in [0, \pi]$ suffices to describe the whole interface.

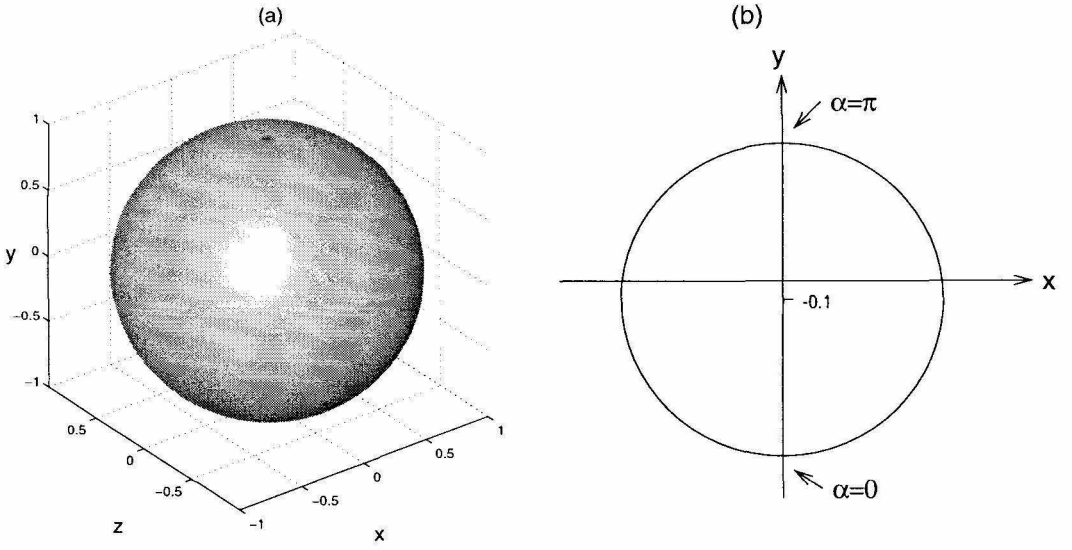

Figure 5.1: Spherical surface: (a) Three-dimensional perspective and (b) curve representing the cross section of the flow in the $x-y$ plane.

Taking into account the sink, the radial (u) and axial (v) velocities are given by [8]

$$u(\alpha,t) = \frac{1}{2\pi x}\int_0^{\pi}\gamma'\frac{y'-y}{\rho_2}\left[F(\lambda)-\frac{(y'-y)^2+x'^2+x^2}{\rho_1^2}E(\lambda)\right]d\alpha' + Q\frac{x}{(x^2+y^2)^{3/2}}, \tag{5.6}$$

$$v(\alpha,t) = \frac{1}{2\pi}\int_0^{\pi}\gamma'\frac{1}{\rho_2}\left[F(\lambda)-\frac{(y'-y)^2+x'^2-x^2}{\rho_1^2}E(\lambda)\right]d\alpha' + Q\frac{y}{(x^2+y^2)^{3/2}}, \tag{5.7}$$

where $\rho_1^2=(y-y')^2+(x-x')^2$ and $\rho_2^2=(y-y')^2+(x+x')^2$. Here γ is the analogue to the two-dimensional vortex sheet strength. $F(\lambda)$ and $E(\lambda)$ are the complete elliptic integrals of the first and second kind given by:

$$F(\lambda) = \int_0^{\frac{\pi}{2}}\frac{d\theta}{\sqrt{1-\lambda^2\cos^2\theta}},$$

$$E(\lambda) = \int_0^{\frac{\pi}{2}}\sqrt{1-\lambda^2\cos^2\theta}\,d\theta,$$

with $\lambda^2=4xx'/\rho_2^2$. The integrals in (5.6) and (5.7) are understood as principal-value integrals. Following the derivation for Hele-Shaw flow (see, for example [10, 63]), we get

a similar integral equation for γ at the cross section with the x-y plane:

$$\gamma(\alpha, t) = \frac{2}{s_\alpha}(x_\alpha u + y_\alpha v) + S\kappa_\alpha. \tag{5.8}$$

Here, $S = \tau k/\mu$ is a scaled surface tension parameter. Thus, the motion of the axisymmetric flow through porous media with suction is described by Eqs. (5.6), (5.7), and (5.8). We nondimensionalize the equations of motion by setting $Q = -1$ and by taking the initial radius of the interface to be 1. Finally, the mean curvature can be computed using the following formula:

$$\kappa = \frac{x_\alpha y_{\alpha\alpha} - x_{\alpha\alpha} y_\alpha}{s_\alpha^3} + \frac{y_\alpha}{x s_\alpha}, \tag{5.9}$$

where $s_\alpha = \sqrt{x_\alpha^2 + y_\alpha^2}$. For future reference, we write the two components of the curvature separately as

$$\kappa_1 = \frac{x_\alpha y_{\alpha\alpha} - x_{\alpha\alpha} y_\alpha}{s_\alpha^3}, \tag{5.10}$$

$$\kappa_2 = \frac{y_\alpha}{x s_\alpha}. \tag{5.11}$$

We see that the governing equations are very similar to those for the two-dimensional Hele-Shaw flow, except for the additional component κ_2 of the mean curvature, and the integrands of the boundary integrals. Also the point sink has a different form.

5.2 The Numerical Method

There are two main components in obtaining a numerical solution to the initial value problem given by (5.6), (5.7), and (5.8): an accurate discretization in space which includes the evaluation of the principal-value integrals and the solution of the integral equation for γ, and an efficient and accurate time marching scheme. The appropriate choice of each discretization is nontrivial as the boundary-integral formulation is very sensitive to numerical instabilities. In addition, in the presence of small surface tension, discretetizations become even more sensitive due to the ill-posedness of the underlying zero-surface-tension problem [17, 26]. We describe in this section our discretization

choices and illustrate why high accuracy and delicate numerical filtering are required to compute reliably the nonlinear interface evolution.

5.2.1 Evaluation of the Principal-value Integrals

Unlike the case for the analogous two-dimensional motion, the integrands in the boundary integrals for three-dimensional axisymmetric flow have a very complex structure involving poles and logarithmic singularities. Even if the leading order singularities are extracted, some derivative of the integrands will be singular and as a result standard quadrature rules will have a non-smooth discretization error. Moreover, as noted by Baker *et al.* [4], the integrands change rapidly at the two poles where the surface intersects the axis of symmetry. This makes the accurate evaluation of the principal-value integrals for axisymmetric flow even more difficult to achieve.

Here, we use a high order quadrature due to Nitsche [44]. This quadrature achieves a uniform discretization error. We implement this quadrature to fifth order for the computations accounted here. We present next only the main ideas in the construction of this quadrature and refer the reader to [44] for the the implementation details.

Each boundary integral can be written in the following form:

$$w(\alpha,t) = \int_0^\pi G(\alpha,\alpha',t)d\alpha', \tag{5.12}$$

where

$$G(\alpha,\alpha',t) = G(\gamma(\alpha',t),x(\alpha,t),y(\alpha,t),x(\alpha',t),y(\alpha',t)) \tag{5.13}$$

is a function given in terms of the elliptic integrals $F(\lambda)$ and $E(\lambda)$ as expressed in Eq. (5.6) and Eq. (5.7). Note that there is a different G for each boundary integral. Expanding the elliptic integrals around $\lambda = 1$ and performing a Taylor expansion around $\alpha' = \alpha$, it follows that

$$G(\alpha,\alpha',t) = G_s(\alpha,\alpha',t) + \frac{c_{-1}(\alpha,t)}{\alpha'-\alpha} + \sum_{k=0}^{\infty} c_k(\alpha,t)(\alpha'-\alpha)^k \log|\alpha'-\alpha|, \tag{5.14}$$

where $G_s(\alpha,\alpha',t)$ is a smooth function in both α and α'. Consider a uniform mesh in α

given by $\alpha_i = ih$ for $i = 0, 1, \ldots, N$ and $h = \pi/N$. Sidi and Israeli [57] show that

$$\begin{aligned}\int_0^\pi G(\alpha_i, \alpha', t)d\alpha' = h\sum_{j\neq i} G(\alpha_i, \alpha_j, t) + hG_s(\alpha_i, \alpha_j, t) + c_0(\alpha_i, t)h\log\frac{h}{2\pi} \\ + \sum_{k=2}^{2m} \nu_k c_k(\alpha_i, t)h^{k+1} \\ + \sum_{k=1}^{2m+1} \gamma_k[\frac{\partial^k}{\partial\alpha'^k}G(\alpha_i, \pi, t) - \frac{\partial^k}{\partial\alpha'^k}G(\alpha_i, 0, t)]h^{k+1} + O(h^{2m+3})\end{aligned} \tag{5.15}$$

for any integer $m \geq 1$. The constants ν_k and γ_k (not to be confused with the vortex sheet strength γ) are given in [57]. The first term in the right-hand side of (5.15) corresponds to the ring vortex approximation while the first three terms together give the de Bernadinis and Moore quadrature. Quadratures of higher order may be constructed by approximating the principal-value integral by the right-hand side of (5.15) for a given $m \geq 1$. However, the error for all these quadratures is nonuniform and deteriorates severely near the poles of the symmetry axis ($\alpha = 0$ and $\alpha = \pi$). As pointed out by Nitsche [45], this is because both the coefficients c_k and the derivatives $\partial^k G/\partial\alpha'^k$ are not uniformly bounded. In fact, Nitsche [44] shows that, as $\alpha_i \to 0$, they behave asymptotically as

$$c_k(\alpha_i, t) \sim \frac{1}{\alpha_i^{k-1}} \qquad \text{and} \qquad \frac{\partial^k}{\partial\alpha'^k}G(\alpha_i, 0, t) \sim \frac{1}{\alpha_i^{k-1}}, \tag{5.16}$$

for the boundary integral in the radial velocity u given by (5.6), and as

$$c_k(\alpha_i, t) \sim \frac{1}{\alpha_i^{k}} \qquad \text{and} \qquad \frac{\partial^k}{\partial\alpha'^k}G(\alpha_i, 0, t) \sim \frac{1}{\alpha_i^{k}}, \tag{5.17}$$

for the boundary integral in the axial velocity v given by (5.7). Similar estimates hold for $\alpha_i \to \pi$.

The main idea of Nitsche's quadrature is to construct functions B^0 and B^π that approximate G at the symmetry poles $\alpha = 0$ and $\alpha = \pi$ to get corrections for the nonuniform quadratures derived from (5.15). The functions B^0 and B^π are obtained by Taylor expanding the integrand G about the poles. Let us denote any of the nonuniform quadrature rules by $Q[\cdot]$. Near $\alpha = 0$, $G - B^0$ is smoother than G and consequently

$Q[G - B^0] = Q[G] - Q[B^0]$ has a smoother discretization error than $Q[G]$. Therefore, the approximation

$$\int_0^\pi G d\alpha' \approx Q[G] - Q[B^0] + \int B^0 d\alpha' \tag{5.18}$$

behaves better than $Q[G]$ near $\alpha = 0$. Note that

$$E_Q[B^0] = \int B^0 d\alpha' - Q[B^0] \tag{5.19}$$

acts as a local correction to the error in $Q[G]$. A similar correction $E_Q[B^\pi]$ can be obtained near $\alpha = \pi$. The final approximation due to Nitsche [44] can be written as

$$\int_0^\pi G(\alpha_i, \alpha', t) d\alpha' \approx Q[G] + w_1(\alpha_i) E_Q[B^0] + w_2(\alpha_i) E_Q[B^\pi], \tag{5.20}$$

where w_1 and w_2 are positive weight functions that satisfy $w_1 + w_2 = 1$. Both $E_Q[B^0]$ and $E_Q[B^\pi]$ can be computed efficiently with a very small overhead to $Q[G]$. Except for simple factors, the corrections are time-independent and can be precomputed. We find that due to cancellation of digits, the time-independent terms in the corrections need to be precomputed using quadruple precision to achieve the $O(h^5)$ quadrature we employ here. This quadrature is obtained from (5.15) for $m = 1$ and the appropriate corrections $E_Q[B^0]$ and $E_Q[B^\pi]$.

5.2.2 Time Integration: Removing the Surface-tension Induced Stiffness

Through the curvature, surface tension introduces high order derivatives of the interface position that couple nonlinearly and nonlocally with the flow. The presence of high order space derivatives causes a severe time step stability constraint for explicit time integration schemes. Hou *et al.* [23] have designed an ingenious technique to remove the severe stability constraint, i.e., stiffness. In their method, the interface evolution

equations in terms of the tangent angle θ and the arclength metric $s_\alpha = \sqrt{x_\alpha^2 + y_\alpha^2}$ are

$$s_{\alpha t} = T_\alpha - \theta_\alpha U, \tag{5.21}$$

$$\theta_t = \frac{1}{s_\alpha}(U_\alpha + T\theta_\alpha), \tag{5.22}$$

where T and U are the interface tangential and normal velocity respectively. The stiffness is hidden at the small spatial scales of U_α in the θ-equation. The leading order behavior of U at small scales can be obtained by noting that, for $x \neq 0$, the leading order terms of the integrands in the velocity [Eq. (5.6) and Eq. (5.7)] are

$$-\frac{2x\gamma y_\alpha}{s_\alpha^2(\alpha' - \alpha)} \quad \text{and} \quad \frac{2\gamma x_\alpha}{s_\alpha^2(\alpha' - \alpha)} \tag{5.23}$$

for the radial and axial velocity respectively. Therefore, it can be easily shown that

$$U(\alpha, t) \sim \frac{1}{2s_\alpha}\mathcal{H}[\gamma](\alpha, t), \tag{5.24}$$

where $\mathcal{H}$ is the Hilbert transform which is diagonalizable by the Fourier transform as $\hat{\mathcal{H}}[f] = -i\text{sign}(k)\hat{f}$. Moreover, γ is dominated by the surface tension term $S\kappa_1$ at small scales, that is

$$\gamma(\alpha, t) \sim S\kappa_{1\alpha} = S\left(\frac{\theta_\alpha}{s_\alpha}\right)_\alpha. \tag{5.25}$$

Therefore,

$$U(\alpha, t) \sim \frac{S}{2s_\alpha}\mathcal{H}[(\theta_\alpha/s_\alpha)_\alpha](\alpha, t). \tag{5.26}$$

This dominant term at small scales simplifies if the arc-length metric s_α is constant in space. This can be achieved by exploiting the freedom in selecting the tangential velocity, as the interface motion is solely determined by the normal velocity U. By letting

$$T(\alpha, t) = \int_0^\alpha \theta_{\alpha'} U d\alpha' - \frac{\alpha}{2\pi}\int_0^{2\pi} \theta_{\alpha'} U d\alpha', \tag{5.27}$$

s_α is maintained constant and equal to its mean at all times, i.e., $s_\alpha = L(t)/2\pi$, where $L(t)$ is the total length of the curve in the cross section at time t. The equations of motion can now be written as

$$L_t = -\int_0^{2\pi} \theta_{\alpha'} U d\alpha', \tag{5.28}$$

$$\theta_t = \frac{S}{2}\left(\frac{2\pi}{L}\right)^3 \mathcal{H}[\theta]_{\alpha\alpha\alpha} + P, \tag{5.29}$$

where P represents lower order terms at small spatial scales. L can be updated by an explicit method as Eq. (5.28) is free of stiffness. To remove the high-order stiffness, it is sufficient to discretize implicitly the leading order term in Eq. (5.29) and to treat the lower order term P explicitly. This gives a linear time-step stability constraint, i.e., $\Delta t \leq Ch$, where Δt is the time-step size and C is a constant. Moreover, because of its constant coefficients, the implicit term can be easily inverted by using the fast Fourier transform. Here, we use the fourth order explicit/implicit method to update θ (Eq. (4.22)).

Note that, at each time step, γ has to be obtained from the integral Eq. (5.8) to compute the velocities. As pointed out by Baker *et al.* [3], (5.8) can be solved efficiently by fixed point iteration accelerated with a good initial guess. Here, we use a fourth order extrapolated initial guess constructed from previous time steps. It typically takes a few iterations to obtain a convergent solution for γ when the interface is relatively smooth.

5.2.3 Filtering and Numerical Stability

To test our implementation of the fifth order quadrature for the evaluation of the principal-value boundary integrals, we compute the motion of a vortex sheet in a homogeneous incompressible inviscid fluid in the absence of surface tension. This test example allows us also to illustrate some important issues concerning numerical stability. We use the following initial data:

$$x(\alpha, 0) = \cos(\alpha), \qquad y(\alpha, 0) = \sin(\alpha), \qquad \gamma(\alpha, 0) = \cos(\alpha),$$

which corresponds to the cross section of a spherical sheet. This is the problem computed by Nitsche [44], and by Nie and Baker [41], using two different quadratures. Note that for this problem γ is constant in time and only the interface position needs to be updated. Thus, the computational cost is significantly less than that of the axisymmetric suction flow where γ has to be obtained from the integral Eq. (5.8) every time step.

Figure 5.2 shows the Fourier spectrum of the boundary integrals for the initial data. This is a plot of the magnitude of the Fourier coefficients of the complex vortex sheet velocity $u + iv$ [Eq. (5.6) and Eq. (5.7) with $Q = 0$]. The integrals are computed using

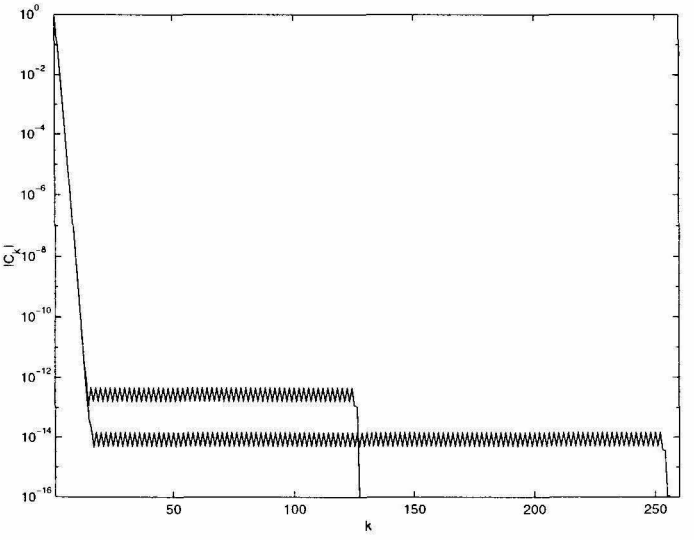

Figure 5.2: Fourier spectrum of the velocity $u + iv$ for the initial data of the spherical vortex sheet. The velocity was computed using the fifth order quadrature with $N = 256$ and $N = 512$.

Nitsche's fifth order quadrature with $N = 256$ and $N = 512$. Here N is the total number of uniformly spaced points along the complete interface ($\alpha \in [0, 2\pi]$). Note that there is a plateau of high frequency modes for each N. The plateau comes from the non-smooth discretization error. Its level decreases by approximately a factor of 32 when the resolution is doubled. If this plateau is not removed, the coupling of the interface position with the velocity will cause a rapid growth of the high frequency modes of the numerical solution and this will in turn lead to numerical instability.

Krasny filtering [37] provides a way of removing the high frequency modes introduced by the non-smooth discretization error in the velocity integrals. Given a grid-defined function f_i, Krasny filter is implemented by taking the FFT of f_i, setting to zero all

the Fourier modes of f_i whose magnitude are below a certain level, and transforming back. Note that to maintain accuracy, the filter level must be chosen as low as possible. Typically, it is selected in the order of 10^3 times the round-off error.

Using the L-θ formulation given by (5.28) and (5.29) with $N = 2048$ points and $\Delta t = 0.0001$, we compute the motion of the initially spherical vortex sheet. At every time step, the velocity is filtered with a level set to 7.5×10^{-11}. All the computations presented here are performed with standard double precision. In addition, to prevent the spurious growth of round-off error high-frequency modes under the Kelvin-Helmholtz instability, Krasny filtering is applied to θ with a filter level set to 10^{-13}. Figure 5.3 shows the interface profile, the mean curvature, and the spectrum of the velocity at $t = 1.09$. Figure 5.3(b) gives clear indications of a curvature singularity developing at the interface. The spectrum of the velocity is free of any sign of numerical instability.

It is important to note that the vortex sheet remains smooth at the poles $\alpha = 0$ and $\alpha = \pi$ at all times. As we will see in the next section, this is not the case for the axisymmetric flows we are interested in. Since the quadrature we use is based on a Taylor expansion about the symmetry poles, the accuracy deteriorates as the poles lose regularity. Very high spatial resolution is required to maintain the high frequency components of the non-smooth discretization error below an acceptable filter level. In addition, γ couples with the principal-value boundary integrals through the integral Eq. (5.8). This extra coupling makes the computation more sensitive to numerical instability than that for a vortex sheet where γ is constant (zero surface tension) or explicitly determined (with surface tension). In our implementation, the integral equation (5.8) is solved iteratively. The iteration process is stopped when the difference between two subsequent iterations is less than a tolerance set to 10^{-11}. Krasny filtering is applied to u and v given by (5.6) and (5.7) in every iteration used to solve for γ. The filter level for u and v is selected lower (smaller) than 10^{-11} to guarantee the convergence of the iterations up to the tolerance level but high enough so that the non-smooth part of the error is removed. After the iterations are completed at every time step, γ is also filtered wit h a filter level slightly higher than the iteration tolerance. To summarize, filtering is applied as follows for the computation of the axisymmetric flow interface motion:

- Filter θ every time step with a level set to 10^{-13}. This is a typical filter level for

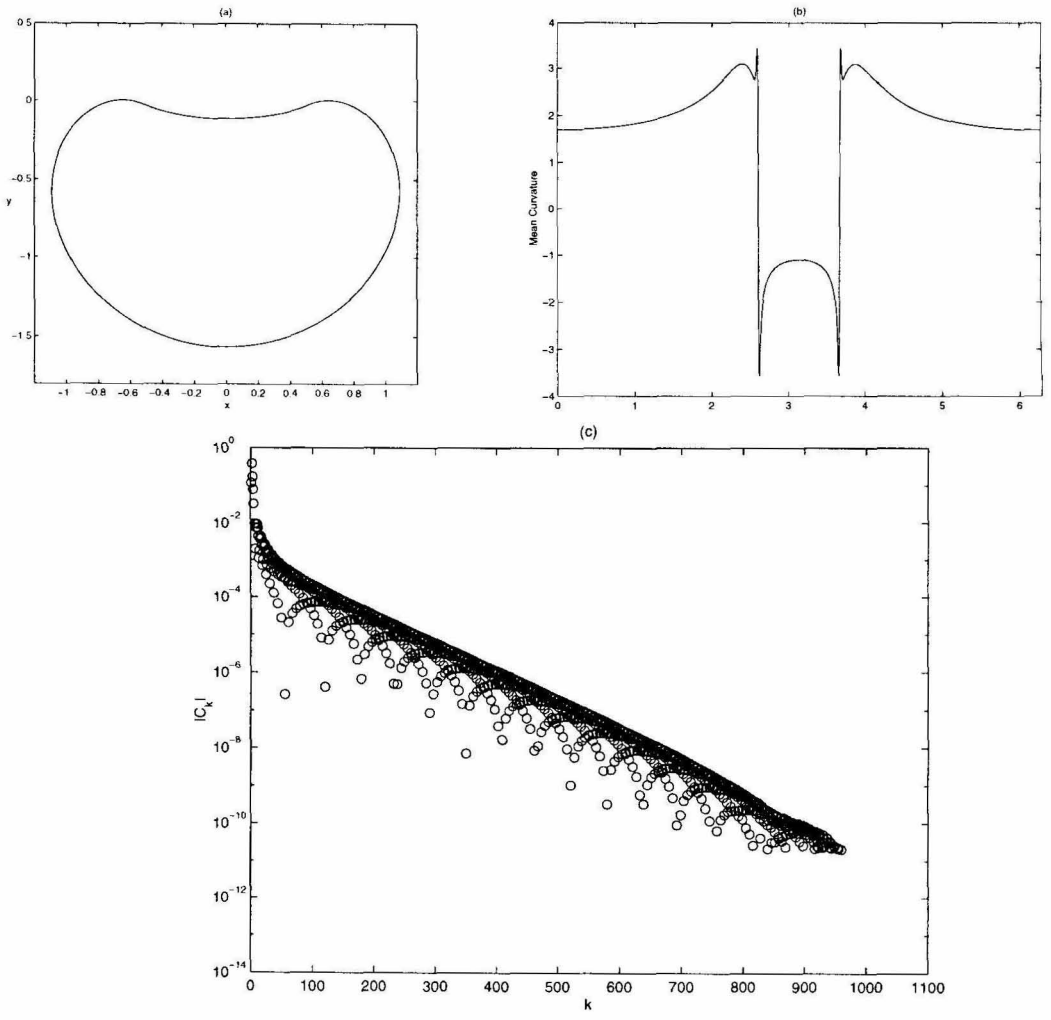

Figure 5.3: Vortex sheet test run. These plots correspond to $t = 1.09$ with $N = 2048$ and $\Delta t = 0.0001$. (a) Cross section of the vortex sheet. (b) Mean curvature versus α. (c) Fourier coefficient $|c_k|$ of the complex velocity $u + iv$.

double precision computations.

- Filter u and v for every iteration used to solve for γ with a level equal to 10^{-12}.
- Filter γ after the iterations are completed at every time step with a level set to 2.5×10^{-11}.
- Filter the boundary integrals (u and v) with a level set to 7.5×10^{-11} to compute the normal velocity. This filter level is higher because of the filtering applied to γ.

5.3 Numerical Results

We now present the numerical results obtained for two different sets of initial data: a spherical interface centered at $(0, -0.1, 0)$ (see Fig. 5.1) and a slightly perturbed spherical interface corresponding to one of the Hele-Shaw flows considered by Nie and Tian [42]. In both cases the sink is located at the origin. Most of the computations start with $N = 512$ and $\Delta t = 0.0001$. N is doubled before all the Fourier modes of the tangent angle $\theta(\alpha, t)$ are above the filter level equal to 10^{-13}. The time step Δt is selected so that decreasing it further would not produce any appreciable difference within plotting resolution in the curvature of the interface. At the same time, Δt is chosen sufficiently small so that with Krasny filtering applied every time step, the growth of the high frequency components introduced by the discretization error in the boundary integrals is kept under control. This is in effect what dictates the size of Δt and not the surface tension stiffness which has been removed by the technique of Hou *et al.* [23]. Indeed, we find that, before the interface begins to deform at one pole, the method we use has only the linear constraint $\Delta t \leq Ch$.

We consider first the initially spherical interface. Figure 5.4 shows the interface cross section profile at different times for $S = 0.01$. A three-dimensional perspective of the interface for the last computed time $t = 0.179876$ is presented in Fig. 5.5. Just as in the Hele-Shaw flow, a thin finger develops. As it gets closer to the sink, the finger evolves rapidly into a cone. The cone forms much earlier than the wedge in the Hele-Shaw flow. Also, the diameter of the top of the finger is smaller for the axisymmetric flow. These differences may be due in part to the stronger suction force in the three-dimensional flow.

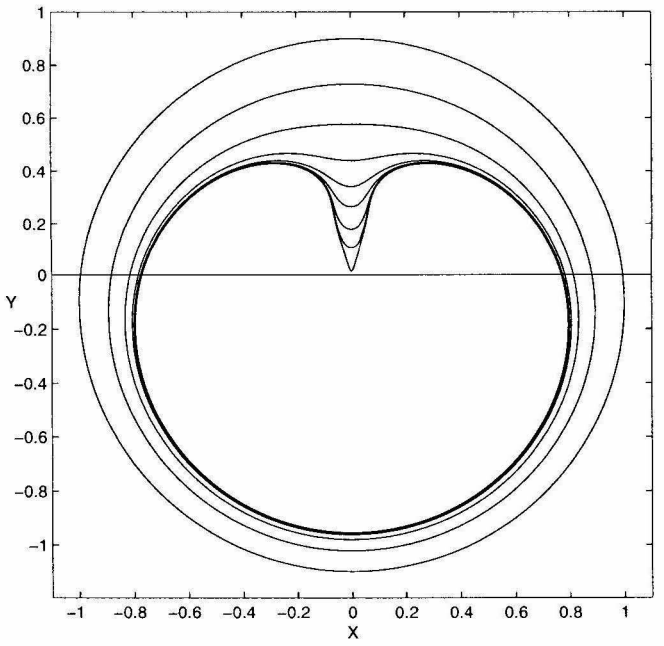

Figure 5.4: Evolution of the initially spherical blob of fluid with $S = 0.01$. The interface profiles, from the outer perimeter inwards, correspond to the times $t = 0$, 0.1, 0.15, 0.171, 0.1768, 0.1786, 0.1795, 0.1798, and 0.179876. $N = 4096$ and $\Delta t = 5 \times 10^{-8}$ for the last stage of the motion.

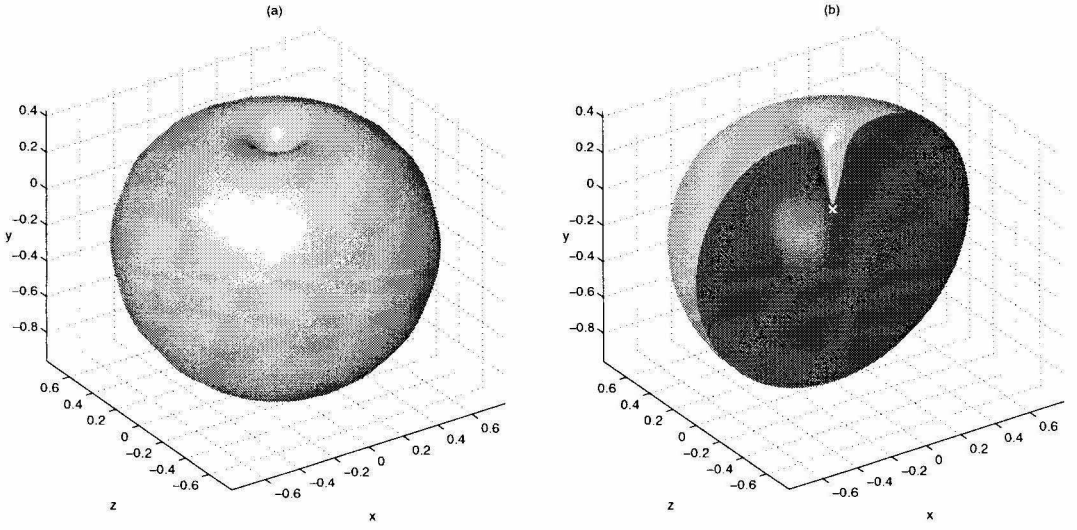

Figure 5.5: The fluid surface for $S = 0.01$ at $t = 0.179876$. (a) Three-dimensional perspective. (b)Cut-away plot.

We stop the computation when the distance of the cone tip to the sink is 0.0148. At this time, the formation of a corner singularity at the tip of the cone as the it reaches the sink is evident. This can be clearly appreciated in the plot of the tangent angle $\theta(\alpha, t)$ in Fig. 5.6. The angle appears to develop a discontinuity at the finger tip ($\alpha = \pi$). The mean curvature at the tip at that time is around -671. We use $N = 4096$ and

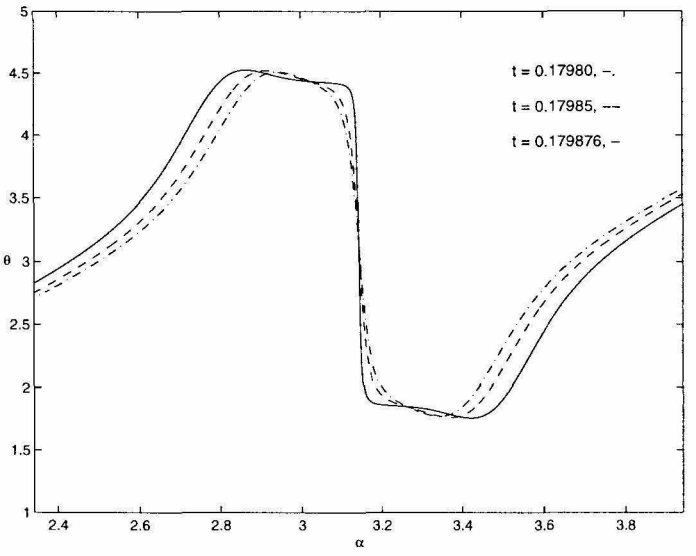

Figure 5.6: Behavior of the tangent angle $\theta(\alpha, t)$ around the finger tip ($\alpha = 0$) as the interface is about to collapse, for $S = 0.01$. The tangent angle, plotted against α at the times $t = 0.17980$, $t = 0.17985$, and $t = 0.179876$, appears to develop a discontinuity. $N = 4096$ and $\Delta t = 1 \times 10^{-7}$ for $t = 0.17980$ and $t = 0.17985$. $N = 4096$ and $\Delta t = 5 \times 10^{-8}$ for $t = 0.179876$.

$\Delta t = 5 \times 10^{-8}$ for the last stage of the computation. This is the maximum resolution we can afford and, as we explain next, it is also the minimum resolution needed to compute the motion up to this stage.

As mentioned before, the accuracy in the evaluation of the boundary integrals in the equations of motion relies on the smoothness of interface at the symmetry poles $\alpha = 0$ and $\alpha = \pi$. However, for the initial data we just considered, the interface is the least smooth, and eventually singular, precisely at one of the poles where the finger develops. As a result, we are forced to increase the spatial resolution to maintain accuracy and to keep the non-smooth discretization error in the approximation of the boundary integrals below our filter level. Figure 5.3 shows the spectrum of the normal velocity for two different resolutions at $t = 0.1723$, right after the interface begins to deform at the north

pole $\alpha = \pi$. As illustrated by this figure, it is necessary to use $N = 1024$ to have the

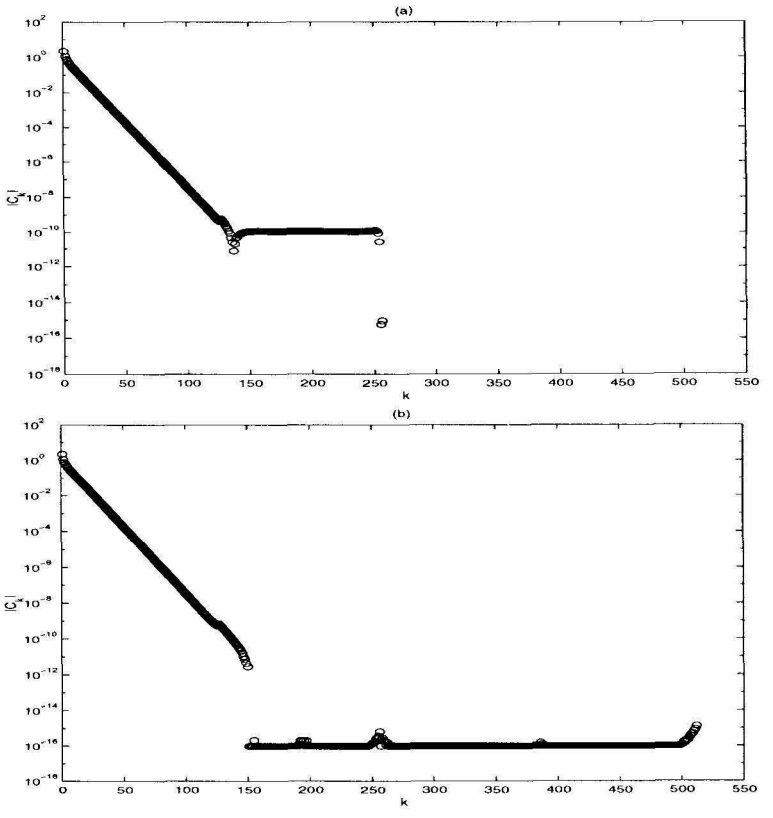

Figure 5.7: The Fourier coefficients $|c_k|$ of the normal velocity at $t = 0.1723$: (a) $N = 512$ and (b) $N = 1024$.

plateau of high frequency components below the filter level. Note that this happens well before all the Fourier modes of the numerical solution has been used for the $N = 512$ resolution.

An additional factor that makes our computation very sensitive to numerical instability is the coupling of γ with the principal-value boundary integrals. This coupling occurs through the integral equation which is solved for γ iteratively every time step. After the iterations are completed at every time step, Krasny filtering is also applied to γ. The time step Δt is selected sufficiently small so that, with Krasny filtering applied to θ and γ every time step, the growth of the discretization error in the boundary integrals is kept under control. Figure 5.8 shows that a very small Δt is required to suppress the growth of unstable high frequency modes in the normal velocity.

We now decrease the surface tension to the value $S = 4 \times 10^{-4}$. Figure 5.9 shows

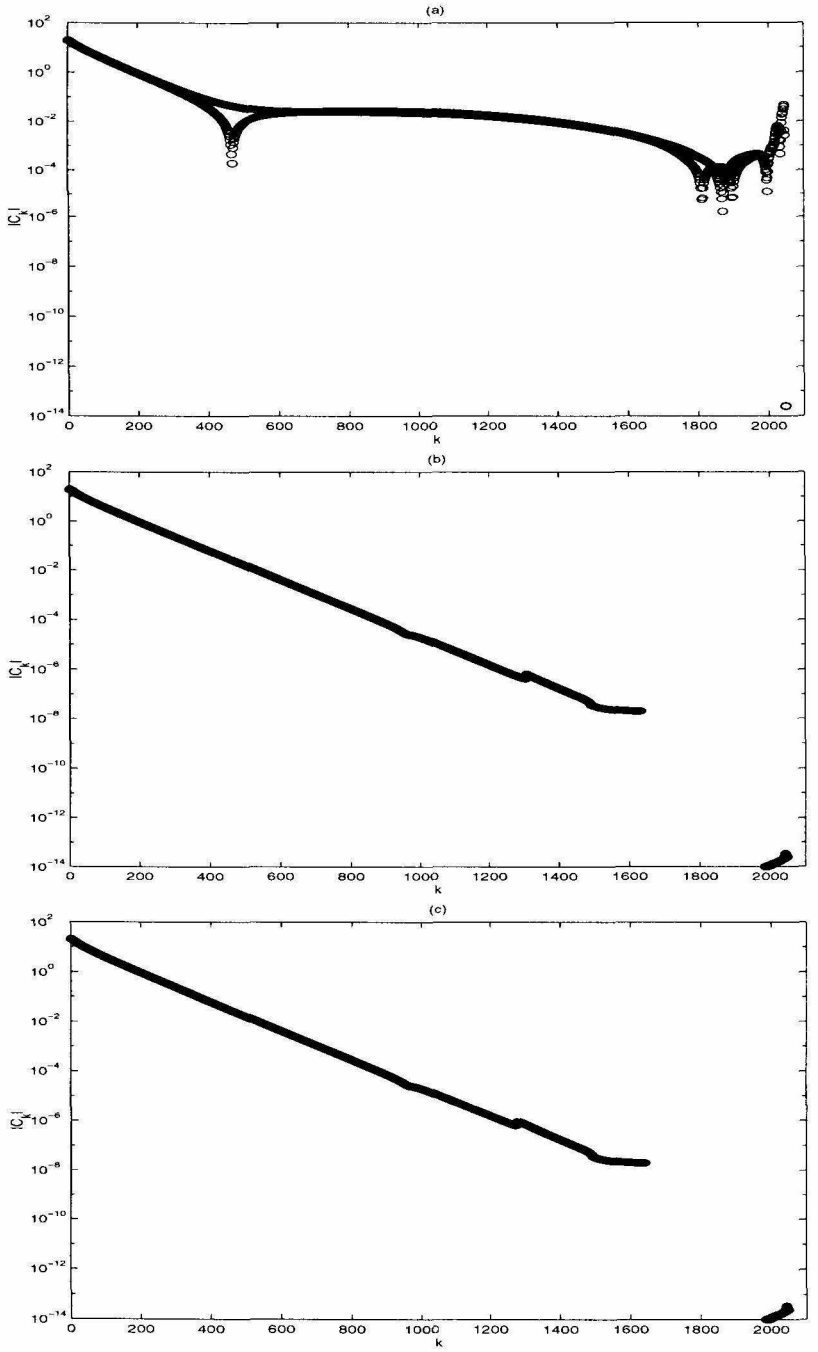

Figure 5.8: The Fourier coefficients $|c_k|$ of the normal velocity at $t = 0.17987$ with $N = 4096$: (a) $\Delta t = 2 \times 10^{-7}$; (b) $\Delta t = 1 \times 10^{-7}$; (c) $\Delta t = 5 \times 10^{-8}$.

the interface cross section profile at various times. The developed finger now clearly

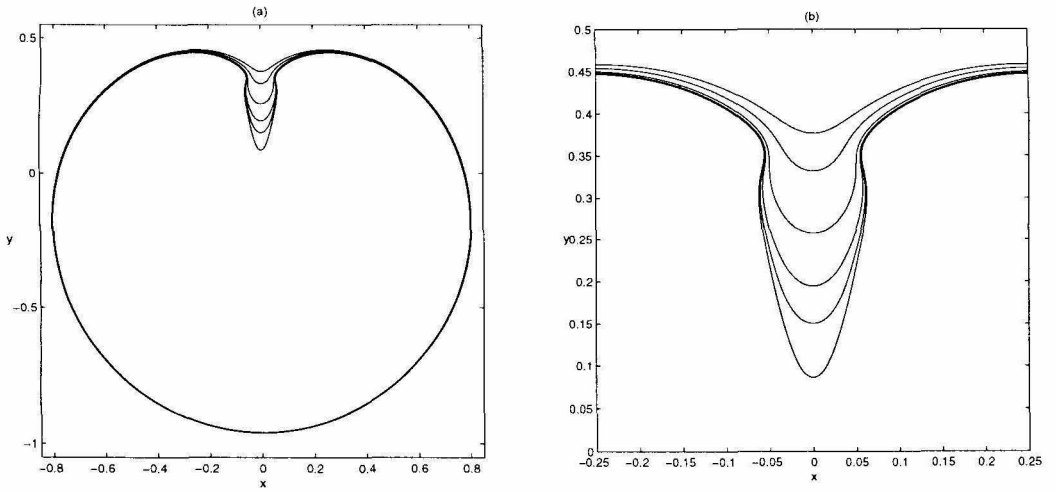

Figure 5.9: Evolution of the fluid interface for $S = 4 \times 10^{-4}$. (a) The interface cross section profile plotted at $t = 0.1729$, 0.1739, 0.1749, 0.1754, 0.1756, and 0.175734. (b) A close-up of the finger formation. $N = 4096$ and $\Delta t = 2 \times 10^{-8}$ for the last stage of the motion.

bulges and a well defined neck is observed. A comparison with the Hele-Shaw flow for the same value of surface tension appears in Fig. 5.10. The interfaces are not plotted at the same time t but when the tip of the finger reaches 0.0865 for both cases. The finger in the axisymmetric flow shows a more visible bulging and a more pronounced neck. A curvature plot for these two interfaces given in Fig. 5.11 shows that the two-dimensional mean curvature κ_1 is more singular in the axisymmetric flow. In Fig. 5.11, the two symmetric spikes correspond to the location of the neck while the two small dips next to the spikes correspond to the bulging area. The large negative spike at $\alpha = \pi$ points to the formation of a corner singularity.

In Fig. 5.12, we plot the two principal curvatures κ_1 and κ_2, and the mean curvature $\kappa = \kappa_1 + \kappa_2$ for the interface in the axisymmetric flow with $S = 4 \times 10^{-4}$ at $t = 0.175734$. From this plot, we see the effect of the curvature in the axial direction. At the location of the neck, κ_1 has a positive spike while κ_2 is negative. This smooths the interface at the neck (but κ_1 is still dominant). However, at the bulging area, immediately next to the neck, both κ_1 and κ_2 are negative and thus, together, enhance the finger bulging.

For Hele-Shaw flow, there is an asymptotic shape of the fingers at the late stage of the interface motion [10]. We compare in Fig. 5.13 the interface profile for the axisymmetric

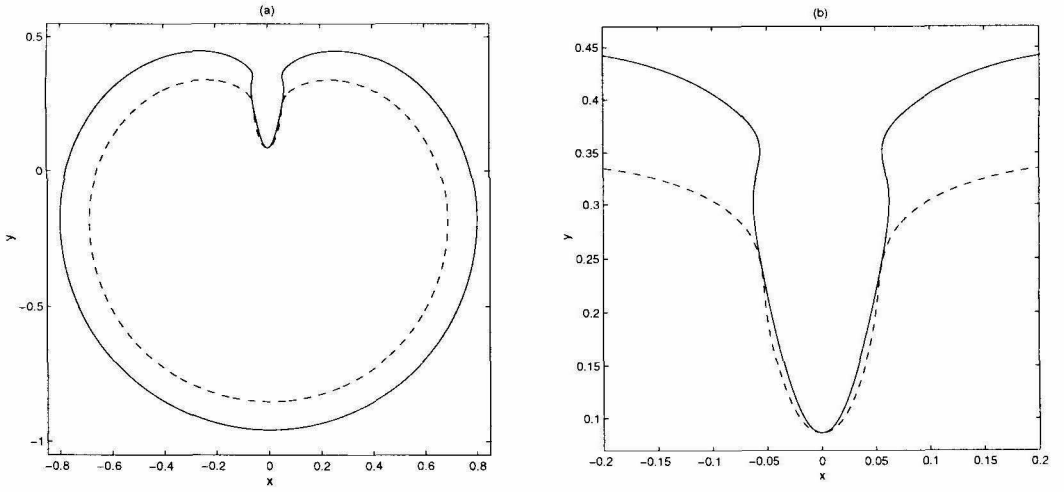

Figure 5.10: (a) Cross section profile of the axisymmetric flow at $t = 0.175734$ and the Hele-Shaw flow at $t = 0.2922625$ with the same surface tension $S = 4 \times 10^{-4}$. (b) A close-up look of the fingers. The solid curve corresponds to the axisymmetric flow and the dashed line corresponds to the Hele-Shaw flow. $N = 4096$ and $\Delta t = 2 \times 10^{-8}$ for the axisymmetric flow. $N = 2048$ and $\Delta t = 2.5 \times 10^{-6}$ for the Hele-Shaw flow.

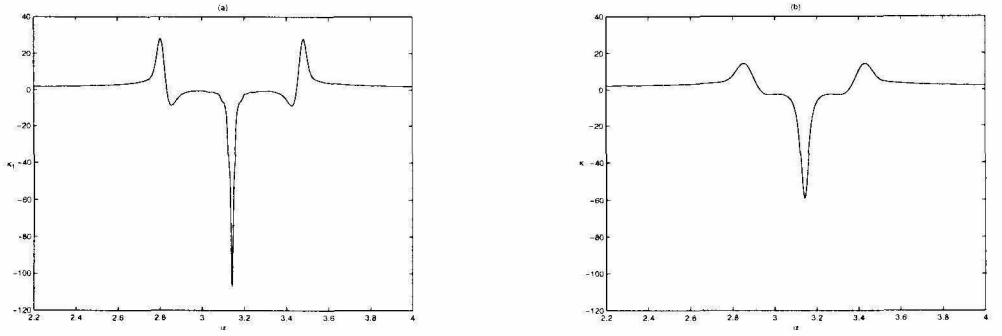

Figure 5.11: Comparison of the interface two-dimensional mean curvature (κ_1) for the axisymmetric and the Hele-Shaw flows with $S = 4 \times 10^{-4}$. (a) κ_1 versus α for the axisymmetric flow at $t = 0.175734$. $N = 4096$ and $\Delta t = 2 \times 10^{-8}$. (b) κ_1 versus α for the Hele-Shaw flow at $t = 0.2922625$. $N = 2048$ and $\Delta t = 2.5 \times 10^{-6}$.

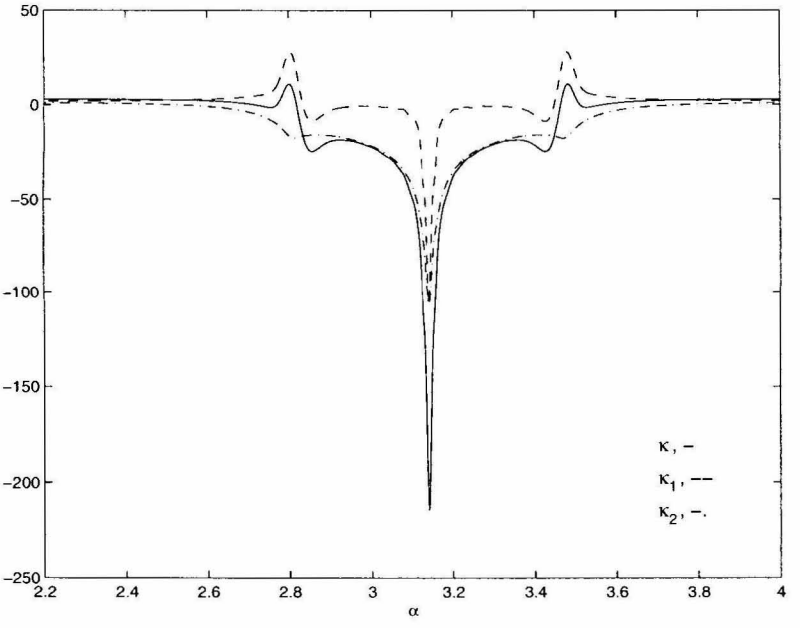

Figure 5.12: Axisymmetric-flow curvature components at $t = 0.175734$ for $S = 4 \times 10^{-4}$. The solid line corresponds to $\kappa = \kappa_1 + \kappa_2$. The dashed line corresponds to κ_1 (two-dimensional mean curvature) and the dashed-dotted line to κ_2. $N = 4096$ and $\Delta t = 2 \times 10^{-8}$.

flow for $S = 4 \times 10^{-4}$ at $t = 0.175734$ and for $S = 8 \times 10^{-4}$ at $t = 0.176129$ when the finger tip reaches around 0.086. The finger width varies very little away from the neck and an asymptotic shape is conceivable based on the similar behavior observed in the Hele-Shaw flow.

Next, we consider the second initial data. The initial interface is now given by the conformal mapping [42]

$$f(\omega) = \alpha\omega + \frac{\beta\omega}{1 - \omega_0\omega}. \tag{5.30}$$

Here $f = x + iy$ and the coefficients α, β, and ω_0 are determined by the following system of equations

$$\alpha\beta + \alpha^2 = r_1^2 + 1/2, \tag{5.31}$$

$$\frac{\beta^2}{(1-\omega_0^2)^2} + \alpha\beta = r_2^2, \tag{5.32}$$

$$\frac{\omega_0}{1-\omega_0^2}\beta + \omega_0\alpha = r_1 + r_2, \tag{5.33}$$

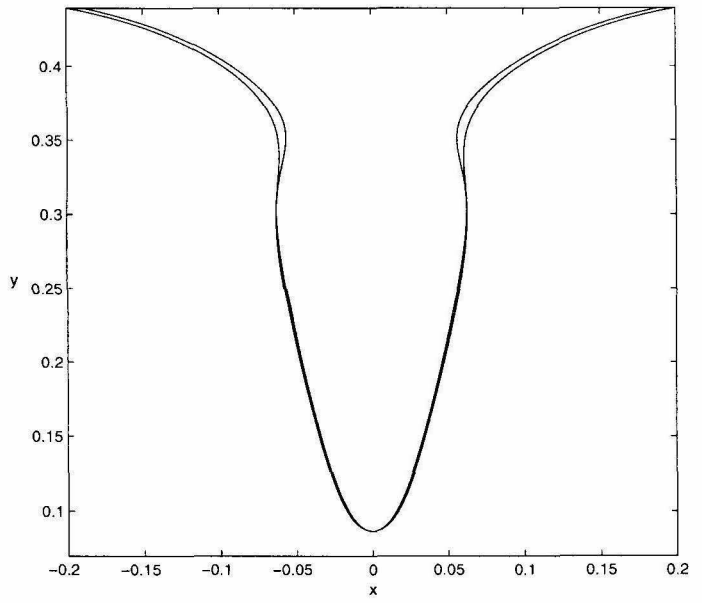

Figure 5.13: Comparison of the interface finger in the axisymmetric flow for two different values of surface tension, $S = 4 \times 10^{-4}$ at $t = 0.175734$ and $S = 8 \times 10^{-4}$ at $t = 0.176129$. $N = 4096$ and $\Delta t = 2 \times 10^{-8}$ for $S = 4 \times 10^{-4}$. $N = 4096$ and $\Delta t = 2.5 \times 10^{-8}$ for $S = 8 \times 10^{-4}$.

with $r_1 = 0.7$ and $r_2 = 0.1$. After solving numerically (5.31), (5.32), and (5.33), we get $\alpha \approx 0.9902$, $\beta \approx 0.0094$, and $\omega \approx 0.78799$. The mapping f generates a slightly perturbed circular profile in the $x - y$ plane. The point sink is, as before, at the origin. This is one of the sets of initial data considered by Nie and Tian [42]. In the absence of surface tension, the Hele-Shaw interface separates into one big and one small circle. Nie and Tian refer to this as the "big and small circle" data. One reason we choose this initial interface is that the fingers will not form at the poles and thus, the quadrature maintains its accuracy better.

Figure 5.14 presents the Hele-Shaw interface at various times with surface tension $S = 0.002$. Two long fingers form and approach the sink at the same pace. Each finger develops a corner at its tip when it touches the sink. In our computation for the axisymmetric flow, we start with $N = 256$ points and we are able to use all the modes of the numerical solution before we double the number of points. Figure 5.15 pictures the axisymmetric flow interface at various times for $S = 0.002$. Similar to the Hele-Shaw flow, the interface forms two long fingers which are drawn into the sink. We stop our computation at $t = 0.283179$. At this stage we use $N = 4096$ and $\Delta t =$

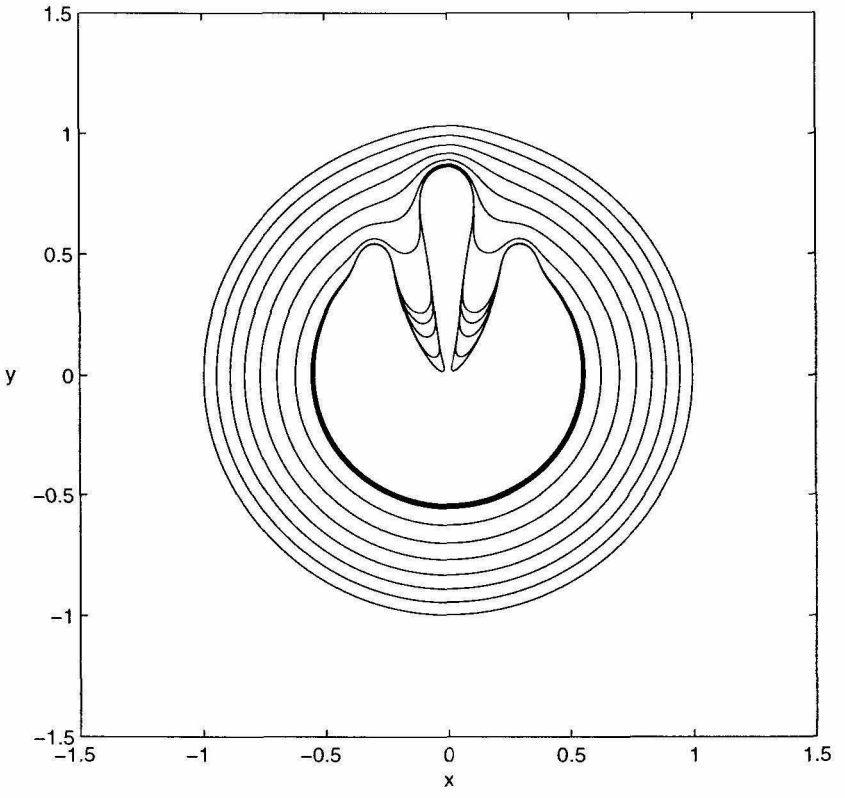

Figure 5.14: Evolution of the "big and small circles" initial interface with $S = 0.002$ for a Hele-Shaw flow. The interface profiles, from the outer perimeter inwards, correspond to the times $t = k \times 0.05$ for $k = 0, .., 6, t = 0.342 + k \times 0.04$, for $k = 0, .., 4$, and $t = 0.355388$. $N = 4096$ and $\Delta t = 1 \times 10^{-6}$ for the last stage of the motion.

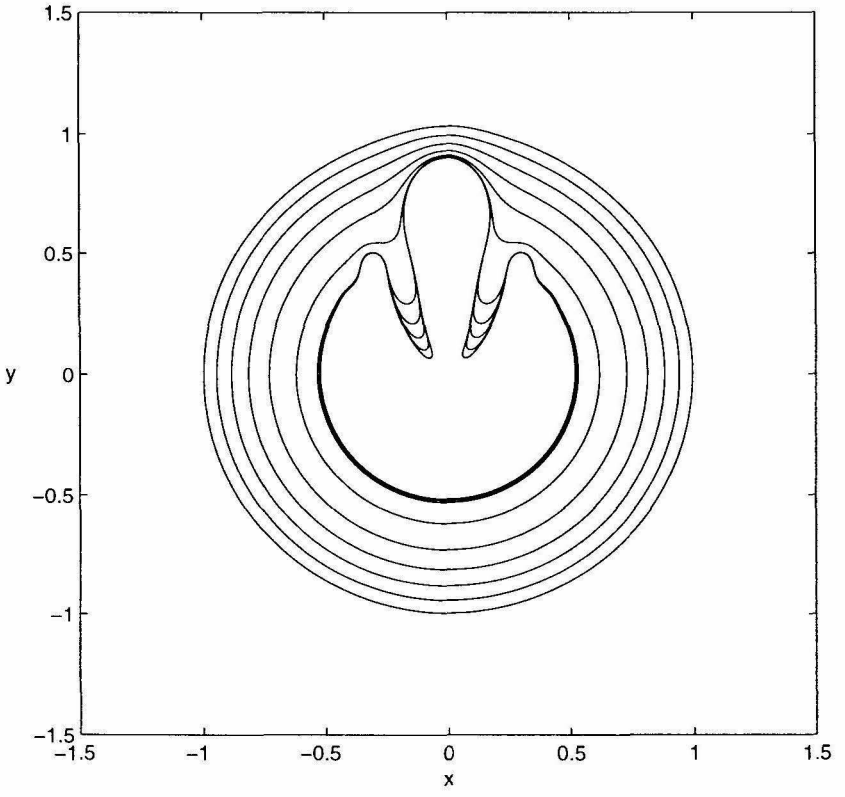

Figure 5.15: Evolution of the fluid interface in the axisymmetric flow for the slightly perturbed sphere corresponding to the two-dimensional "big and small circles" initial data with $S = 0.002$. The curves, from the outer perimeter inwards, correspond to the times $t = 0, 0.05$, 0.10, 0.15, 0.20, 0.25, 0.279, 0.2815, 0.2825, 0.283, and 0.283179. $N = 4096$ and $\Delta t = 5 \times 10^{-7}$ for the last stage of the motion.

5×10^{-7}. Continuing the computation requires using $N = 8192$ points and turns out to be prohibitly expensive as the number of iterations to solve for γ also increases.

The three-dimensional perspective of the fluid interface at $t = 0.283179$ is shown in Fig. 5.16.

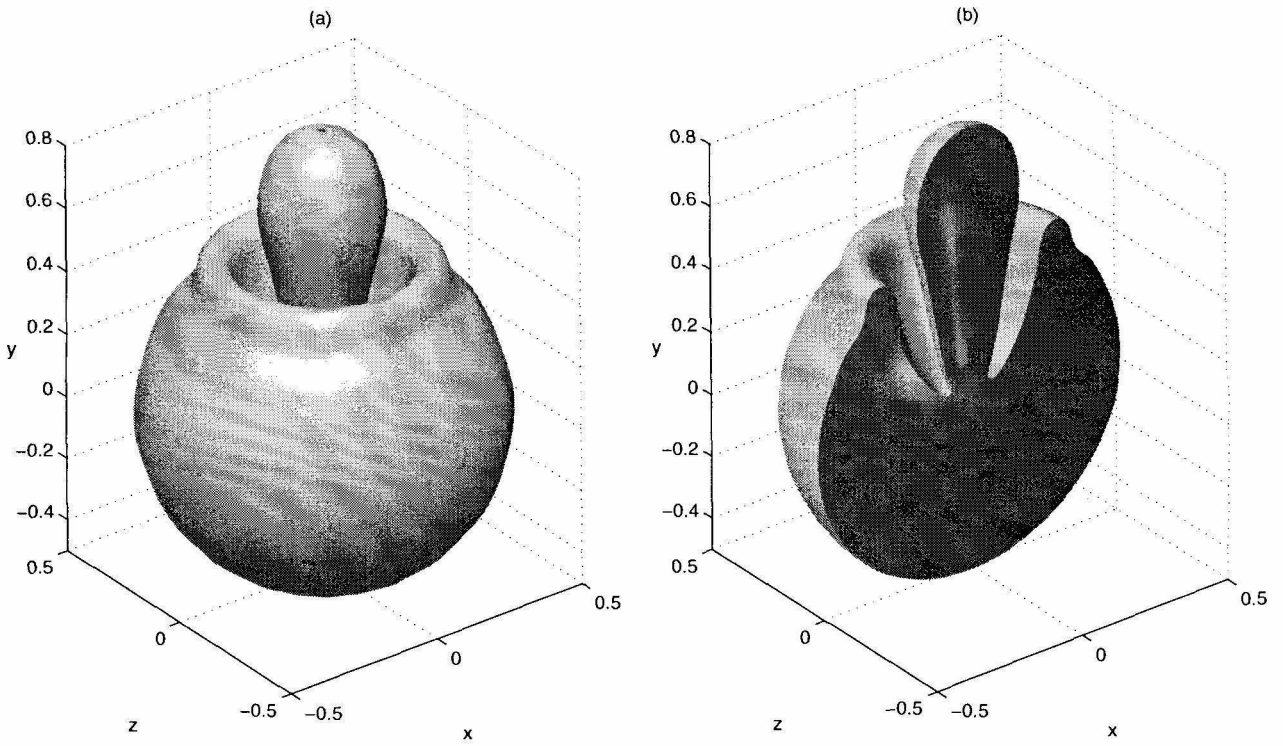

Figure 5.16: The fluid interface for the slightly perturbed spherical initial surface corresponding to the two-dimensional "big and small circles" for $S = 0.002$ at $t = 0.179876$. (a) Three-dimensional perspective. (b) Cut-away plot.

The sequence of pictures presented in Fig. 5.17 contrasts the differences between the Hele-Shaw and the axisymmetric flow interfaces. Note that the central bulb is wider in the axisymmetric flow but the fingers are thinner.

We now decrease the surface tension to the value $S = 5 \times 10^{-4}$. Figure 5.18 shows the axisymmetric flow interface at different times as it evolves. Due to the growth of the round-off error noise, and to the interface singular behavior, well resolved computations for such small values of surface tension are extremely difficult. We compare the profile of the interfaces for $S = 5 \times 10^{-4}$ and $S = 2.5 \times 10^{-4}$ in Fig. 5.19 when they reach around the same level in y. The oscillation next to the fingers is likely to be due to the influence of noise. Figure 5.19(b) shows the close-up plots of the two fingers. We shift

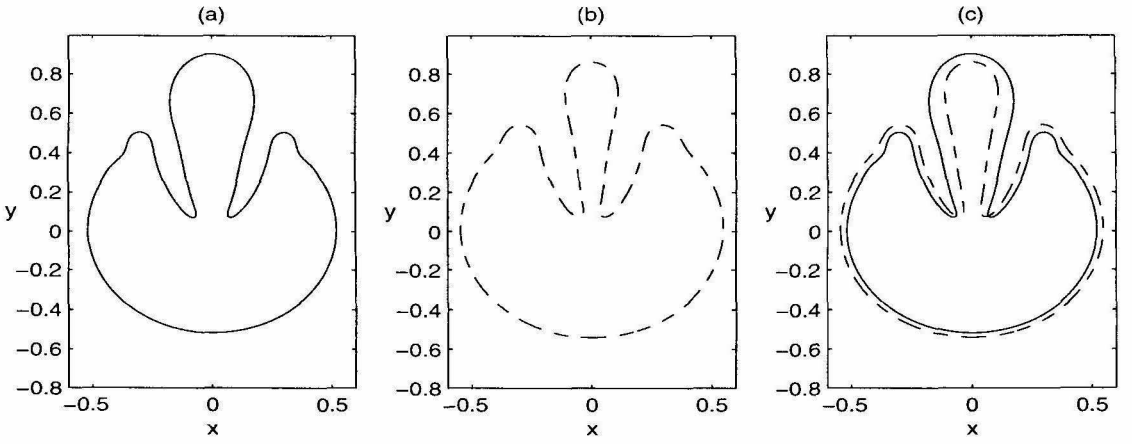

Figure 5.17: Comparison of the axisymmetric flow at $t = 0.283179$ with the Hele-Shaw flow at $t = 0.3542$. (a) Axisymmetric flow. (b) Hele-Shaw. (c) Both interfaces; solid line axisymmetric flow and dashed line Hele-Shaw flow. $N = 4096$ and $\Delta t = 5 \times 10^{-7}$ for the axisymmetric flow. $N = 2048$ and $\Delta t = 5 \times 10^{-6}$ for the Hele-Shaw flow.

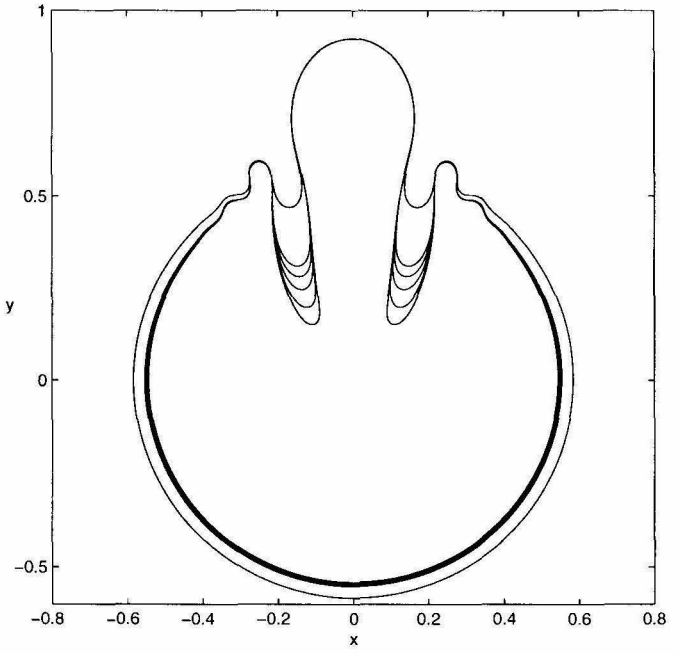

Figure 5.18: Cross section interface profiles showing the evolution of the axisymmetric flow for the slightly perturbed spherical initial data for $S = 5 \times 10^{-4}$ at $t = 0.2625$, 0.2725, 0.2735, 0.2745, 0.2755, and 0.276152. $N = 2048$ and $\Delta t = 2 \times 10^{-6}$ for the last stage of the computation.

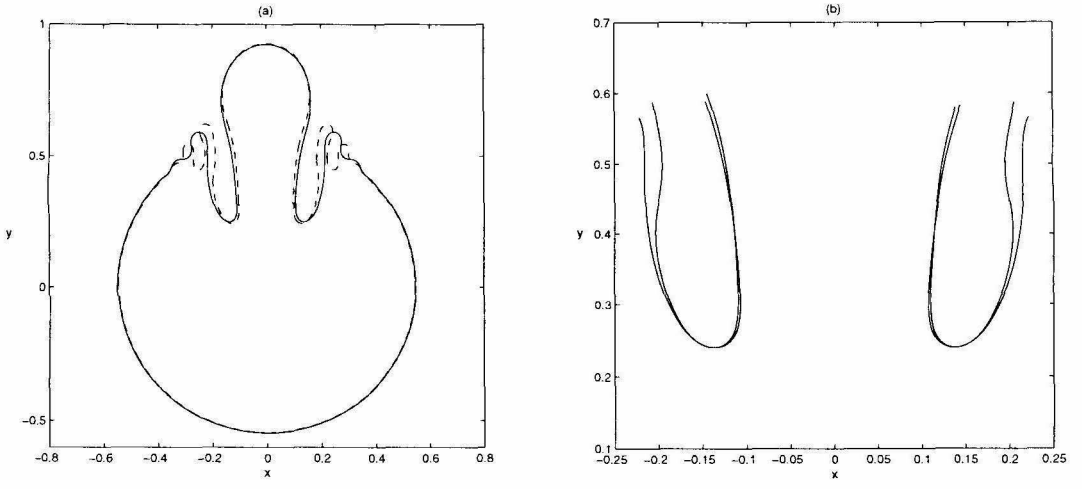

Figure 5.19: Comparison of the interface profiles for the axisymmetric flow with $S = 5 \times 10^{-4}$ at $t = 0.2745$ and $S = 2.5 \times 10^{-4}$ at $t = 0.275$. (a) Cross section profile. The solid line corresponds to $S = 5 \times 10^{-4}$ and the dashed line corresponds to $S = 2.5 \times 10^{-5}$. (b) Close-up look at the interface fingers. The inner curve is for $S = 2.5 \times 10^{-4}$, but it has been translated to align with the $S = 5 \times 10^{-4}$ fingers. $N = 2048$ and $\Delta t = 2 \times 10^{-6}$.

the fingers for $S = 2.5 \times 10^{-4}$ in x direction to align with the $S = 5 \times 10^{-4}$ fingers to ease the comparison. For $S = 5 \times 10^{-4}$, the narrowest width for the finger is about 0.1, and it is about 0.06 for $S = 2.5 \times 10^{-4}$.

Chapter 6

Conclusions

In the first part of this thesis, new formulations and new methods are presented for computing the motion of a curvature driven three-dimensional filament and surface. These numerical methods have no high order time step stability constraints. We applied our methods to compute the motion of two-dimensional vortex sheets with surface tension, motion of three-dimensional filament by curvature, the Kirchhoff rod model, anti–parallel vortex filaments and simplified three-dimensional water wave model on Gaussian waves and gravity waves. Our numerical results convincingly demonstrate that our methods remove the severe time step stability constraint associated with explicit discretizations for both two-dimensional and three-dimensional interfaces.

In the second part of this thesis, we numerically study the two-dimensional Hele-Shaw problem with suction and three-dimensional axisymmetric flow through porous media with suction. We find several interesting phenomena as surface tension is decreased for both flows. Fingers form and quickly develop into wedges, in two dimensions, and cones, in three dimensions, as they approaches the sink. An asymptotic shape of the fingers is observed at the late stages of the interface motion and the angle of the wedge and cone at the tip of the finger is selected in the limit as surface tension tends to zero. Moreover, for sufficiently small values of surface tension, a well-defined neck develops at the top of the finger. The developing finger bulges but, being drawn strongly by the sink, quickly evolves into the wedge or cone. We also observe that the axisymmetric flow develops narrower fingers than those found in the Hele-Shaw counterpart. The additional azimuthal component of the mean curvature simultaneously enhances the definition of the finger neck and smoothes the interface there.

Bibliography

[1] U.M. Ascher, S.J. Ruuth, and B. Wetton. Implicit-explicit methods for time-dependent partial differential equations. *SIAM J. Numer. Anal.*, 32:797–823, 1995.

[2] G.R. Baker, D.I. Meiron, and S.A. Orszag. Vortex simulations of the Rayleigh-Taylor instability. *Phys. Fluids*, 23:1485–1490, 1980.

[3] G.R. Baker, D.I. Meiron, and S.A. Orszag. Generalized vortex methods for free-surface flow problems. *J. Fluid Mech.*, 123:477–501, 1982.

[4] G.R. Baker, D.I. Meiron, and S.A. Orszag. Boundary integral methods for axisymmetric and three-dimensional Rayleigh-Taylor instability problems. *Physica D*, 12:19–31, 1984.

[5] G.R. Baker and M.J. Shelley. On the connection between thin vortex layers and vortex sheets. *J. Fluid Mech.*, 215:161–194, 1990.

[6] D. Bensimon. Stability of viscous fingering. *Phys. Rev. A*, 33(2):1302–1308, 1986.

[7] B.De Bernadinis and D.W. Moore. *A ring-vortex representation of an axi-symmetric vortex sheet, in Studies of Vortex Dominated Flows.* Springer-Verlag, Berlin/New York, 1986.

[8] R.E. Caflisch and X.F. Li. Lagrangian theory for 3D vortex sheets with axial or helical symmetry, Transport Theory Statist. Phys., 21:559–, 1992.

[9] A.J. Callegari and L. Ting. Motion of a curved vortex filament with decaying vortical core and axial velocity. *SIAM J. Appl. Maths*, 35:148–175, 1978.

[10] H.D. Ceniceros, T.Y. Hou, and H. Si. Numerical study of Hele-Shaw flow with suction. *Phys. of Fluids*, 11(9):2471–2486, 1999.

[11] E.S. Chan and W.K. Melville. Deep-water plunging wave pressures on a vertical plane wall. *Proc. R. Soc. Lond. A*, 417:95–131, 1988.

[12] M.J. Cooker and D.H. Peregrine. Violent water motion at breaking-wave impact. *Coastal Engineering*, 1:164–176, 1990.

[13] M.J. Cooker and D.H. Peregrine. Violent motion as near breaking waves meet a vertical wall at breaking-wave impact. *Breaking Waves (IUTAM Symposium Sidney), Australia*, 1:291–297, 1992.

[14] S. Crow. Stability theory for a pair of trailing vortices. *AIAA J.*, 8:2172–2179, 1970.

[15] W. Dai and M.J. Shelley. A numerical study of the effect of surface tension and noise on an expanding Hele-Shaw bubble. *Phys. Fluids A*, 5:2131–2146, 1993.

[16] A.J. DeGregoria and L.W. Schwartz. A boundary-integral method for two-phase displacement in Hele-Shaw cells. *J. Fluid Mech.*, 164:383–400, 1986.

[17] E. DiBenedetto and A. Friedman. The ill-posed Hele-Shaw model and the Stefan problem for supercooled water. *Trans. Am. Math. Soc.*, 282:183–204, 1984.

[18] D.J. Dichmann, Y. Li, and J.H. Maddocks. Hamiltonian formulations and symmetries in rod mechanics. *IMA Volumes in Mathematics and its Applications*, 82, 1996.

[19] E.H. Dill. Kirchhoff theory of rods. *Arch. Hist. Exact*, 44:1–23, 1992.

[20] J. Duchon and R. Robert. Évolution d'une interface par capillarité et diffusion de volume I. Existence locale en temps. *Ann. Inst. Henri Poincaré*, 1(5):361–378, 1984.

[21] D. Haroldsen and D. Meiron. Numerical calculation of three-dimensional interfacial potential flows using the point vortex method *SIAM J. Sci. Comput.*, 20(2):648–683, 1999.

[22] T.Y. Hou, I. Klapper, and H. Si. Removing the stiffness of curvature in computing 3-D filaments. *J. Comput. Phys.*, 143:628–664, 1998.

[23] T.Y. Hou, J.S. Lowengrub, and M.J. Shelley. Removing the stiffness from interfacial flows with surface tension. *J. Comput. Phys.*, 114:312–338, 1994.

[24] T.Y. Hou, Z.H. Teng, and P.W. Zhang. Well-posedness of linearized motion for 3-D water-waves far from equilibrium. *Communications in Partial Diff. Equations*, 21:1551–1585, 1996.

[25] S.D. Howison, A.A. Lacey, and J.R. Ockendon. Hele-Shaw free-boundary problems with suction. *Q. JI Mech. Appl. Math.*, 41:183–193, 1988.

[26] S.D. Howison, J.R. Ockendon, and A.A. Lacey. Singularity development in moving-boundary problems. *Q. JI Mech. Appl. Math.*, 38:343–360, 1985.

[27] J.S. Janger. Instabilities and pattern formation in crystal growth. *Rev. Modern Phys.*, 52:1–28, 1980.

[28] J.P. Keener and J.J. Tyson. The dynamics of scroll waves in excitable media. *SIAM rev.*, 34:1–39, 1992.

[29] E.D. Kelly and E.J. Hinch. Numerical simulations of sink flow in the Hele-Shaw cell with small surface tension. *Euro. Jnl. of Applied Maths*, 8(6):533–550, 1997.

[30] D.A. Kessler, J. Koplik, and H. Levine. Geometrical models of interface evolution. ii. numerical simulation. *Physical Review A*, 3161–3174, 1984.

[31] G. Kirchhoff. *Mechanik*, 28, 1876.

[32] I. Klapper. Biological applications of the dynamics of twisted elastic rods. *J. Comput. Phys.*, 125(2):325–337, 1996.

[33] I. Klapper and M. Tabor. A new twist in the kinematics and elastic dynamics of thin filamentsand ribbons. *J. Phy. A*, 27:4919–4924, 1994.

[34] R. Klein and O.M. Knio. Asymptotic vorticity structure and numerical simulation of slender vortex filaments. *J. Fluid Mech.*, 284:275–321, 1995.

[35] R. Klein and A. Majda. Self-stretching of a perturbed vortex filament i. the asymptotic equations for deviations from a straight line. *Physica D*, 49:323–352, 1991a.

[36] R. Klein, A.J. Majda, and K. Damodaran. Simplified equations for the interaction of nearly parallel vortex filaments. *J. Fluid Mech.*, 288:201–248, 1995.

[37] R. Krasny. A study of singularity formation in a vortex sheet by the point vortex approximation. *J. Fliud Mech.*, 167:65–93, 1986.

[38] D.W. Longcope and I. Klapper. Dynamics of a thin twisted flux tube. *Astrophys. J.*, 488:443–453, 1997.

[39] E. Meiburg and G.M. Homsy. Nonlinear unstable viscous fingers in Hele-Shaw flows .2. Numerical simulation. *Phys. Fluids*, 31(3):429–439, 1988.

[40] M. Muskat. *The flow of homogeneous fluids through porous media.* McGraw-Hill, New York, 1937.

[41] Q. Nie and G.R. Baker. Application of Adaptive Quadrature to Axi-symmetric Vortex Sheet Motion. *J. Comp. Phys.*, 143:49–69, 1998.

[42] Q. Nie and F.R. Tian. Singularities in Hele-Shaw flows. *SIAM J. Appl. Math*, 58(1):34–54, 1998.

[43] H. Nishimura and S. Takewaka. Experimental and numerical study on solitary wave breaking. *Coastal Engineering*, 1:1033–1045, 1990.

[44] M. Nitsche. Axisymmetric Vortex Sheet Motion: Accurate Evaluation of the Principal Value Integral. To appear in *SIAM J. Sci. Comp.*, 1999.

[45] M. Nitsche. Private communication, 1999.

[46] M. Ortiz and G. Gioia. The morphology and folding patterns of buckling-driven thin film blisters. *J. Mech. Phys. Solids*, 42:531–559, 1994.

[47] M. Ortiz, E. Repetto, and H. Si. Continuum model of kinetic roughening and coarsening in thin films. *J. Mech. Phys. Solids*, 47: 697–730, 1999.

[48] L. Paterson. Radial fingering in a Hele-Shaw cell. *J. Fluid Mech.*, 113:513–529, 1981.

[49] D. I. Pullin. Numerical studies of surface-tension effects in nonlinear Kelvin-Helmhotz and Rayleigh-Taylor instability. *J. Fluid Mech.*, 119:507–532, 1982.

[50] G. Ramachandran and T. Schlick. *Beyond Optimization: Simulating the Dynamics of Supercoiled DNA by a Macroscopic Model.* Am. Math. Soc., Providence, Rhode Island, 1995.

[51] S. Richardson. Hele-Shaw flows with a free boundary produced by the injection of fluid into a narrow channel. *Fluid Mech.*, 56:609–618, 1972.

[52] A. J. Roberts. A stable anad accurate numerical method to calculate the motion of a sharp interface between fluids. *IMA J. Appl. Math*, 31:13–35, 1983.

[53] P.G. Saffman and G.R. Baker. Vortex interaction. *Annu. Rev. Fluid. Mech.*, 11:95, 1979.

[54] T. Schlick. Modeling superhelical dna: Recent analytical and dynamic approaches. *Curr. Opin. Struct. Biol.*, 5:245–262, 1995.

[55] J. Sethian and J. Strain. Crystal growth and dendritic solidification. *J. Comp. Phys.*, 98:231–253, 1992.

[56] M.J. Shelley. A study of singularity formation in vortex sheet motion by a spectrally accurate vortex method. *J. Fluid Mech.*, 244:493–526, 1992.

[57] A. Sidi and M. Israeli. Quadrature methods for periodic singular and weakly singular Fredholm integral equations. *J. Sci. Comp.*, 3:201–231, 1988.

[58] M. Siegel, S. Tanveer, and W. Dai. Singular effects of surface tension in evolving Hele-Shaw flows. *J. Fluid Mech.*, 323:201–236, 1996.

[59] J.J. Stoker *Differential Geometry*, Pure and Applied Mathematics XX, Wiley-interscience, 1969.

[60] S. Tanveer. Evolution of Hele-Shaw interface for small surface tension. *Phil. Trans. R. Soc. Londs. A*, 343:155–204, 1993.

[61] F.R. Tian. On the breakdown of Hele-Shaw solutions with non-zero surface tension. *J. Nonlinear Sci.*, 5:479–484, 1995.

[62] G. Tryggvason. Numerical simulations of the Rayleigh-Taylor instability. *J. Comp. Phys.*, 75:253–282, 1988.

[63] G. Tryggvason and H. Aref. Numerical experiments in Hele-Shaw flows with a sharp interface. *J. Fluid Mech.*, 136:1–30, 1983.

[64] J.J. Tyson and S.H. Strogatz. *Int. J. Bifur. Chaos*, 1:723, 1991.

[65] E.E. Zajac. *J. Applied Mechanics*, 29:138, 1962.